

ABSTRACT

Title of Document: PRACTICAL ASPECTS OF ACOUSTIC SOURCE LOCALIZATION USING POLYMER-CARBON BLACK COMPOSITE PHASED ARRAYS.

Robert T. Cullen, Master of Science, 2015

Directed By: Professor Amr Baz, Mechanical Engineering

An array of Carbon Black (*CB*) filled polyurethane sensors is developed to identify the location and intensity of a single acoustic source. The manufacturing procedure of the proposed array is outlined, in details, and several prototypes are manufactured. Characterization of the viscoelastic and piezo-resistive material properties of different samples of the *CB* filled polyurethane is carried out using Dynamic, Mechanical, Thermal Analyzer (*DMTA*) and uni-axial compression testing. The structural, dynamical, and sensing performance characteristics of the array sensor are modeled mathematically using the theory of finite elements and utilizing the well-known localization theories of phased arrays.

The experimental performance characteristics of the proposed array sensor are evaluated in comparison to an array of conventional condenser microphones. The purpose of such an experimental effort is to demonstrate the capabilities and

limitations of the proposed array sensor as compared with conventional condenser microphones. Furthermore, the obtained experimental results are utilized to validate the theoretical predictions of the localization of acoustic sources.

It is envisioned that the proposed *CB* filled polyurethane array sensor presents a cost effective and viable means for identifying the location and intensity of acoustic sources which can vary from stationary to moving sources in air or underwater. Accordingly, the applications of such an array sensor are only limited by our imagination.

PRACTICAL ASPECTS OF ACOUSTIC SOURCE LOCALIZATION USING
POLYMER-CARBON BLACK COMPOSITE PHASED ARRAYS.

By

Robert T. Cullen

Thesis submitted to the Faculty of the Graduate School of the
University of Maryland, College Park, in partial fulfillment
the requirements for the degree of
[Master of Science]
[2015]

Advisory Committee:
Professor Amr Baz Chair
Professor Jaydev Desai
Professor Nikhil Chopra

© Copyright by

Robert T. Cullen

2015

Acknowledgements

This research has been funded by King Saud University (Visiting Professors Program) and by King Abdul-Aziz City for Science and Technology (*KACST*), Project Number 30-380.

Table of Contents

Acknowledgements.....	ii
Table of Contents	iii
List of Tables	v
List of Figures	vi
Chapter 1: Introduction	1
1.1 Overview.....	1
1.2 Background on Pressure Measurement.....	2
1.3 Array Processing.....	8
1.4 Scope of the Thesis	14
Chapter 2: Manufacturing Procedure.....	16
2.1 Introduction.....	16
2.1.1 Polyurethane	16
2.1.2 Conductivity.....	16
2.1.3 Carbon Black (<i>CB</i>) Particles.....	17
2.1.4 Polyurethane Manufacturing Process	17
2.2 Manufacturing Procedure Development	18
2.2.1 Inclusion of <i>CB</i> Particles in Polyurethane	19
2.2.2 Amount of <i>CB</i> Filled Polyurethane.....	22
2.2.3 Vacuum Treatment.....	22
2.2.4 Curing	24
2.2.5 Mold Design.....	26
2.3 Finalized Manufacturing Procedure.....	29
2.4 Summary	32
Chapter 3: Material Property Characterization	33
3.1 Background	33
3.1.1 Complex Modulus.....	33
3.1.2 DMTA Testing.....	34
3.1.3 Polarization	37
3.2 DMTA Testing Results	37
3.2.1 Oven-Curing vs. Press-Curing.....	40
3.2.2 Impact of <i>CB</i> Inclusion on Polyurethane Material Properties	43
3.2.3 Consistency of Viscoelastic Properties	46
3.2.4 Polarization Effect on Viscoelastic Properties.....	51
3.2.5 Average Viscoelastic Properties	59
3.3 Summary	60
Chapter 4: Carbon Black Sensor Model	62
4.1 Base Vibration Model.....	62
4.1.1 Introduction.....	62
4.1.2 Single Element Definition.....	63
4.1.3 Generation of Interpolation Equations – Single Element	64
4.1.4 Displacement & Velocity Fields – Single Element	68
4.1.5 Kinetic Energy – Single Element.....	70

4.1.6 Strain Field – Single Element	76
4.1.7 Potential Energy – Single Element	88
4.1.8 Generation of Global Kinetic & Potential Energy Equations	93
4.1.9 Equations of Motion	96
4.2 Plate Model Results	97
4.2.1 Plate Model Details	97
4.2.2 Natural Frequencies & Mode Shapes	98
4.2.3 Forced Response	101
4.3 Inclusion of Conductive Polymer Sensors	106
4.4 Coupled Model Forced Response Results	112
4.5 Calculation of Input Force	126
4.6 Summary	128
Chapter 5: Acoustic Model	130
5.1 Acoustic Source Model	130
5.2 Acoustic Source Localization Method (Pressure Sensor Array)	138
5.3 Forced Response of the System Due to Acoustic Source	143
5.4 Acoustic Source Localization Method (CB Sensor Array)	149
5.5 Summary	154
Chapter 6: Acoustic Source Localization Experiment (Condenser Microphone Array)	
.....	155
6.1 Experimental Setup	155
6.2 Results	159
6.3 Summary	167
Chapter 7: Acoustic Source Localization (Carbon Black Sensors)	168
7.1 Experimental Setup	170
7.1.1 Setup Details	170
7.1.2 Selection of Acoustic Source	177
7.2 Results	181
7.2.1 Introduction	181
7.2.2 Comparison of Experimental Setup to Vibration Model	183
7.2.3 Array Processing Results	194
7.3 Summary	203
Chapter 8: Conclusions & Future Work	206
8.1 Conclusions	206
8.2 Future Work	208
Appendix A	210
Appendix B	213
Bibliography	216

List of Tables

Table 2.1: Manufacturer advertised material properties for polyurethane.	16
Table 2.2: List of materials necessary to manufacture the <i>CB</i> filled polyurethane block used in this study.....	29
Table 3.1: List of DMTA tests performed.	39
Table 4.1: Boundary conditions of single-element.	66
Table 4.2: Plate properties.	98
Table 4.3: Comparison of plate model results to derived results from Leissa [10]. .	101
Table 5.1: Experimental source locations.	133
Table 6.1: Condenser microphone signal conditioning circuit component values. ..	158
Table 7.1: <i>CB</i> sensor signal condition element values.	176

List of Figures

Figure 1.1: Smart piezoelectric composite paint [29].	4
Figure 1.2: Pressure sensitive smart paint [8].	5
Figure 1.3: Relationship between the <i>Change in Resistivity</i> ($\Delta R/R$) of the <i>CB</i> filled polyurethane sensor, and the <i>Strain</i> (ϵ) experienced by the sensor.	6
Figure 1.4: <i>CB</i> filled polyurethane sensor positioned below an electromechanical speaker.	7
Figure 1.5: Results from Reference [4].	8
Figure 1.6: Pressure waves impinging on an array of receivers.	9
Figure 2.1: Vacuum pump used in <i>CB</i> manufacturing process.	23
Figure 2.2: Hydraulic press used in <i>CB</i> manufacturing process.	25
Figure 2.3: Polycarbonate mold. The black material on the surface of the polycarbonate mold above is <i>CB</i> filled polyurethane that cured to the mold when the mold release failed.	27
Figure 2.4: Aluminum mold with Teflon® coating.	29
Figure 3.1: Example of DMTA test sample configuration [11].	36
Figure 3.2: Comparison of Block 2 (oven-cured) and Block 3 (press-cured) storage moduli.	41
Figure 3.3: Comparison of Block 2 (oven-cured) and Block 3 (press-cured) loss factors.	42
Figure 3.4: % difference in storage modulus referenced to B1-S1.	42
Figure 3.5: % difference in loss factor referenced to B1-S1.	43
Figure 3.6: Comparison of Block 1 (polyurethane only) and Block 3 (20% <i>CB</i> fill) storage moduli.	45
Figure 3.7: Comparison of Block 1 (polyurethane only) and Block 3 (20% <i>CB</i> fill) loss factors.	45
Figure 3.8: Comparison of Block 4 sample storage modulus over time.	46
Figure 3.9: Comparison of Block 4 sample loss factors over time.	47
Figure 3.10: % difference in storage modulus referenced to B4-S1-96.	47
Figure 3.11: % difference in loss factor referenced to B4-S1-96.	48
Figure 3.12: Comparison of storage modulus results for various unpolarized blocks.	49
Figure 3.13: Comparison of loss factor results for various unpolarized blocks.	49
Figure 3.14: % Difference in storage modulus results referenced to B3-S1.	50
Figure 3.15: % Difference in storage loss factor results referenced to B3-S1.	50
Figure 3.16: Storage modulus values of Block 5 samples.	52
Figure 3.17: Loss factor values of Block 5 samples.	53
Figure 3.18: % Difference in Block 5 sample storage modulus values referenced to B5-S1-C144.	53
Figure 3.19: % Difference in Block 5 sample loss factor values referenced to B5-S1-C144.	54
Figure 3.20: Storage modulus values of Block 6 samples.	55
Figure 3.21: Loss factor values of Block 6 samples.	55
Figure 3.22: % Difference in Block 6 sample storage modulus values referenced to B6-S1-C120.	56

Figure 3.23: % Difference in Block 6 sample loss factor values referenced to B6-S1-C120.....	56
Figure 3.24: Storage modulus values of Block 7 samples.....	57
Figure 3.25: Storage modulus values of Block 7 samples.....	57
Figure 3.26: % Difference in Block 7 sample storage modulus values referenced to B7-S1-C168.....	58
Figure 3.27: % Difference in Block 7 sample loss factor values referenced to B7-S1-C168.....	58
Figure 3.28: <i>CB</i> filled polyurethane storage modulus.....	59
Figure 3.29: <i>CB</i> filled polyurethane loss factor.....	60
Figure 4.1: Single-element of aluminum plate FEM.....	63
Figure 4.2: Stress field in an elastic solid element due to external forces.....	76
Figure 4.3: Displacement in the x-direction due to in-plane motion of the elastic solid in the x-direction.....	78
Figure 4.4: Displacement in the x-direction due to bending of the elastic solid about the y-axis.....	79
Figure 4.5: Deformation of the elastic solid in the x-y plane.....	81
Figure 4.6: Deformation of the elastic solid in the x-z plane.....	81
Figure 4.7: Deformation of the elastic solid in the y-z plane.....	81
Figure 4.8: Assembly of individual plate elements into the complete plate system...	93
Figure 4.9: First 6 mode shapes of the aluminum plate calculated using the model derived in Chapter 4.....	100
Figure 4.10: Force distribution on aluminum plate model.....	101
Figure 4.11: Input receptance (magnitude) of the plate @ <i>CB</i> sensor array locations (No <i>CB</i>).....	103
Figure 4.12: Input receptance (phase) of plate @ <i>CB</i> sensor array locations (No <i>CB</i>).....	103
Figure 4.13: Input receptance (magnitude) of the plate @ <i>CB</i> sensor array locations (No <i>CB</i>), 900Hz - 1100Hz.....	104
Figure 4.14: Displacement of plate @ <i>CB</i> sensor array locations (No <i>CB</i>) due to 1 N distributed force.....	105
Figure 4.15: Displacement of plate @ <i>CB</i> sensor array locations (No <i>CB</i>) due to a 1N distributed force (900-1100Hz).....	105
Figure 4.16: <i>CB</i> sensor array configuration.....	107
Figure 4.17: Distributed force acting on <i>CB</i> sensors and base plate.....	108
Figure 4.18: Lumped parameter model of the <i>n</i> th <i>CB</i> sensor.....	109
Figure 4.19: Force distribution on coupled model.....	112
Figure 4.20: Transfer receptance (magnitude) between the displacement of the plate due to an input force on the <i>CB</i> sensor.....	113
Figure 4.21: Transfer receptance (phase) between the displacement of the plate due to an input force on the <i>CB</i> sensor.....	114
Figure 4.22: Input receptance (magnitude) of the <i>CB</i> sensor @ each sensor array location.....	114
Figure 4.23: Input receptance (phase) of the <i>CB</i> sensor @ each sensor array location.....	115

Figure 4.24: Comparison of plate displacement at <i>CB</i> sensor location 1 with and without <i>CB</i> sensor.	115
Figure 4.25: Comparison of plate displacement at <i>CB</i> sensor location 1 with and without <i>CB</i> sensor (900-1100Hz).	116
Figure 4.26: Comparison of plate displacement at <i>CB</i> sensor location 2 with and without <i>CB</i> sensor (900-1100Hz).	117
Figure 4.27: Comparison of plate displacement at <i>CB</i> sensor location 3 with and without <i>CB</i> sensor (900-1100Hz).	117
Figure 4.28: Comparison of plate displacement at <i>CB</i> sensor location 4 with and without <i>CB</i> sensor (900-1100Hz).	118
Figure 4.29: Comparison of plate displacement at <i>CB</i> sensor location 5 with and without <i>CB</i> sensor (900-1100Hz).	118
Figure 4.30: Comparison of plate displacement at <i>CB</i> sensor location 6 with and without <i>CB</i> sensor (900-1100Hz).	119
Figure 4.31: Comparison of plate displacement at <i>CB</i> sensor location 7 with and without <i>CB</i> sensor (900-1100Hz).	119
Figure 4.32: Comparison of plate displacement at <i>CB</i> sensor location 8 with and without <i>CB</i> sensor (900-1100Hz).	120
Figure 4.33: Comparison of plate displacement at <i>CB</i> sensor location 9 with and without <i>CB</i> sensor (900-1100Hz).	120
Figure 4.34: Comparison between <i>CB</i> sensor 1 displacement and corresponding plate displacement due to a 1 N distributed force (900-1100Hz).	121
Figure 4.35: Comparison between <i>CB</i> sensor 2 displacement and corresponding plate displacement due to a 1 N distributed force (900-1100Hz).	121
Figure 4.36: Comparison between <i>CB</i> sensor 3 displacement and corresponding plate displacement due to a 1 N distributed force (900-1100Hz).	122
Figure 4.37: Comparison between <i>CB</i> sensor 4 displacement and corresponding plate displacement due to a 1 N distributed force (900-1100Hz).	122
Figure 4.38: Comparison between <i>CB</i> sensor 5 displacement and corresponding plate displacement due to a 1 N distributed force (900-1100Hz).	123
Figure 4.39: Comparison between <i>CB</i> sensor 6 displacement and corresponding plate displacement due to a 1 N distributed force (900-1100Hz).	123
Figure 4.40: Comparison between <i>CB</i> sensor 7 displacement and corresponding plate displacement due to a 1 N distributed force (900-1100Hz).	124
Figure 4.41: Comparison between <i>CB</i> sensor 8 displacement and corresponding plate displacement due to a 1 N distributed force (900-1100Hz).	124
Figure 4.42: Comparison between <i>CB</i> sensor 9 displacement and corresponding plate displacement due to a 1 N distributed force (900-1100Hz).	125
Figure 4.43: Relative displacement between <i>CB</i> sensors and plate due to a 1 N distributed force (900-1100Hz).	126
Figure 4.44: Calculation of the input force applied to the <i>CB</i> Sensors (1 N Distributed Force)	128
Figure 5.1: Acoustic source coordinate system convention for the azimuthal angle θ	132
Figure 5.2: Acoustic source coordinate system convention for the elevation angle Φ	132

Figure 5.3: Modeled pressure distribution for a source at $ \vec{R} = 0.2032\text{m}$, $\theta = 0^\circ$, and $\varphi = 0^\circ$	133
Figure 5.4: Modeled pressure time data for a source at $ \vec{R} = 0.2032\text{m}$, $\theta = 0^\circ$, and $\varphi = 0^\circ$	134
Figure 5.5: Modeled pressure distribution for a source at $ \vec{R} = 0.2032\text{m}$, $\theta = 90^\circ$, and $\varphi = 45^\circ$	135
Figure 5.6: Modeled pressure time data for a source at $ \vec{R} = 0.2032\text{m}$, $\theta = 90^\circ$, and $\varphi = 45^\circ$	136
Figure 5.7: Modeled pressure distribution for a source at $ \vec{R} = 0.2032\text{m}$, $\theta = 120^\circ$, and $\varphi = 60^\circ$	137
Figure 5.8: Modeled pressure time data for a source at $ \vec{R} = 0.2032\text{m}$, $\theta = 120^\circ$, and $\varphi = 60^\circ$	137
Figure 5.9: Acoustic source localization of a source at $ \vec{R} = 0.2032\text{m}$, $\theta = 0^\circ$, and $\varphi = 0^\circ$ using an array of modeled pressure sensor data.....	139
Figure 5.10: Acoustic source localization of a source at $ \vec{R} = 0.2032\text{m}$, $\theta = 0^\circ$, and $\varphi = 0^\circ$ using an array of modeled pressure sensor data.....	140
Figure 5.11: Acoustic source localization of a source at $ \vec{R} = 0.2032\text{m}$, $\theta = 90^\circ$, and $\varphi = 45^\circ$ using an array of modeled pressure sensor data.....	140
Figure 5.12: Acoustic source localization of a source at $ \vec{R} = 0.2032\text{m}$, $\theta = 90^\circ$, and $\varphi = 45^\circ$ using an array of modeled pressure sensor data.....	141
Figure 5.13: Acoustic source localization of a source at $ \vec{R} = 0.2032\text{m}$, $\theta = 120^\circ$, and $\varphi = 60^\circ$ using an array of modeled pressure sensor data.....	141
Figure 5.14: Acoustic source localization of a source at $ \vec{R} = 0.2032\text{m}$, $\theta = 120^\circ$, and $\varphi = 60^\circ$ using an array of modeled pressure sensor data.....	142
Figure 5.15: Modeled input force on the <i>CB</i> sensors due to an acoustic source at $ \vec{R} = 0.2032\text{m}$, $\theta = 0^\circ$, and $\varphi = 0^\circ$	144
Figure 5.16: Modeled absolute plate displacement at the <i>CB</i> sensor locations due to an acoustic source at $ \vec{R} = 0.2032\text{m}$, $\theta = 0^\circ$, and $\varphi = 0^\circ$	145
Figure 5.17: Modeled absolute <i>CB</i> sensor displacement due to an acoustic source at $ \vec{R} = 0.2032\text{m}$, $\theta = 0^\circ$, and $\varphi = 0^\circ$	145
Figure 5.18: Modeled relative displacement between the <i>CB</i> sensors and the plate due to an acoustic source at $ \vec{R} = 0.2032\text{m}$, $\theta = 0^\circ$, and $\varphi = 0^\circ$	146
Figure 5.19: Modeled input force on the <i>CB</i> sensors due to an acoustic source at $ \vec{R} = 0.2032\text{m}$, $\theta = 90^\circ$, and $\varphi = 45^\circ$	147

Figure 5.20: Modeled absolute plate displacement at the <i>CB</i> sensor locations due to an acoustic source at $ \vec{R} = 0.2032\text{m}$, $\theta = 90^\circ$, and $\varphi = 45^\circ$	148
Figure 5.21: Modeled absolute <i>CB</i> sensor displacement due to an acoustic source at $ \vec{R} = 0.2032\text{m}$, $\theta = 90^\circ$, and $\varphi = 45^\circ$	148
Figure 5.22: Modeled relative displacement between the <i>CB</i> sensors and the plate due to an acoustic source at $ \vec{R} = 0.2032\text{m}$, $\theta = 90^\circ$, and $\varphi = 45^\circ$	149
Figure 5.23: Calculated input force on the <i>CB</i> sensors due to an acoustic source at $ \vec{R} = 0.2032\text{m}$, $\theta = 0^\circ$, and $\varphi = 0^\circ$	150
Figure 5.24: Calculated input force on the <i>CB</i> sensors due to an acoustic source at $ \vec{R} = 0.2032\text{m}$, $\theta = 90^\circ$, and $\varphi = 45^\circ$	150
Figure 5.25: Acoustic source localization of a source at $ \vec{R} = 0.2032\text{m}$, $\theta = 0^\circ$, and $\varphi = 0^\circ$ using an array of pressure force data.....	151
Figure 5.26: Acoustic source localization of a source at $ \vec{R} = 0.2032\text{m}$, $\theta = 0^\circ$, and $\varphi = 0^\circ$ using an array of pressure force data.....	152
Figure 5.27: Acoustic source localization of a source at $ \vec{R} = 0.2032\text{m}$, $\theta = 90^\circ$, and $\varphi = 45^\circ$ using an array of pressure force data.....	152
Figure 5.28: Acoustic source localization of a source at $ \vec{R} = 0.2032\text{m}$, $\theta = 90^\circ$, and $\varphi = 45^\circ$ using an array of pressure force data.....	153
Figure 6.1: Photo of condenser microphone experiment setup.....	156
Figure 6.2: Condenser microphone experiment system diagram.....	157
Figure 6.3: Condenser microphone signal conditioning electronics circuit diagram.....	158
Figure 6.4: Condenser Microphone experiment raw pilot signal for source at $ \vec{R} = 0.2032\text{m}$, $\theta = 0^\circ$, and $\varphi = 0^\circ$	160
Figure 6.5: Pilot signal phase delay artifact based on data recording window.....	160
Figure 6.6: Condenser microphone experiment pilot phase adjusted & filtered pilot signal for source at $ \vec{R} = 0.2032\text{m}$, $\theta = 0^\circ$, and $\varphi = 0^\circ$	161
Figure 6.7: Condenser microphone experiment raw CM data for source at $ \vec{R} = 0.2032\text{m}$, $\theta = 0^\circ$, and $\varphi = 0^\circ$	162
Figure 6.8: Condenser microphone experiment pilot phase adjusted & filtered CM data for source at $ \vec{R} = 0.2032\text{m}$, $\theta = 0^\circ$, and $\varphi = 0^\circ$	162
Figure 6.9: Acoustic source localization of a source at $ \vec{R} = 0.2032\text{m}$, $\theta = 0^\circ$, and $\varphi = 0^\circ$ using an array of measured CM sensor data.....	163
Figure 6.10: Acoustic source localization of a source at $ \vec{R} = 0.2032\text{m}$, $\theta = 0^\circ$, and $\varphi = 0^\circ$ using an array of measured CM sensor data.....	163

Figure 6.11: Condenser microphone experiment raw pilot signal for source at $ \vec{R} = 0.2032\text{m}$, $\theta = 120^\circ$, and $\varphi = 60^\circ$	164
Figure 6.12: Condenser microphone experiment pilot phase adjusted & filtered pilot signal for source at $ \vec{R} = 0.2032\text{m}$, $\theta = 120^\circ$, and $\varphi = 60^\circ$	165
Figure 6.13: Condenser microphone experiment raw CM data for source at $ \vec{R} = 0.2032\text{m}$, $\theta = 120^\circ$, and $\varphi = 60^\circ$	165
Figure 6.14: Condenser microphone experiment pilot phase adjusted & filtered CM data for source at $ \vec{R} = 0.2032\text{m}$, $\theta = 120^\circ$, and $\varphi = 60^\circ$	166
Figure 6.15: Acoustic source localization of a source at $ \vec{R} = 0.2032\text{m}$, $\theta = 120^\circ$, and $\varphi = 60^\circ$ using an array of measured CM sensor data.	166
Figure 6.16: Acoustic source localization of a source at $ \vec{R} = 0.2032\text{m}$, $\theta = 120^\circ$, and $\varphi = 60^\circ$ using an array of measured CM sensor data.	167
Figure 7.1: <i>CB</i> sensor voltage divider circuit.	169
Figure 7.2: Photo of <i>CB</i> sensor experiment setup (View 1).	171
Figure 7.3: Photo of <i>CB</i> sensor experiment setup (View 2).	172
Figure 7.4: Photo of <i>CB</i> sensor experiment setup (View 3).	172
Figure 7.5: Photo of <i>CB</i> sensor experiment setup (View 4).	173
Figure 7.6: <i>CB</i> sensor experiment system diagram.	173
Figure 7.7: Compressor used to drive the air-horn.	174
Figure 7.8: <i>CB</i> sensor voltage divider circuit.	175
Figure 7.9: Individual <i>CB</i> sensor signal conditioning circuit diagram.	175
Figure 7.10: Time-frequency plot of a single <i>CB</i> sensor output voltage signal for a 1kHz speaker source.	178
Figure 7.11: Time-frequency plot of a single <i>CB</i> sensor output voltage signal for a 1kHz speaker source, with the leads disconnected from the <i>CB</i> sensor.	179
Figure 7.12: Time-frequency plot of a single <i>CB</i> sensor output voltage signal for a horn source.	180
Figure 7.13: Time-frequency plot of a single <i>CB</i> sensor output voltage signal for a horn source with the leads disconnected from the <i>CB</i> sensor.	181
Figure 7.14: Comparison of mode shapes 1-3.	184
Figure 7.15: Comparison of mode shapes 4-6.	185
Figure 7.16: Measured absolute plate displacement at the <i>CB</i> sensor locations due to a horn source at $ \vec{R} = 0.2032\text{m}$, $\theta = 0^\circ$, and $\varphi = 0^\circ$	187
Figure 7.17: Measured relative displacement between the <i>CB</i> sensors and the plate due to a horn source at $ \vec{R} = 0.2032\text{m}$, $\theta = 0^\circ$, and $\varphi = 0^\circ$	187
Figure 7.18: Calculated input force on the <i>CB</i> sensors due to an acoustic source at $ \vec{R} = 0.2032\text{m}$, $\theta = 0^\circ$, and $\varphi = 0^\circ$	188
Figure 7.19: Breakdown of measured reaction forces in the <i>CB</i> sensor due to applied pressure force ($ \vec{R} = 0.2032\text{m}$, $\theta = 0^\circ$, and $\varphi = 0^\circ$).	189

Figure 7.20: Breakdown of modeled reaction forces in the <i>CB</i> sensor due to applied pressure force ($ \vec{R} = 0.2032\text{m}$, $\theta = 0^\circ$, and $\varphi = 0^\circ$).	189
Figure 7.21: Measured absolute plate displacement at the <i>CB</i> sensor locations due to a horn source at $ \vec{R} = 0.2032\text{m}$, $\theta = 90^\circ$, and $\varphi = 45^\circ$	190
Figure 7.22: Measured relative displacement between the <i>CB</i> sensors and the plate due to a horn source at $ \vec{R} = 0.2032\text{m}$, $\theta = 90^\circ$, and $\varphi = 45^\circ$	191
Figure 7.23: Calculated input force on the <i>CB</i> sensors due to an acoustic source at $ \vec{R} = 0.2032\text{m}$, $\theta = 90^\circ$, and $\varphi = 45^\circ$	192
Figure 7.24: Breakdown of measured reaction forces in the <i>CB</i> sensor due to applied pressure force ($ \vec{R} = 0.2032\text{m}$, $\theta = 90^\circ$, and $\varphi = 45^\circ$).	193
Figure 7.25: Breakdown of modeled reaction forces in the <i>CB</i> sensor due to applied pressure force ($ \vec{R} = 0.2032\text{m}$, $\theta = 90^\circ$, and $\varphi = 45^\circ$).	193
Figure 7.26: Array processing results for a horn source located at $ \vec{R} = 0.2032\text{m}$, $\theta = 0^\circ$, and $\varphi = 0^\circ$	195
Figure 7.27: Array processing results for a horn source located at $ \vec{R} = 0.2032\text{m}$, $\theta = 90^\circ$, and $\varphi = 45^\circ$	195
Figure 7.28: Ensemble-to-ensemble phase delay between the (9) separate <i>CB</i> sensor locations (Calculated pressure force, $ \vec{R} = 0.2032\text{m}$, $\theta = 0^\circ$, and $\varphi = 0^\circ$).	197
Figure 7.29: Ensemble-to-ensemble phase delay between the (9) separate runs (Microphone 1 $ \vec{R} = 0.2032\text{m}$, $\theta = 0^\circ$, and $\varphi = 0^\circ$).	198
Figure 7.30: Ensemble-to-ensemble phase delay between the (9) separate runs (Microphone 2 $ \vec{R} = 0.2032\text{m}$, $\theta = 0^\circ$, and $\varphi = 0^\circ$).	198
Figure 7.31: Ensemble-to-ensemble phase delay between the (9) separate LDV locations (Plate displacement, $ \vec{R} = 0.2032\text{m}$, $\theta = 0^\circ$, and $\varphi = 0^\circ$).	199
Figure 7.32: Ensemble-to-ensemble phase delay between the (9) separate <i>CB</i> sensor locations (Relative motion between the <i>CB</i> sensors and the plate, $ \vec{R} = 0.2032\text{m}$, $\theta = 0^\circ$, and $\varphi = 0^\circ$).	200
Figure 7.33: Ensemble-to-ensemble phase delay between the (9) separate <i>CB</i> sensor locations (Calculated pressure force, $ \vec{R} = 0.2032\text{m}$, $\theta = 90^\circ$, and $\varphi = 45^\circ$).	201
Figure 7.34: Ensemble-to-ensemble phase delay between the (9) separate runs (Microphone 1 $ \vec{R} = 0.2032\text{m}$, $\theta = 90^\circ$, and $\varphi = 45^\circ$).	201
Figure 7.35: Ensemble-to-ensemble phase delay between the (9) separate runs (Microphone 2 $ \vec{R} = 0.2032\text{m}$, $\theta = 90^\circ$, and $\varphi = 45^\circ$).	202

Figure 7.36: Ensemble-to-ensemble phase delay between the (9) separate LDV locations (Plate displacement, $|\vec{R}| = 0.2032\text{m}$, $\theta = 90^\circ$, and $\varphi = 45^\circ$)..... 202

Figure 7.37: Ensemble-to-ensemble phase delay between the (9) separate *CB* sensor locations (Relative motion between the *CB* sensors and the plate, $|\vec{R}| = 0.2032\text{m}$, $\theta = 90^\circ$, and $\varphi = 45^\circ$)..... 203

Chapter 1: Introduction

1.1 Overview

Acoustic source localization is a well-established practice that has been successfully implemented in a wide-range of applications. For instance, ships and submarines use SONAR to locate underwater objects. In seismology, acoustic source localization techniques are exploited to identify the origin of earthquakes and other seismic events. Increasingly, acoustic source localization techniques are also being applied in modern communication technologies. As an example, videoconferencing technology has started incorporating source localization to track the camera to voices in conference rooms [19]. Acoustic source localization capabilities are also being integrated into robotics technology. Reference [25] and Reference [24] propose methods for using acoustic source localization to allow robots to track and locate sound sources within their environment.

Traditionally, acoustic source localization has involved measuring the incident pressure from an acoustic source using an array of microphones. Array processing techniques are then applied to the microphone signals to identify the location of the source. Although the use of microphones in acoustic source localization applications has been very successful, the approach presents some performance limitations. An integral component of array processing performance is the size and density of the sensor array – the higher the array density, the higher the localization resolution and noise rejection. Recently, there have been many attempts to measure pressure using

new types of sensors, which have the potential of being able to offer higher array densities, at lower-costs than an equivalent array density of traditional microphones. Reference [10] presents a technique for using pressure-sensitive paint to optically measure pressure fluctuations. Reference [22] presents a technique for using a piezoelectric polymer as a high-frequency membrane hydrophone. The aforementioned are just two examples of many other novel approaches to increase array densities for acoustic source localization applications.

This thesis focuses on the use of an array of carbon black filled polyurethane conductive polymer composite sensors to perform a source localization measurement. The following sections presents a background on different methods for measuring the pressure from an acoustic source, a brief background on the array processing technique applied in this thesis, and an outline of the scope of this thesis.

1.2 Background on Pressure Measurement

Traditionally, electret condenser microphones have been used in acoustic source localization applications. These microphones offer precise pressure measurements, but can become expensive when applied in high density sensor arrays. As a result, the aerospace industry has devoted considerable attention to developing Microelectromechanical Systems (MEMS) pressure transducer arrays as a lower-cost alternative to electret condenser microphone arrays. Reference [17] and Reference [21] provide extensive reviews of the current MEMS pressure sensor technology, as well as the technologies capability to measure fluctuating pressure. Reference [26]

and Reference [14] demonstrate how MEMS pressure transducer arrays can be used to perform acoustic source localization measurements.

While MEMS microphones may offer a lower-cost alternative to electret condenser microphones in high array density applications, they still require considerable resources to manufacture. The MEMS manufacturing process utilizes specialized machinery and equipment, and usually is executed in a clean room. This thesis proposes leveraging recent developments in the field of smart paints and conductive polymer sensors as a lower-cost alternative to both traditional electret condenser microphones, as well as MEMS pressure sensors.

Considerable attention has been focused recently on the development of a wide variety of smart paints to be used as sensors for vibration, noise, and health monitoring applications. These smart paints are radically different from conventional paints, which have been traditionally used on structures to provide protective and decorative functions. One type of smart paint that is currently available is smart piezoelectric composite paint, which consists of piezoelectric powder embedded in epoxy resins. This type of smart paint forms the commonly known “0-3” composites, which consist of piezo particles randomly dispersed in a polymer matrix ([8], [11], [12], [13]).

Smart piezoelectric composite paints have received considerable acceptance as an effective class of sensors as they combine the attractive attributes of both polymer and piezoelectric particles. For example, these paints offer the high electro-active properties of piezoelectric materials and the mechanical flexibility of polymers.

However, the piezoelectric composite must be coated with layers of electrodes and then poled using a very high voltage to impart the sensing capability to the paint, as demonstrated graphically in Figure 1.1. Such complex manufacturing processes make this type of paint very expensive. Furthermore, expensive charge amplifiers are needed to monitor the capacitive signals of the smart paint sensor, making smart piezoelectric composite paints costly alternatives to traditional and MEMS microphones if used in an acoustic source localization application.

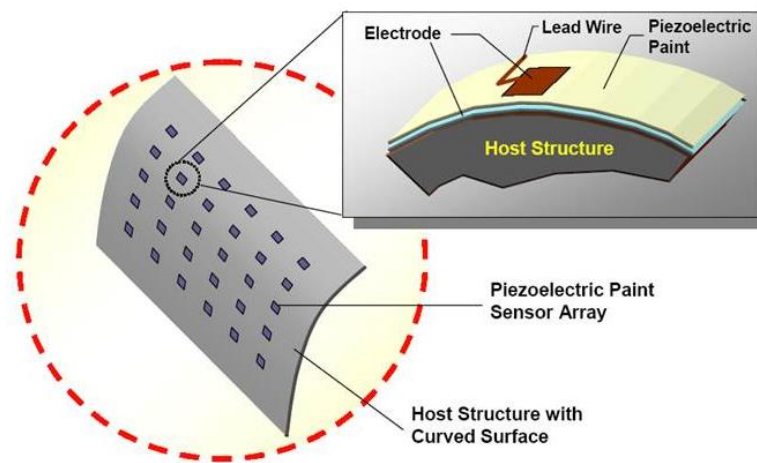


Figure 1.1: Smart piezoelectric composite paint [31].

Another type of smart paint that is currently available is pressure sensitive smart paint, shown in Figure 1.2. This type of smart paint modulates light intensity through a repeatable chemical interaction of the sensing layer with atmospheric oxygen. In order to measure the response of the paint, an expensive photo-detector such as a photomultiplier tube is required [10]. Similar to smart piezoelectric composite paints, pressure sensitive smart paints would be costly alternatives to traditional or MEMS microphones if used in an acoustic source localization application.

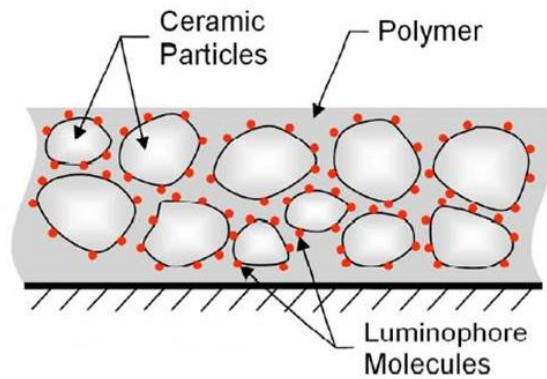


Figure 1.2: Pressure sensitive smart paint [10].

As a more cost effective approach, this thesis proposes using an array of conductive polymer composites to perform acoustic source localization. In this class of sensors, inherently insulating polymers can be made conductive when mixed with electrically conducting fillers, such as carbon black particles. The electric conduction mechanism is attributed to percolation and tunneling effect ([29], [30]). When subjected to tensile loading, the separation between adjacent filler particles increases, causing the electrical resistivity to increase. Upon application of compressive loading, the reverse scenario occurs. In this manner, strain sensing can be achieved. The sensitivity of the sensor to the applied strain depends on various factors including the type of polymer matrix, type of conductive filler, method of filler loading, and degree of strain.

Reference [1] demonstrated experimentally that a Carbon Black (CB) filled polyurethane conductive polymer composite could be used to measure the strain experienced by a cantilevered beam subjected to base excitation. Reference [1] further demonstrated that there is a relationship between the *Change in Resistivity*

($\Delta R/R$) of the *CB* filled polyurethane sensor, and the *Strain* (ε) experienced by the sensor. This relationship is illustrated in Figure 1.3 below.

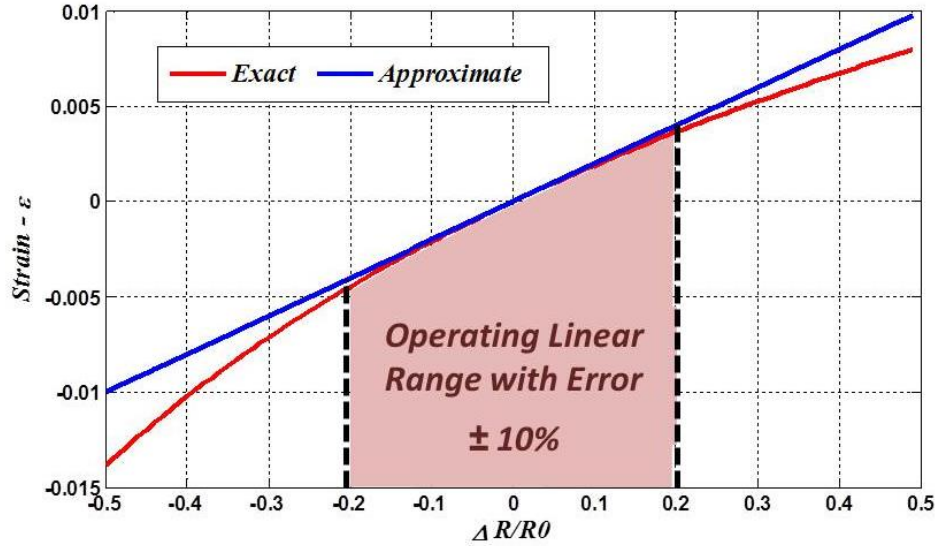


Figure 1.3: Relationship between the *Change in Resistivity* ($\Delta R/R$) of the *CB* filled polyurethane sensor, and the *Strain* (ε) experienced by the sensor.

The blue line in Figure 1.3 represents a linear approximation of the relationship between the *Strain* (ε) and *Change in Resistivity* ($\Delta R/R$), given by the following equation:

$$\varepsilon \cong \frac{1}{\bar{\gamma}} \left(\frac{\Delta R}{R} \right) \quad (1.2.1)$$

Figure 1.3 indicates that the relationship in equation (1.2.1) is only valid under the following condition if an error of less than $\pm 10\%$ between the linear approximation, and the exact relationship between the *Strain* (ε) and *Change in Resistivity* ($\Delta R/R$), is desired:

$$-0.2 < \frac{\Delta R}{R} < 0.2$$

Reference [4] expanded upon the above application and proposed using a layer of *CB* filled polyurethane to measure the incident pressure from an acoustic source. The experimental setup used in Reference [4], an electromechanical speaker positioned above a 1/16th inch thick layer of *CB* filled polyurethane, is presented below in Figure 1.4.

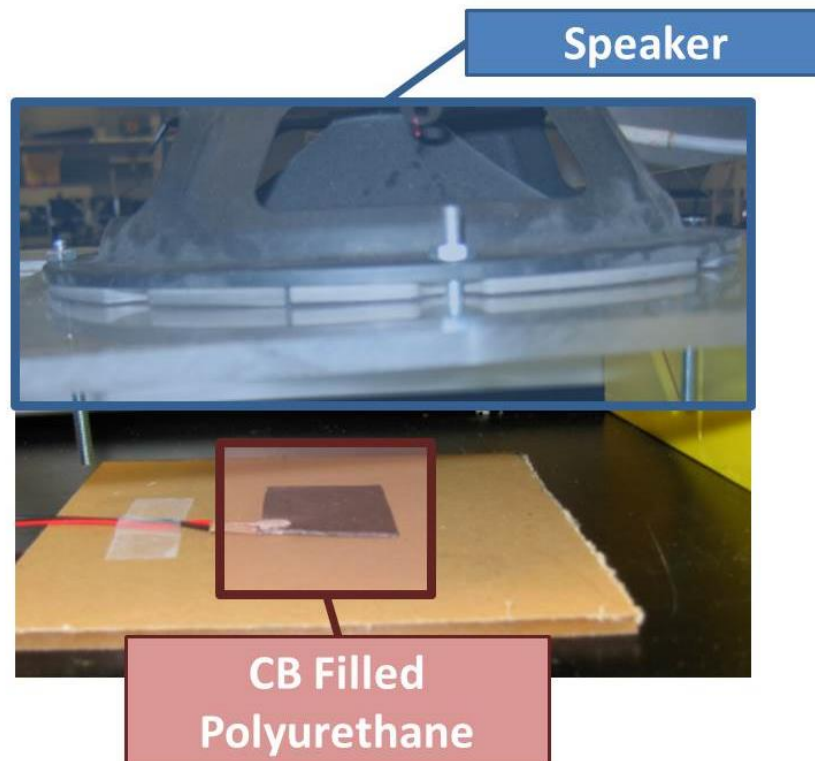


Figure 1.4: *CB* filled polyurethane sensor positioned below an electromechanical speaker.

The experiment consisted of generating a single tone with the electromechanical speaker, and then measuring the compressional strain induced in the *CB* filled polyurethane layer due to the incident pressure wave. The experiment was conducted with a 100 Hz and 1 kHz tone. The results are presented below in Figure 1.5.

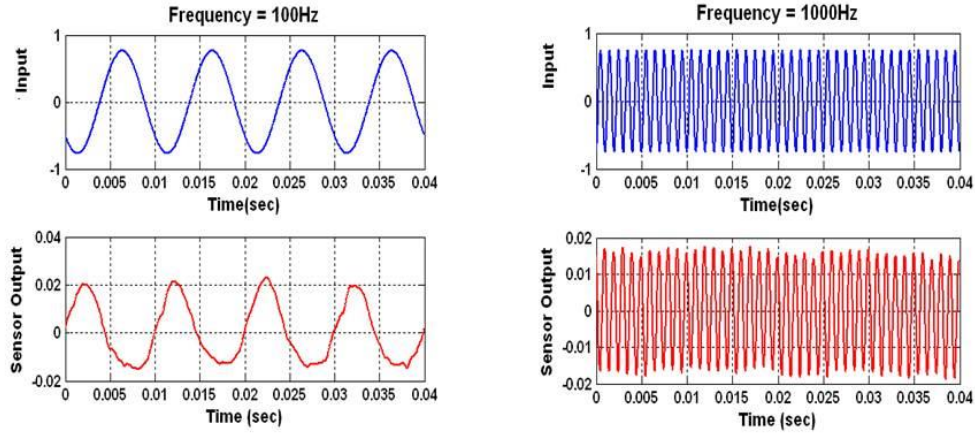


Figure 1.5: Results from Reference [4].

The results in Figure 1.5 indicate that the *CB* filled polyurethane is capable of measuring the pressure wave emitted by the electromechanical speaker at both 100 Hz and 1 kHz. The phase delay between the input signal and the signal measured by the *CB* filled polyurethane sensor is most likely due to the time it takes for the pressure wave to travel from the speaker and reach the sensor.

The purpose of this thesis is to expand upon the work of Reference [4] and use an array of *CB* filled polyurethane sensors to perform acoustic source localization. In order to accomplish this task, an array processing technique must be applied to the signals measured by the *CB* filled polyurethane. The following section provides a background on array processing, and details the technique that was applied in this study.

1.3 Array Processing

Array processing is an established practice that involves leveraging the signals measured by an array of distinct sensors to increase the fidelity of a measurement. The goals of array processing are to combine the individual sensors outputs' cleverly

so as to enhance the signal-to-noise ratio beyond that of a single sensors' output, to characterize the field by determining the number of sources of propagating energy, the locations of these sources, the waveforms these sources are emitting, and to track the energy of sources as they move in space [15]. In this thesis, the author focuses on using a conventional array processing technique to perform an acoustic source localization demonstration. The following section provides a brief description of array processing, the array processing technique applied in this thesis, and a discussion of practical considerations when implementing array processing.

Consider an acoustic source that emits a signal $S(\omega)$, and an array of n sensors that measure the signals $X_n(\omega)$. This scenario is illustrated below in Figure 1.6.

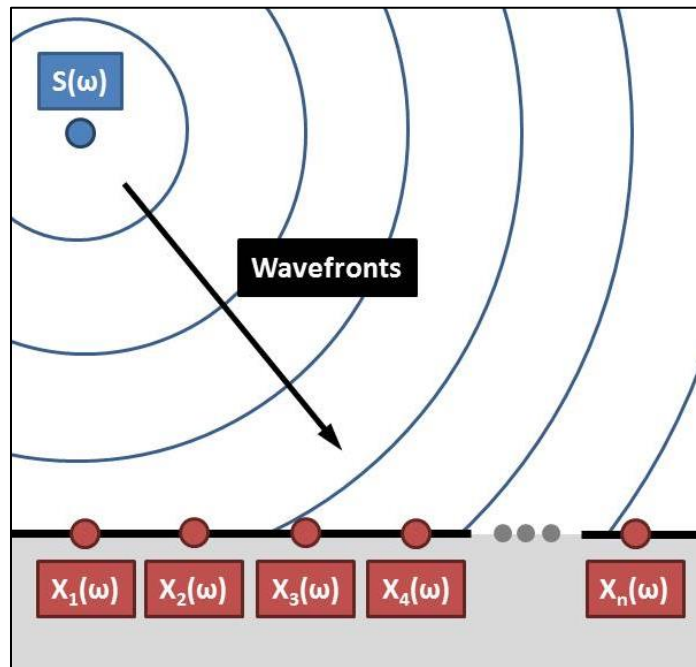


Figure 1.6: Pressure waves impinging on an array of receivers.

As evident in Figure 1.6, there is a *Phase Delay* θ between the signals measured by the sensors, $X_n(\omega)$, relative to the source signal $S(\omega)$. This relationship

between the source and receivers is represented mathematically by the following expression:

$$\underbrace{\{X(\omega)\}}_{(n \times 1)} = \underbrace{\{a(\theta)\}}_{(n \times 1)} S(\omega) \quad (1.3.1)$$

The vector $\{a(\theta)\}$ in equation (1.3.1) is referred to in array processing literature as the *Steering Vector*. The *Steering Vector* is composed of complex exponential functions, as follows:

$$\underbrace{\{a(\theta)\}}_{(n \times 1)} = \{e^{j\theta_1} \quad \dots \quad e^{j\theta_n}\}^T \quad (1.3.2)$$

The *Phase Delays* (θ_n) in equation (1.3.2) depend on the location of the n sensors with respect to the source signal, the frequency of the source signal, the medium in which the source is located, and the assumption about the wavefront propagating from the source. For a source that produces a spherically spreading wavefront, the *Phase Delays* (θ_n) are given by the following relationship:

$$\theta_n = \frac{\omega r_n}{c} = kr \quad (1.3.3)$$

where

$\omega =$	<i>The frequency of the source (Hz)</i>
$c =$	<i>The speed of sound of the medium where the source is operating</i>
$r_n =$	<i>The distance between the source and the n^{th} sensor</i>
$k =$	<i>Wavenumber</i>

Typically, while assumptions can be made about the type of source, the only information that is known from equation (1.3.1) is the output signal of the n sensors in the sensor array, $\{X(\omega)\}$. However, through array processing, these output signals can be linearly combined to determine the location of the source signal. This linear combination of the sensor outputs amounts to spatially filtering the sensor field such

that a signal from a particular angle, or set of angles, is enhanced by a constructive combination and noise from other angles is rejected by destructive interference [28].

Let $Y(\omega)$ represent a linear combination of the n sensor output signals, as follows:

$$Y(\omega) = \underbrace{\{w\}^H}_{(1 \times n)} \underbrace{\{X(\omega)\}}_{(n \times 1)} \quad (1.3.4)$$

The vector $\{w\}$ in equation (1.3.4) represents the *Spatial Filter* applied to the n sensor output signals $\{X(\omega)\}$, and H represents the *Hermitian*. In array processing, it is often convenient to analyze the *Output Power*, $P(\omega)$, of the sensor array, which is given by the following expression:

$$P(\omega) = \frac{1}{n} Y(\omega) Y(\omega)^H \quad (1.3.5)$$

Plugging equation (1.3.4) into equation (1.3.5) yields the following:

$$P(\omega) = \frac{1}{n} \underbrace{\{w\}^H}_{(1 \times n)} \underbrace{\{X(\omega)\}^H}_{(n \times 1)} \underbrace{\{X(\omega)\}}_{(1 \times n)} \underbrace{\{w\}}_{(n \times 1)} \quad (1.3.6)$$

Equation (1.3.6) can be simplified as follows:

$$P(\omega) = \underbrace{\{w\}^H}_{(1 \times n)} \underbrace{[G_{xy}]}_{(n \times n)} \underbrace{\{w\}}_{(n \times 1)} \quad (1.3.7)$$

where $[G_{xy}] =$ *The Cross-Power Spectral Densities (CPSD) between the n sensors of the array*

Different array processing techniques correspond to different choices for the *Spatial Filter* $\{w\}$ [18]. In recent years, there have been many advances in acoustic source localization through array signal processing. Reference [18] and Reference [15] provide excellent overviews of some of the advances in array processing techniques. For this thesis, conventional Bartlett array processing is sufficient to demonstrate the effectiveness of the *CB* filled polyurethane sensor array. Bartlett

array processing involves maximizing the *Output Power* $P(\omega)$ of the sensor array. It can be shown that the following formulation of the *Spatial Filter* (w) maximizes the *Output Power* $P(\omega)$ in equation (1.3.7):

$$\underbrace{\{w_m\}}_{(n \times 1)} = \frac{\underbrace{\{a_m(\theta)\}}_{(n \times 1)}}{\sqrt{\underbrace{\{a_m(\theta)\}^H}_{(1 \times n)} \underbrace{\{a_m(\theta)\}}_{(n \times 1)}}} \quad (1.3.8)$$

Plugging equation (1.3.8) into equation (1.3.7) yields the following:

$$P_m(\omega) = \frac{\underbrace{\{a_m(\theta)\}^H}_{(1 \times n)} \underbrace{[G_{xy}]}_{(n \times n)} \underbrace{\{a_m(\theta)\}}_{(n \times 1)}}{\underbrace{\{a_m(\theta)\}^H}_{(1 \times n)} \underbrace{\{a_m(\theta)\}}_{(n \times 1)}} \quad (1.3.9)$$

Bartlett array processing involves making an assumption about the type of source in the field. The *Spatial Filter* (w) characteristics, and then the *Output Power* $P(\omega)$ of the array are calculated based on this assumed source location. By repeating this process for m different assumed source locations, the array output can be “steered” to identify the maximum *Output Power*. The idea is that the maximum power calculated through this process will correspond to the actual source location.

When implementing array processing techniques, there are many details that need to be considered that affect the performance of the array. First, the sensors that compose the array spatially sample the output signal from the source. Similar to the *Nyquist Frequency* in temporal sampling theorem, there is a minimum spatial sampling interval necessary to prevent aliasing of the signal. The minimum *Spatial Sampling Interval* (d) is given by the following equation:

$$d = \frac{c}{2f} = \frac{\lambda}{2} \quad (1.3.10)$$

where $c =$ *The speed of sound of the medium where the source is operating*
 $f =$ *Frequency of the source (Hz)*
 $\lambda =$ *Wavelength of the output signal from the source*

Another important consideration in array processing is the shape of the spatial filter. The spatial filter consists of a single main lobe that accepts energy from signals from angles that fall within the main lobe, and rejects signals from all other angles. Acoustic source localization involves “steering” this main lobe in multiple directions to locate the area of maximum output power, which corresponds to the location of the source. The main lobe width decreases with the number of sensors used and the width of the array. Either action serves to increase the array’s spatial extent and to improve resolution [15]. Due to the finite nature of practical sensor arrays, the spatial filter also includes side lobes, which accept signals from angles outside the spatial extent of the main lobe. These side lobes become particularly important when attempting to localize a single source amongst other sources, as it is difficult to distinguish between the source of interest and the other, so called “noise” sources.

This thesis focuses on identifying the location of a single source using an array of *CB* filled polyurethane sensors. The experiment was setup to minimize extraneous noise sources. Therefore, minimizing the width of the main lobe, and minimizing the presence of side lobes in the spatial filter to improve resolution were not a high priority. However, there has been extensive research into maximizing the spatial extent of the array through clever choices of the spatial filter implemented when processing the array output data.

1.4 Scope of the Thesis

In this thesis, the author proposes using the outputs from an array of *CB* filled polyurethane sensors to perform acoustic source localization. The thesis is organized into the eight chapters.

Chapter 2 presents a description of the procedure developed to manufacture the *CB* filled polyurethane sensors. This procedure builds on the work accomplished by Reference [1], and includes lessons learned in the attempt to improve the process to produce similar material properties from sensor to sensor. In array processing, it is important that all of the sensors in the array perform similarly.

Chapter 3 presents the results of material property characterization testing. The testing presented in this chapter was designed to demonstrate that different samples of the *CB* filled polyurethane had similar material properties.

Chapter 4 presents a structural model of the conductive polymer sensor system. The model includes a model backing structure of the array, as well as a model of the dynamics of the sensors themselves.

Chapter 5 presents a model of an acoustic source. The results include expected pressure measurements at each of the sensor locations. This chapter also includes a theoretical demonstration of the array processing technique discussed in Chapter 1, and describes how to manipulate the output signal from the *CB* sensors to perform source localization.

Chapter 6 presents the results of an experimental acoustic source localization using an array of conventional condenser microphones. The purpose of this experiment was to demonstrate that acoustic source localization could be successfully performed using the array processing technique described in Chapter 1.

Chapter 7 presents the results of using an array of *CB* filled polyurethane sensors to perform acoustic source localization.

Chapter 8 summarizes the major conclusions and recommendations from this work.

Chapter 2: Manufacturing Procedure

2.1 Introduction

Conductive polymers are materials that exhibit changes in resistivity when subjected to mechanical stress or strain. This effect is often referred to as piezoresistivity. This investigation focuses on a polyurethane composite with conductivity properties induced by the inclusion of carbon black particles during the manufacturing process. In this case, the conductive polymer being investigated is a composite of 20% carbon black particles and 80% polyurethane.

2.1.1 Polyurethane

The polyurethane used in this study is a two-part polymer manufactured by Forsch Polymer Corporation. Part A of the two-part polyurethane is Isocyanate 110A and Part B is Polyol 5000B. The manufacturer suggests that the two components are combined such that there is a ratio of 100 parts of Polyol 5000B (Part B) to 40 parts of Isocyanate 110A (Part A) by weight. The material properties of the two-part polymer are listed below in Table 2.1.

Table 2.1: Manufacturer advertised material properties for polyurethane.

Property	Value
Hardness, Shore A	58-62
Tensile Strength, Ultimate (psi)	1,400
Elongation (%)	480
Tear Strength (PLI)	175

2.1.2 Conductivity

The conductivity of the composite being investigated is induced by the inclusion of carbon black (*CB*) particles during the polyurethane mixing process. Numerous studies have shown that the ratio of *CB* particles to the polyurethane

determines the level of conductivity of the material. These studies have identified a percolation threshold effect, where there is an extreme change of certain physical properties, including conductivity, within a narrow concentration range of the filler material [5]. With respect to conductivity, the percolation threshold effect manifests itself as a dramatic increase of conductivity by several orders of magnitude in a rather narrow concentration range of the filler material around the percolation threshold [5]. Reference [1] contains a literature review of investigations into the percolation threshold effect on conductive polymer materials. Reference [1] also presents experimental data indicating that for the polyurethane and *CB* particles used in this study, the highest conductivity is attained by creating a composite with a ratio of 20% *CB* particles to 80% polyurethane.

2.1.3 Carbon Black (CB) Particles

The carbon black particles used in this study are acetylene black purchased from Alfa Aesar Company (Ward Hill, MA). The particles have an average particle size 42 nm, a surface area 75 m²/g, a density 1.75 g/cm³ and a bulk density 94.5–102.5 kg/m³.

2.1.4 Polyurethane Manufacturing Process

The manufacturer of the two-part polyurethane, Forsch polymer, recommends processing parameters to follow in order to achieve their advertised material properties. The manufacturer's processing parameters are as follows:

1. Melt and process Polyol 5000B at 120 to 160 degrees F.
2. Melt Isocyanate 110A if frozen at 100 degrees F., otherwise use at 70-85 degrees F.

3. Mold temperature: 120 to 160 degrees F.
4. Mix Ratio: 100.00 parts Polyol 5000B to 40.00 parts Isocyanate 110A by weight.
5. Degas mixture if possible or pre-degas Polyol in dispensing equipment prior to casting.
6. Pot life: (200g mass) (100 degrees F) 5-8 minutes
7. Demold: 1-2 hours or 30-45 minutes with maximum process and mold temperature.
8. Post-Cure: 16-24 hours at 140 degrees F.

It is important to note that the manufacturing process described above does not take into account the addition of a large percentage of filler material to the mixture. In the case of this experiment, carbon black particles made up 20% of the mixture. The manufacturing process was altered to accommodate the inclusion of filler material. The altered manufacturing process is discussed later in this Chapter.

2.2 Manufacturing Procedure Development

The recommended manufacturing procedure of the two-part polyurethane is described earlier in this Chapter. However, this procedure does not take into account the addition of filler material during the manufacturing process. Initial attempts to manufacture 20% *CB* filled polyurethane blocks using the procedure in 1 did not yield successful results; the manufactured blocks contained numerous internal and surface air-pockets. Several iterations of modified manufacturing procedures were

applied before a finalized procedure was established. The sections below provide background on the development of the manufacturing procedure used in this study.

2.2.1 Inclusion of *CB* Particles in Polyurethane

The recommended manufacturing procedure recommended by the manufacturer does not address the addition of filler materials to the polyurethane mixture. Therefore, several procedures for combining the *CB* particles to the polyurethane were evaluated in this study. The block of *CB* filled polyurethane used in this study had a total volume of 1 cm³, which required a relatively small amount of material to create. Therefore, all of the mixing processes investigated in this study involved combining the three components (Part A and Part B, and *CB* particles) in an approximately 350 ml plastic mixing cup.

The first mixing procedure evaluated in this study involved combining all three components simultaneously in a plastic mixing cup and mixing them by hand using a tongue depressor. It should be noted that the two components of the polyurethane (Part A and Part B) are initially liquid in form. When the two polyurethane components were combined, without the addition of *CB* particles, they remained in liquid form until they began to cure. As the mixture began to cure, its viscosity increased and the mixture became more difficult to mix by hand using a single tongue depressor. The addition of *CB* particles at the beginning of the mixing process significantly increased the viscosity of the composite material. When all three components were combined, the resulting material was more like a paste than a

liquid, and was very difficult to mix by hand using a tongue depressor. Consequently, other methods of mixing the three components were investigated.

Another mixing procedure also involved combining all three components simultaneously in a plastic mixing cup. However, this time a Makita DA391D model hand drill was used to mix the components instead of a tongue depressor. A ¼ inch diameter, 6 inch long bolt was used, instead of a drill-bit, to mix the three components together.

It was just as difficult to mix the three components together using the drill as using a tongue depressor. Additionally, the *CB* filled polyurethane blocks made using this procedure contained more air pockets than the blocks made with material mixed by a tongue depressor.

One of the main issues with mixing the three component materials together was that the composite material began to cure a few minutes after the two parts of the polyurethane are combined. Due to the short amount of time available to mix the components, and the high viscosity of the material when all three components were combined simultaneously, it was difficult to uniformly mix the three components before they began to cure. As a result, different methods of combining the three materials were investigated, rather than combining all three simultaneously.

The first method involved slowly adding *CB* particles to Part B, which produced a very viscous paste similar to adding all three components simultaneously. The difference being that the mixture could be mixed to a uniform consistency using a tongue depressor for a long amount of time without the material curing. Once a uniform mixture was achieved, Part A of the two-part polyurethane was added. However, this procedure was ineffective because Part A and Part B did not react with each other to form polyurethane.

Another method investigated involved combining Part A and Part B of the two-part polyurethane, and then slowly adding the *CB* particles to the mixture. Adding the *CB* particles slowly allowed each little amount of the particles to be uniformly mixed in before more particles were added. However, this procedure was ineffective because Part A and Part B began to cure before all of the *CB* particles could be added to the mixture.

One final method of combining the three component materials involved modifying the tongue depressor method first investigated. The three components (Part A, Part B, and *CB* particles) were combined simultaneously in a plastic mixing cup and mixed by hand using a tongue depressor until the mixture attained a paste-like consistency. Then, the material was removed from the plastic cup and kneaded by hand until the material was uniform. This method proved to be the most effective in producing a uniform consistency of the composite material. The finalized procedure is presented in detail later in this Chapter.

2.2.2 Amount of *CB* Filled Polyurethane

The size of the *CB* filled polyurethane block used in this study was determined to be 4”×4”×1/16”. After some trial and error, 35g of material was chosen as the optimal amount to create a 4”×4”×1/16” block. Using the mixing ratios provided by the manufacturer, and the desire to have a 20% ratio of *CB* particles to total weight, a 35g block of material requires the following amounts of the constituent materials:

- 7 g *CB* particles
- 8 g Part A
- 20 g Part B

2.2.3 Vacuum Treatment

The recommended manufacturing procedure in Section 2.1 suggests degassing the polyurethane prior to placing the material in a mold to cure. In order to degas the *CB* filled polyurethane, the mixture was placed under a vacuum. The vacuum chamber system used in this study is presented in Figure 2.1.

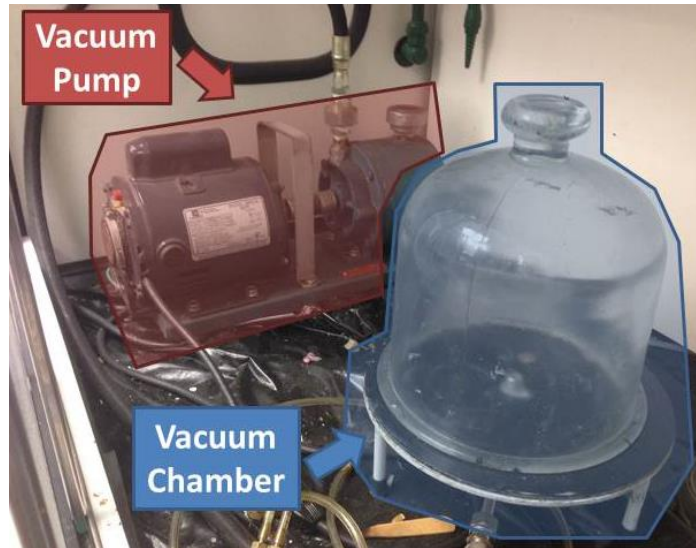


Figure 2.1: Vacuum pump used in *CB* manufacturing process.

The *CB* filled polyurethane was placed inside the chamber and the pump was turned on to remove the air from the chamber.

The length of time that the mixture can be placed under vacuum is limited by the gel time of the polyurethane, which is approximately 6 minutes. In other words, the *CB* filled polyurethane must be placed in the mold to begin curing no later than 6 minutes after the two-part polyurethane is combined or the material will begin to set. Since it takes approximately 2-3 minutes to completely mix the *CB* particles with the two-part polyurethane, the degassing time was conservatively set at 30 seconds. However, the blocks of material created using this degassing time contained numerous surface air pockets. After several iterations of manufacturing blocks using different degassing times, it was discovered that degassing the *CB* filled polyurethane for a minimum of 2 minutes provided the best results with the fewest surface air pockets.

2.2.4 Curing

After the polyurethane has been degassed and placed into a mold to cure, the manufacturer recommends leaving it in the mold to cure for 1-2 hours at room temperature. Following the 1-2 hour period, the manufacturer recommends removing the material from the mold and allowing it to continue to cure at a temperature of 140 degrees F. In this study, the blocks of *CB* filled polyurethane manufactured using these recommendations contained large internal and surface air pockets. These air pockets affect the material properties of the block. As a result, several attempts were made to develop a curing procedure that would produce *CB* filled polyurethane blocks without air pockets.

The first attempt to develop an acceptable curing procedure involved applying pressure to the mold containing the *CB* filled polyurethane during the initial 1-2 hour room temperature curing period. The pressure was applied using the hydraulic press presented in Figure 2.2.



Figure 2.2: Hydraulic press used in *CB* manufacturing process.

Following the 1-2 hour curing period in the hydraulic press, the *CB* filled polyurethane block was removed from the mold and placed in an oven to cure at 140 degrees F. Prior to placing the *CB* filled polyurethane in the oven, there were no noticeable surface air pockets in the blocks made using this method. However, surface air pockets were visible when the *CB* filled polyurethane block was removed from the oven after 22 hours. Placing the mold in the hydraulic press did reduce the number of surface air pockets as compared to blocks that were manufactured without using the press.

Since applying pressure to the mold did seem to have an effect on the presence of surface air pockets, several blocks were manufactured by leaving the

mold in the hydraulic press for 22 hours instead of heat-treating the material at 140 degrees F. The purpose of heat-treating the polyurethane at 140 degrees F is to accelerate the curing time of the material. As a result, it was felt that not including this step would not alter the properties of the *CB* filled polyurethane composite.

The blocks manufactured by placing the mold in the hydraulic press for 22 hours did not have any noticeable surface air pockets. In order to verify that the exclusion of the heat treatment step from the manufacturing process did not significantly alter the material properties of the *CB* filled polyurethane, these properties were measured over time on several samples of the *CB* filled polyurethane. An additional purpose of these material property tests was to determine if leaving the mold in the hydraulic press also prevented the formation of internal air pockets, which if present would also affect the material properties of the *CB* filled polyurethane. The results of these tests are presented and discussed in Chapter 3.

2.2.5 Mold Design

The original mold used to manufacture the *CB* filled polyurethane blocks was a two-piece mold made of polycarbonate. This material was selected because it is easy to machine. A picture of the original mold is presented below in Figure 2.3.

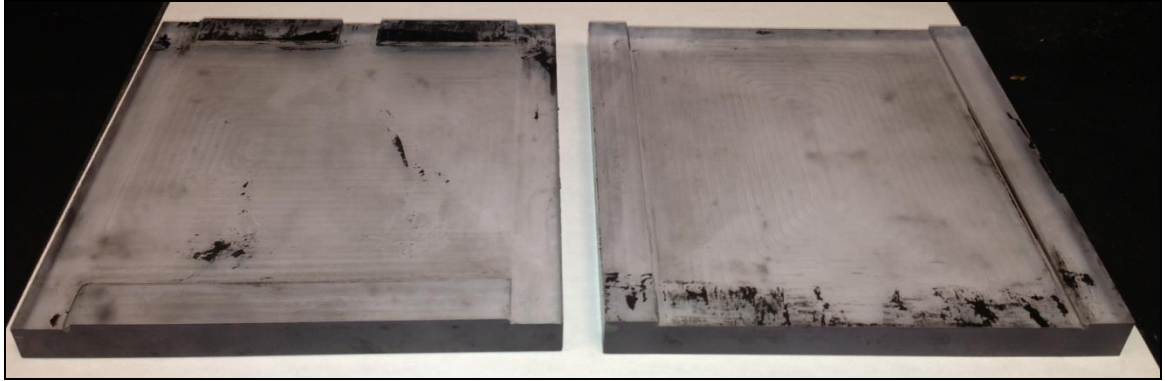


Figure 2.3: Polycarbonate mold. The black material on the surface of the polycarbonate mold above is *CB* filled polyurethane that cured to the mold when the mold release failed.

The two pieces in Figure 2.3 were machined so that when they were assembled, one piece slotted into the other piece to form a 4"×4"×1/16" cavity. One mold piece also contained a recessed channel to allow excess *CB* filled polyurethane to exit the mold. A temporary mold release was applied to the surfaces of the mold that would be in contact with the *CB* filled polyurethane to prevent the material from permanently adhering to the mold after curing. The temporary mold release was a water soluble mold release manufactured by Resin Crafts and was reapplied by hand each time a new block was manufactured. After approximately 1 hour, the liquid mold release cured and formed a thin film on the surface of the mold pieces. Once the mold release cured, *CB* filled polyurethane was placed in the bottom piece and compressed between the top and bottom pieces to create a block with the desired shape. Once the *CB* filled polyurethane block was finished curing, it was removed from the mold. The mold release was then removed using water.

One issue with this particular procedure was the type of mold release used to prevent the *CB* filled polyurethane from adhering to the mold surface. Once cured,

the mold release formed a thin film that was very sensitive to slight disturbances. On several occasions this film tore during the manufacturing process. As a result, blocks of *CB* filled polyurethane had to be discarded because they stuck to the surfaces of the mold and tore upon removal from the mold. The mold then needed to be sanded to remove the pieces of the *CB* filled polyurethane that attached during the curing process. The *CB* filled polyurethane that cured to the mold pieces is evident in Figure 2.3.

Another issue with this particular procedure involved properly aligning the two mold pieces. Recall that the curing process involves placing the mold in a hydraulic press for 24 hours to cure. In order for the mold to form the proper cavity shape, the two pieces had to be aligned exactly in order to slot together. The alignment process often required rotating one of the pieces to line up exactly. As discussed above, the slight disturbance of rotating one of the pieces frequently resulted in a tear in the mold release film. Additionally, the compression process in the hydraulic press began to deform the soft polycarbonate material of the mold when the two mold pieces were not aligned exactly. This deformation of the mold resulted in a cavity that was not the desired shape.

In order to prevent the mold release issue from occurring, permanent mold release options were investigated. It was decided to apply Teflon® coating to the mold surfaces that come in contact with the *CB* filled polyurethane. It was not possible to apply this coating to the polycarbonate mold pieces. As a result, a new

mold was constructed of aluminum. The new mold with the Teflon® coating is presented in Figure 2.4.



Figure 2.4: Aluminum mold with Teflon® coating.

As pictured in Figure 2.4, the mold design was also changed to correct the alignment issues discussed above. Rather than having the two pieces slot together to form a 4”×4”×1/16” cavity, the cavity is recessed into only one of the pieces while the other piece is completely flat. The piece with the cavity also includes four recessed channels to allow excess material to exit the mold during curing.

2.3 Finalized Manufacturing Procedure

This section presents a step-by-step procedure to manufacture the *CB* filled polyurethane blocks used in this study. The materials necessary to produce these blocks are listed below in Table 2.2.

Table 2.2: List of materials necessary to manufacture the *CB* filled polyurethane block used in this study.

Quantity	Item
1	Mixing cup
3	Measuring spoon
1	Aluminum mold with Teflon® coating
1	Scale
7 grams	Carbon black particles
8 grams	Isocyanate 110A (Manufactured by Forsch Polymer)

20 grams	Polyol 5000B (Manufactured by Forsch Polymer)
1	Tongue depressor
1	Temperature controlled oven
1	Hydraulic press
1	Vacuum pump
1	Timer

Step 1: Polyol B can become frozen at room temperature. To return the Polyol B to the liquid state necessary for mixing, place it into a temperature controlled oven. The oven used in this study was a Delta Design Model 5900. Set the temperature to 160 Degrees F and leave the Polyol B in the oven until it has completely returned to a liquid form. This process typically takes about 1 hour.

Step 2: Prepare the hydraulic press, vacuum pump, and mold to receive the *CB* filled polyurethane composite.

Step 3: Using the scale and one of the measuring spoons, carefully measure 7 grams of the *CB* particles into the mixing cup.

Step 4: Remove the Polyol B from the temperature controlled oven once it has liquefied. Using the scale and a different measuring spoon than used for the *CB* particles, carefully measure 20 grams of the Polyol B into the mixing cup.

Step 5: The Isocyanate 110A does not solidify at room temperature so it does not need to be placed in the oven like the Polyol B. Using the scale and the third measuring spoon, carefully measure 8 grams of the Isocyanate 110A into the mixing cup.

Step 6: Immediately after Step 4, start the timer and slowly begin mixing the *CB* particles into the Isocyanate 110A and Polyol B mixture. It is important to mix slowly at first to avoid dispersing the fine *CB* particles into the air.

Step 7: Once the *CB* particles are sufficiently mixed into the Isocyanate 110A and Polyol B mixture (approximately 1 minute after beginning the mixing process), begin mixing faster. Continue mixing until the mixture is a silky smooth paste and until the time indicates 4 minutes have passed since adding the Isocyanate 110A.

Step 8: After 4 minutes of mixing, scrape the *CB* filled polyurethane paste into the bottom half of the mold.

Step 9: Place the top half of the mold on top of the *CB* filled polyurethane. Do not press down on the top half of the mold.

Step 10: Place the mold into the vacuum chamber and run the pump until the time reads 6 minutes.

Step 11: When the timer reads 6 minutes, remove the mold from the vacuum chamber and place it immediately into the hydraulic press. Leave the mold in the press for 24 hours.

Step 12: Remove the mold from the press. Remove the cured *CB* filled polyurethane sample from the mold.

2.4 Summary

Chapter 2 presents the method developed to manufacture the *CB* filled polyurethane sensors. It includes the necessary ingredients, tools, a step-by-step manufacturing procedure, and lessons learned in the development of this procedure..

Chapter 3: Material Property Characterization

The purpose of this testing is to characterize the viscoelastic properties of a carbon black (*CB*) filled polyurethane composite material. These viscoelastic properties will be used in a mathematical model of the *CB* filled polyurethane composite subjected to an acoustic field, and will be determined through the use of Dynamic Mechanical Analysis (DMTA). The objectives of this testing are the following:

1. Establish the parameters of the manufacturing process.
2. Determine the effect of *CB* inclusion on the polyurethane material properties.
3. Demonstrate that the manufacturing process can produce samples with consistent viscoelastic properties.
4. Investigate the effects of polarization of the material on its viscoelastic properties.
5. Identify the composite material's material properties for use in the analytical model.

3.1 Background

3.1.1 Complex Modulus

The *Stress* (σ) and *Strain* (ε) of viscoelastic materials can be described by the following equation:

$$\sigma = E^* \varepsilon \tag{3.1.1}$$

where $E^* =$ *Complex modulus of the viscoelastic material*

The *Complex Modulus* (E^*) can be expanded into its real (E') and imaginary (E'') components as follows:

$$E^* = E' + iE'' \quad (3.1.2)$$

Typically, the *Complex Modulus* (E^*) is written in the following form:

$$E^* = E'(1 + i\eta) \quad (3.1.2)$$

where $E' =$ *Storage Modulus of the material*
 $\eta =$ *Loss Factor of the material*

The *Loss Factor* (η) can be described by the following equation:

$$\eta = \frac{E''}{E'} \quad (3.1.3)$$

The *Storage Modulus* (E') and *Loss Factor* (η) will be measured experimentally and used to model the *CB* filled polyurethane.

3.1.2 DMTA Testing

Dynamic Mechanical Analysis (DMTA) testing was performed on samples of the *CB* filled polyurethane composite to determine the composite's viscoelastic properties. Specifically, this testing identified the *Storage Modulus* (E') and *Loss Factor* (η) of the composite material. DMTA can be simply described as applying an oscillating force to a sample and analyzing the material's response to that force [23]. The Dynamic Mechanical Analyzer (DMTA) supplies an oscillatory force, causing a sinusoidal stress to be applied to the sample, which generates a sinusoidal strain. By measuring both the amplitude of the deformation at the peak of the sine wave and the

lag between the stress and strain sine waves, the storage modulus and loss factor can be calculated [23].

DMTA experiments can be classed as temperature-time studies, frequency studies, and dynamic stress-strain curves. Temperature-time scans hold the frequency constant as the temperature or time at temperature changes. Frequency scans vary the frequency at a set temperature [23]. The method used in this study to determine the viscoelastic properties of the *CB* filled polyurethane, time-temperature superposition, combines these two scans into one experiment. Time-temperature superposition is described as a “method of reduced variables”; shifting series of multiplexed frequency scans relative to a reference curve performs the superposition [23]. After the curves are shifted, the combined curves, the master curve, can be used to predict behavior over a wide range of frequencies [23]. Further description of the methodology behind time-temperature superposition testing is described in-depth in Reference [23].

DMTA tests are performed in commercially available machines known as dynamic mechanical thermal analyzers. Small samples of the material of interest are placed in the machine and tested using one of many different testing methods, including bending, torsion, and extension tests. The method used in this study is the extension test. Extension or tensile analysis is performed on samples of all types and is one of the more commonly done experiments [23]. Preparation of the sample for an extension test involves gluing blocks, in this case aluminum, on two opposite faces

of a rectangular test sample. The blocks are then loaded by an oscillatory stress (σ). Figure 3.1 provides an example of a test sample with end blocks attached, as well as the loading direction.

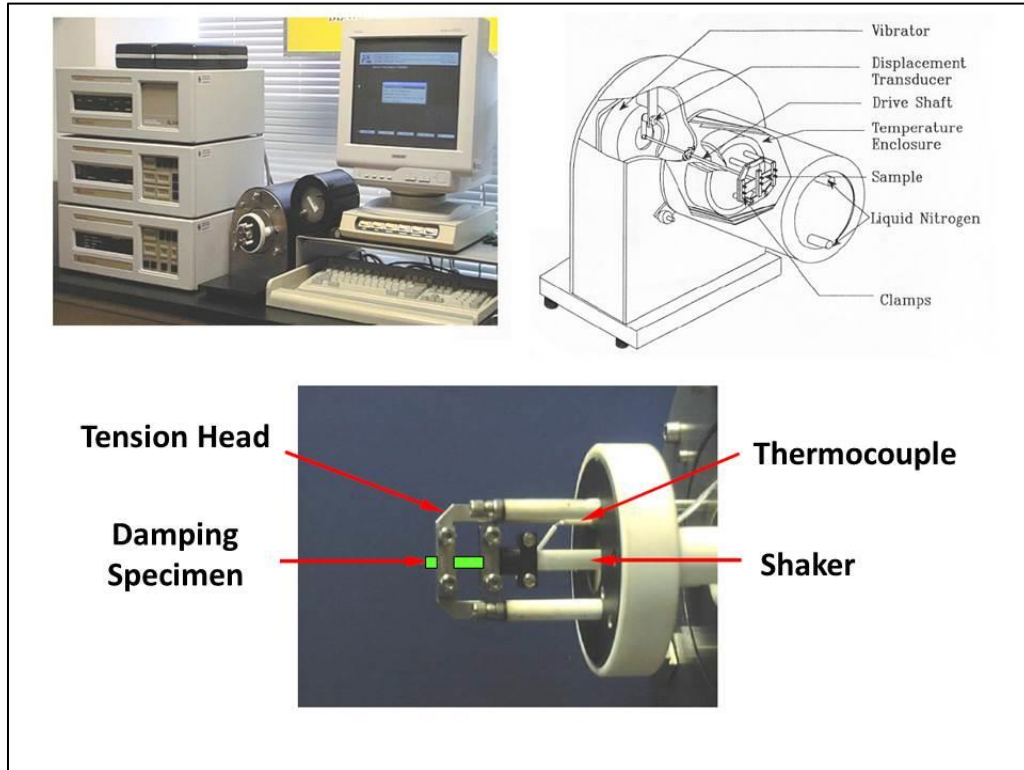


Figure 3.1: Example of DMTA test sample configuration [19].

This geometry is more sensitive to loading and positioning of the sample than most other geometries [23]. Any damage or distress to the edges of the sample as well will cause inaccuracies in the measurements. A nick in the edge will also often cause early failure, as it acts as a stress concentrator. After loading a film or fiber in extension, it is important to adjust it so that there are not any twists, the sides are perpendicular to the bottom, and there are no crinkles [23].

Reference [1] demonstrated that in addition to deformities in the test samples, proper specimen preparation, maintaining appropriate aspect ratio (span to thickness ratio) to reduce the transverse shear deformation, and sufficient loading are critical to measure correct properties from DMTA test. If these conditions are satisfied, Reference [27] demonstrated that DMTA testing can accurately calculate the dynamic stiffness values of a material to within 1% of the actual value.

3.1.3 Polarization

Reference [1] demonstrated that polarization, or exposing the polymer to an electric field, produces a change in the response of the material to applied strain; for a sinusoidal applied stress, the *CB* filled polyurethane sample that had been polarized exhibited a sinusoidal response with significantly decreased noise than the response of non-polarized samples. Objective 4 of this testing was to expand upon this discovery and determine the specific effect of polarization on the viscoelastic properties of the *CB* filled polyurethane composite. Polarization was achieved by placing the *CB* filled polyurethane samples between two conductive plates. A 20V DC voltage was then applied across the plates, and the *CB* filled polyurethane samples were polarized by the generated electric field. The samples remained in the electric field for a total of 10 minutes.

3.2 DMTA Testing Results

DMTA tests were conducted on several samples of the conductive polymer composite. This study will refer to “samples” as pieces of the *CB* filled polyurethane cut from larger blocks. Additionally, samples are referred to by the naming

convention B#-S#, where B# corresponds to the block number and S# corresponds to the sample number cut from that block. The samples tested measured $3/8'' \times 7/16'' \times 1/16''$. Table 3.1 below presents a list of the DMTA tests performed and associated details.

Table 3.1: List of DMTA tests performed.

Test #	Block #	Sample #	CB %	Cure Time Before Testing (Hours)	Polarization Voltage (V)	Time After Polarization (Hours)
1	1	1	0	360+	-	-
2	2	1	20	120+	-	-
3	2	2	20	120+	-	-
4	2	3	20	120+	-	-
5	3	1	20	120+	-	-
6	3	2	20	120+	-	-
7	3	3	20	120+	-	-
8	4	1	20	96	-	-
9	4	1	20	120	-	-
10	4	1	20	144	-	-
11	4	1	20	168	-	-
12	4	1	20	312	-	-
13	4	2	20	264	-	-
14	4	3	20	288	-	-
15	5	1	20	144	-	-
16	5	2	20	168	5	24
17	5	2	20	192	5	48
18	5	2	20	216	5	72
19	5	2	20	240	5	96
20	5	2	20	312	5	168
21	5	3	20	336	5	192
22	5	4	20	360	5	216
23	6	1	20	120	20	-
24	6	2	20	168	20	24
25	6	2	20	192	20	48
26	6	2	20	216	20	72
27	6	2	20	288	20	144
28	6	3	20	312	20	168
29	6	4	20	336	20	192
30	7	1	20	24	-	-
31	7	1	20	168	-	-
32	7	2	20	192	20	24
33	7	2	20	216	20	48
34	7	2	20	240	20	72
35	7	2	20	312	20	144
36	7	2	20	336	20	168
37	7	3	20	360	20	192
38	7	4	20	384	20	216

A procedure similar to that described in Reference [19] was used to perform the time-temperature superposition analysis on the acquired DMTA data. The DMTA tests were run from -50 to +50°C in 5°C steps and the data was shifted to a reference temperature by 10°C, by the storage shear modulus only, for an assumed Poisson's ratio of 0.4995. The stress on the samples was applied on an axis perpendicular to the 7/16" x 1/16" face.

3.2.1 Oven-Curing vs. Press-Curing

Objective 1 of the material property tests was to establish the parameters of the *CB* filled polyurethane manufacturing process. Several blocks of the *CB* filled polyurethane were originally fabricated using oven curing as in [1]. However, these samples often formed air bubbles on the surface of the material. These air bubbles could indicate the presence of sub-surface voids, which would create inhomogeneous material properties throughout a single block of the *CB* filled polyurethane. Inhomogeneous material properties throughout a block are undesirable since all *CB* filled polyurethane sensors used for beamforming will be cut from the same block. Consequently, different methods of allowing the manufactured blocks to cure were explored. The final solution was to leave the *CB* filled polyurethane block in the hydraulic press (see Chapter 2) for an extended period of time instead of oven curing. There were not any blocks manufactured containing surface air bubbles using the press-cure method.

Block 2 in Table 3.1 was oven cured for 24 hours following manufacture. Three samples of Block 2 were cut for DMTA testing (B2-S1, B2-S2, and B2-S3). Block 2 did not appear to have any significant surface bubbles. Block 3 in Table 3.1 was placed in a hydraulic press for 24 hours following manufacture. Three samples of Block 3 were cut for DMTA testing (B3-S1, B3-S2, B3-S3). The viscoelastic properties of these (6) samples are presented below in Figure 3.2 through Figure 3.5.

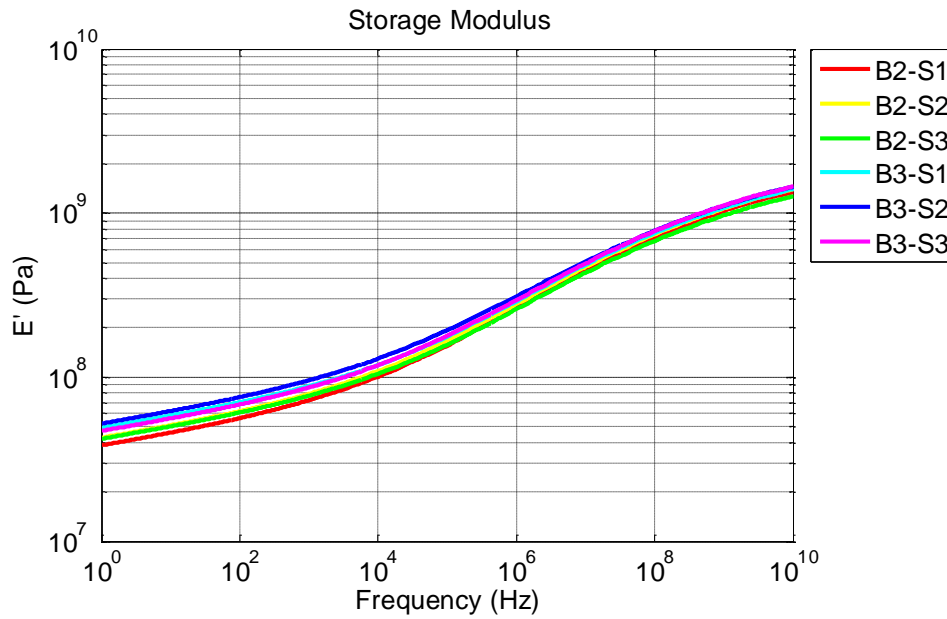


Figure 3.2: Comparison of Block 2 (oven-cured) and Block 3 (press-cured) storage moduli.

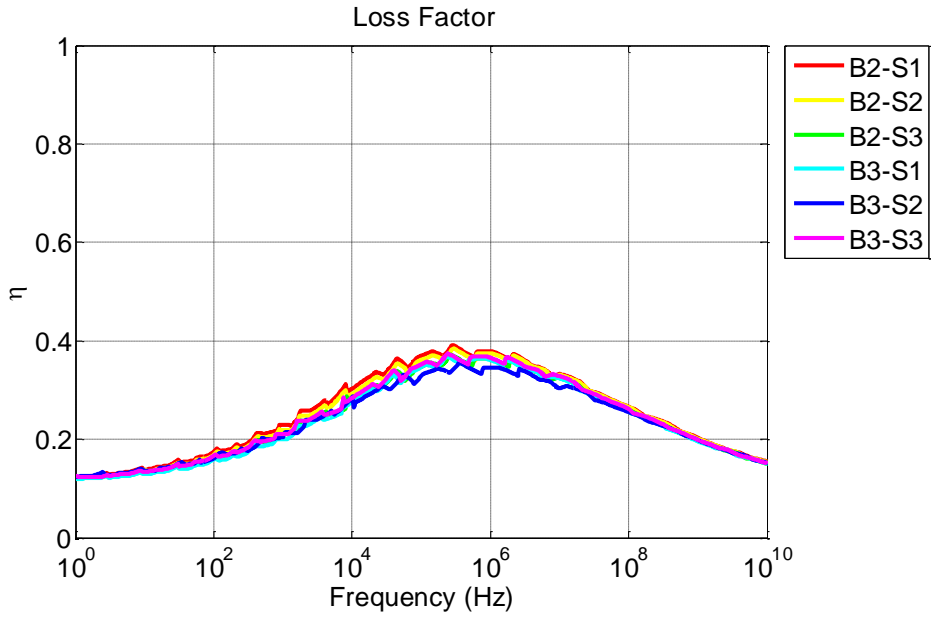


Figure 3.3: Comparison of Block 2 (oven-cured) and Block 3 (press-cured) loss factors.

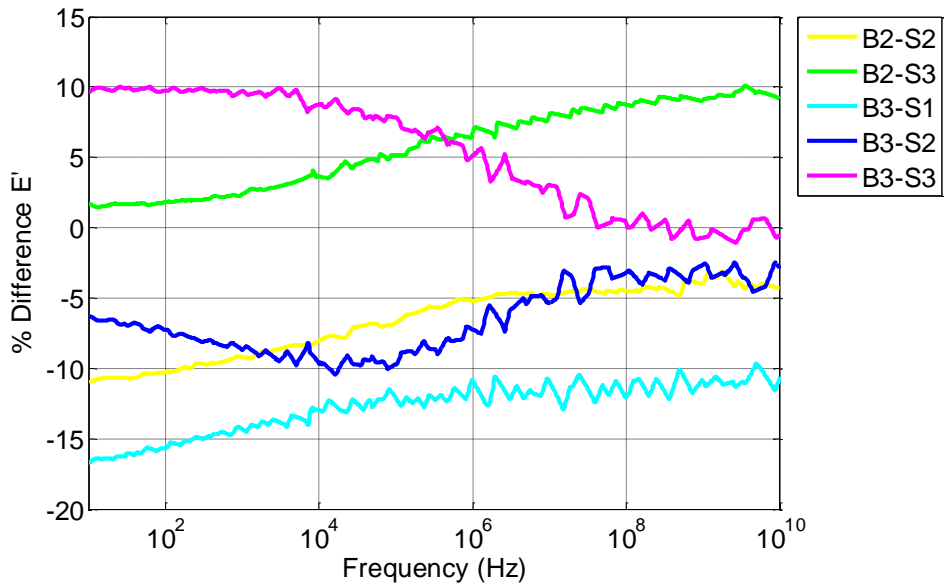


Figure 3.4: % difference in storage modulus referenced to B1-S1.

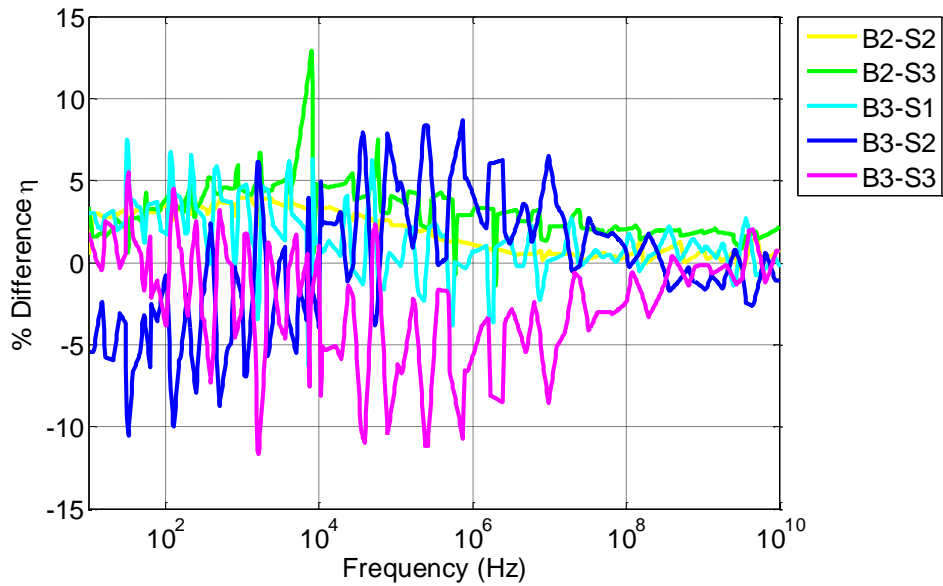


Figure 3.5: % difference in loss factor referenced to B1-S1.

Figure 3.2 presents a comparison of the *Storage Modulus* of oven-cured and press-cured samples. For a better comparison, Figure 3.4 presents the % difference between the samples when compared to sample B2-S1. Figure 3.4 indicates that there can be up to an 18% difference in the *Storage Modulus* values of the different samples. Additionally, there does not appear to be a trend between oven-cured and press-cured blocks. Similar observations can be made about the *Loss Factor* results presented in Figure 3.3 and Figure 3.5. The data indicates that there is not a discernable difference in viscoelastic properties between oven-cured and press-cured samples. However, to avoid any inhomogeneity due to surface or sub-surface voids, the press-cured method was implemented for all remaining blocks manufactured for this study, and is included in the manufacturing procedure presented in Chapter 2.

3.2.2 Impact of CB Inclusion on Polyurethane Material Properties

Objective 2 of the material tests was to determine the effect of *CB* inclusion on the polyurethane properties. Block 1 in Table was made only of the polyurethane

specified in Chapter 2. Testing of Block 1 indicated that the polyurethane had a *Specific Gravity* of 1.035 and a *Shore A Hardness* of 59 @ 1 second. These properties fall within the ranges advertised by the manufacture, presented in Table 2.1.

These measurements were repeated on Block 3, which was manufactured following the procedure in Chapter 2 (20% fill ratio of *CB*, press-cured). The *Specific Gravity* of Block 3 measured 1.96, and the *Shore A Hardness* of Block 3 measured 76 @ 1 second. The increase in density of the *CB* filled polyurethane block is expected due to the inclusion of the *CB* particles. The increase of the *Shore A Hardness* measurement indicates that the *CB* filled polyurethane has a higher resistance to permanent indentation than the polyurethane alone.

Figure 3.6 and Figure 3.7 present a comparison between the *Storage Modulus* and *Loss Factor* of Block 1 (polyurethane only) and Block 3 (20% *CB* fill), respectively.

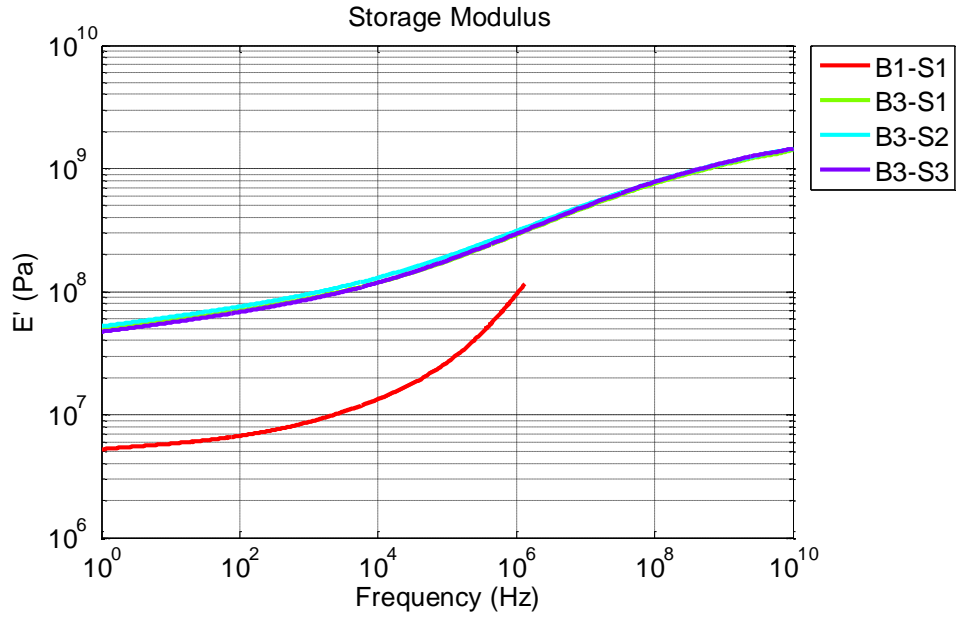


Figure 3.6: Comparison of Block 1 (polyurethane only) and Block 3 (20% *CB* fill) storage moduli.

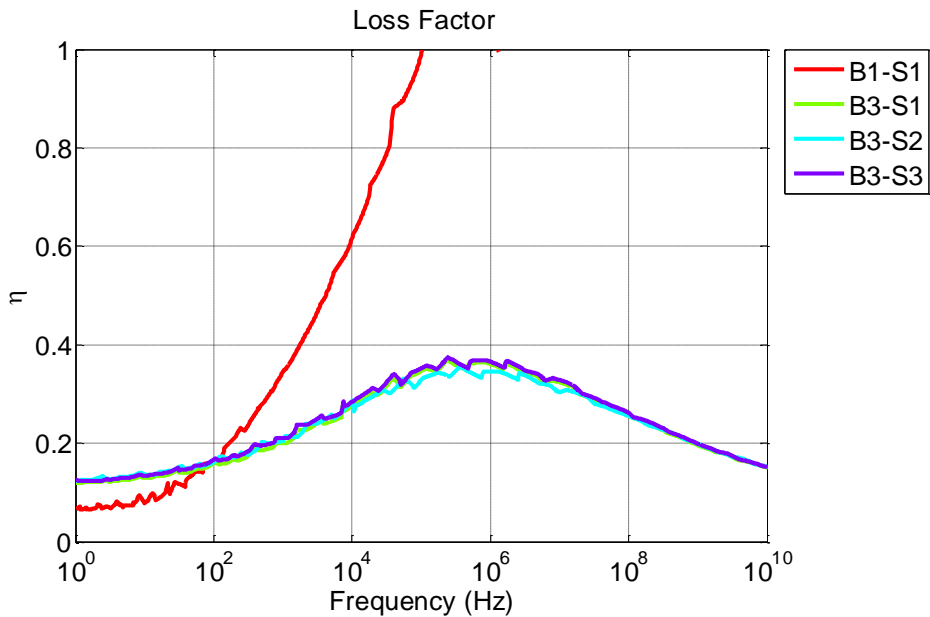


Figure 3.7: Comparison of Block 1 (polyurethane only) and Block 3 (20% *CB* fill) loss factors.

The results indicate that Block 1 (polyurethane only) has a much lower *Storage Modulus* than Block 3 (20% *CB* fill). Consequently, inclusion of the *CB* particles in the polyurethane significantly stiffens the resulting composite. This

outcome is expected, and consistent with the results of the *Shore A Hardness* tests. The *Loss Factor* data indicate that the inclusion of the *CB* particles increases the *Loss Factor* at lower frequencies when compared to the polyurethane only.

3.2.3 Consistency of Viscoelastic Properties

Objective 3 of the material tests was to demonstrate that the manufacturing process can produce samples with consistent viscoelastic properties. Block 4 was manufactured using the procedure outlined in Chapter 2. DMTA tests were performed on a total of (3) samples from Block 4. B4-S1 was tested at 96 hours, and then for every 24 hours until 312 hours post creation. Additionally, B4-S2 was tested 264 hours post creation, and B4-S3 was tested 288 hours post creation. The viscoelastic properties of the Block 4 samples are presented below in Figure 3.8 through Figure 3.11.

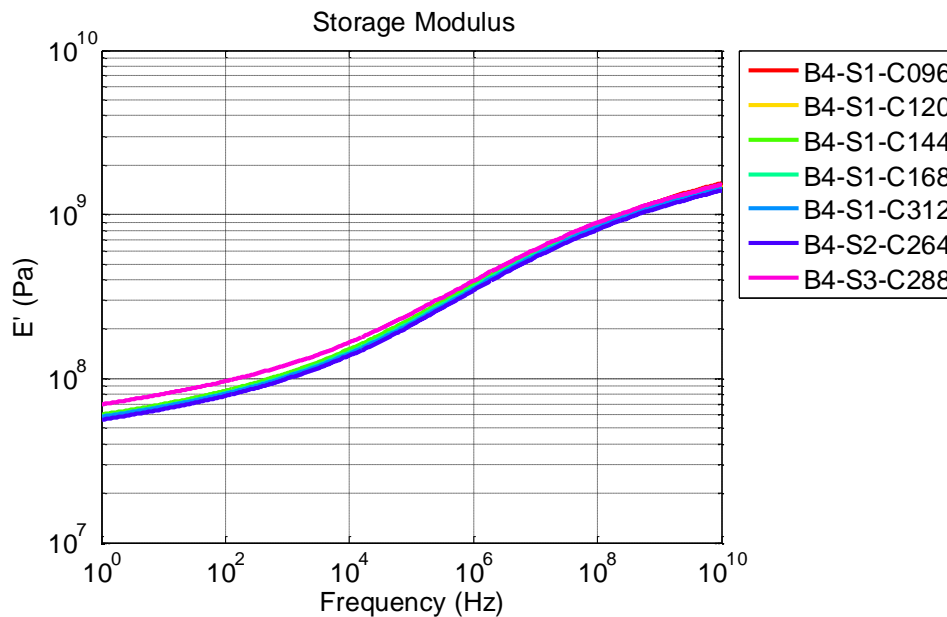


Figure 3.8: Comparison of Block 4 sample storage modulus over time.

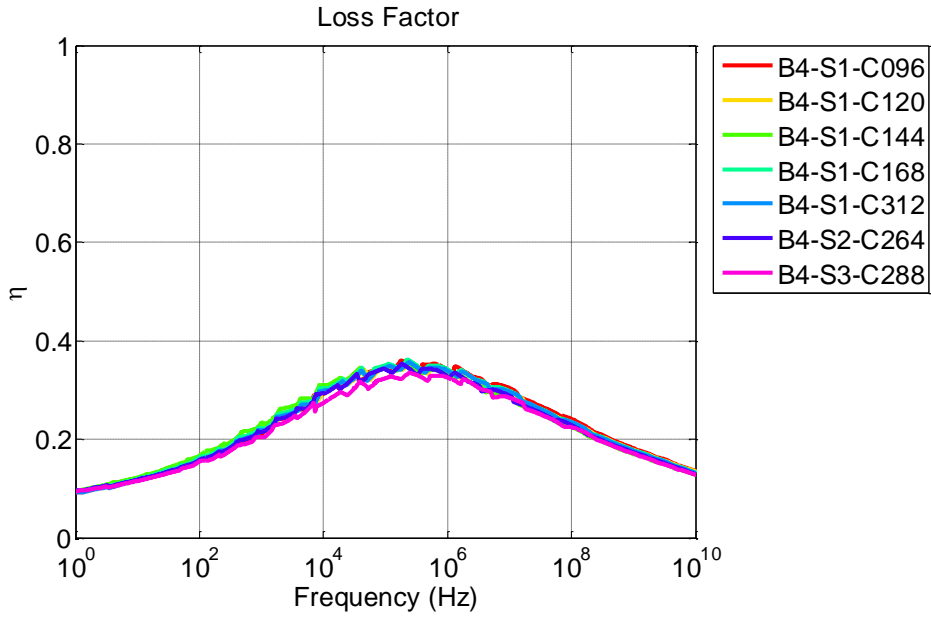


Figure 3.9: Comparison of Block 4 sample loss factors over time.

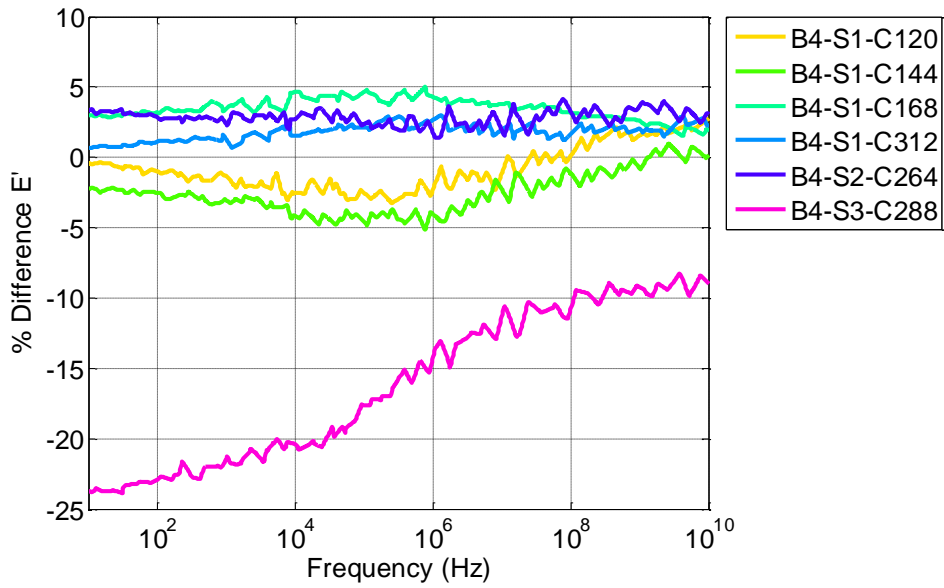


Figure 3.10: % difference in storage modulus referenced to B4-S1-96.

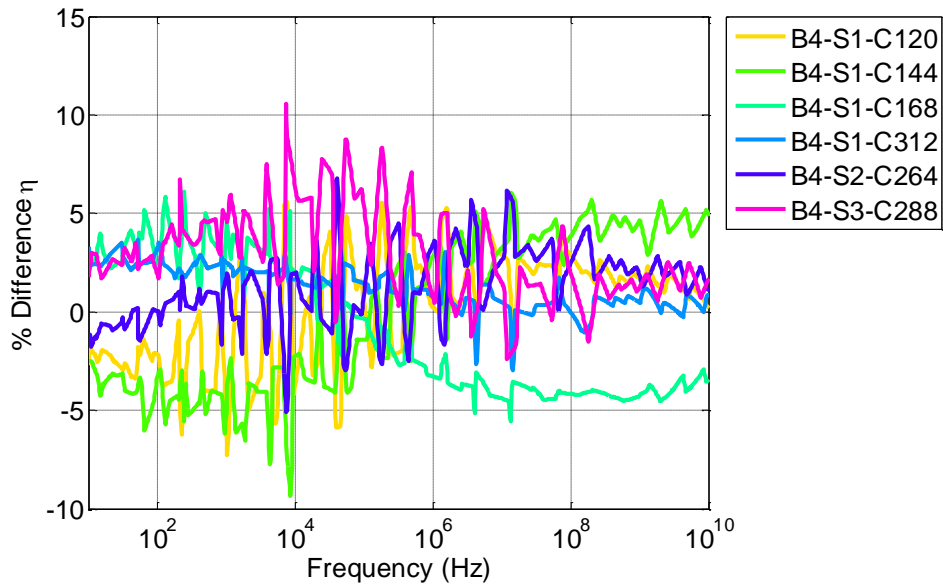


Figure 3.11: % difference in loss factor referenced to B4-S1-96.

Figure 3.8 presents a comparison of the *Storage Modulus* of the various Block 4 samples. For a better comparison, Figure 3.10 presents the % difference between the samples when compared to sample B4-S1-C96. Figure 3.10 indicates that there is not a significant difference in the storage modulus properties of B4-S1 over time, as the results only vary up to about 5%. Additionally, the *Storage Modulus* values of B4-S2 do not vary significantly than the values measured of B4-S1. However, the *Storage Modulus* of B4-S3 varies significantly from the other Block 4 samples. This observation will be explored later in this section when repeatability of the *CB* filled polyurethane properties is compared between blocks, and between samples within a block. Similar observations about the *Loss Factor* results can be made by examining Figure 3.9 and Figure 3.11.

Further investigation into Objective 3 was conducted by comparing the viscoelastic properties of samples from Blocks 3, 4, 5, 6, and 7. The viscoelastic

properties of these samples are presented below in Figure 3.12 through Figure 3.15. Note that Blocks 5, 6, and 7 were polarized. However, the results presented in Figure 3.12 through Figure 3.15 were obtained prior to polarization.

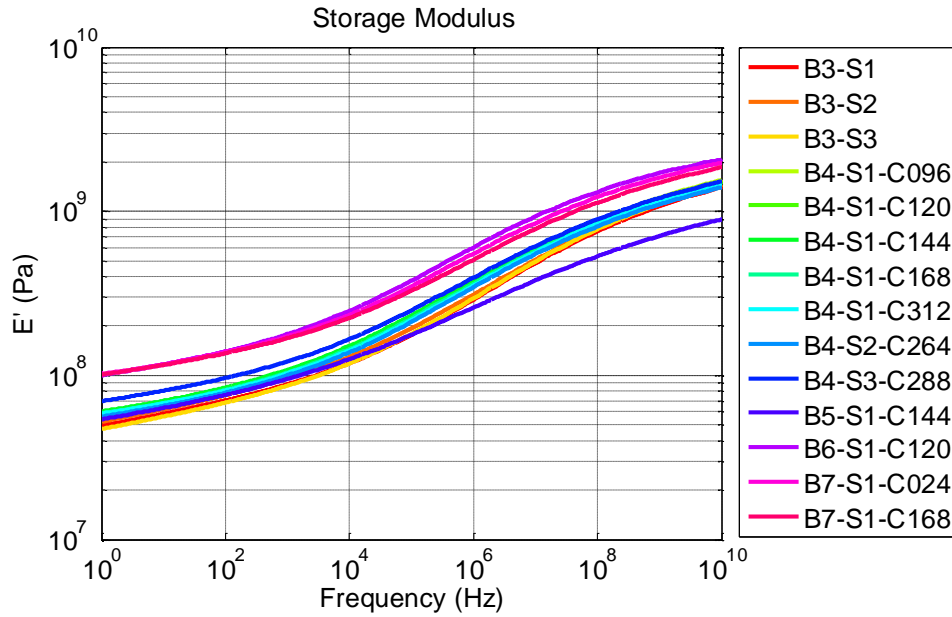


Figure 3.12: Comparison of storage modulus results for various unpolarized blocks.

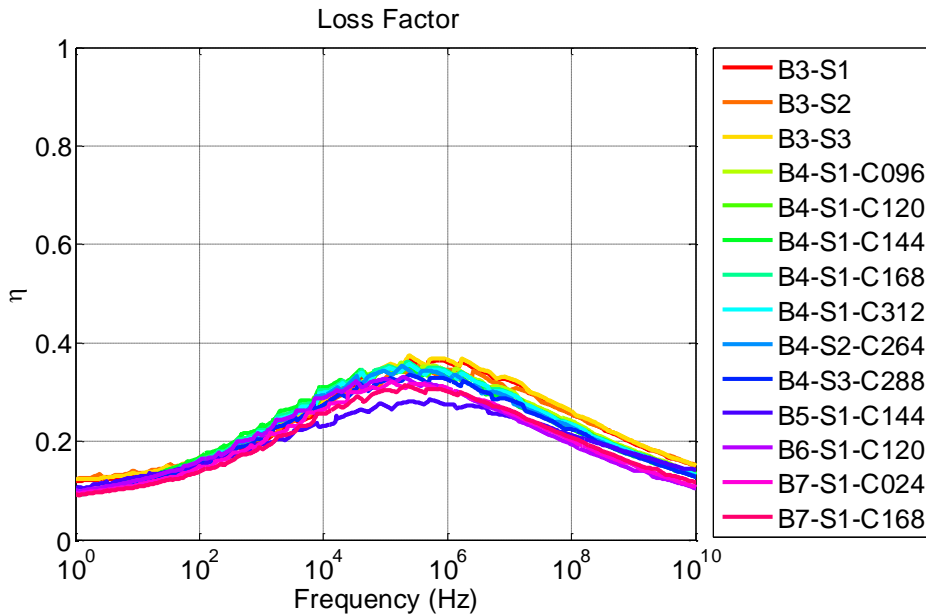


Figure 3.13: Comparison of loss factor results for various unpolarized blocks.

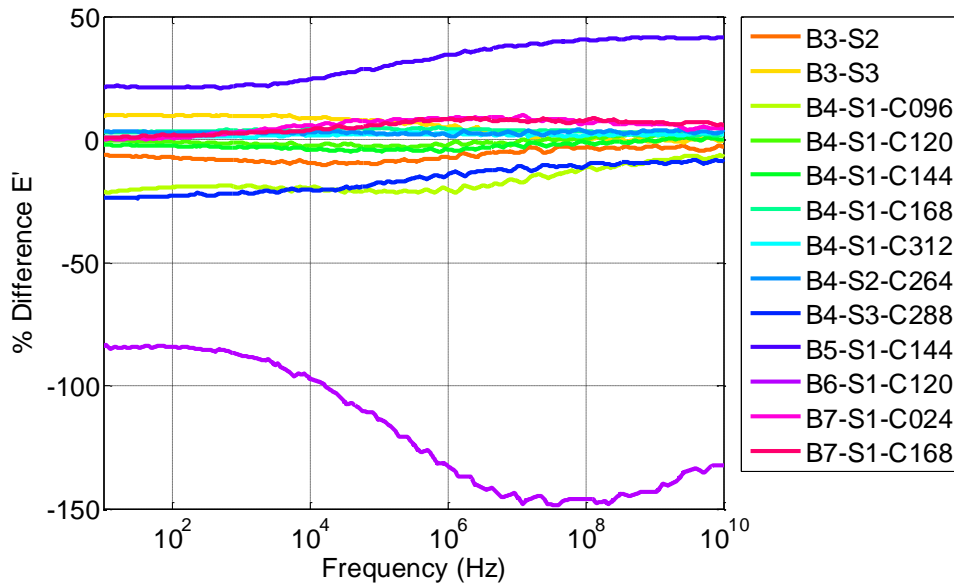


Figure 3.14: % Difference in storage modulus results referenced to B3-S1.

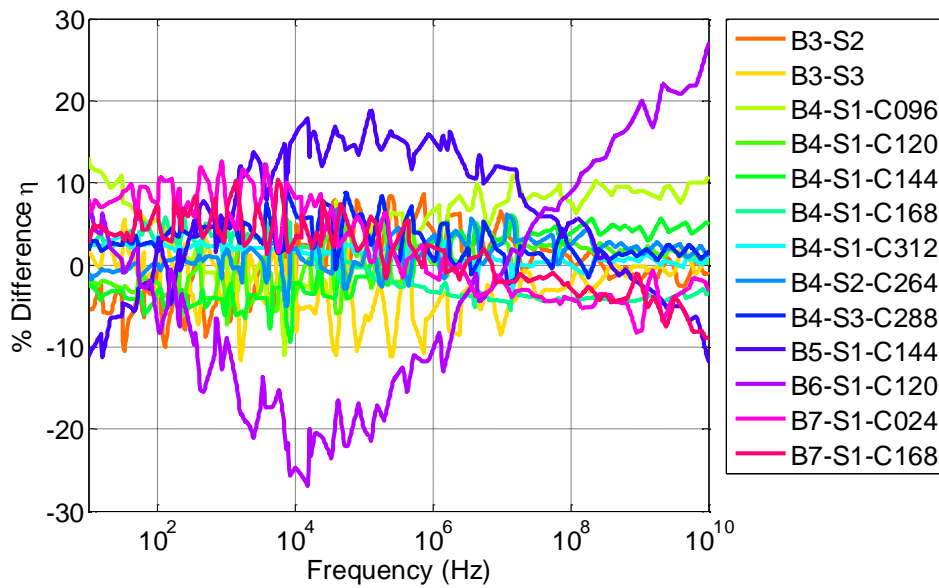


Figure 3.15: % Difference in storage loss factor results referenced to B3-S1.

Figure 3.12 presents a comparison of the *Storage Modulus* of the Block 3, 4, 5, 6 and 7 samples. For a better comparison, Figure 3.14 presents the % difference between the samples when compared to sample B3-S1. Figure 3.14 indicates that a majority of the samples have *Storage Modulus* values that fall within $\pm 10\%$ of the

reference sample. The inconsistent sample B6-S1-C024 result may be caused by a local inhomogeneity such as a sub-surface air void. Similar observations about the *Loss Factor* results can be made by examining Figure 3.13 and Figure 3.15. Therefore, samples cut from a single block of *CB* filled polyurethane can have viscoelastic properties that vary within 10% sample-to-sample. This result is acceptable for this investigation due to the method of manufacturing the material. It is expected that improved manufacturing methods would decrease the variability of the material properties of the samples.

3.2.4 Polarization Effect on Viscoelastic Properties

Objective 4 of the material tests was to investigate the effects of polarization of the *CB* filled polyurethane on its viscoelastic properties. Block's 5, 6, and 7 were fabricated using the procedure presented in Chapter 2. Due to the nature of the DMTA testing, it was not possible to test an unpolarized sample, polarize it, and then retest the sample. Polarizing the unpolarized test sample would require destructively altering the sample, which would affect the DMTA test results. Recall that Section 3.2.3 demonstrated that there is not a significant difference between samples taken from a single block, or from different blocks. Therefore, an unpolarized sample was tested from a given block, the remaining block was polarized, and then (3) more polarized samples were removed and tested. Sample 2 from a given block was tested every 24 hours after polarization. Samples 3 and 4 of a given block were tested to verify the consistency of viscoelastic properties between samples within in given block. This procedure was repeated on Blocks 5, 6, and 7.

The Block 5 data is presented below in Figure 3.16 through Figure 3.19. Note that the polarized samples are referred to by the naming convention B#-S#-C#-V#, where B# corresponds to the block number, S# corresponds to the sample number from that block, C# corresponds to the number of hours since that block was created, and V# corresponds to the number of hours since polarization.

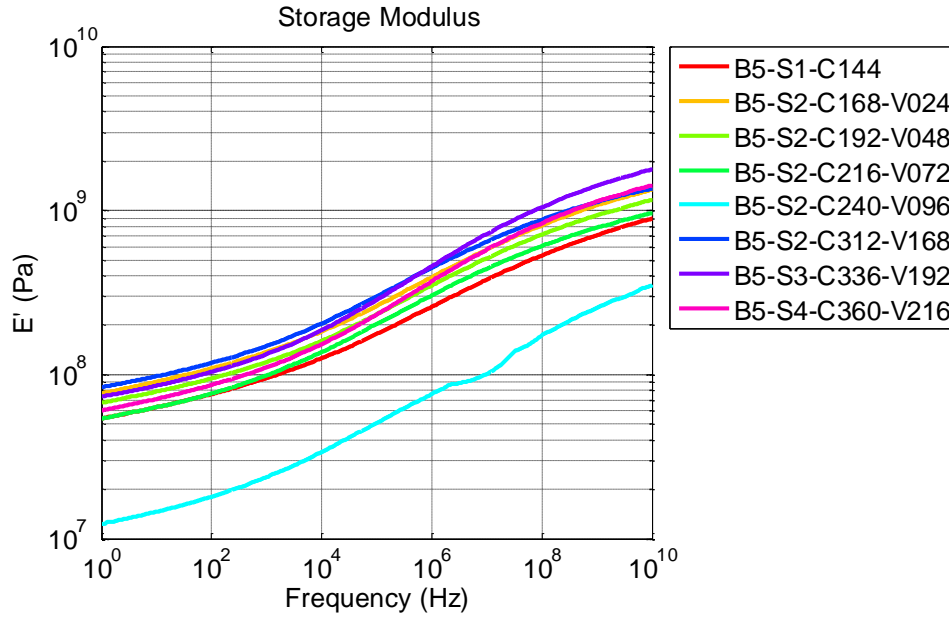


Figure 3.16: Storage modulus values of Block 5 samples.

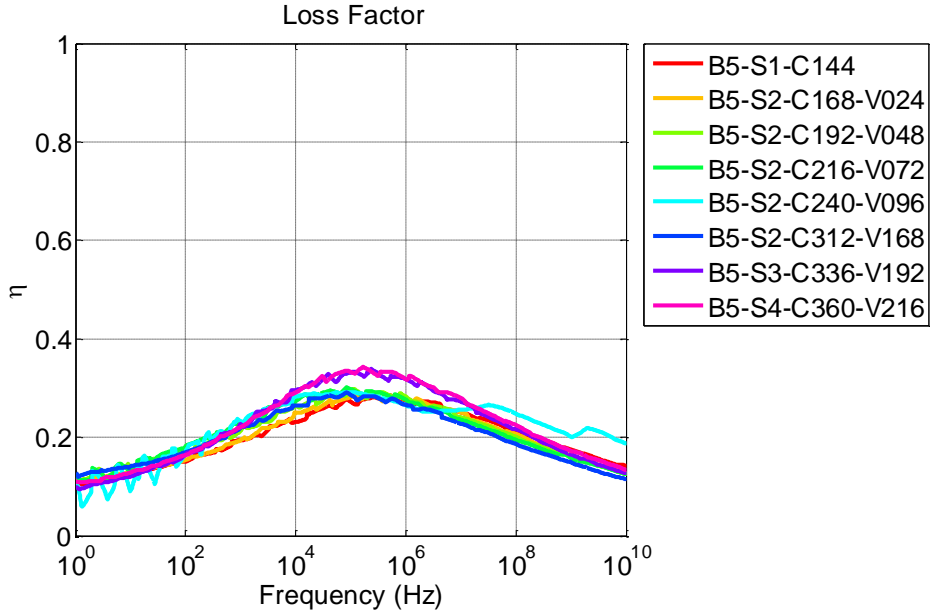


Figure 3.17: Loss factor values of Block 5 samples.

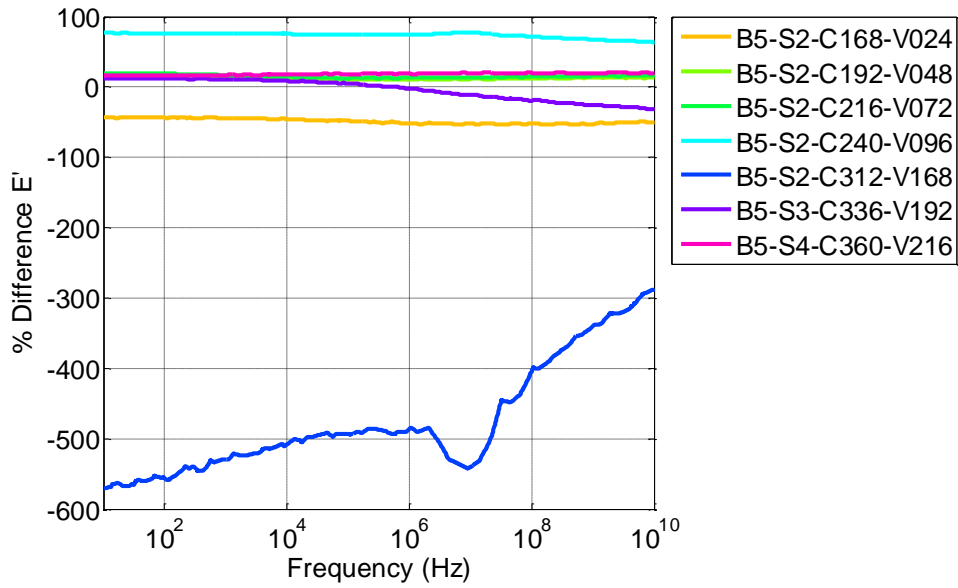


Figure 3.18: % Difference in Block 5 sample storage modulus values referenced to B5-S1-C144.

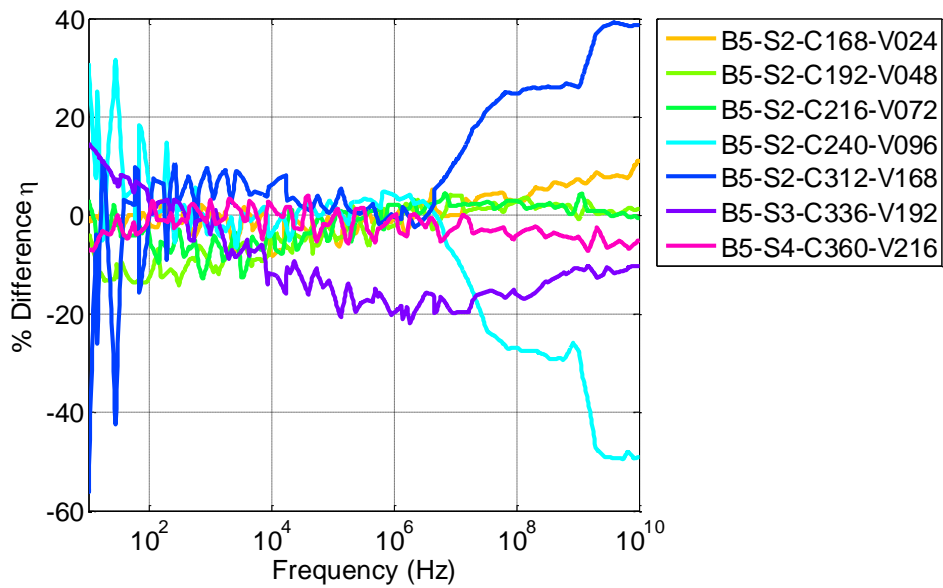


Figure 3.19: % Difference in Block 5 sample loss factor values referenced to B5-S1-C144.

Figure 3.16 presents a comparison of the *Storage Modulus* values of the Block 5 samples. Note that while testing Sample B5-S2-C240-V096 the sample came loose from the mounting blocks. Therefore, the data from this sample does not accurately represent the viscoelastic properties of the sample. The mounting blocks were reattached for the remaining tests. For a better comparison, Figure 3.18 presents the % difference between the samples when compared to the unpolarized sample B5-S1-C144. The data indicates that while the viscoelastic properties of Sample 2 change with time, they do not appear to follow a consistent trend. Additionally, the results of testing multiple samples of Block 5 are consistent with the results of testing multiple samples of the unpolarized blocks in that there does not appear to be a significant difference in viscoelastic properties between samples. Similar observations can be made about the *Loss Factor* data presented in Figure 3.17 and Figure 3.19. As a consistency check, this series of tests was repeated on Block 6 and Block 7. The

Block 6 DMTA test data results are presented below in Figure 3.20 through Figure 3.23.

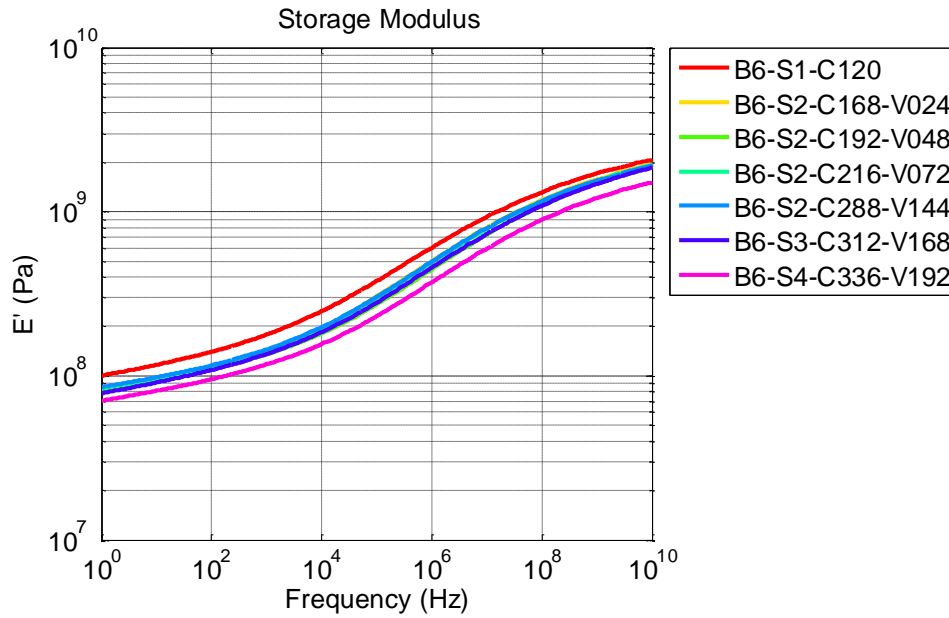


Figure 3.20: Storage modulus values of Block 6 samples.

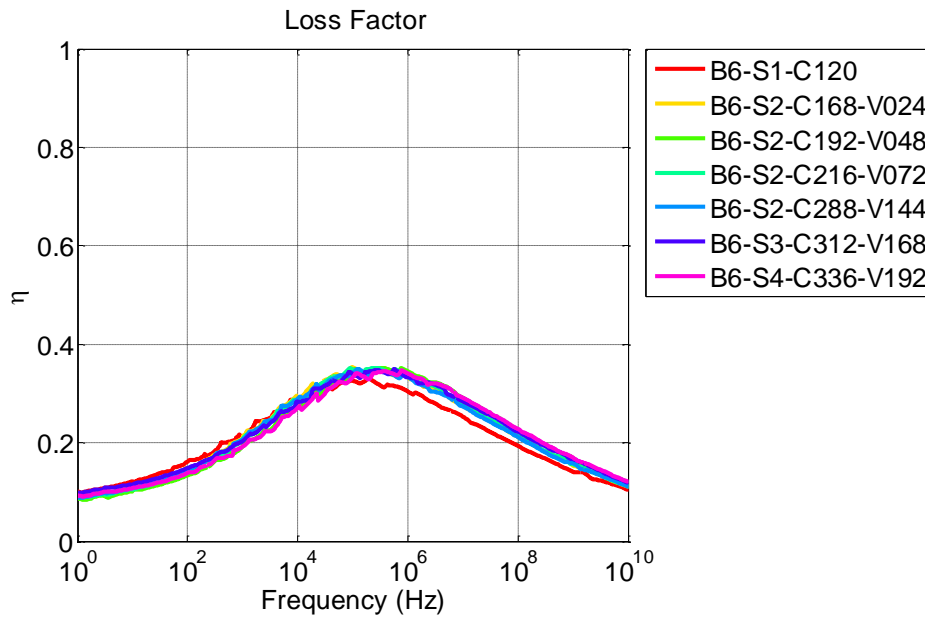


Figure 3.21: Loss factor values of Block 6 samples.

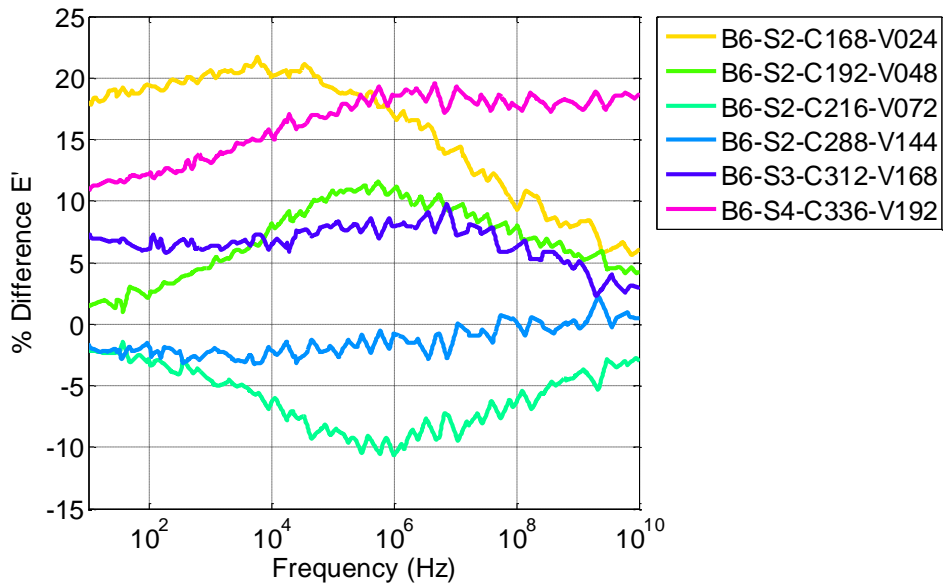


Figure 3.22: % Difference in Block 6 sample storage modulus values referenced to B6-S1-C120.

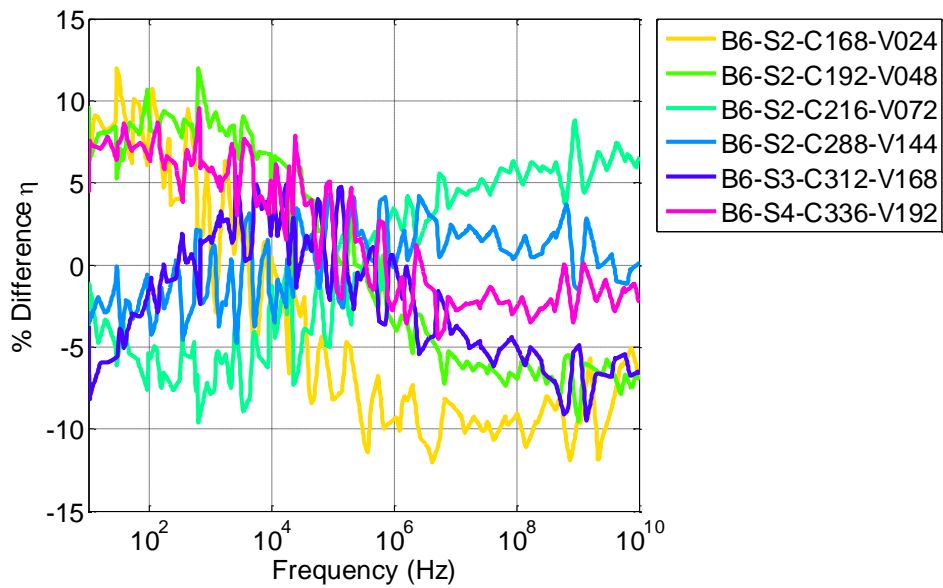


Figure 3.23: % Difference in Block 6 sample loss factor values referenced to B6-S1-C120.

The Block 7 DMTA test data results are presented below in Figure 3.24 through Figure 3.27.

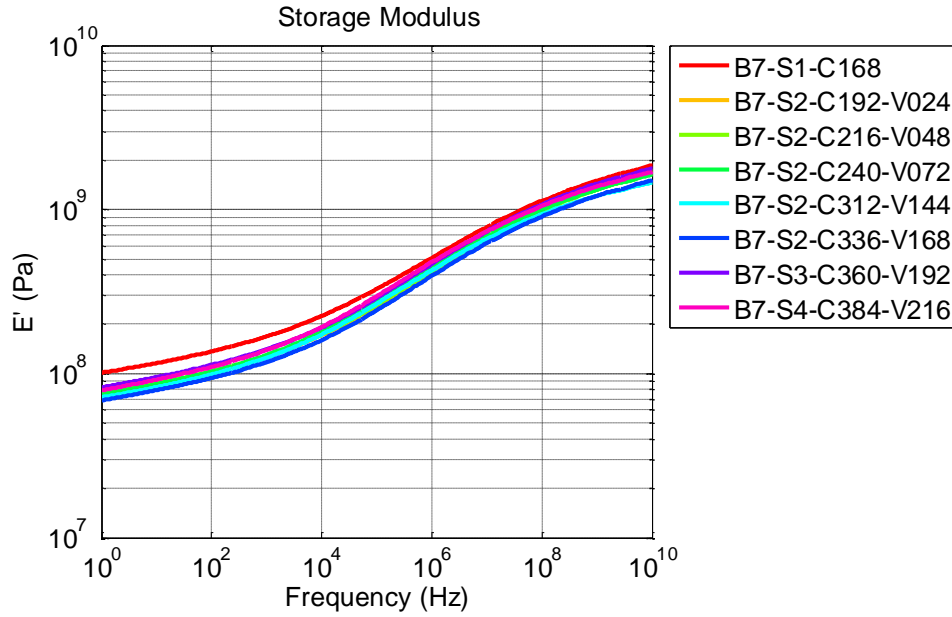


Figure 3.24: Storage modulus values of Block 7 samples.

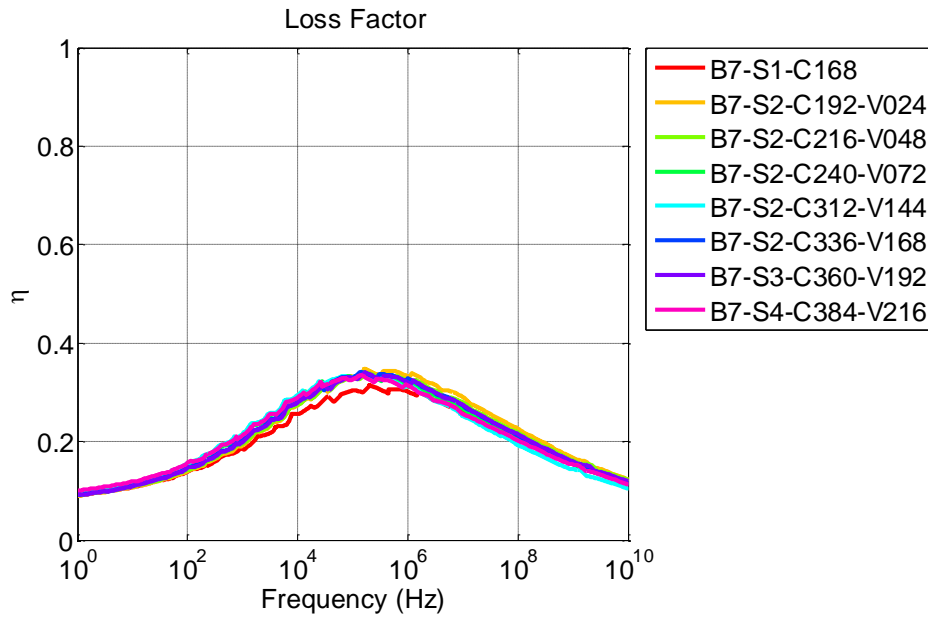


Figure 3.25: Storage modulus values of Block 7 samples.

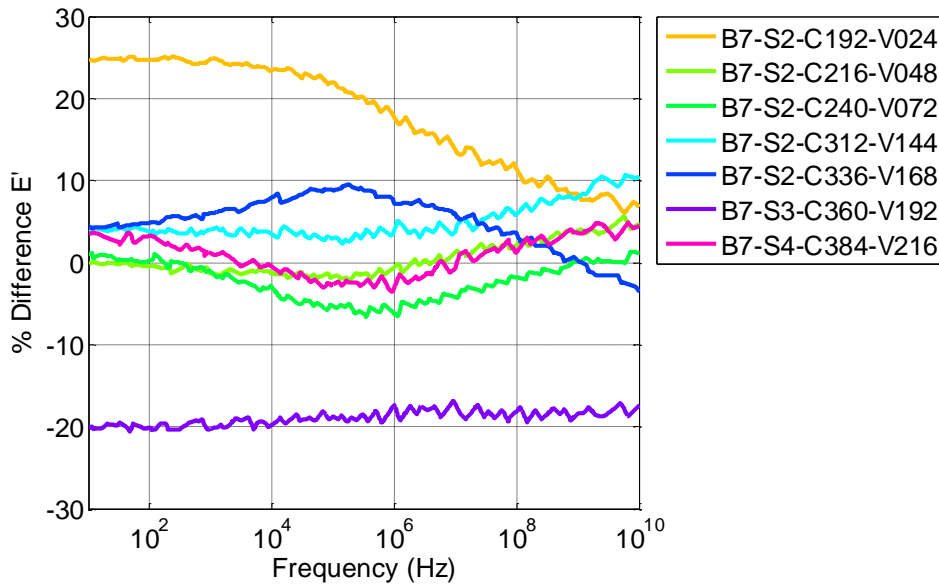


Figure 3.26: % Difference in Block 7 sample storage modulus values referenced to B7-S1-C168.

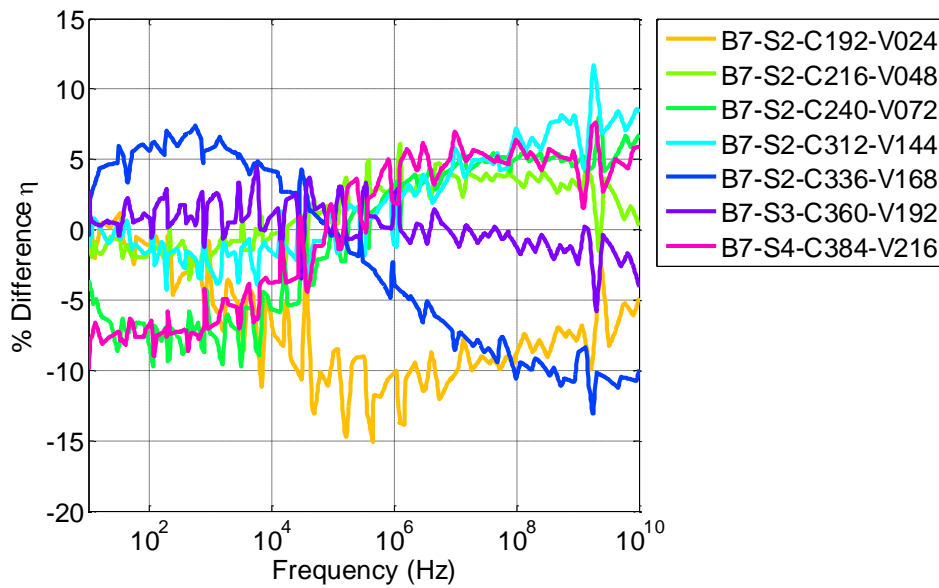


Figure 3.27: % Difference in Block 7 sample loss factor values referenced to B7-S1-C168.

Figure 3.20 and Figure 3.27 indicate that the DMTA testing results of Block 6 and Block 7 are consistent with the results from Block 5. The results from testing Block 5, Block 6, and Block 7 indicate that there is not a significant difference

between viscoelastic properties of unpolarized and polarized samples. Additionally, once a sample is polarized, the properties do change in time following any trend.

3.2.5 Average Viscoelastic Properties

Reference [1] demonstrated that polarization, or exposing the polymer to an electric field, produces a change in the response of the material to applied strain; for a sinusoidal applied stress, the *CB* filled polyurethane sample that had been polarized exhibited a sinusoidal response with significantly decreased noise than the response of non-polarized samples. Therefore, the viscoelastic properties of the polarized *CB* filled polyurethane blocks will be used in this study. Due to the consistency of the Blocks 5, 6, and 7 results, an average of the viscoelastic properties of each sample was calculated and used as the representative viscoelastic properties of the *CB* filled polyurethane. These properties are presented below in Figure 3.28 and Figure 3.29.

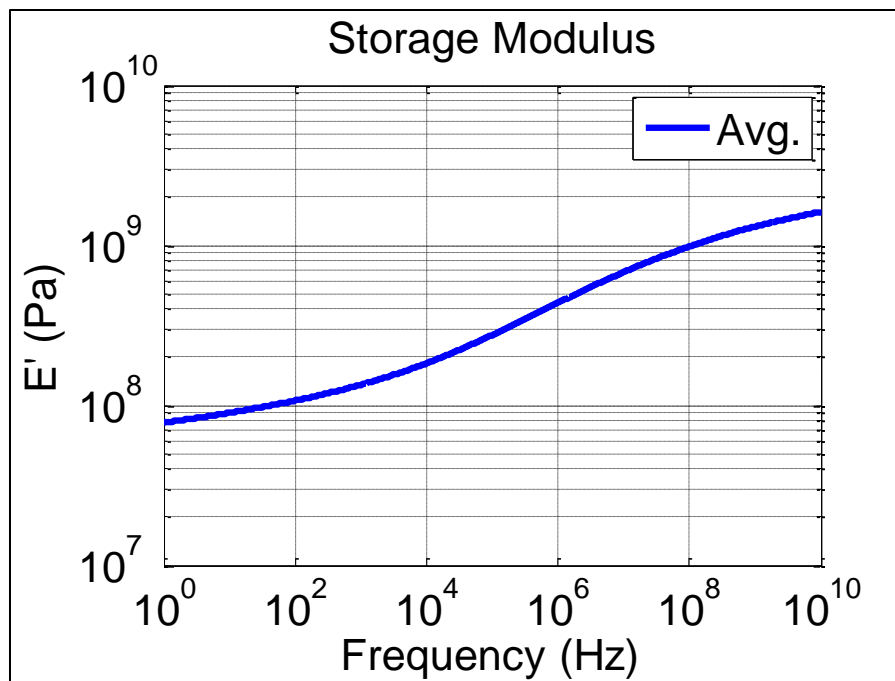


Figure 3.28: *CB* filled polyurethane storage modulus.

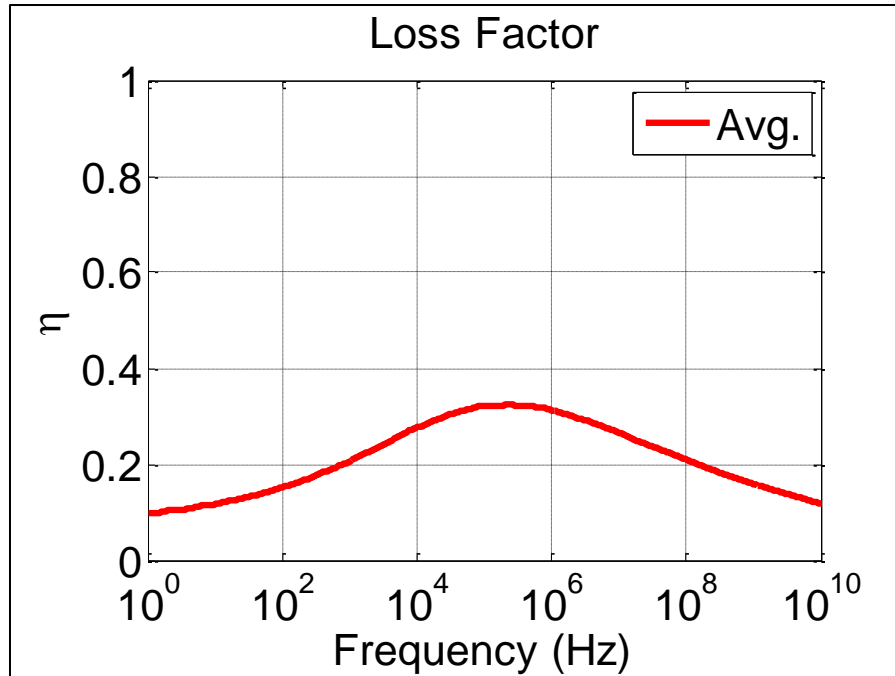


Figure 3.29: *CB* filled polyurethane loss factor.

3.3 Summary

The following conclusions can be drawn from DMTA testing of the *CB* filled polyurethane:

1. Oven-cured blocks tend to contain surface bubbles, which could indicate subsurface voids and lead to inhomogeneous properties throughout the block. Press-cured blocks do not exhibit any surface bubbles. However, there is no discernable difference in the viscoelastic properties of the oven-cured and press-cured blocks.
2. The addition of *CB* particles stiffens the polyurethane and increases the *Loss Factor* at low frequencies.
3. The variability in viscoelastic properties between different samples of the *CB* filled polyurethane is within an acceptable variation.

4. The viscoelastic properties of the *CB* filled polyurethane do not appear to change significantly over time.
5. Polarization of the *CB* filled polyurethane does not discernably affect the viscoelastic properties as compared to the unpolarized case.

The following Chapters will use the results from Section 3.2.5 to explore the use of the *CB* filled polyurethane as an array of pressure sensors to localize an acoustic sources location.

Chapter 4: Carbon Black Sensor Model

The primary objective of this study was to use an array of *CB* filled polyurethane sensors to measure the sound pressure from an acoustic source in a sound field, and identify the source's location in the field. The process of using an array of sensors to sample a sound field and filter those samples to favor signals from a particular direction is known as acoustic source localization. A more general term for acoustic source localization is spatial filtering; using an array to spatially sample a sound field at different locations and then combining those samples to receive sound from one direction while attenuating signals from other directions [9]. The purpose of this Chapter is to develop an analytical model of the *CB* filled polyurethane sensors, and the structure on which these sensors are mounted. The results of this Chapter will be used in Chapter 5 to study the reality of the using *CB* filled polyurethane sensors to execute acoustic source localization.

4.1 Base Vibration Model

4.1.1 Introduction

The purpose of this section is to present a model of the dynamic response of the aluminum plate that serves as the base of the *CB* filled polyurethane sensor array. This model will be used in conjunction with the acoustic model developed in Section 5.1, and the *CB* filled polyurethane model developed in Section 4.2, to study the response of the *CB* filled polyurethane sensor array to incident pressure waves.

The plate was an aluminum plate modeled in Matlab® using finite element analysis (FEA) techniques, including Kirchoff's thin plate theory. The derivation of this FEM model relied heavily on the derivations in Reference [3].

4.1.2 Single Element Definition

A single-element of the plate model is presented below in Figure 4.1.

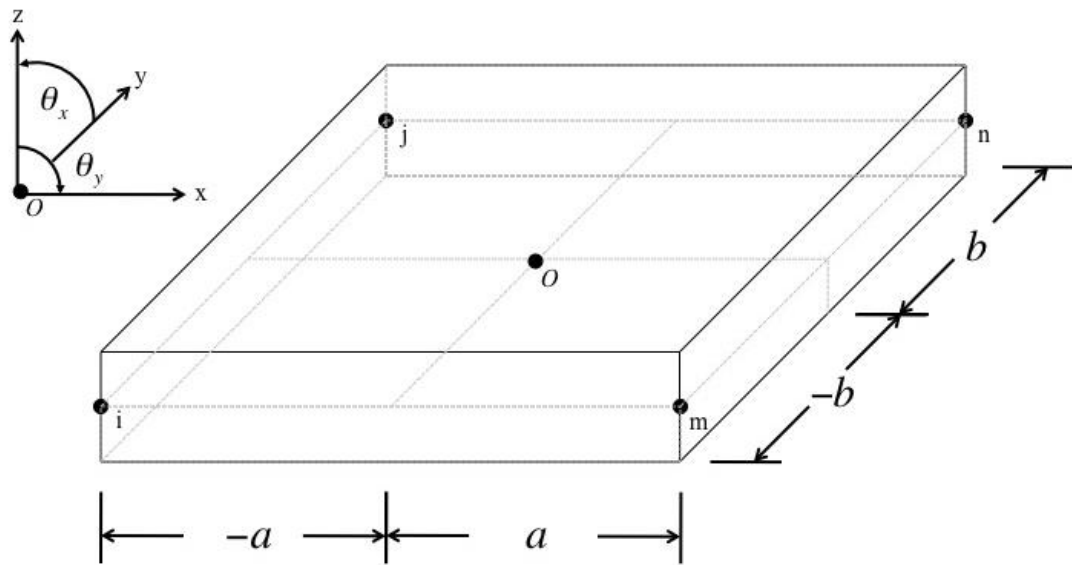


Figure 4.1: Single-element of aluminum plate FEM.

Figure 4.1 indicates that four nodes bound a single element of the plate FEM. The motion of each of these nodes is comprised of (5) degrees of freedom (DOF); (3) translational DOF, and (2) rotational DOF. The DOF of the element are described in further detail below:

- $u_k \Rightarrow$ Displacement of the plate element (x-direction)
- $v_k \Rightarrow$ Displacement of the plate element (y-direction)
- $w_k \Rightarrow$ Displacement of the plate element (z-direction)
- $\theta_{y,k} = -\frac{\partial w_k}{\partial x} = -w_{x,k} \Rightarrow$ Angular displacement of the plate element about the y-axis

$$\theta_{x,k} = \frac{\partial w_k}{\partial y} = w_{y,k} \Rightarrow \text{Angular displacement of the plate element about the } x\text{-axis}$$

The index k above is given by $k = i, j, m, n$, where i, j, m , and n represent each of the four nodes of the single-element. The right-hand-rule was used to determine the orientation and signs of the above angular displacements (θ).

The dimensions of the single plate element are related to the dimensions of the assembled plate by the following equations:

$$2a = \frac{L_x}{M} \quad (4.1.2.1)$$

$$2b = \frac{L_y}{N} \quad (4.1.2.2)$$

where

$2a =$	<i>Size of the single plate element in the x-direction</i>
$2b =$	<i>Size of the single plate element in the y-direction</i>
$L_x =$	<i>Length of the assembled plate in the x-direction</i>
$L_y =$	<i>Length of the assembled plate in the y-direction</i>
$M =$	<i>Number of elements in the x-direction</i>
$N =$	<i>Number of elements in the y-direction</i>

4.1.3 Generation of Interpolation Equations – Single Element

The *Nodal Displacement Vector* $\{\Delta_k\}$ for each node of a single plate element is given by the following expression:

$$\underbrace{\{\Delta_k\}}_{1 \times 5} = \{u_k \quad v_k \quad w_k \quad -w_{x,k} \quad w_{y,k}\} \quad (4.1.3.1)$$

The *Nodal Displacement Vector* $\{\Delta_e\}$ for the entire element is given by the following expression:

$$\underbrace{\{\Delta_e\}}_{20 \times 1} = \left\{ \underbrace{\{\Delta_i\}}_{1 \times 5} \quad \underbrace{\{\Delta_j\}}_{1 \times 5} \quad \underbrace{\{\Delta_m\}}_{1 \times 5} \quad \underbrace{\{\Delta_n\}}_{1 \times 5} \right\}^T \quad (4.1.3.2)$$

Finite element analysis utilizes interpolation to describe the motion of elements of the structure. To interpolate is to approximate the value of a function between known values by operating on the known values with a formula different from the function itself. In the case of finite element analysis, the “known values” are the *DOF* to be found at the nodes of each element. The interpolation function is referred to here as the shape function

The motion in the z-direction, $w(x,y)$, is assumed to be described by a linear shape function. Since each element has 20 *DOF* (4 nodes, 5 *DOF* per node), a shape function with 20 constants must be applied. The following shape functions, written in vector form, will be used to represent the deflections $u(x,y)$, $v(x,y)$, and $w(x,y)$ of a single aluminum plate element:

$$\underbrace{u(x, y)}_{1 \times 1} = \underbrace{\{f_1(x, y)\}}_{1 \times 20} \underbrace{\{\alpha\}}_{20 \times 1} \quad (4.1.3.3)$$

$$\underbrace{v(x, y)}_{1 \times 1} = \underbrace{\{f_2(x, y)\}}_{1 \times 20} \underbrace{\{\alpha\}}_{20 \times 1} \quad (4.1.3.4)$$

$$\underbrace{w(x, y)}_{1 \times 1} = \underbrace{\{f_3(x, y)\}}_{1 \times 20} \underbrace{\{\alpha\}}_{20 \times 1} \quad (4.1.3.5)$$

The vector $\{\alpha\}$ in equations (4.1.3.3) through (4.1.3.5) is defined as follows:

$$\underbrace{\{\alpha\}}_{20 \times 1} = \left\{ \underbrace{\{\alpha_1\}}_{1 \times 4} \quad \underbrace{\{\alpha_2\}}_{1 \times 4} \quad \underbrace{\{\alpha_3\}}_{1 \times 2} \right\}^T \quad (4.1.3.6)$$

The vectors $\{\alpha_1\}$, $\{\alpha_2\}$, and $\{\alpha_3\}$, $\{\alpha_{3,1}\}$, $\{\alpha_{3,2}\}$, and $\{\alpha_{3,3}\}$ in expression (4.1.3.6) are composed of the following constants:

$$\underbrace{\{\alpha_1\}}_{1 \times 4} = \{a_1 \quad a_2 \quad a_3 \quad a_4\} \quad (4.1.3.7)$$

$$\underbrace{\{\alpha_2\}}_{1 \times 4} = \{a_5 \quad a_6 \quad a_7 \quad a_8\} \quad (4.1.3.8)$$

$$\underbrace{\{\alpha_3\}}_{1 \times 12} = \{b_1 \quad b_2 \quad b_3 \quad b_4 \quad b_5 \quad b_6 \quad b_7 \quad b_8 \quad b_9 \quad b_{10} \quad b_{11} \quad b_{12}\} \quad (4.1.3.9)$$

The vectors $\{f_1(x,y)\}$, $\{f_2(x,y)\}$, and $\{f_3(x,y)\}$ in equations (4.1.3.3) through (4.1.3.5) are composed of the following terms:

$$\underbrace{\{f_1(x,y)\}}_{1 \times 20} = \left\{ 1 \quad x \quad y \quad xy \quad \underbrace{\{0\}}_{1 \times 16} \right\} \quad (4.1.3.10)$$

$$\underbrace{\{f_2(x,y)\}}_{1 \times 20} = \left\{ \underbrace{\{0\}}_{1 \times 4} \quad 1 \quad x \quad y \quad xy \quad \underbrace{\{0\}}_{1 \times 12} \right\} \quad (4.1.3.11)$$

$$\underbrace{\{f_3(x,y)\}}_{1 \times 20} = \left\{ \underbrace{\{0\}}_{1 \times 8} \quad 1 \quad x \quad y \quad x^2 \quad xy \quad y^2 \quad x^3 \quad x^2y \quad xy^2 \quad y^3 \quad x^3y \quad xy^3 \right\} \quad (4.1.3.12)$$

The boundary conditions at the four nodes of the single-element, based on the geometry presented in Figure 4.1, are presented below in Table 4.1.

Table 4.1: Boundary conditions of single-element.

@ $x_i = -a$ and $y_i = -b$	$u = u_i$	$v = v_i$	$w = w_i$	$w_x = w_{x,i}$	$w_y = w_{y,i}$
@ $x_j = -a$ and $y_j = -b$	$u = u_j$	$v = v_j$	$w = w_j$	$w_x = w_{x,j}$	$w_y = w_{y,j}$
@ $x_m = -a$ and $y_m = -b$	$u = u_m$	$v = v_m$	$w = w_m$	$w_x = w_{x,m}$	$w_y = w_{y,m}$
@ $x_n = -a$ and $y_n = -b$	$u = u_n$	$v = v_n$	$w = w_n$	$w_x = w_{x,n}$	$w_y = w_{y,n}$

Applying the boundary conditions to the shape functions in equation (4.1.3.3) through equation (4.1.3.5), the *Nodal Displacement Vector* $\{\Delta_e\}$ in equation (4.1.3.1) can be expressed as follows:

$$\underbrace{\{\Delta_e\}}_{20 \times 1} = \underbrace{[A]}_{20 \times 20} \underbrace{\{\alpha\}}_{20 \times 1} \quad (4.1.3.13)$$

The matrix $[A]$ in equation (4.1.3.13) is given by the following expression:

$$\underbrace{[A]}_{20 \times 20} = \begin{bmatrix} \underbrace{[A_i]}_{5 \times 20} \\ \underbrace{[A_j]}_{5 \times 20} \\ \underbrace{[A_m]}_{5 \times 20} \\ \underbrace{[A_n]}_{5 \times 20} \end{bmatrix} \quad (4.1.3.14)$$

The individual matrices $[A_k]$ ($k = i, j, m, n$) in equation (4.1.3.14) are given by the following:

$$\underbrace{[A_k]}_{5 \times 20} = \begin{bmatrix} \underbrace{\{f_1(x_k, y_k)\}}_{1 \times 20} \\ \underbrace{\{f_2(x_k, y_k)\}}_{1 \times 20} \\ \underbrace{\{f_3(x_k, y_k)\}}_{1 \times 20} \\ \underbrace{\frac{\partial \{f_3(x_k, y_k)\}}{\partial x}}_{1 \times 20} \\ \underbrace{\frac{\partial \{f_3(x_k, y_k)\}}{\partial y}}_{1 \times 20} \end{bmatrix} \quad (4.1.3.15)$$

The vectors $\{f_1(x_k, y_k)\}$, $\{f_2(x_k, y_k)\}$, and $\{f_3(x_k, y_k)\}$, are the shape functions given in equations (4.1.3.10) through (4.1.3.12) evaluated at the four nodes i, j, m , and n , respectively.

Solving for $\{\alpha\}$ in equation (4.1.3.13) yields the following:

$$\underbrace{\{\alpha\}}_{20 \times 1} = \underbrace{[A]}_{20 \times 20}^{-1} \underbrace{\{\Delta_e\}}_{20 \times 1} \quad (4.1.3.16)$$

4.1.4 Displacement & Velocity Fields – Single Element

The following vector represents the *Displacement Field* $\{q\}$ of the plate element:

$$\underbrace{\{q\}}_{5 \times 1} = \underbrace{\begin{Bmatrix} u(x, y) \\ v(x, y) \\ w(x, y) \\ \theta_y(x, y) \\ \theta_x(x, y) \end{Bmatrix}}_{5 \times 1} = \underbrace{\begin{Bmatrix} u(x, y) \\ v(x, y) \\ w(x, y) \\ -w_x(x, y) \\ w_y(x, y) \end{Bmatrix}}_{5 \times 1} \quad (4.1.4.1)$$

The *Displacements* in equation (4.1.4.1) are defined as follows:

$$\begin{aligned} u(x, y) &\Rightarrow \text{Displacement of the plate element (x-direction)} \\ v(x, y) &\Rightarrow \text{Displacement of the plate element (y-direction)} \\ w(x, y) &\Rightarrow \text{Displacement of the plate element (z-direction)} \\ \theta_y(x, y) &= -\frac{\partial}{\partial x} w(x, y) = -w_x(x, y) \Rightarrow \text{Angular displacement of the plate element about the y-axis} \\ \theta_x(x, y) &= \frac{\partial}{\partial y} w(x, y) = w_y(x, y) \Rightarrow \text{Angular displacement of the plate element about the x-axis} \end{aligned}$$

Similar to the derivation of the *Nodal Displacement Vectors* in Chapter 4.2.3, the *Angular Velocities* of the top-constraining layer are assumed to be functions of the displacement in the *z-direction*. Recall that equations (4.2.3.3) through (4.2.3.5) describe the motion of the top-constraining layer. Plugging these equations into equation (4.2.4.1) yields the following:

$$\begin{aligned}
\underbrace{\{q\}}_{5 \times 1} &= \underbrace{\begin{Bmatrix} u(x, y) \\ v(x, y) \\ w(x, y) \\ \theta_y(x, y) \\ \theta_x(x, y) \end{Bmatrix}}_{5 \times 1} = \underbrace{\begin{Bmatrix} u(x, y) \\ v(x, y) \\ w(x, y) \\ -w_x(x, y) \\ w_y(x, y) \end{Bmatrix}}_{5 \times 1} = \begin{bmatrix} \underbrace{\{f_1(x, y)\}}_{1 \times 20} \\ \underbrace{\{f_2(x, y)\}}_{1 \times 20} \\ \underbrace{\{f_3(x, y)\}}_{1 \times 20} \\ -\underbrace{\frac{\partial \{f_3(x, y)\}}{\partial x}}_{1 \times 20} \\ \underbrace{\frac{\partial \{f_3(x, y)\}}{\partial y}}_{1 \times 20} \end{bmatrix} \underbrace{\{\alpha\}}_{20 \times 1} \quad (4.1.4.2)
\end{aligned}$$

Equation (4.2.4.2) is composed of the *Shape Functions* established in equations (4.2.3.10) through (4.2.3.12), and the unknown constants solved for in equation (4.2.3.16). Plugging equation (4.2.3.16) into equation (4.2.4.2) yields the following:

$$\begin{aligned}
\underbrace{\{q\}}_{5 \times 1} &= \underbrace{\begin{Bmatrix} u(x, y) \\ v(x, y) \\ w(x, y) \\ \theta_y(x, y) \\ \theta_x(x, y) \end{Bmatrix}}_{5 \times 1} = \underbrace{\begin{Bmatrix} u(x, y) \\ v(x, y) \\ w(x, y) \\ -w_x(x, y) \\ w_y(x, y) \end{Bmatrix}}_{5 \times 1} = \begin{bmatrix} \underbrace{\{f_1(x, y)\}}_{1 \times 20} \\ \underbrace{\{f_2(x, y)\}}_{1 \times 20} \\ \underbrace{\{f_3(x, y)\}}_{1 \times 20} \\ -\underbrace{\frac{\partial \{f_3(x, y)\}}{\partial x}}_{1 \times 20} \\ \underbrace{\frac{\partial \{f_3(x, y)\}}{\partial y}}_{1 \times 20} \end{bmatrix} \underbrace{[A]^{-1}}_{20 \times 20} \underbrace{\{\Delta_e\}}_{20 \times 1} \quad (4.1.4.3)
\end{aligned}$$

Equation (4.2.4.3) can be simplified as follows:

$$\underbrace{\{q\}}_{5 \times 1} = \underbrace{\begin{Bmatrix} u(x, y) \\ v(x, y) \\ w(x, y) \\ -w_x(x, y) \\ w_y(x, y) \end{Bmatrix}}_{5 \times 1} = \begin{bmatrix} \underbrace{\{N_1\}}_{1 \times 20} \\ \underbrace{\{N_2\}}_{1 \times 20} \\ \underbrace{\{N_3\}}_{1 \times 20} \\ -\underbrace{\{N_3\}_x}_{1 \times 20} \\ \underbrace{\{N_3\}_y}_{1 \times 20} \end{bmatrix} \underbrace{\{\Delta_e\}}_{20 \times 1} \quad (4.1.4.5)$$

The individual vectors $\{N_{\#}\}$ in equation (4.2.4.5) are given by the following:

$$\begin{bmatrix} \underbrace{\{N_1\}}_{1 \times 20} \\ \underbrace{\{N_2\}}_{1 \times 20} \\ \underbrace{\{N_3\}}_{1 \times 20} \\ -\underbrace{\{N_3\}_x}_{1 \times 20} \\ \underbrace{\{N_3\}_y}_{1 \times 20} \end{bmatrix} = \begin{bmatrix} \underbrace{\{f_1(x, y)\}}_{1 \times 20} \\ \underbrace{\{f_2(x, y)\}}_{1 \times 20} \\ \underbrace{\{f_3(x, y)\}}_{1 \times 20} \\ -\underbrace{\frac{\partial \{f_3(x, y)\}}{\partial x}}_{1 \times 20} \\ \underbrace{\frac{\partial \{f_3(x, y)\}}{\partial y}}_{1 \times 20} \end{bmatrix} \underbrace{[A]^{-1}}_{20 \times 20} \quad (4.1.4.6)$$

The *Velocity Field* is given by taking the time-derivative of equation (4.2.4.5), as follows:

$$\frac{d}{dt} \underbrace{\{q\}}_{5 \times 1} = \underbrace{\{\dot{q}\}}_{5 \times 1} = \underbrace{\begin{Bmatrix} \dot{u}(x, y) \\ \dot{v}(x, y) \\ \dot{w}(x, y) \\ -\dot{w}_x(x, y) \\ \dot{w}_y(x, y) \end{Bmatrix}}_{5 \times 1} = \begin{bmatrix} \underbrace{\{N_1\}}_{1 \times 20} \\ \underbrace{\{N_2\}}_{1 \times 20} \\ \underbrace{\{N_3\}}_{1 \times 20} \\ -\underbrace{\{N_3\}_x}_{1 \times 20} \\ \underbrace{\{N_3\}_y}_{1 \times 20} \end{bmatrix} \underbrace{\{\dot{\Delta}_e\}}_{20 \times 1} \quad (4.1.4.7)$$

4.1.5 Kinetic Energy – Single Element

The *Kinetic Energy* (T) of an object is given by the following equation:

$$T = \frac{1}{2} \int_V \rho \{v\} \cdot \{v\} dV = \frac{1}{2} \int_V \rho \{v\}^T \{v\} dV \quad (4.1.5.1)$$

where, $\{v\} = \text{Vector of velocities of the object}$
 $\rho = \text{Density of the object}$
 $V = \text{Volume of the object}$

A detailed derivation of equation (4.2.5.1) is presented in Appendix A. Plugging the *Velocity Field* calculated in equation (4.1.4.7) into equation (4.1.5.1), and integrating over the *Volume* (V_e) of the plate element, yields the following expression for the *Kinetic Energy* (T_e):

$$\begin{aligned} \underline{T_e} &= \frac{1}{2} \int_{V_e} \rho(x, y, z) \underbrace{\{\dot{q}(x, y)\}}_{(1 \times 5)}^T \underbrace{\{\dot{q}(x, y)\}}_{(5 \times 1)} dV_e \\ \underline{T_e} &= \frac{1}{2} \int_{V_e} \rho(x, y, z) \underbrace{\left\{ \begin{array}{ccccc} \dot{u}(x, y) & \dot{v}(x, y) & \dot{w}(x, y) & -\dot{w}_x(x, y) & \dot{w}_y(x, y) \end{array} \right\}}_{(1 \times 5)} \underbrace{\left\{ \begin{array}{c} \dot{u}(x, y) \\ \dot{v}(x, y) \\ \dot{w}(x, y) \\ -\dot{w}_x(x, y) \\ \dot{w}_y(x, y) \end{array} \right\}}_{5 \times 1} dV_e \end{aligned} \quad (4.1.5.2)$$

The *Density* (ρ) of the plate element is independent of the *Volume* (V_e).

Therefore, equation (4.1.5.2) can be rewritten, and simplified, as follows:

$$\underline{T_e} = \frac{1}{2} \rho \int_{V_e} \underbrace{\left\{ \begin{array}{ccccc} \dot{u}(x, y) & \dot{v}(x, y) & \dot{w}(x, y) & -\dot{w}_x(x, y) & \dot{w}_y(x, y) \end{array} \right\}}_{(1 \times 5)} \underbrace{\left\{ \begin{array}{c} \dot{u}(x, y) \\ \dot{v}(x, y) \\ \dot{w}(x, y) \\ -\dot{w}_x(x, y) \\ \dot{w}_y(x, y) \end{array} \right\}}_{5 \times 1} dV_e$$

$$\begin{aligned}
\underbrace{T_e}_{(1 \times 1)} &= \underbrace{\frac{1}{2} \rho \int_{V_e} \underbrace{\dot{u}(x, y)^T}_{(1 \times 1)} \underbrace{\dot{u}(x, y)}_{(1 \times 1)} dV_e + \frac{1}{2} \rho \int_{V_e} \underbrace{\dot{v}(x, y)^T}_{(1 \times 1)} \underbrace{\dot{v}(x, y)}_{(1 \times 1)} dV_e + \dots}_{\text{Kinetic Energy due to in-plane motion}} \\
&\dots + \underbrace{\frac{1}{2} \rho \int_{V_e} \underbrace{\dot{w}(x, y)^T}_{(1 \times 1)} \underbrace{\dot{w}(x, y)}_{(1 \times 1)} dV_e + \dots}_{\text{Kinetic Energy due to bending}} \\
&\dots + \underbrace{\frac{1}{2} \rho \int_{V_e} \underbrace{\dot{w}_x(x, y)^T}_{(1 \times 1)} \underbrace{\dot{w}_x(x, y)}_{(1 \times 1)} dV_e + \frac{1}{2} \rho \int_{V_e} \underbrace{\dot{w}_y(x, y)^T}_{(1 \times 1)} \underbrace{\dot{w}_y(x, y)}_{(1 \times 1)} dV_e}_{\text{Kinetic Energy due to rotational inertia}}
\end{aligned} \tag{4.1.5.3}$$

As indicated in equation (4.1.5.3), the *Kinetic Energy* (T_e) of the plate element is a combination of the *Kinetic Energy* due to in-plane motion, *Kinetic Energy* due to bending, and *Kinetic Energy* due to rotational inertia. The *Kinetic Energy* due to rotational inertia of the plate element is assumed to be negligible. Consequently, equation (4.1.5.3) can be simplified as follows:

$$\begin{aligned}
\underbrace{T_e}_{(1 \times 1)} &= \underbrace{\frac{1}{2} \rho \int_{V_e} \underbrace{\dot{u}(x, y)^T}_{(1 \times 1)} \underbrace{\dot{u}(x, y)}_{(1 \times 1)} dV_e + \frac{1}{2} \rho \int_{V_e} \underbrace{\dot{v}(x, y)^T}_{(1 \times 1)} \underbrace{\dot{v}(x, y)}_{(1 \times 1)} dV_e + \dots}_{\text{Kinetic Energy due to in-plane motion}} \\
&\dots + \underbrace{\frac{1}{2} \rho \int_{V_e} \underbrace{\dot{w}(x, y)^T}_{(1 \times 1)} \underbrace{\dot{w}(x, y)}_{(1 \times 1)} dV_e}_{\text{Kinetic Energy due to bending}}
\end{aligned} \tag{4.1.5.4}$$

For simplification, equation (4.1.5.4) can be rewritten as follows:

$$\underbrace{T_e}_{(1 \times 1)} = \underbrace{T_{p,e}}_{(1 \times 1)} + \underbrace{T_{b,e}}_{(1 \times 1)} \tag{4.1.5.5}$$

The individual components of equation (4.1.5.5) are given by the following equations:

$$\begin{aligned}
\underbrace{T_{p,e}}_{(1 \times 1)} &= \frac{1}{2} \rho \int_{V_e} \underbrace{\dot{u}(x, y)^T}_{(1 \times 1)} \underbrace{\dot{u}(x, y)}_{(1 \times 1)} dV_e + \frac{1}{2} \rho \int_{V_e} \underbrace{\dot{v}(x, y)^T}_{(1 \times 1)} \underbrace{\dot{v}(x, y)}_{(1 \times 1)} dV_e \\
\underbrace{T_{p,e}}_{(1 \times 1)} &= \frac{1}{2} \rho \int_{V_e} \left(\underbrace{\dot{u}(x, y)^T}_{(1 \times 1)} \underbrace{\dot{u}(x, y)}_{(1 \times 1)} + \underbrace{\dot{v}(x, y)^T}_{(1 \times 1)} \underbrace{\dot{v}(x, y)}_{(1 \times 1)} \right) dV_e
\end{aligned} \tag{4.1.5.6}$$

$$\underbrace{T_{b,e}}_{(1 \times 1)} = \frac{1}{2} \rho \int_{V_e} \underbrace{\dot{w}(x, y)^T}_{(1 \times 1)} \underbrace{\dot{w}(x, y)}_{(1 \times 1)} dV_e \quad (4.1.5.7)$$

where $T_{p,e} =$ Kinetic Energy due to in-plane motion
 $T_{b,e} =$ Kinetic energy due to bending

Consider equation (4.1.5.6), which represents the *Kinetic Energy* ($T_{p,e}$) due to in-plane motion. Plugging the *Velocity* relationships equation (4.1.4.7) into equation (4.1.5.6), yields the following:

$$\begin{aligned} \underbrace{T_{p,e}}_{(1 \times 1)} &= \frac{1}{2} \rho \int_{V_e} \left(\underbrace{\dot{u}(x, y)^T}_{(1 \times 1)} \underbrace{\dot{u}(x, y)}_{(1 \times 1)} + \underbrace{\dot{v}(x, y)^T}_{(1 \times 1)} \underbrace{\dot{v}(x, y)}_{(1 \times 1)} \right) dV_e \\ \underbrace{T_{p,e}}_{(1 \times 1)} &= \frac{1}{2} \rho \int_{V_e} \left(\underbrace{\{N_1\} \{\dot{\Delta}_e\}}_{1 \times 20 \quad 20 \times 1} \right)^T \left(\underbrace{\{N_1\} \{\dot{\Delta}_e\}}_{1 \times 20 \quad 20 \times 1} \right) + \left(\underbrace{\{N_2\} \{\dot{\Delta}_e\}}_{1 \times 20 \quad 20 \times 1} \right)^T \left(\underbrace{\{N_2\} \{\dot{\Delta}_e\}}_{1 \times 20 \quad 20 \times 1} \right) dV_e \\ \underbrace{T_{p,e}}_{(1 \times 1)} &= \frac{1}{2} \rho \int_{V_e} \left(\underbrace{\{\dot{\Delta}_e\}^T}_{1 \times 20} \underbrace{\{N_1\}^T}_{20 \times 1} \underbrace{\{N_1\}}_{1 \times 20} \underbrace{\{\dot{\Delta}_e\}}_{20 \times 1} + \underbrace{\{\dot{\Delta}_e\}^T}_{1 \times 20} \underbrace{\{N_2\}^T}_{20 \times 1} \underbrace{\{N_2\}}_{1 \times 20} \underbrace{\{\dot{\Delta}_e\}}_{20 \times 1} \right) dV_e \\ \underbrace{T_{p,e}}_{(1 \times 1)} &= \frac{1}{2} \rho \int_{V_e} \underbrace{\{\dot{\Delta}_e\}^T}_{1 \times 20} \left[\underbrace{\{N_1\}^T}_{20 \times 1} \underbrace{\{N_1\}}_{1 \times 20} + \underbrace{\{N_2\}^T}_{20 \times 1} \underbrace{\{N_2\}}_{1 \times 20} \right] \underbrace{\{\dot{\Delta}_e\}}_{20 \times 1} dV_e \end{aligned} \quad (4.1.5.8)$$

The time-derivative of the *Nodal Displacement Vector* $\{\dot{\Delta}_e\}$, the *Nodal Velocity Vector* $\{\dot{\Delta}_e\}$ represents the velocity of the element at the nodal boundaries. Therefore, the *Nodal Velocity Vector* is independent of the element *Volume* (V_e). Applying this observation to equation (4.1.5.8) yields the following:

$$\underbrace{T_{p,e}}_{(1 \times 1)} = \frac{1}{2} \underbrace{\{\dot{\Delta}_e\}^T}_{1 \times 40} \left[\rho \int_{V_e} \left(\underbrace{\{N_1\}^T}_{20 \times 1} \underbrace{\{N_1\}}_{1 \times 20} + \underbrace{\{N_2\}^T}_{20 \times 1} \underbrace{\{N_2\}}_{1 \times 20} \right) dV_e \right] \underbrace{\{\dot{\Delta}_e\}}_{20 \times 1} \quad (4.1.5.9)$$

A similar derivation can be applied to equation (4.1.5.7), yielding the following:

$$\underbrace{T_{b,e}}_{(1 \times 1)} = \frac{1}{2} \underbrace{\{\dot{\Delta}_e\}^T}_{1 \times 20} \left[\rho \int_{V_e} \underbrace{\{N_3\}^T}_{20 \times 1} \underbrace{\{N_3\}}_{1 \times 20} dV_e \right] \underbrace{\{\dot{\Delta}_e\}}_{20 \times 1} \quad (4.1.5.10)$$

Appendix A relates the *Kinetic Energy* of a body to its' *Infinitesimal Mass* (dm) and *Velocity* (v). Applying this relationship to equation (4.1.5.9) and equation (4.1.5.10) yields the following:

$$\underbrace{T_{p,e}}_{(1 \times 1)} = \frac{1}{2} \underbrace{\{\dot{\Delta}_e\}^T}_{1 \times 20} \underbrace{[M_{p,e}]}_{20 \times 20} \underbrace{\{\dot{\Delta}_e\}}_{20 \times 1} \quad (4.1.5.11)$$

$$\underbrace{T_{b,e}}_{(1 \times 1)} = \frac{1}{2} \underbrace{\{\dot{\Delta}_e\}^T}_{1 \times 20} \underbrace{[M_{b,e}]}_{20 \times 20} \underbrace{\{\dot{\Delta}_e\}}_{20 \times 1} \quad (4.1.5.12)$$

From equation (4.1.5.9) and equation (4.1.5.11), the *Mass Matrix* $[M_{p,e}]$ of the plate element, due to in-plane motion, is given by the following:

$$\underbrace{[M_{p,e}]}_{(20 \times 20)} = \rho \int_{V_e} \left(\underbrace{\{N_1\}^T}_{20 \times 1} \underbrace{\{N_1\}}_{1 \times 20} + \underbrace{\{N_2\}^T}_{20 \times 1} \underbrace{\{N_2\}}_{1 \times 20} \right) dV_e \quad (4.1.5.13)$$

From equation (4.1.5.10) and equation (4.1.5.12), the *Mass Matrix* $[M_{b,e}]$ of the plate element, due to bending, is given by the following:

$$\underbrace{[M_{b,e}]}_{(20 \times 20)} = \rho \int_{V_e} \underbrace{\{N_3\}^T}_{20 \times 1} \underbrace{\{N_3\}}_{1 \times 20} dV_e \quad (4.1.5.14)$$

Expanding the integration limits of equations (4.1.5.13) and (4.1.5.14), based on the geometry in Figure , yields the following:

$$\underbrace{[M_{p,e}]}_{(20 \times 20)} = \rho \int_{-h/2}^{+h/2} \int_{-b-a}^b \int_a^a \left(\underbrace{\{N_1\}^T}_{20 \times 1} \underbrace{\{N_1\}}_{1 \times 20} + \underbrace{\{N_2\}^T}_{20 \times 1} \underbrace{\{N_2\}}_{1 \times 20} \right) dx dy dz \quad (4.1.5.15)$$

$$\underbrace{[M_{b,e}]}_{(20 \times 20)} = \rho \int_{+h/2}^{+h/2} \int_{-b-a}^b \int_a^a \left(\underbrace{\{N_3\}^T}_{20 \times 1} \underbrace{\{N_3\}}_{1 \times 20} \right) dx dy dz \quad (4.1.5.16)$$

The vectors $\{N_1\}$, $\{N_2\}$, and $\{N_3\}$ are not functions of the z -direction. Consequently, evaluating the integral with respect to the z -direction in equations (4.1.5.15) and (4.1.5.16) yields the following:

$$\underbrace{[M_{p,e}]}_{(20 \times 20)} = \rho h \int_{-b-a}^b \int_{-a}^a \left(\underbrace{\{N_1\}^T}_{20 \times 1} \underbrace{\{N_1\}}_{1 \times 20} + \underbrace{\{N_2\}^T}_{20 \times 1} \underbrace{\{N_2\}}_{1 \times 20} \right) dx dy \quad (4.1.5.17)$$

$$\underbrace{[M_{b,e}]}_{(20 \times 20)} = \rho h \int_{-b-a}^b \int_{-a}^a \left(\underbrace{\{N_3\}^T}_{20 \times 1} \underbrace{\{N_3\}}_{1 \times 20} \right) dx dy \quad (4.1.5.18)$$

Recall that equation (4.1.5.5) describes the *Kinetic Energy* (T_e) of a single plate element as a combination of the *Kinetic Energy* ($T_{p,e}$) due to in-plane motion, and the *Kinetic Energy* ($T_{b,e}$) due to bending. Plugging equations (4.1.5.11) and (4.1.5.12) into equation (4.1.5.5) yields the following:

$$\begin{aligned} \underbrace{T_e}_{(1 \times 1)} &= \underbrace{T_{p,e}}_{(1 \times 1)} + \underbrace{T_{b,e}}_{(1 \times 1)} \\ \underbrace{T_e}_{(1 \times 1)} &= \frac{1}{2} \underbrace{\{\dot{\Delta}_e\}^T}_{1 \times 20} \underbrace{[M_{p,e}]}_{20 \times 20} \underbrace{\{\dot{\Delta}_e\}}_{20 \times 1} + \frac{1}{2} \underbrace{\{\dot{\Delta}_e\}^T}_{1 \times 20} \underbrace{[M_{b,e}]}_{20 \times 20} \underbrace{\{\dot{\Delta}_e\}}_{20 \times 1} \end{aligned} \quad (4.1.5.19)$$

in-planemotion bending

The *Total Mass Matrix* $[M_e]$ of the plate element can be described by the following equation:

$$\underbrace{[M_e]}_{(20 \times 20)} = \underbrace{[M_{p,e}]}_{(20 \times 20)} + \underbrace{[M_{b,e}]}_{(20 \times 20)} \quad (4.1.5.20)$$

In summary, the *Kinetic Energy* (T_e) of plate element can be described by the following expression, where the *Total Mass Matrix* $[M_e]$ and its components are presented in equations (4.1.5.20) (4.1.5.17) and (4.1.5.18), respectively:

$$\underbrace{T_e}_{(1 \times 1)} = \frac{1}{2} \underbrace{\{\dot{\Delta}_e\}^T}_{1 \times 20} \underbrace{[M_e]}_{20 \times 20} \underbrace{\{\dot{\Delta}_e\}}_{20 \times 1} \quad (4.1.5.21)$$

4.1.6 Strain Field – Single Element

Applying an external force to an elastic solid produces internal *Stresses* and *Strains* within the solid. Consider the single-element of an elastic solid, presented below in Figure 4.2.

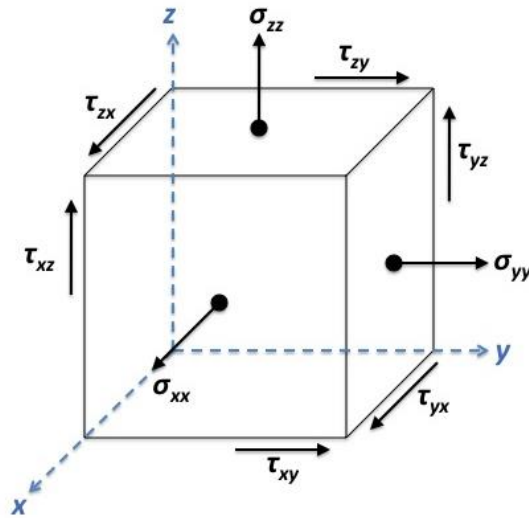


Figure 4.2: Stress field in an elastic solid element due to external forces.

From Figure 4.2, the *Stress Field* of the element can be described by the following matrix:

$$\underbrace{\{\sigma(x, y)\}}_{(3 \times 3)} = \begin{bmatrix} \sigma_{xx}(x, y) & \tau_{xy}(x, y) & \tau_{xz}(x, y) \\ \tau_{yx}(x, y) & \sigma_{yy}(x, y) & \tau_{yz}(x, y) \\ \tau_{zx}(x, y) & \tau_{zy}(x, y) & \sigma_{zz}(x, y) \end{bmatrix} \quad (4.1.6.1)$$

Note that the following *Shear Stress* relationships exist due to force equilibrium:

$$\tau_{xy}(x, y) = \tau_{yx}(x, y) \quad \tau_{yz}(x, y) = \tau_{zy}(x, y) \quad \tau_{xz}(x, y) = \tau_{zx}(x, y)$$

The *Stress* components in equation (4.1.6.1) are defined as follows:

$$\sigma_{xx}(x, y) \Rightarrow \text{Normal stress in the } y\text{-}z \text{ plane acting in the } x\text{-direction}$$

- $\sigma_{yy}(x, y) \Rightarrow$ Normal stress in the x - z plane acting in the y -direction
 $\sigma_{zz}(x, y) \Rightarrow$ Normal stress in the x - y plane acting in the z -direction
 $\tau_{xy}(x, y) \Rightarrow$ Shear stress acting on the z - y plane in the y -direction
 $\tau_{yx}(x, y) \Rightarrow$ Shear stress acting on the x - z plane in the x -direction
 $\tau_{yz}(x, y) \Rightarrow$ Shear stress acting on the x - z plane in the z -direction

The corresponding *Strain Field* produced in the elastic solid is given by the following:

$$\underbrace{\{\boldsymbol{\varepsilon}(x, y)\}}_{(3 \times 3)} = \begin{bmatrix} \varepsilon_{xx}(x, y) & \gamma_{xy}(x, y) & \gamma_{xz}(x, y) \\ \gamma_{yx}(x, y) & \varepsilon_{yy}(x, y) & \gamma_{yz}(x, y) \\ \gamma_{zx}(x, y) & \gamma_{zy}(x, y) & \varepsilon_{zz}(x, y) \end{bmatrix} \quad (4.1.6.2)$$

Note that the following *Shear Strain* relationships exist due to force equilibrium:

$$\gamma_{xy}(x, y) = \gamma_{yx}(x, y) \quad \gamma_{yz}(x, y) = \gamma_{zy}(x, y) \quad \gamma_{xz}(x, y) = \gamma_{zx}(x, y)$$

The *Strain* components in equation (4.1.6.2) are defined as follows:

$\varepsilon_{xx}(x, y) \Rightarrow$	Normal strain in the x -direction, or the ratio of the extension of the elastic solid in the x -direction to the original length in the x -direction, when subjected to an external force in the x -direction
$\varepsilon_{yy}(x, y) \Rightarrow$	Normal strain in the y -direction, or the ratio of the extension of the elastic solid in the y -direction to the original length in the y -direction, when subjected to an external force in the y -direction
$\varepsilon_{zz}(x, y) \Rightarrow$	Normal strain in the z -direction, or the ratio of the extension of the elastic solid in the z -direction to the original length in the z -direction, when subjected to an external force in the z -direction
$\gamma_{xy}(x, y) \Rightarrow$	Total shear strain in the x - y plane, or for small deformations, combination of the ratio of the extension of the elastic solid in the x -direction to the original length in the y -direction and the ratio of the extension of the elastic solid in the y -direction to the original length in the x -direction, when subjected to an external shear load in the x - y plane
$\gamma_{yx}(x, y) \Rightarrow$	Total shear strain in the y - z plane, or for small deformations, the combination of the ratio of the extension of the elastic solid in the y -direction to the original length in the z -direction and the ratio of the extension of the elastic solid in the z -direction to the original length in the y -direction, when subjected to an external shear load in the y - z plane

$\gamma_{xz}(x, y) \Rightarrow$	<i>Total shear strain in the x-z plane, or for small deformations, the combination of the ratio of the extension of the elastic solid in the x-direction to the original length in the z-direction and the ratio of the extension of the elastic solid in the z-direction to the original length in the x-direction, when subjected to an external shear load in the x-z plane</i>
---------------------------------	--

Based on the descriptions above, the *Normal Strains* in equation (4.1.6.2) can be described in terms of the *Displacements* of the elastic solid as follows:

$$\varepsilon_{xx}(x, y) = \frac{du(x, y)}{dx} \tag{4.1.6.3}$$

$$\varepsilon_{yy}(x, y) = \frac{dv(x, y)}{dy} \tag{4.1.6.4}$$

$$\varepsilon_{zz}(x, y) = \frac{dw(x, y)}{dz} \tag{4.1.6.5}$$

The *Displacement* in the *x-direction*, $u(x, y)$, is composed of two components: a component due to *in-plane* motion of the elastic solid in the *x-direction*, $u_p(x, y)$, and a component due to *bending* of the elastic solid about the *y-axis*, $u_b(x, y)$. These *Displacements* are displayed below in Figure 4.3 and Figure 4.4.

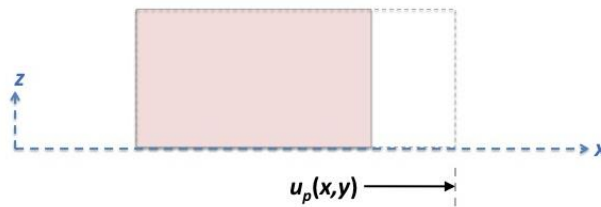


Figure 4.3: Displacement in the x-direction due to in-plane motion of the elastic solid in the x-direction.

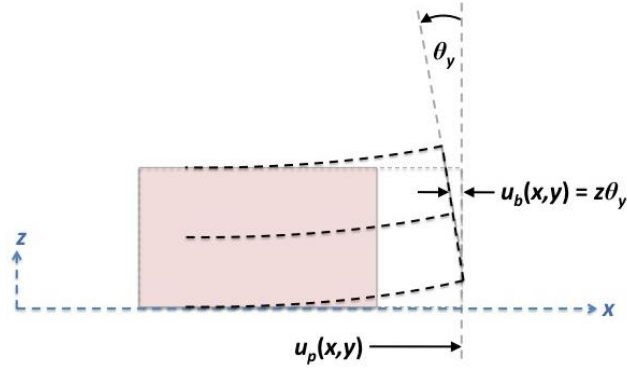


Figure 4.4: Displacement in the x-direction due to bending of the elastic solid about the y-axis.

The total *Displacement* in the *x-direction*, $u(x, y)$, is given by the following expression:

$$u(x, y) = \underbrace{u_p(x, y)}_{\text{in-plane motion}} - \underbrace{u_b(x, y)}_{\text{bending}} \quad (4.1.6.6)$$

From Figure 4.4, it is evident that the *Displacement* in the *x-direction* due to *bending* about the *y-axis*, $u_b(x, y)$, can be described by the following equation:

$$\underbrace{u_b(x, y)}_{\text{bending}} = z\theta_y(x, y) = z \frac{dw(x, y)}{dx} \quad (4.1.6.7)$$

Note that the small-angle approximation was applied in equation (4.1.6.7). Plugging equation (4.1.6.7) into equation (4.1.6.6) yields the total *Displacement* of the elastic solid in the *x-direction*, as follows:

$$u(x, y) = u_p(x, y) - z \frac{dw(x, y)}{dx} \quad (4.1.6.8)$$

Plugging equation (4.1.6.8) into equation (4.1.6.3) yields the *Normal Strain* of the elastic solid in the *x-direction*, $\varepsilon_{xx}(x, y)$, as follows:

$$\varepsilon_{xx}(x, y) = \frac{du(x, y)}{dx} = \frac{du_p(x, y)}{dx} - \frac{d}{dx} \left[z \frac{dw(x, y)}{dx} \right]$$

$$\varepsilon_{xx}(x, y) = \frac{du(x, y)}{dx} = \underbrace{\frac{du_p(x, y)}{dx}}_{\text{d u o i n - p l a n m o t i o n}} - z \underbrace{\frac{d^2w(x, y)}{dx^2}}_{\text{d u o b e n d i n g}} \quad (4.1.6.9)$$

A similar derivation can be followed that yields the total *Displacement* in the *y-direction*, $v(x, y)$, and the *Normal Strain* of the elastic solid in the *y-direction*, $\varepsilon_{yy}(x, y)$, as follows:

$$v(x, y) = v_p(x, y) - z \frac{dw(x, y)}{dy} \quad (4.1.6.10)$$

$$\varepsilon_{yy}(x, y) = \frac{dv(x, y)}{dy} = \underbrace{\frac{dv_p(x, y)}{dy}}_{\text{d u o i n - p l a n m o t i o n}} - z \underbrace{\frac{d^2w(x, y)}{dy^2}}_{\text{d u o b e n d i n g}} \quad (4.1.6.11)$$

For a general elastic solid, the *Displacement* in the *z-direction*, $w(x, y)$ would be a function of the following components: *in-plane* motion of the elastic solid in the *z-direction* and *bending* of the elastic solid about the *z-axis*. However, due to the nature of the elastic solid in this study (thin elastic plate), it is assumed herein that the *bending* of the elastic solid about the *z-axis* is negligible compared to the *bending* about the *x-* and *y-axes*. Therefore, the *Displacement* in the *z-direction*, $w(x, y)$, is only a function of the *in-plane* motion in the *z-direction*.

To express the *Shear Strains* in equation (4.1.6.2), consider Figure 4.5, Figure 4.6, and Figure 4.7 below.

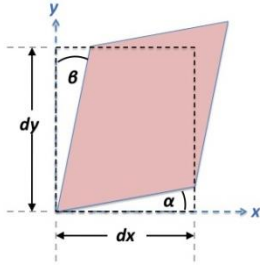


Figure 4.5: Deformation of the elastic solid in the x-y plane.

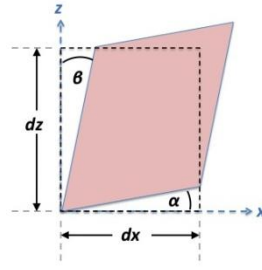


Figure 4.6: Deformation of the elastic solid in the x-z plane.

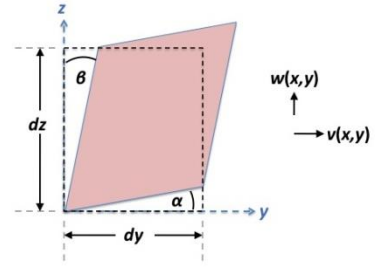


Figure 4.7: Deformation of the elastic solid in the y-z plane.

Consider Figure 4.5, which depicts the deformation of the elastic solid in the x-y plane. For small displacements, the small angle approximation yields the following relationships:

$$\sin(\alpha) \approx \alpha \approx \frac{dv(x, y)}{dx} \quad (4.1.6.12)$$

$$\sin(\beta) \approx \beta \approx \frac{du(x, y)}{dy} \quad (4.1.6.13)$$

From Figure 4.5, the total *Shear Strain* in the x-y plane, $\gamma_{xy}(x, y)$, is given by the following equation:

$$\gamma_{xy}(x, y) = \alpha + \beta \quad (4.1.6.14)$$

Inserting equation (4.1.6.12) and equation (4.1.6.13) into (4.1.6.14) yields the following expression for the *Shear Strain* in the x-y plane $\gamma_{xy}(x, y)$:

$$\gamma_{xy}(x, y) = \frac{du(x, y)}{dy} + \frac{dv(x, y)}{dx} \quad (4.1.6.15)$$

Recall equation (4.1.6.8) and (4.1.6.10), which describe the total *Displacement* of the elastic solid in the *x-direction* and *y-direction*, respectively.

Plugging these two relationships into equation (4.1.6.15), and simplifying, yields:

$$\gamma_{xy}(x, y) = \frac{d}{dy} \left[u_p(x, y) - z \frac{dw(x, y)}{dx} \right] + \frac{d}{dx} \left[v_p(x, y) - z \frac{dw(x, y)}{dy} \right]$$

$$\gamma_{xy}(x, y) = \frac{du_p(x, y)}{dy} - z \frac{d^2w(x, y)}{dxdy} + \frac{dv_p(x, y)}{dx} - z \frac{d^2w(x, y)}{dxdy}$$

$$\gamma_{xy}(x, y) = \underbrace{\frac{du_p(x, y)}{dy} + \frac{dv_p(x, y)}{dx}}_{\text{d u o i n - p l a n e m o t i o n}} - \underbrace{2z \frac{d^2w(x, y)}{dxdy}}_{\text{d u o b e n d i n g}} \quad (4.1.6.16)$$

Following a similar procedure for Figure 4.6 and Figure 4.7 yields the following expressions for the *Shear Strain* in the x-z plane, $\gamma_{xz}(x, y)$, and *Shear Strain* in the y-z plane, $\gamma_{yz}(x, y)$, respectively:

$$\gamma_{xz}(x, y) = \underbrace{\frac{du_p(x, y)}{dz} + \frac{dw(x, y)}{dx}}_{\text{d u o i n - p l a n e m o t i o n}} - \underbrace{z \frac{d^2w(x, y)}{dxdz}}_{\text{d u o b e n d i n g}} \quad (4.1.6.17)$$

$$\gamma_{yz}(x, y) = \underbrace{\frac{dv_p(x, y)}{dz} + \frac{dw(x, y)}{dy}}_{\text{d u o i n - p l a n e m o t i o n}} - \underbrace{z \frac{d^2w(x, y)}{dydz}}_{\text{d u o b e n d i n g}} \quad (4.1.6.18)$$

For a general, isotropic, elastic body, the following constitutive equations relate the *Stresses* and *Strains*:

$$\varepsilon_{xx}(x, y) = \frac{1}{E} \{ \sigma_{xx}(x, y) - \nu [\sigma_{yy}(x, y) - \sigma_{zz}(x, y)] \} \quad (4.1.6.19)$$

$$\varepsilon_{yy}(x, y) = \frac{1}{E} \{ \sigma_{yy}(x, y) - \nu [\sigma_{xx}(x, y) - \sigma_{zz}(x, y)] \} \quad (4.1.6.20)$$

$$\varepsilon_{zz}(x, y) = \frac{1}{E} \{ \sigma_{zz}(x, y) - \nu [\sigma_{xx}(x, y) - \sigma_{yy}(x, y)] \} \quad (4.1.6.21)$$

$$\gamma_{xy}(x, y) = \frac{1}{G} \tau_{xy}(x, y) \quad (4.1.6.22)$$

$$\gamma_{yz}(x, y) = \frac{1}{G} \tau_{yz}(x, y) \quad (4.1.6.23)$$

$$\gamma_{xz}(x, y) = \frac{1}{G} \tau_{xz}(x, y) \quad (4.1.6.24)$$

where $E =$ Elastic Modulus of the elastic body
 $G =$ Shear Modulus of the elastic body
 $\nu =$ Poisson's Ratio of the elastic body

The *Poisson's Ratio* (ν) relates the *Shear Modulus* (G) to the *Elastic Modulus* (E) for an isotropic elastic solid, as follows:

$$G = \frac{E}{2(1+\nu)} \quad (4.1.6.25)$$

Applying the relationship in equation (4.1.6.25) to equation (4.1.6.19) through equation (4.1.6.24), and rewriting in matrix form, yields the following:

$$\underbrace{\begin{Bmatrix} \varepsilon_{xx}(x, y) \\ \varepsilon_{yy}(x, y) \\ \varepsilon_{zz}(x, y) \\ \gamma_{xy}(x, y) \\ \gamma_{yz}(x, y) \\ \gamma_{xz}(x, y) \end{Bmatrix}}_{\text{Strain Field}} = \frac{1}{E} \begin{bmatrix} 1 & -\nu & -\nu & 0 & 0 & 0 \\ -\nu & 1 & -\nu & 0 & 0 & 0 \\ -\nu & -\nu & 1 & 0 & 0 & 0 \\ 0 & 0 & 0 & 2(1+\nu) & 0 & 0 \\ 0 & 0 & 0 & 0 & 2(1+\nu) & 0 \\ 0 & 0 & 0 & 0 & 0 & 2(1+\nu) \end{bmatrix} \underbrace{\begin{Bmatrix} \sigma_{xx}(x, y) \\ \sigma_{yy}(x, y) \\ \sigma_{zz}(x, y) \\ \tau_{xy}(x, y) \\ \tau_{yz}(x, y) \\ \tau_{xz}(x, y) \end{Bmatrix}}_{\text{Stress Field}} \quad (4.1.6.26)$$

Equation (4.1.6.26) establishes a general expression to relate the *Strain Field* and *Stress Field* of an isotropic elastic solid. The remainder of this section presents the *Strain Field* and *Stress Field* relationships for the specific elastic solids used in this model.

It is assumed herein that the plate element undergoes *Plane Stress*. Consequently, the *Strain Field* $\{S_e\}$ and *Stress Field* $\{\sigma_e\}$ of the plate element were developed using the following assumptions:

1. Plane sections remain perpendicular to the neutral axis of the solid.

$$\begin{aligned}\gamma_{yz}(x, y) &= \gamma_{xz}(x, y) = 0 \\ \tau_{yz}(x, y) &= \tau_{xz}(x, y) = 0\end{aligned}$$

2. *Normal Strains* only exist in the *x-direction* (ϵ_{xx}) and *y-direction* (ϵ_{yy}).

$$\epsilon_{zz}(x, y) = 0$$

Consequently, equation (4.1.6.26) can be reduced to the following:

$$\underbrace{\begin{Bmatrix} \epsilon_{xx}(x, y) \\ \epsilon_{yy}(x, y) \\ \gamma_{xy}(x, y) \end{Bmatrix}}_{\text{Strain Field}} = \frac{1}{E} \begin{bmatrix} 1 & -\nu & 0 \\ -\nu & 1 & 0 \\ 0 & 0 & 2(1+\nu) \end{bmatrix} \underbrace{\begin{Bmatrix} \sigma_{xx}(x, y) \\ \sigma_{yy}(x, y) \\ \tau_{xy}(x, y) \end{Bmatrix}}_{\text{Stress Field}} \quad (4.1.6.27)$$

where $E_1 =$ *Elastic Modulus of the plate element*
 $\nu_1 =$ *Poisson's Ratio of the plate element*

Applying equation (4.1.6.16), equation (4.1.6.9), and equation (4.1.6.11) to equation (4.1.6.27), yields the following:

$$\underbrace{\begin{Bmatrix} \frac{du(x, y)}{dx} - z \frac{d^2w(x, y)}{dx^2} \\ \frac{dv(x, y)}{dy} - z \frac{d^2w(x, y)}{dy^2} \\ \frac{du(x, y)}{dy} + \frac{dv(x, y)}{dx} - 2z \frac{d^2w(x, y)}{dxdy} \end{Bmatrix}}_{\text{Strain Field}} = \frac{1}{E} \begin{bmatrix} 1 & -\nu & 0 \\ -\nu & 1 & 0 \\ 0 & 0 & 2(1+\nu) \end{bmatrix} \underbrace{\begin{Bmatrix} \sigma_{xx}(x, y) \\ \sigma_{yy}(x, y) \\ \tau_{xy}(x, y) \end{Bmatrix}}_{\text{Stress Field}}$$

$$\underbrace{\begin{Bmatrix} \frac{du(x, y)}{dx} \\ \frac{dv(x, y)}{dy} \\ \frac{du(x, y)}{dy} + \frac{dv(x, y)}{dx} \end{Bmatrix}}_{\text{Strain Field due to in-plane motion}} + \underbrace{\begin{Bmatrix} -z \frac{d^2w(x, y)}{dx^2} \\ -z \frac{d^2w(x, y)}{dy^2} \\ -2z \frac{d^2w(x, y)}{dxdy} \end{Bmatrix}}_{\text{Strain Field due to bending}} = \frac{1}{E} \begin{bmatrix} 1 & -\nu & 0 \\ -\nu & 1 & 0 \\ 0 & 0 & 2(1+\nu) \end{bmatrix} \underbrace{\begin{Bmatrix} \sigma_{xx}(x, y) \\ \sigma_{yy}(x, y) \\ \tau_{xy}(x, y) \end{Bmatrix}}_{\text{Stress Field}} \quad (4.1.6.28)$$

For simplicity, the vector containing the *Strains* due to *in-plane motion* ($S_{p,e}$), the *Strains* due to *bending* ($S_{b,e}$), and the *Stress Field* (σ_e), for the plate element, are defined as follows:

$$\underbrace{\{S_{p,e}\}}_{3 \times 1} = \left\{ \frac{du(x,y)}{dx} \quad \frac{dv(x,y)}{dy} \quad \left(\frac{du(x,y)}{dy} + \frac{dv(x,y)}{dx} \right) \right\}^T \quad (4.1.6.29)$$

$$\underbrace{\{S_{b,e}\}}_{3 \times 1} = -z \left\{ \frac{d^2w(x,y)}{dx^2} \quad \frac{d^2w(x,y)}{dy^2} \quad 2 \frac{d^2w(x,y)}{dxdy} \right\}^T \quad (4.1.6.30)$$

$$\underbrace{\{\sigma_e\}}_{3 \times 1} = \left\{ \sigma_{xx}(x,y) \quad \sigma_{yy}(x,y) \quad \tau_{xy}(x,y) \right\}^T \quad (4.1.6.31)$$

Recall that the *Displacement Field* of the top-constraining layer is given by the following expression:

$$\underbrace{\{q\}}_{5 \times 1} = \underbrace{\begin{Bmatrix} u(x,y) \\ v(x,y) \\ w(x,y) \\ -w_x(x,y) \\ w_y(x,y) \end{Bmatrix}}_{5 \times 1} = \begin{bmatrix} \underbrace{\{N_1\}}_{1 \times 20} \\ \underbrace{\{N_2\}}_{1 \times 20} \\ \underbrace{\{N_3\}}_{1 \times 20} \\ -\underbrace{\{N_3\}_x}_{1 \times 20} \\ \underbrace{\{N_3\}_y}_{1 \times 20} \end{bmatrix} \underbrace{\{\Delta_e\}}_{20 \times 1} \quad (4.1.4.5)$$

Applying equation (4.1.4.2) to equation (4.1.6.29) equation (4.1.6.30), and simplifying, yields the following:

$$\underbrace{\{S_{p,e}\}}_{(3 \times 1)} = \begin{bmatrix} \underbrace{\{N_1\}_x}_{(1 \times 20)} \\ \underbrace{\{N_2\}_y}_{(1 \times 20)} \\ \underbrace{\{N_1\}_y + \{N_2\}_x}_{(1 \times 20)} \end{bmatrix} \underbrace{\{\Delta_e\}}_{20 \times 1} \quad (4.1.6.32)$$

$$\underbrace{\{S_{b,e}\}}_{(3 \times 1)} = -z \begin{bmatrix} \underbrace{\{N_3\}_{xx}}_{(1 \times 20)} \\ \underbrace{\{N_3\}_{yy}}_{(1 \times 20)} \\ \underbrace{\{N_3\}_{xy}}_{(1 \times 20)} \end{bmatrix} \underbrace{\{\Delta_e\}}_{20 \times 1} \quad (4.1.6.33)$$

For simplicity, let the matrices $[B_{p,e}]$ and $[B_{b,e}]$ be defined as follows:

$$\underbrace{[B_{p,e}]}_{(3 \times 20)} = \begin{bmatrix} \underbrace{\{N_1\}_x}_{(1 \times 20)} \\ \underbrace{\{N_2\}_y}_{(1 \times 20)} \\ \underbrace{\{N_1\}_y + \{N_2\}_x}_{(1 \times 20)} \end{bmatrix} \quad (4.1.6.34)$$

$$\underbrace{[B_{b,e}]}_{(3 \times 20)} = \begin{bmatrix} \underbrace{\{N_3\}_{xx}}_{(1 \times 20)} \\ \underbrace{\{N_3\}_{yy}}_{(1 \times 20)} \\ \underbrace{\{N_3\}_{xy}}_{(1 \times 20)} \end{bmatrix} \quad (4.1.6.35)$$

Applying equation (4.1.6.34) and equation (4.1.6.35) to equation (4.1.6.32) and equation (4.1.6.33), respectively, yields the following:

$$\underbrace{\{S_{p,e}\}}_{(3 \times 1)} = \underbrace{[B_{p,e}]}_{(3 \times 20)} \underbrace{\{\Delta_e\}}_{(20 \times 1)} \quad (4.1.6.36)$$

$$\underbrace{\{S_{b,e}\}}_{(3 \times 1)} = -z \underbrace{[B_{b,e}]}_{(3 \times 20)} \underbrace{\{\Delta_e\}}_{(20 \times 1)} \quad (4.1.6.37)$$

Applying equation (4.1.6.36), equation (4.1.6.37), and equation (4.1.6.31) to equation (4.1.6.28) yields the following:

$$\underbrace{\{S_{p,e}\}}_{(3 \times 1)} + \underbrace{\{S_{b,e}\}}_{(3 \times 1)} = \frac{1}{E} \begin{bmatrix} 1 & -\nu & 0 \\ -\nu & 1 & 0 \\ 0 & 0 & 2(1+\nu) \end{bmatrix} \underbrace{\{\sigma_e\}}_{(3 \times 1)} \quad (4.1.6.38)$$

Solving for the *Stress Field* (σ_e) in equation (4.1.6.38) yields the following:

$$\begin{aligned} \underbrace{\{\sigma_e\}}_{(3 \times 1)} &= E \begin{bmatrix} 1 & -\nu & 0 \\ -\nu & 1 & 0 \\ 0 & 0 & 2(1+\nu) \end{bmatrix}^{-1} \left\{ \underbrace{\{S_{p,e}\}}_{(3 \times 1)} + \underbrace{\{S_{b,e}\}}_{(3 \times 1)} \right\} \\ \underbrace{\{\sigma_e\}}_{(3 \times 1)} &= \frac{E}{1-\nu^2} \begin{bmatrix} 1 & \nu & 0 \\ \nu & 1 & 0 \\ 0 & 0 & \frac{(1-\nu)}{2} \end{bmatrix} \left\{ \underbrace{\{S_{p,e}\}}_{(3 \times 1)} + \underbrace{\{S_{b,e}\}}_{(3 \times 1)} \right\} \end{aligned} \quad (4.1.6.39)$$

For simplicity, the relationship between the *Strain Field* and *Stress Field* for the plate element is referred to as the *Structural Rigidity* (D) is defined as follows:

$$\underbrace{[D]}_{(3 \times 3)} = \frac{E}{1-\nu^2} \begin{bmatrix} 1 & \nu & 0 \\ \nu & 1 & 0 \\ 0 & 0 & \frac{(1-\nu)}{2} \end{bmatrix} \quad (4.1.6.40)$$

Plugging equation (4.1.6.40) into equation (4.1.6.39), and simplifying, yields:

$$\begin{aligned} \underbrace{\{\sigma_e\}}_{(3 \times 1)} &= \underbrace{[D]}_{(3 \times 3)} \left\{ \underbrace{\{S_{p,e}\}}_{(3 \times 1)} + \underbrace{\{S_{b,e}\}}_{(3 \times 1)} \right\} \\ \underbrace{\{\sigma_e\}}_{(3 \times 1)} &= \underbrace{[D]}_{(3 \times 3)} \underbrace{\{S_{p,e}\}}_{(3 \times 1)} + \underbrace{[D]}_{(3 \times 3)} \underbrace{\{S_{b,e}\}}_{(3 \times 1)} \end{aligned} \quad (4.1.6.41)$$

From equation (4.1.6.41), the *Stress* in the plate element due to *in-plane motion* ($\sigma_{p,e}$) and *Stress* due to *bending* ($\sigma_{b,e}$) are defined as follows:

$$\underbrace{\{\sigma_{p,e}\}}_{(3 \times 1)} = \underbrace{[D]}_{(3 \times 3)} \underbrace{\{S_{p,e}\}}_{(3 \times 1)} \quad (4.1.6.42)$$

$$\underbrace{\{\sigma_{b,e}\}}_{(3 \times 1)} = \underbrace{[D]}_{(3 \times 3)} \underbrace{\{S_{b,e}\}}_{(3 \times 1)} \quad (4.1.6.43)$$

4.1.7 Potential Energy – Single Element

The *Potential Energy* (U) of an object is given by the following equation:

$$U = \frac{1}{2} \int_V \{\varepsilon\} \{\sigma\} dV = \frac{1}{2} \int_V \{\varepsilon\}^T \{\sigma\} dV \quad (4.1.7.1)$$

where, $\{\varepsilon\}$ = Vector of strains of the object
 $\{\sigma\}$ = Vector of stresses of the object
 V = Volume of the object

A detailed derivation of equation (4.1.7.1) is presented in Appendix B. The *Potential Energy* (U_e) of a single plate element can be described as a combination of the *Potential Energy* ($U_{p,e}$) due to in-plane motion, and the *Potential Energy* ($U_{b,e}$) due to bending, as follows:

$$\underbrace{U_e}_{(1 \times 1)} = \underbrace{U_{p,e}}_{(1 \times 1)} + \underbrace{U_{b,e}}_{(1 \times 1)} \quad (4.1.7.2)$$

Consider the *Potential Energy* ($U_{p,e}$) due to in-plane motion of the plate element. Applying equation (4.1.7.1) for this case, and integrating over the *Volume* (V_e) of the plate element, yields the following expression:

$$\underbrace{U_{p,e}}_{(1 \times 1)} = \frac{1}{2} \int_{V_e} \underbrace{\{S_{p,e}\}^T}_{(1 \times 3)} \underbrace{\{\sigma_{p,e}\}}_{(3 \times 1)} dV_e \quad (4.1.7.3)$$

Recall from equation (4.1.6.42) that the *Stress* ($\sigma_{p,e}$) and *Strain* ($S_{p,e}$) in the plate element due to in-plane motion are related by the *Structural Rigidity* (D) of the element as follows:

$$\underbrace{\{\sigma_{p,e}\}}_{(3 \times 1)} = \underbrace{[D]}_{(3 \times 3)} \underbrace{\{S_{p,e}\}}_{(3 \times 1)} \quad (4.1.6.42)$$

Plugging equation (4.1.6.42) into equation (4.1.7.3) yields the following:

$$\underbrace{U_{p,e}}_{(1 \times 1)} = \frac{1}{2} \int_{V_e} \underbrace{\{S_{p,e}\}^T}_{(1 \times 3)} \underbrace{[D]}_{(3 \times 3)} \underbrace{\{S_{p,e}\}}_{(3 \times 1)} dV_e \quad (4.1.7.4)$$

Plugging the expression relating the *Strain Field* ($S_{p,e}$) of the plate element due to in-plane motion to the *Nodal Displacement Vector* (Δ_e) presented in equation (4.1.6.36), into equation (4.1.7.4), yields the following:

$$\begin{aligned} \underbrace{U_{p,e}}_{(1 \times 1)} &= \frac{1}{2} \int_{V_e} \underbrace{\{S_{p,e}\}^T}_{(1 \times 3)} \underbrace{[D]}_{(3 \times 3)} \underbrace{\{S_{p,e}\}}_{(3 \times 1)} dV_e \\ \underbrace{U_{p,e}}_{(1 \times 1)} &= \frac{1}{2} \int_{V_e} \underbrace{\{\Delta_e\}^T}_{(1 \times 20)} \underbrace{[B_{p,e}]^T}_{(20 \times 3)} \underbrace{[D]}_{(3 \times 3)} \underbrace{[B_{p,e}]}_{(3 \times 20)} \underbrace{\{\Delta_e\}}_{(20 \times 1)} dV_e \end{aligned} \quad (4.1.7.5)$$

The matrix $[B_{p,e}]$ is defined in equation. Now consider the *Potential Energy* ($U_{b,e}$) due to bending of the plate element. Applying equation (4.1.7.1) for this case, and integrating over the *Volume* (V_e) of the plate element, yields the following expression:

$$\underbrace{U_{b,e}}_{(1 \times 1)} = \frac{1}{2} \int_{V_e} \underbrace{\{S_{b,e}\}^T}_{(1 \times 3)} \underbrace{\{\sigma_{b,e}\}}_{(3 \times 1)} dV_e \quad (4.1.7.6)$$

Recall from equation (4.1.6.43) that the *Stress* ($\sigma_{b,e}$) and *Strain* ($S_{b,e}$) in the plate element due to bending are related by the *Structural Rigidity* (D) of the element as follows:

$$\underbrace{\{\sigma_{b,e}\}}_{(3 \times 1)} = \underbrace{[D]}_{(3 \times 3)} \underbrace{\{S_{b,e}\}}_{(3 \times 1)} \quad (4.1.6.43)$$

Plugging equation (4.1.6.43) into equation (4.1.7.6) yields the following:

$$\underbrace{U_{b,e}}_{(1 \times 1)} = \frac{1}{2} \int_{V_e} \underbrace{\{S_{b,e}\}^T}_{(1 \times 3)} \underbrace{[D]}_{(3 \times 3)} \underbrace{\{S_{b,e}\}}_{(3 \times 1)} dV_e \quad (4.1.7.7)$$

Plugging the expression relating the *Strain Field* ($S_{b,e}$) of the plate element due to bending to the *Nodal Displacement Vector* (Δ_e) presented in equation (4.1.6.37), into equation (4.1.7.7), yields the following:

$$\underbrace{U_{b,e}}_{(1 \times 1)} = \frac{1}{2} \int_{V_e} \underbrace{\{S_{b,e}\}^T}_{(1 \times 3)} \underbrace{[D]}_{(3 \times 3)} \underbrace{\{S_{b,e}\}}_{(3 \times 1)} dV_e$$

$$\underbrace{U_{b,e}}_{(1 \times 1)} = \frac{1}{2} \int_{V_e} z^2 \underbrace{\{\Delta_e\}^T}_{(1 \times 20)} \underbrace{[B_{b,e}]}_{(20 \times 3)} \underbrace{[D]}_{(3 \times 3)} \underbrace{[B_{b,e}]}_{(3 \times 20)} \underbrace{\{\Delta_e\}}_{(20 \times 1)} dV_e \quad (4.1.7.8)$$

The matrix $[B_{b,e}]$ is defined in equation (4.1.6.35). The *Nodal Displacement Vector* $\{\Delta_e\}$ represents the displacement of the plate element at the nodal boundaries. Therefore, the *Nodal Displacement Vector* is independent of the element *Volume* (V_e). Applying this observation to equation (4.1.7.5) and equation (4.1.7.8) yields the following:

$$\underbrace{U_{p,e}}_{(1 \times 1)} = \frac{1}{2} \underbrace{\{\Delta_e\}^T}_{(1 \times 20)} \left[\int_{V_e} \underbrace{[B_{p,e}]}_{(20 \times 3)} \underbrace{[D]}_{(3 \times 3)} \underbrace{[B_{p,e}]}_{(3 \times 20)} dV_e \right] \underbrace{\{\Delta_e\}}_{(20 \times 1)} \quad (4.1.7.9)$$

$$\underbrace{U_{b,e}}_{(1 \times 1)} = \frac{1}{2} \underbrace{\{\Delta_e\}^T}_{(1 \times 20)} \left[\int_{V_e} z^2 \underbrace{[B_{b,e}]}_{(20 \times 3)} \underbrace{[D]}_{(3 \times 3)} \underbrace{[B_{b,e}]}_{(3 \times 20)} dV_e \right] \underbrace{\{\Delta_e\}}_{(20 \times 1)} \quad (4.1.7.10)$$

The *Potential Energy* of an elastic body can be described by the following relationship:

$$U = \frac{1}{2} kx^2 \quad (4.1.7.11)$$

where $k =$ The stiffness of the elastic body
 $x =$ Displacement of the elastic body

In this case, the displacement is represented by the *Nodal Displacement Vector* $\{\Delta_e\}$. Applying the relationship in equation (4.1.7.11) to equation (4.1.7.9) and equation (4.1.7.10) yields the following:

$$\underbrace{U}_{(1 \times 1)}_{p,e} = \frac{1}{2} \underbrace{\{\Delta_e\}}_{1 \times 20}^T \underbrace{[K_{p,e}]}_{20 \times 20} \underbrace{\{\Delta_e\}}_{20 \times 1} \quad (4.1.7.12)$$

$$\underbrace{U}_{(1 \times 1)}_{b,e} = \frac{1}{2} \underbrace{\{\Delta_e\}}_{1 \times 20}^T \underbrace{[K_{b,e}]}_{20 \times 20} \underbrace{\{\Delta_e\}}_{20 \times 1} \quad (4.1.7.13)$$

From equation (4.1.7.9) and equation (4.1.7.12), the *Stiffness Matrix* $[K_{p,e}]$ of the plate element, due to in-plane motion, is given by the following:

$$\underbrace{[K_{p,e}]}_{(20 \times 20)} = \int_{V_e} \underbrace{[B_{p,e}]}_{(20 \times 3)}^T \underbrace{[D]}_{(3 \times 3)} \underbrace{[B_{p,e}]}_{(3 \times 20)} dV_e \quad (4.1.7.14)$$

From equation (4.1.7.10) and equation (4.1.7.13), the *Stiffness Matrix* $[K_{b,e}]$ of the plate element, due to bending, is given by the following:

$$\underbrace{[K_{b,e}]}_{(20 \times 20)} = \int_{V_e} z^2 \underbrace{[B_{b,e}]}_{(20 \times 3)}^T \underbrace{[D]}_{(3 \times 3)} \underbrace{[B_{b,e}]}_{(3 \times 20)} dV_e \quad (4.1.7.15)$$

Expanding the integration limits of equations (4.1.7.14) and (4.1.7.15), based on the geometry in Figure , yields the following:

$$\underbrace{[K_{p,e}]}_{(20 \times 20)} = \int_{-h/2}^{+h/2} \int_{-b-a}^b \int_a^a \left(\underbrace{[B_{p,e}]}_{(20 \times 3)}^T \underbrace{[D]}_{(3 \times 3)} \underbrace{[B_{p,e}]}_{(3 \times 20)} \right) dx dy dz \quad (4.1.7.16)$$

$$\underbrace{[K_{b,e}]}_{(20 \times 20)} = \int_{-h/2}^{+h/2} \int_{-b-a}^b \int_a^a \left(z^2 \underbrace{[B_{b,e}]}_{(20 \times 3)}^T \underbrace{[D]}_{(3 \times 3)} \underbrace{[B_{b,e}]}_{(3 \times 20)} \right) dx dy dz \quad (4.1.7.17)$$

The vectors $\{N_1\}$, $\{N_2\}$, and $\{N_3\}$ that comprise the matrices $[B_{p,e}]$ and $[B_{b,e}]$ are not functions of the *z-direction*. Consequently, evaluating the integral with respect to the *z-direction* in equations (4.1.7.16) and (4.1.7.17) yields the following:

$$\underbrace{[K_{p,e}]}_{(20 \times 20)} = h \int_{-b}^b \int_{-a}^a \left(\underbrace{[B_{p,e}]}_{(20 \times 3)}^T \underbrace{[D]}_{(3 \times 3)} \underbrace{[B_{p,e}]}_{(3 \times 20)} \right) dx dy \quad (4.1.7.18)$$

$$\underbrace{[K_{b,e}]}_{(20 \times 20)} = \frac{h^3}{12} \int_{-b}^b \int_{-a}^a \left(\underbrace{[B_{b,e}]}_{(20 \times 3)}^T \underbrace{[D]}_{(3 \times 3)} \underbrace{[B_{b,e}]}_{(3 \times 20)} \right) dx dy \quad (4.1.7.19)$$

Recall that equation (4.1.7.2) describes the *Potential Energy* (U_e) of a single plate element as a combination of the *Potential Energy* ($U_{p,e}$) due to in-plane motion, and the *Potential Energy* ($U_{b,e}$) due to bending. Plugging equations (4.1.7.12) and (4.1.7.13) into equation (4.1.7.2) yields the following:

$$\begin{aligned} \underbrace{U_e}_{(1 \times 1)} &= \underbrace{U_{p,e}}_{(1 \times 1)} + \underbrace{U_{b,e}}_{(1 \times 1)} \\ \underbrace{U_e}_{(1 \times 1)} &= \frac{1}{2} \underbrace{\{\Delta_e\}^T}_{(1 \times 20)} \underbrace{[K_{p,e}]}_{(20 \times 20)} \underbrace{\{\Delta_e\}}_{(20 \times 1)} + \frac{1}{2} \underbrace{\{\Delta_e\}^T}_{(1 \times 20)} \underbrace{[K_{b,e}]}_{(20 \times 20)} \underbrace{\{\Delta_e\}}_{(20 \times 1)} \\ \underbrace{U_e}_{(1 \times 1)} &= \frac{1}{2} \underbrace{\{\Delta_e\}^T}_{(1 \times 20)} \left(\underbrace{[K_{p,e}]}_{(20 \times 20)} + \underbrace{[K_{b,e}]}_{(20 \times 20)} \right) \underbrace{\{\Delta_e\}}_{(20 \times 1)} \end{aligned} \quad (4.1.7.20)$$

The *Total Stiffness Matrix* $[K_e]$ of the plate element can be described by the following relationship:

$$\underbrace{[K_e]}_{(20 \times 20)} = \underbrace{[K_{p,e}]}_{(20 \times 20)} + \underbrace{[K_{b,e}]}_{(20 \times 20)} \quad (4.1.7.21)$$

In summary, the *Potential Energy* (U_e) of the plate element can be described by the following expressions, where the *Total Stiffness Matrix* $[K_e]$ and its components are presented in equations (4.1.7.21), (4.1.7.18), and (4.1.7.19), respectively:

$$\underbrace{U_e}_{(1 \times 1)} = \frac{1}{2} \underbrace{\{\Delta_e\}^T}_{(1 \times 20)} \underbrace{[K_e]}_{(20 \times 20)} \underbrace{\{\Delta_e\}}_{(20 \times 1)} \quad (4.1.7.22)$$

4.1.8 Generation of Global Kinetic & Potential Energy Equations

The previous sections derived the formulas for calculating the *Kinetic* (T_e) and *Potential* (U_e) energies of a single plate element. A complete finite element model typically consists of an $M \times N$ array, or mesh, of these individual elements. Note that M describes the number of elements in the x -direction, and N describes the number of elements in the y -direction. Figure 4.8 presents the details of the meshed model of the plate.

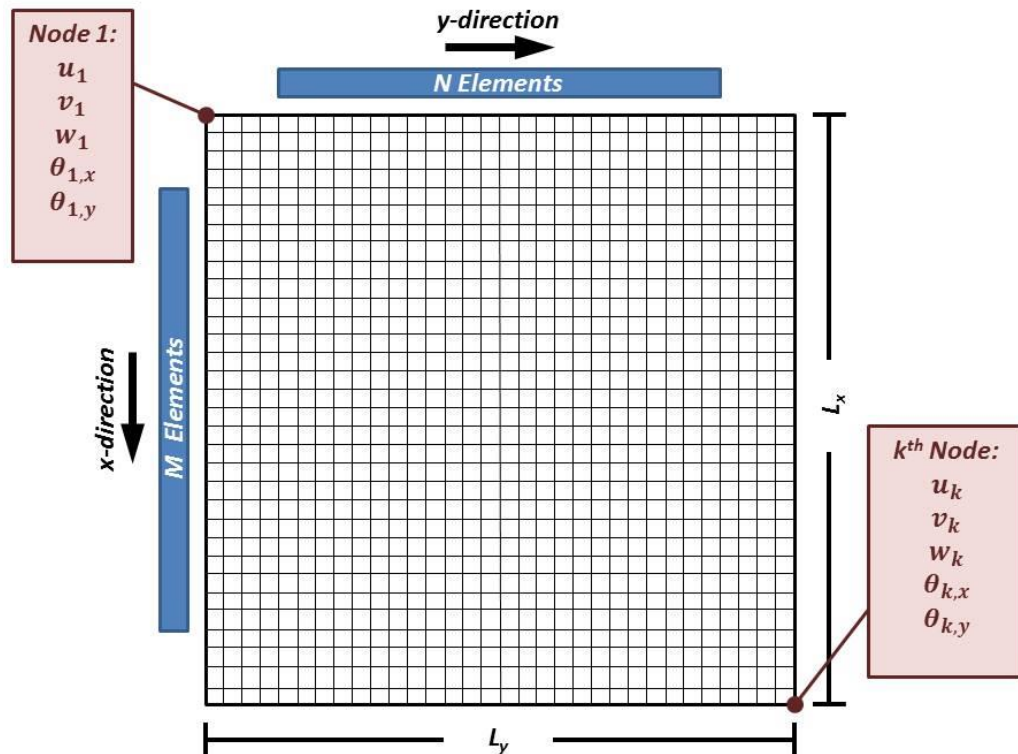


Figure 4.8: Assembly of individual plate elements into the complete plate system.

The following equations describe the *Global Kinetic Energy* (T) and *Global Potential Energy* (U) of the plate, respectively:

$$\underset{(1 \times 1)}{\underline{T}} = \frac{1}{2} \underset{(1 \times nDOF)}{\{\dot{\Delta}\}}^T \underset{(nDOF \times nDOF)}{[M]} \underset{(nDOF \times 1)}{\{\dot{\Delta}\}} \quad (4.1.8.1)$$

$$\underline{U}_{(1 \times 1)} = \frac{1}{2} \underbrace{\{\Delta\}}_{(1 \times nDOF)}^T \underbrace{[K]}_{(nDOF \times nDOF)} \underbrace{\{\Delta\}}_{(nDOF \times 1)} \quad (4.1.8.2)$$

where $nDOF =$ Total Degrees-of-Freedom (DOF) in the plate
 $\{\Delta\} =$ Global Deflection Vector of the plate
 $\{\dot{\Delta}\} =$ Time-derivative of the Global Deflection Vector of the plate

From Figure 4.8 and equation (4.1.3.2), the *Global Deflection Vector* $\{\Delta\}$, and its time derivative $\{\dot{\Delta}\}$, are given by the following equations, respectively:

$$\underbrace{\{\Delta\}}_{nDOF \times 1} = \left\{ \underbrace{\{\Delta_1\}}_{1 \times 5} \quad \underbrace{\{\Delta_2\}}_{1 \times 5} \quad \dots \quad \underbrace{\{\Delta_{nNodes}\}}_{1 \times 5} \right\}^T \quad (4.1.8.3)$$

$$\underbrace{\{\dot{\Delta}\}}_{nDOF \times 1} = \left\{ \underbrace{\{\dot{\Delta}_1\}}_{1 \times 5} \quad \underbrace{\{\dot{\Delta}_2\}}_{1 \times 5} \quad \dots \quad \underbrace{\{\dot{\Delta}_{nNodes}\}}_{1 \times 5} \right\}^T \quad (4.1.8.4)$$

Recall that $\{\Delta_k\}$, where $k = 1, 2, \dots, nNodes$, is presented in (4.1.3.1). The *Total Nodes* ($nNodes$) is related to the number of elements in the *x-direction* (M), and number of elements in the *y-direction* (N), by the following equation:

$$nNodes = (M + 1)(N + 1) \quad (4.1.8.5)$$

The *Total DOF* ($nDOF$) and *Total Nodes* ($nNodes$) are related by the following equation:

$$nDOF = r \cdot nNodes \quad (4.1.8.6)$$

Reference [6] showed that the global *Mass* $[M]$ and *Stiffness* $[K]$ matrices are linear combinations of the *Mass* $[M_e]$ and *Stiffness* $[K_e]$ matrices of the individual elements. Using a similar approach to Reference [6], the global *Mass* $[M]$ and

Stiffness $[K]$ matrices can be calculated using the following formulas, which are functions of the single element *Mass* $[M_e]$ and *Stiffness* $[K_e]$ matrices.

$$\underbrace{[M]}_{(nDOF \times nDOF)} = \underbrace{[T]}_{(nDOF \times 20)}^T \underbrace{[M_e]}_{(20 \times 20)} \underbrace{[T]}_{(20 \times nDOF)} \quad (4.1.8.7)$$

$$\underbrace{[K]}_{(nDOF \times nDOF)} = \underbrace{[T]}_{(nDOF \times 20)}^T \underbrace{[K_e]}_{(20 \times 20)} \underbrace{[T]}_{(20 \times nDOF)} \quad (4.1.8.8)$$

The transformation matrix $[T]$ in equations (4.1.8.7) and (4.1.8.8) can be generated by applying the following formula:

$$T_{mn}(i, j) = \begin{cases} 0, & \text{if } j \neq E_{mn}(i) \\ 1, & \text{if } j = E_{mn}(i) \end{cases} \quad (4.1.8.9)$$

where $m =$ $1:M$ elements in the x -direction
 $n =$ $1:N$ elements in the y -direction
 $i =$ $1:20$ DOF per element
 $j =$ $1:nDOF$ total DOF of the plate

The variable E_{mn} in equation (4.1.8.9) is described by the following vector:

$$\underbrace{\{E_{mn}\}}_{(1 \times 20)} = \left\{ \underbrace{\{E_{mn1}\}}_{(1 \times 5)} \quad \underbrace{\{E_{mn2}\}}_{(1 \times 5)} \quad \underbrace{\{E_{mn3}\}}_{(1 \times 5)} \quad \underbrace{\{E_{mn4}\}}_{(1 \times 5)} \right\} \quad (4.1.8.10)$$

The variables E_{mnl} , where $l = 1:4$, are described by the following expression of a series of numbers:

$$\underbrace{\{E_{mnl}\}}_{(1 \times 5)} = [(a_l - 1)r + 1] : [a_l r] \quad (4.1.8.11)$$

where $r =$ The number of DOF per node ($r = 5$ in this study)

The variables a_l , where $l = 1:4$, are described by the following equations:

$$a_1 = \Delta \quad (4.1.8.12)$$

$$a_2 = \Delta + 1 \quad (4.1.8.13)$$

$$a_3 = \Delta + N + 1 \quad (4.1.8.14)$$

$$a_4 = \Delta + N + 2 \quad (4.1.8.15)$$

$$\Delta = \alpha + \beta \quad (4.1.8.16)$$

$$\alpha = m + n \quad (4.1.8.17)$$

$$\beta = (m-1)N - 1 \quad (4.1.8.18)$$

4.1.9 Equations of Motion

Consider the following equation:

$$L = T - U \quad (4.1.9.1)$$

where $L =$ The Lagrangian of the assembled plate
 $T =$ The Kinetic Energy of the assembled plate
 $U =$ The Potential Energy of the assembled plate

Plugging equation (4.1.8.1) and equation (4.1.8.2) into equation (4.1.9.1)

yields the following:

$$\underset{(1 \times 1)}{\underline{L}} = \frac{1}{2} \underset{(1 \times n \text{DOF})}{\{\dot{\Delta}\}}^T \underset{(n \text{DOF} \times n \text{DOF})}{[M]} \underset{(n \text{DOF} \times 1)}{\{\dot{\Delta}\}} - \frac{1}{2} \underset{(1 \times n \text{DOF})}{\{\Delta\}}^T \underset{(n \text{DOF} \times n \text{DOF})}{[K]} \underset{(n \text{DOF} \times 1)}{\{\Delta\}} \quad (4.1.9.2)$$

The *Equation of Motion (EOM)* of the assembled plate can be described by the following equation:

$$\frac{d}{dt} \left(\frac{\partial L}{\partial \{\dot{\Delta}\}} \right) - \frac{\partial L}{\partial \{\Delta\}} = \{Q\} \quad (4.1.9.3)$$

where $\{Q\} =$ Vector of the external forces and moments acting on the plate

Plugging equation (4.1.9.2) into equation (4.1.9.3), and simplifying, yields the following *Equation of Motion (EOM)* of the assembled plate system:

$$\underbrace{[M]}_{(nDOF \times nDOF)} \underbrace{\{\ddot{\Delta}\}}_{(nDOF \times 1)} + \underbrace{[K]}_{(nDOF \times nDOF)} \underbrace{\{\Delta\}}_{(nDOF \times 1)} = \underbrace{\{Q\}}_{(nDOF \times 1)} \quad (4.1.9.4)$$

For the case where there is an *External Load* applied to each *Degree-of-Freedom (DOF)*, the vector of *External Loads* $\{Q\}$ in equation (4.1.9.4) is given by the following:

$$\underbrace{\{Q\}}_{nDOF \times 1} = \left\{ \underbrace{\{Q_1\}}_{1 \times 5} \quad \underbrace{\{Q_2\}}_{1 \times 5} \quad \dots \quad \underbrace{\{Q_{nNodes}\}}_{1 \times 5} \right\}^T \quad (4.1.9.5)$$

The components of the *External Loads* vector, $\{Q_k\}$, where $k = 1, 2, \dots, nNodes$, can be described by the following:

$$\underbrace{\{Q_k\}}_{1 \times 5} = \{F_{x,k} \quad F_{y,k} \quad F_{z,k} \quad -M_{x,k} \quad M_{y,k}\} \quad (4.1.9.6)$$

where

- $F_{x,k}$ = Translational force in the x-direction
- $F_{y,k}$ = Translational force in the y-direction
- $F_{z,k}$ = Translational force in the z-direction
- $M_{x,k}$ = Moment about the y-axis
- $M_{y,k}$ = Moment about the x-axis

4.2 Plate Model Results

The following section presents a model of the plate that reflects the dimensions, materials, and boundary conditions of the plate that was experimentally analyzed in Chapter 7. A comparison of the modeled results and experimentally measured results is presented in Chapter 7.

4.2.1 Plate Model Details

An aluminum plate was selected as the base to mount the *CB* filled polyurethane sensors. The properties of the plate are presented below in Table 4.2:

Table 4.2: Plate properties.

Length (m)	0.3048
Width (m)	0.3048
Thickness (mm)	0.3960
Density (g/cm³)	2.70
Young's Modulus (GPa)	70
Poisson's Ratio	0.3

To model the plate, a mesh density was selected to accommodate the geometry of the array of *CB* filled polyurethane sensors and allow for each sensor location to coincide with a node of the model. Therefore, a mesh density of 32×32 elements was selected. For a 32×32 element plate, with (5) *DOF* per node, the *Total DOF (nDOF)* is 5445.

$$nDOF = (32 + 1) \times (32 + 1) \times (5) = 5445$$

The plate implemented experimentally was clamped on all 4 edges. Therefore, a clamped boundary condition was applied to the plate model. To implement this boundary condition, the responses of all *DOF* of nodes on the plate edges were set to zero.

4.2.2 Natural Frequencies & Mode Shapes

Consider the homogeneous natural response of the plate when not subjected to external forcing. Rewriting equation (4.1.9.4) for the homogeneous case yields the following:

$$\underbrace{[M]}_{(nDOF \times nDOF)} \underbrace{\{\ddot{\Delta}\}}_{(nDOF \times 1)} + \underbrace{[K]}_{(nDOF \times nDOF)} \underbrace{\{\Delta\}}_{(nDOF \times 1)} = \underbrace{\{0\}}_{(nDOF \times 1)} \quad (4.2.2.1)$$

Assuming a harmonic solution to equation (4.2.2.1), the *Nodal Deflection Vector* can be written as follows:

$$\underbrace{\{\Delta\}}_{(nDOF \times 1)} = \underbrace{\{X\}}_{(nDOF \times 1)} e^{j\omega t} \quad (4.2.2.2)$$

Plugging equation (4.2.2.2) into equation (4.2.2.1), and simplifying, yields the following:

$$\begin{aligned} \underbrace{[M]}_{(nDOF \times nDOF)} \frac{d^2}{dt^2} \left(\underbrace{\{X\}}_{(nDOF \times 1)} e^{j\omega t} \right) + \underbrace{[K]}_{(nDOF \times nDOF)} \underbrace{\{X\}}_{(nDOF \times 1)} e^{j\omega t} &= \underbrace{\{0\}}_{(nDOF \times 1)} \\ -\omega^2 \underbrace{[M]}_{(nDOF \times nDOF)} \underbrace{\{X\}}_{(nDOF \times 1)} e^{j\omega t} + \underbrace{[K]}_{(nDOF \times nDOF)} \underbrace{\{X\}}_{(nDOF \times 1)} e^{j\omega t} &= \underbrace{\{0\}}_{(nDOF \times 1)} \\ \left[-\omega^2 \underbrace{[M]}_{(nDOF \times nDOF)} \underbrace{\{X\}}_{(nDOF \times 1)} + \underbrace{[K]}_{(nDOF \times nDOF)} \underbrace{\{X\}}_{(nDOF \times 1)} \right] e^{j\omega t} &= \underbrace{\{0\}}_{(nDOF \times 1)} \end{aligned} \quad (4.2.2.3)$$

A solution to equation (4.2.2.3) exists if the following is true:

$$-\omega^2 \underbrace{[M]}_{(nDOF \times nDOF)} \underbrace{\{X\}}_{(nDOF \times 1)} + \underbrace{[K]}_{(nDOF \times nDOF)} \underbrace{\{X\}}_{(nDOF \times 1)} = \underbrace{\{0\}}_{(nDOF \times 1)} \quad (4.2.2.4)$$

Rearranging equation (4.2.2.4) yields the following eigenvalue problem:

$$\underbrace{[M]^{-1}}_{(nDOF \times nDOF)} \underbrace{[K]}_{(nDOF \times nDOF)} \underbrace{\{X\}}_{(nDOF \times 1)} = \omega^2 \underbrace{\{X\}}_{(nDOF \times 1)} \quad (4.2.2.5)$$

The *Mode Shapes* and *Natural Frequencies* of the plate system can be determined by solving the eigenvalue problem in equation (4.2.2.5). There are many different methods to solve equation (4.2.2.5). In this case, MATLAB[®] was used to model the plate and solve the eigenvalue problem. Figure 4.9 shows the first (6) calculated *Mode Shapes* and *Natural Frequencies* of the plate described in Chapter 4.2.1.

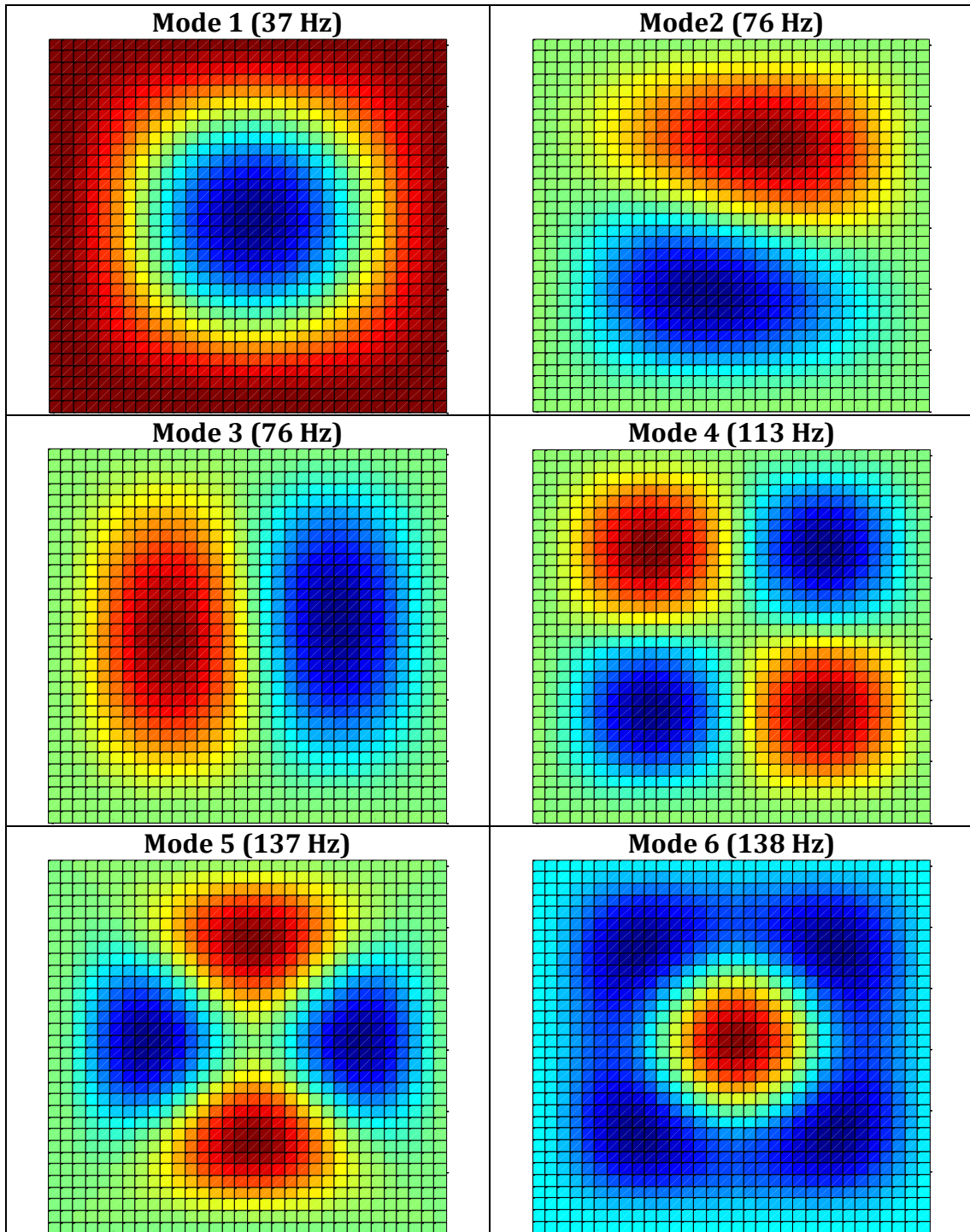


Figure 4.9: First 6 mode shapes of the aluminum plate calculated using the model derived in Chapter 4.

To validate the plate model derived in this Chapter, the results were compared to the results calculated by Leissa in Reference [20]. Leissa only presents the *Natural Frequencies* for the first (5) *Modes* of the fully-clamped boundary condition case. A

comparison of the first (5) *Natural Frequencies* calculated by Leissa, and by the model presented in this study, is presented in Table 4.3.

Table 4.3: Comparison of plate model results to derived results from Leissa Error! Reference source not found..

Mode	Model Results	Leissa
1	37 Hz	37 Hz
2	76 Hz	76 Hz
3	113 Hz	113 Hz
4	137 Hz	137 Hz
5	138 Hz	138 Hz

Table 4.3 indicates excellent agreement between the model presented herein and the results derived by Leissa. The only difference appears to be that the model presented herein calculates a repeated *Mode* at 76 Hz. The model results presented in this Chapter are compared to the experimental results in Chapter 7.

4.2.3 Forced Response

To calculate the forced response of the modeled aluminum plate, a 1 N force was applied to each node, but only to the *z-direction* translational *DOF*. The force applied to all *x-direction* and *y-direction* translational *DOF*, and all rotational *DOF* was zero. Figure 4.10 presents a 2-dimensional representation of the distributed force on the plate. Note that while Figure 4.10 only depicts the *z-y plane*, the force is distributed over the entire *x-y plane* surface.

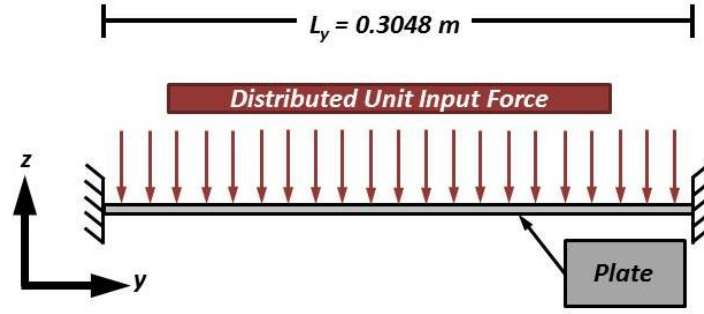


Figure 4.10: Force distribution on aluminum plate model.

Similar to Section 4.2.2, if a harmonic input force and harmonic solution are assumed, the *Equation of Motion* in equation (4.1.9.4) can be rewritten as follows:

$$\left(\begin{matrix} -\omega^2 & [M] \\ (nDOF \times nDOF) & (nDOF \times 1) \end{matrix} \right) \begin{matrix} \{X\} \\ (nDOF \times 1) \end{matrix} + \begin{matrix} [K] \\ (nDOF \times nDOF) \end{matrix} \begin{matrix} \{X\} \\ (nDOF \times 1) \end{matrix} \right) e^{j\omega t} = \begin{matrix} \{Q\} \\ (nDOF \times 1) \end{matrix} e^{j\omega t} \quad (4.2.3.1)$$

Simplifying equation (4.2.3.1) yields the following:

$$\begin{matrix} \{X\} \\ (nDOF \times 1) \end{matrix} = \left(\begin{matrix} -\omega^2 & [M] \\ (nDOF \times nDOF) & (nDOF \times nDOF) \end{matrix} + \begin{matrix} [K] \\ (nDOF \times nDOF) \end{matrix} \right)^{-1} \begin{matrix} \{Q\} \\ (nDOF \times 1) \end{matrix} \quad (4.2.3.2)$$

For simplification, let the *Receptance* matrix (H), or the relationship between the *External Loads* $\{Q\}$ and the *Global Deflection Vector* $\{\Delta\}$, be defined as follows:

$$\begin{matrix} [H] \\ (nDOF \times nDOF) \end{matrix} = \left(\begin{matrix} -\omega^2 & [M] \\ (nDOF \times nDOF) & (nDOF \times nDOF) \end{matrix} + \begin{matrix} [K] \\ (nDOF \times nDOF) \end{matrix} \right)^{-1} \quad (4.2.3.3)$$

Plugging equation (4.2.3.3) into equation (4.2.3.2) yields the following:

$$\begin{matrix} \{X\} \\ (nDOF \times 1) \end{matrix} = \begin{matrix} [H] \\ (nDOF \times nDOF) \end{matrix} \begin{matrix} \{Q\} \\ (nDOF \times 1) \end{matrix} \quad (4.2.3.4)$$

Figure 4.11 and Figure 4.12 present the magnitude and phase of the *Input Receptance* of the plate at the *CB* sensor locations. The results reflect the natural frequencies calculated in Section 4.2.2.

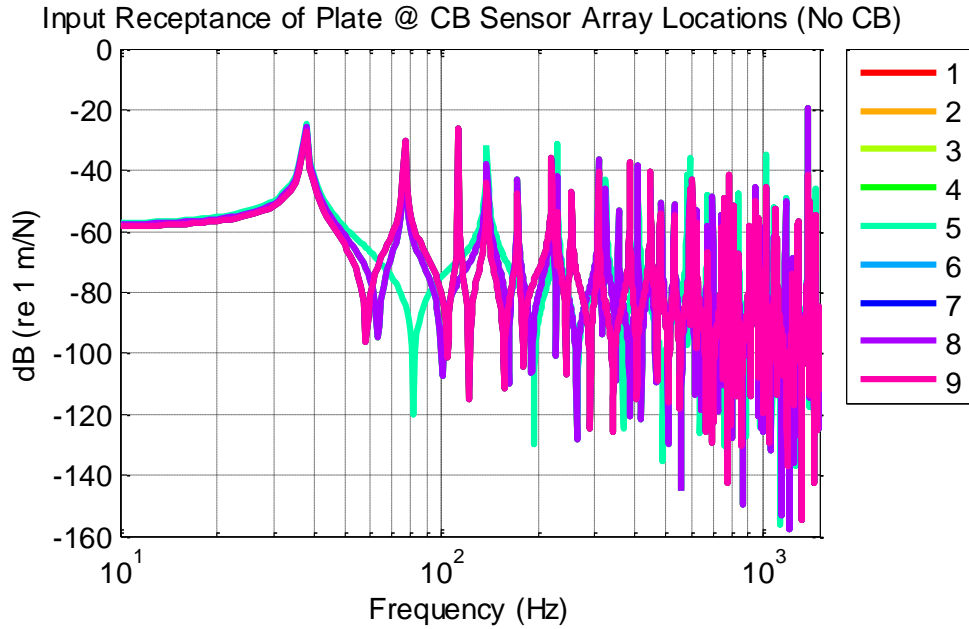


Figure 4.11: Input receptance (magnitude) of the plate @ *CB* sensor array locations (No *CB*).

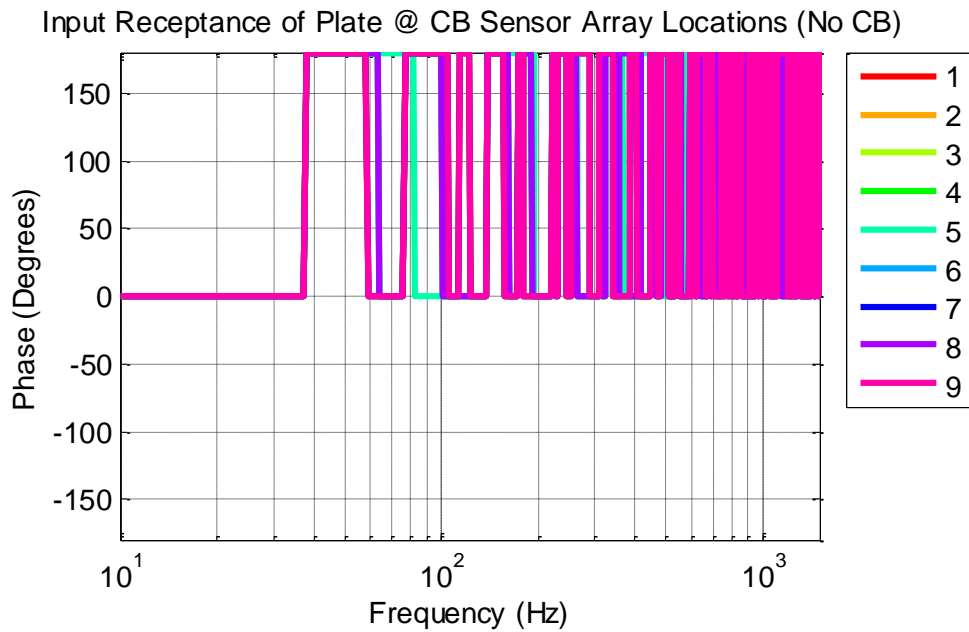


Figure 4.12: Input receptance (phase) of plate @ *CB* sensor array locations (No *CB*).

The *CB* sensor array processing experimental validation, presented in Chapter 7, focuses on frequencies between 1kHz and 1.1kHz. Figure 4.13 presents the *Input Receptance* of the plate over this frequency range.

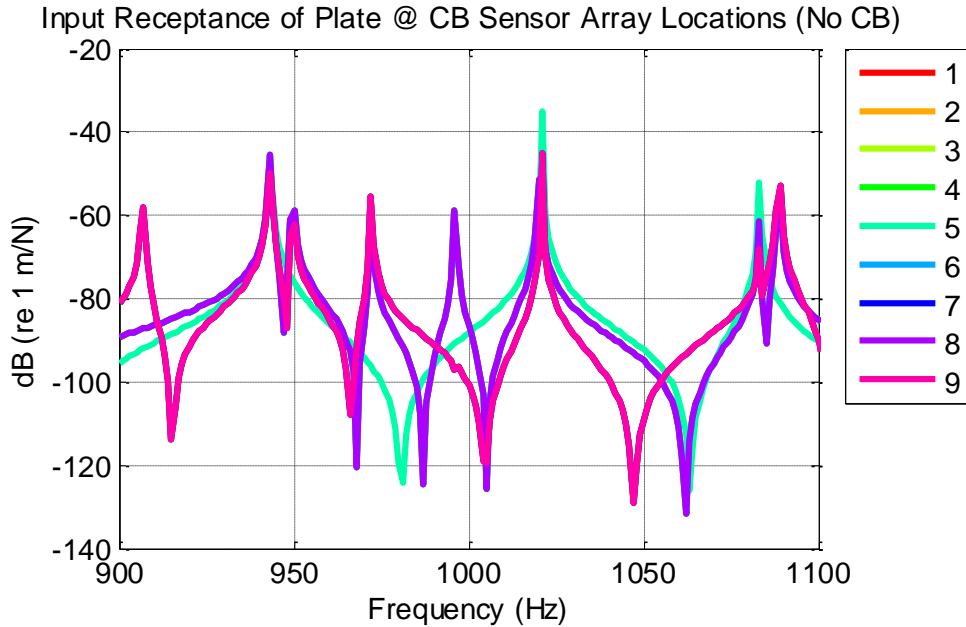


Figure 4.13: Input receptance (magnitude) of the plate @ *CB* sensor array locations (No *CB*), 900Hz - 1100Hz

Figure 4.13 indicates that there are several plate modes in the frequency range of interest. The effects of the modes of the base structure will have to be accounted for when attempting to do phased array processing with the *CB* sensors. Depending on the excitation, it is possible that these modes will not be excited. Figure 4.14 presents the *Displacement* of the plate, at the *CB* sensor locations, due to the distributed 1 N input force. Figure 4.15 focuses on the 1kHz to 1.1kHz frequency range.

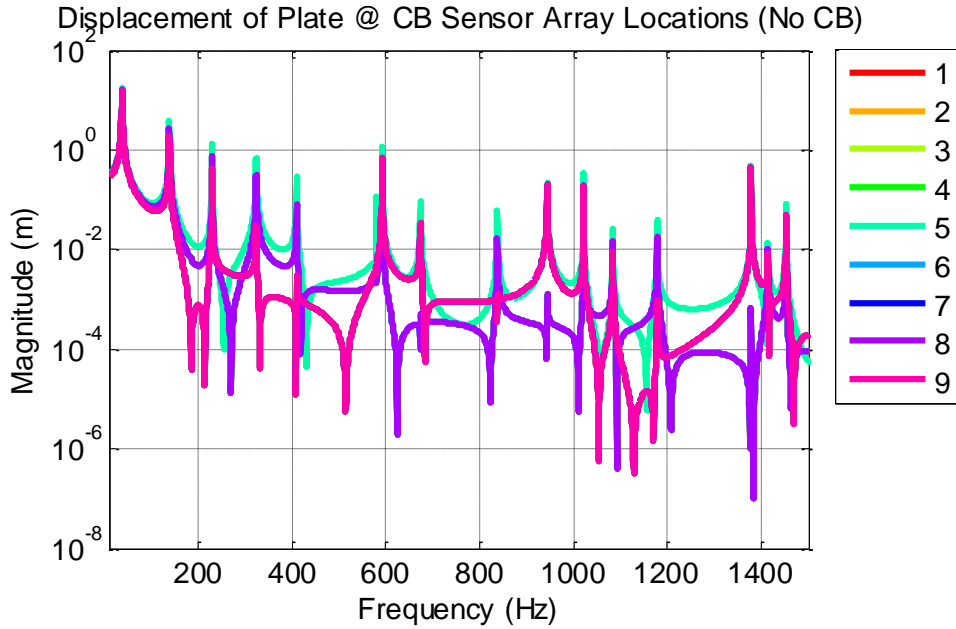


Figure 4.14: Displacement of plate @ *CB* sensor array locations (No *CB*) due to 1 N distributed force.

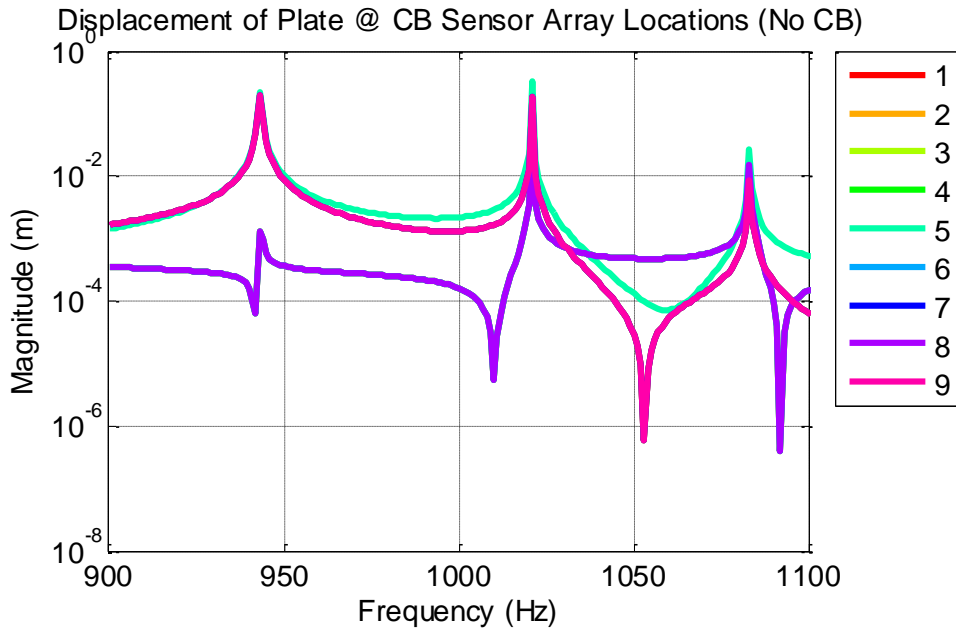


Figure 4.15: Displacement of plate @ *CB* sensor array locations (No *CB*) due to a 1N distributed force (900-1100Hz)

The results indicate that not all of the plate modes are excited by an evenly distributed vertical force. Chapter 4.5 discusses how to account for the plate dynamics when attempting to use phased array processing to identify the location of

the acoustic source. Chapter 5.2 investigates the *CB* sensor displacements due to a distributed force created by an acoustic source.

4.3 Inclusion of Conductive Polymer Sensors

In this study, an individual conductive polymer sensor consists of a $6.35 \times 6.35 \times 1.59$ mm layer of *CB* filled polyurethane fixed to the surface of the aluminum plate discussed in Chapter 4.2. An acoustic source produces a pressure wave that forces the top of the conductive polymer sensor, compressing the sensor and producing internal strain. This strain produces a change in resistance in the sensor, which can be measured when the sensor is part of a voltage divider circuit. An array of these sensors can then be used as a phased array to identify the location of the acoustic source. Figure 4.16 below presents the array configuration implemented in this study, which consists of (9) conductive polymer sensors.

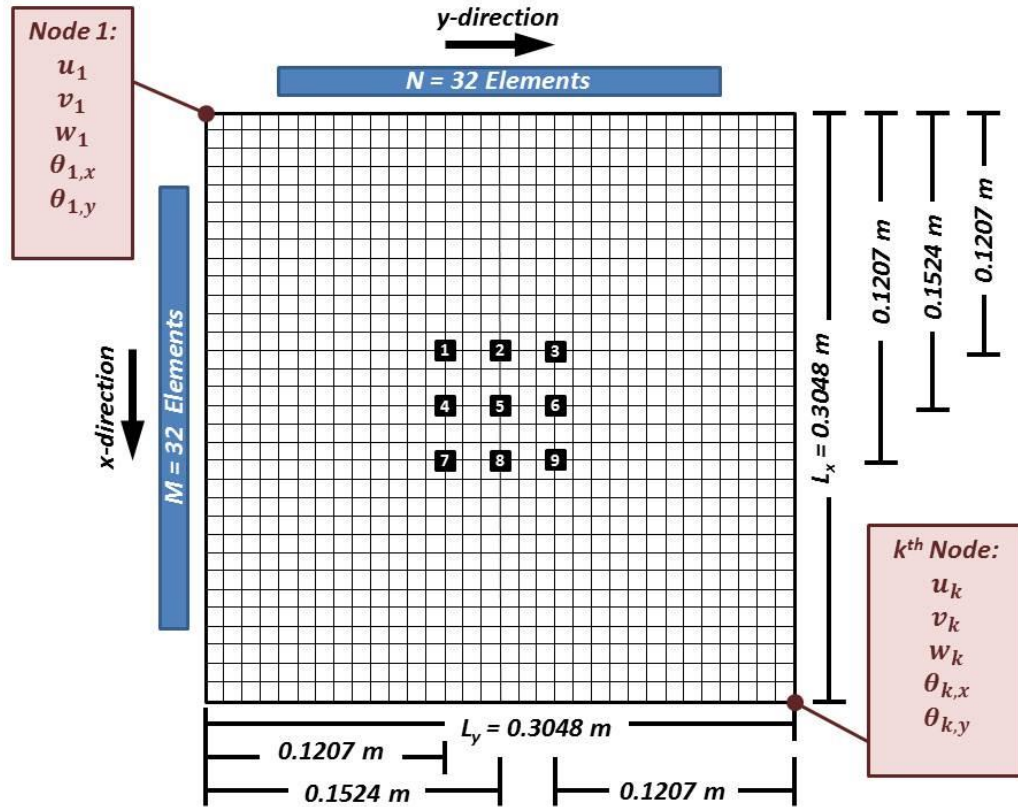


Figure 4.16: CB sensor array configuration.

This study assumes that the pressure wave produced by the acoustic source exerts a force in the z -direction on the top of the conductive polymer sensor. Reference [7] demonstrated that the compression of viscoelastic materials sandwiched between two elastic solids must be considered to accurately model the transverse motion of the composite system. In this case, the CB filled polyurethane is sandwiched between the force exerted by the acoustic pressure wave, and the motion of the base aluminum plate. Figure 4.17 below demonstrates the *Force* (F) acting on the conductive polymer sensor, the *Displacement* (w_{CB}) of the top of the conductive polymer sensor, and the *Displacement* (w_P) of the aluminum base plate.

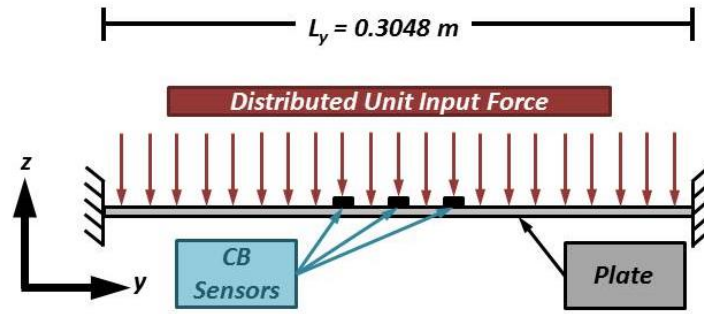


Figure 4.17: Distributed force acting on CB sensors and base plate.

Reference [7] represented the *Stiffness* of the viscoelastic material as a *Spring* (k_{CB}) in compression. The formula for a spring in compression is presented below:

$$k_{CB} = \frac{E^* A}{t} \quad (4.3.1)$$

where

- E^* = Complex modulus of the CB filled polyurethane
- A = Area of the sensor in the x - y plane
- t = Thickness of the sensor in the z -direction

The *Complex Modulus* (E^*) was determined experimentally and is described in Chapter 3. Reference [1] also included the *Mass* (m_{CB}) of the viscoelastic material in the model of the material's response. In this study, the *Mass* (m_{CB}) of the conductive polymer sensor was determined by the following equation:

$$m_{CB} = \frac{\rho_{CB} A t}{\pi^2} \quad (4.3.2)$$

where ρ_{CB} = Density of the CB filled polyurethane

The *Density* (ρ_{CB}) of the CB filled polyurethane was determined experimentally and is presented in Chapter 3. A representation of the lumped parameter model of the conductive polymer sensor is presented below in Figure 4.18.

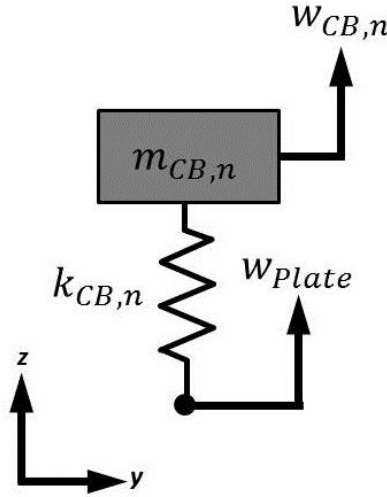


Figure 4.18: Lumped parameter model of the n th CB sensor.

Recall equation (4.1.9.4), which presents the *Equation of Motion (EOM)* of the assembled plate system:

$$\underbrace{[M]}_{(nDOF \times nDOF)} \underbrace{\{\ddot{\Delta}\}}_{(nDOF \times 1)} + \underbrace{[K]}_{(nDOF \times nDOF)} \underbrace{\{\Delta\}}_{(nDOF \times 1)} = \underbrace{\{Q\}}_{(nDOF \times 1)} \quad (4.1.9.4)$$

Rewriting equation (4.1.9.4) to include the additional DOF from the masses representing the CB sensors yields the following *Equation of Motion (EOM)* of the *Total System*:

$$\underbrace{[M_T]}_{(TDOF \times TDOF)} \underbrace{\{\ddot{\Delta}_T\}}_{(TDOF \times 1)} + \underbrace{[K_T]}_{(TDOF \times TDOF)} \underbrace{\{\Delta_T\}}_{(TDOF \times 1)} = \underbrace{\{Q_T\}}_{(TDOF \times 1)} \quad (4.3.3)$$

where $TDOF =$ *Total Degrees-of-Freedom (DOF) in the system, including the $nDOF$ of the plate model, and the 9 DOF representing the CB sensors*

$\{\Delta_T\} =$ *Total Deflection Vector of the combined system*

$[M_T] =$ *Total Mass Matrix of the combined system*

$[K_T] =$ *Total Stiffness Matrix of the combined system*

$\{Q_T\} =$ *Total Input Force Vector of the combined system*

The *Total Deflection Vector* $\{\Delta_T\}$ is composed of the following sub-vectors:

$$\underbrace{\{\Delta_T\}}_{(TDOF \times 1)} = \begin{Bmatrix} \underbrace{\{\Delta_P\}}_{(nDOF \times 1)} \\ \underbrace{\{\Delta_{CB}\}}_{(9 \times 1)} \end{Bmatrix} \quad (4.3.4)$$

where $\{\Delta_P\} =$ *Global Deflection Vector of the plate system defined in Section 4.1.8*
 $\{\Delta_{CB}\} =$ *CB Deflection Vector*

The *CB Deflection Vector* $\{\Delta_{CB}\}$ is composed of the *z-direction displacement DOF* of the (9) *CB sensor masses* as follows:

$$\underbrace{\{\Delta_{CB}\}}_{(9 \times 1)} = \{w_{CB,1} \quad w_{CB,1} \quad \dots \quad w_{CB,9}\}^T \quad (4.3.5)$$

The *Total Mass Matrix* $[M_T]$ is a linear combination of the *Plate Mass Matrix* $[M_P]$ and *CB Mass Matrix* $[M_{CB}]$, as follows:

$$\underbrace{[M_T]}_{(TDOF \times TDOF)} = \underbrace{[M_P]}_{(TDOF \times TDOF)} + \underbrace{[M_{CB}]}_{(TDOF \times TDOF)} \quad (4.3.6)$$

The *Plate Mass Matrix* $[M_P]$ is given by the following, where $[M]$ is the *Mass Matrix* in equation (4.1.9.4):

$$\underbrace{[M_P]}_{(TDOF \times TDOF)} = \begin{bmatrix} \underbrace{[M]}_{(nDOF \times nDOF)} & \underbrace{[0]}_{(nDOF \times 9)} \\ \underbrace{[0]}_{(9 \times nDOF)} & \underbrace{[0]}_{(9 \times 9)} \end{bmatrix} \quad (4.3.7)$$

The *CB Mass Matrix* $[M_{CB}]$ is given by the following expression:

$$\underbrace{[M_{CB}]}_{(TDOF \times TDOF)} = \begin{bmatrix} \underbrace{[0]}_{(nDOF \times nDOF)} & \underbrace{[0]}_{(nDOF \times 9)} \\ \underbrace{[0]}_{(9 \times nDOF)} & \underbrace{\begin{bmatrix} m_{CB,1} & 0 & \dots & 0 \\ 0 & m_{CB,2} & 0 & \vdots \\ \vdots & 0 & \ddots & 0 \\ 0 & \dots & 0 & m_{CB,9} \end{bmatrix}}_{(9 \times 9)} \end{bmatrix} \quad (4.3.8)$$

Similarly, the *Total Stiffness Matrix* $[K_T]$ is a linear combination of the *Plate Stiffness Matrix* $[K_P]$ and *CB Stiffness Matrix* $[K_{CB}]$, as follows:

$$\underbrace{[K_T]}_{(TDOF \times TDOF)} = \underbrace{[K_P]}_{(TDOF \times TDOF)} + \underbrace{[K_{CB}]}_{(TDOF \times TDOF)} \quad (4.3.9)$$

The *Plate Stiffness Matrix* $[M_P]$ is given by the following, where $[M]$ is the *Mass Matrix* in equation (4.1.9.4):

$$\underbrace{[K_P]}_{(TDOF \times TDOF)} = \begin{bmatrix} \underbrace{[K]}_{(nDOF \times nDOF)} & \underbrace{[0]}_{(nDOF \times 9)} \\ \underbrace{[0]}_{(9 \times nDOF)} & \underbrace{[0]}_{(9 \times 9)} \end{bmatrix} \quad (4.3.10)$$

The *CB Stiffness Matrix* $[K_{CB}]$ is a linear combination of the *Stiffness Matrices* $[K_{CB,i}]$ of the individual *CB* sensors, given by the following expression:

$$\underbrace{[K_{CB}]}_{(TDOF \times TDOF)} = \sum_{i=1}^9 \underbrace{[K_{CB,i}]}_{(TDOF \times TDOF)} \quad (4.3.11)$$

The *Stiffness Matrices* $[K_{CB,i}]$ of the individual *CB* sensors are given by the following expression:

$$\underbrace{[K_{CB,i}]}_{(TDOF \times TDOF)} = k_{CB,i} \underbrace{\{d_i\}^T}_{(TDOF \times 1)} \underbrace{\{d_i\}}_{(1 \times TDOF)} \quad (4.3.12)$$

The vector $\{d_i\}$ in equation (4.3.12) is an indexing vector that contains an entry corresponding to each *DOF* of the combined system. The value of each entry is determined based on the following criteria:

$$d_i(j) = \begin{cases} -1 & j = \text{Plate DOF at } CB_i \text{ location} \\ +1 & j = CB_i \text{ DOF} \\ 0 & \text{Everywhere else} \end{cases} \quad (4.3.13)$$

4.4 Coupled Model Forced Response Results

To calculate the forced response of the coupled model, a 1 N force was applied to each node of the plate, excluding the plate nodes connected to a *CB* sensor. A 1 N force was also applied to all *CB* sensor nodes. The force applied at these locations was only applied to the *z-direction* translational *DOF*. The force applied to all *x-direction* and *y-direction* translational *DOF*, and all rotational *DOF* was zero. Figure 4.19 presents a 2-dimensional representation of the distributed force on the plate. Note that while Figure 4.19 only depicts the *z-y plane*, the force is distributed over the entire *x-y plane* surface.

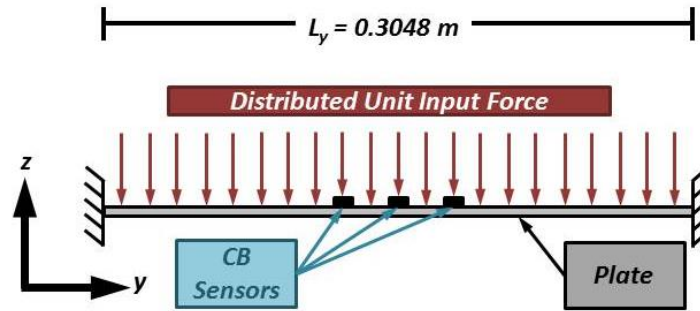


Figure 4.19: Force distribution on coupled model.

An equation similar to equation (4.2.3.2) can be written for the coupled model as follows:

$$\underbrace{\{X_T\}}_{(TDOF \times 1)} = \left(\underbrace{-\omega^2}_{(TDOF \times TDOF)} \underbrace{[M_T]}_{(TDOF \times TDOF)} + \underbrace{[K_T]}_{(TDOF \times TDOF)} \right)^{-1} \underbrace{\{Q_T\}}_{(TDOF \times 1)} \quad (4.4.1)$$

For simplification, let the *Receptance* matrix of the coupled system (H_T), or the relationship between the *External Loads* $\{Q_T\}$ and the *Deflection Vector* $\{\Delta_T\}$ of the coupled system, be defined as follows:

$$\underbrace{[H_T]}_{(TDOF \times TDOF)} = \left(-\omega^2 \underbrace{[M_T]}_{(TDOF \times TDOF)} + \underbrace{[K_T]}_{(TDOF \times TDOF)} \right)^{-1} \quad (4.4.2)$$

Plugging equation (4.4.2) into equation (4.4.1) yields the following:

$$\underbrace{\{X_T\}}_{(TDOF \times 1)} = \underbrace{[H_T]}_{(TDOF \times TDOF)} \underbrace{\{Q_T\}}_{(TDOF \times 1)} \quad (4.4.3)$$

Figure 4.20 and Figure 4.21 present the magnitude and phase of the *Transfer Receptance*, or the relationship between the *Displacements* of the plate to the *Forces* applied to the *CB* sensors. Figure 4.22 and Figure 4.23 present the magnitude and phase of the *Input Receptance* of the *CB* sensors. These results are similar to the results presented in Figure 4.11 and Figure 4.12 for the plate-only system. In both cases, there are a high number of modes up to 1.2 kHz.

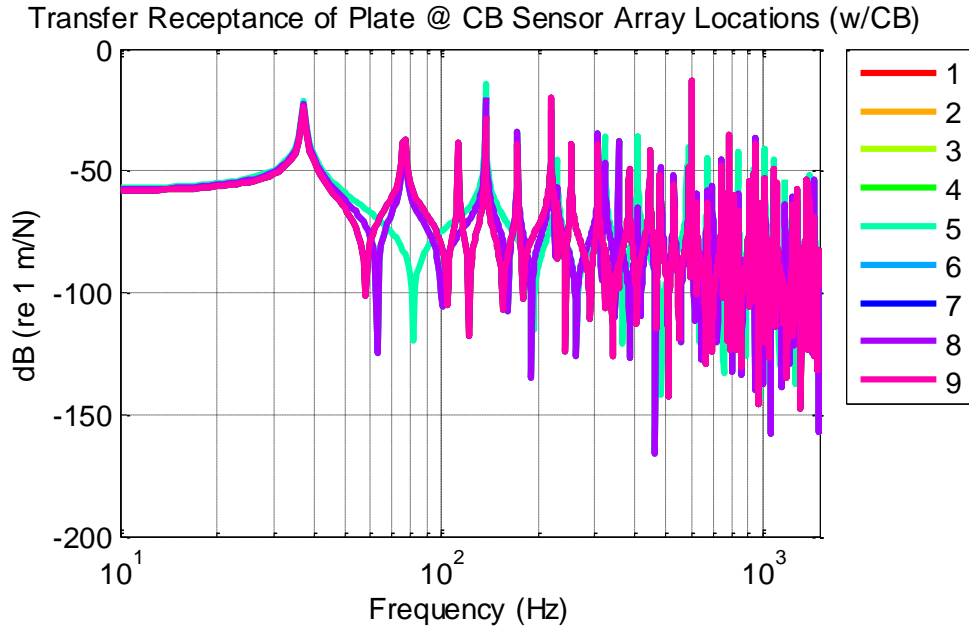


Figure 4.20: Transfer receptance (magnitude) between the displacement of the plate due to an input force on the *CB* sensor.

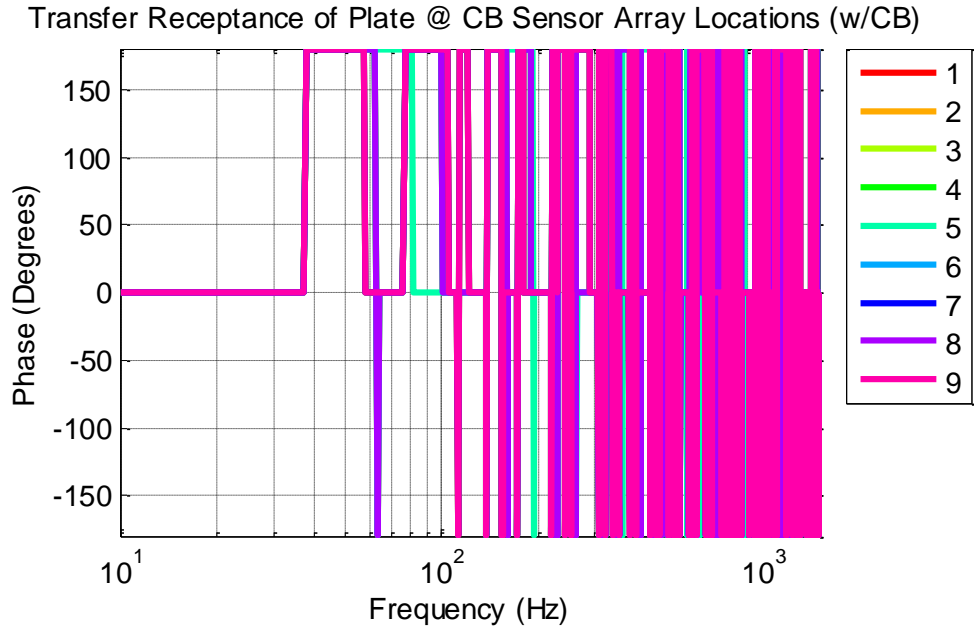


Figure 4.21: Transfer receptance (phase) between the displacement of the plate due to an input force on the *CB* sensor.

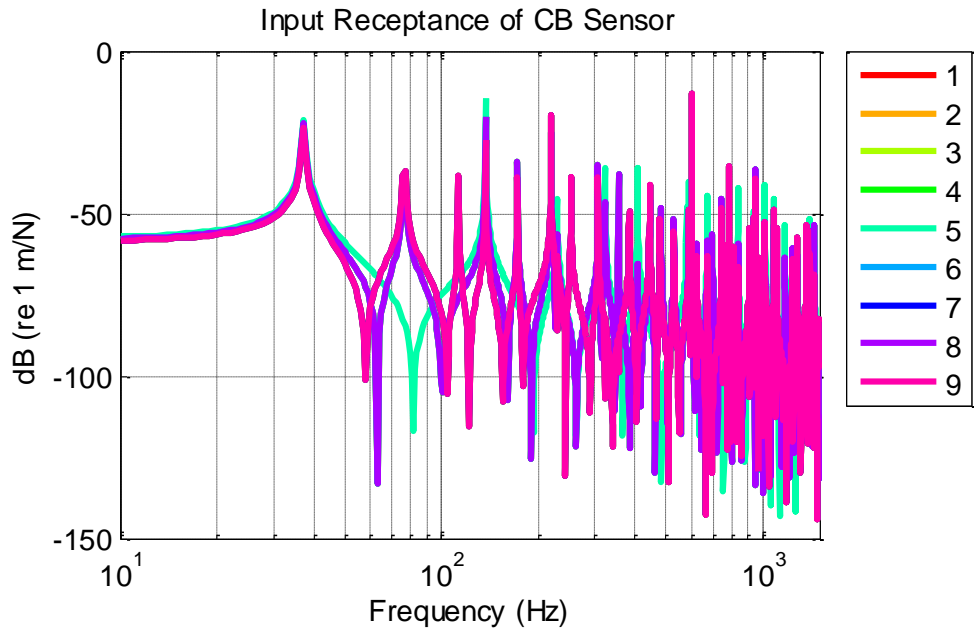


Figure 4.22: Input receptance (magnitude) of the *CB* sensor @ each sensor array location.

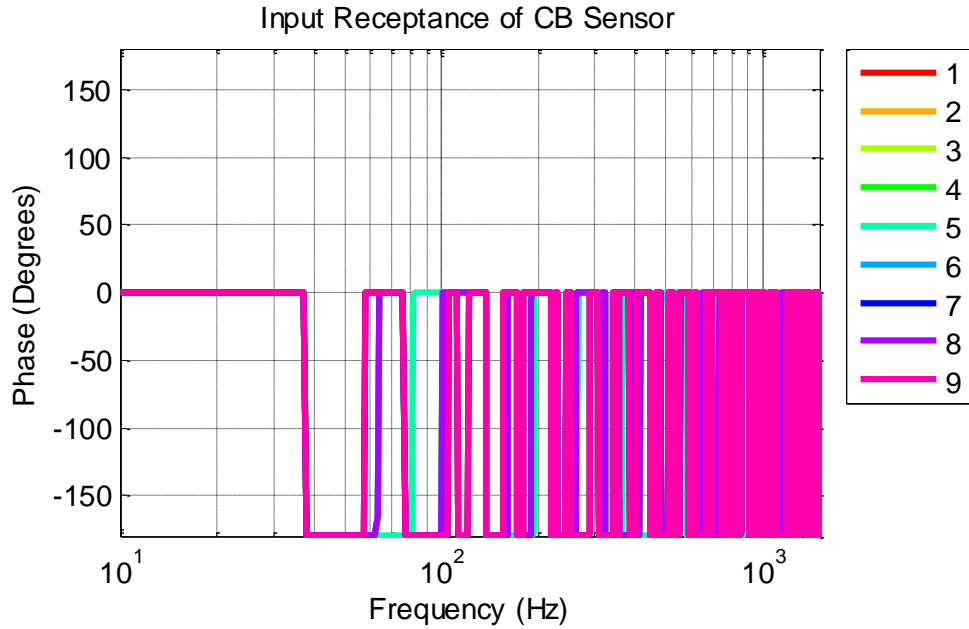


Figure 4.23: Input receptance (phase) of the *CB* sensor @ each sensor array location.

Figure 4.24 presents a comparison of the plate displacement due to the 1 N distributed vertical force, at *CB* sensor location 1, for the plate-only case and the plate-*CB* sensor coupled system.

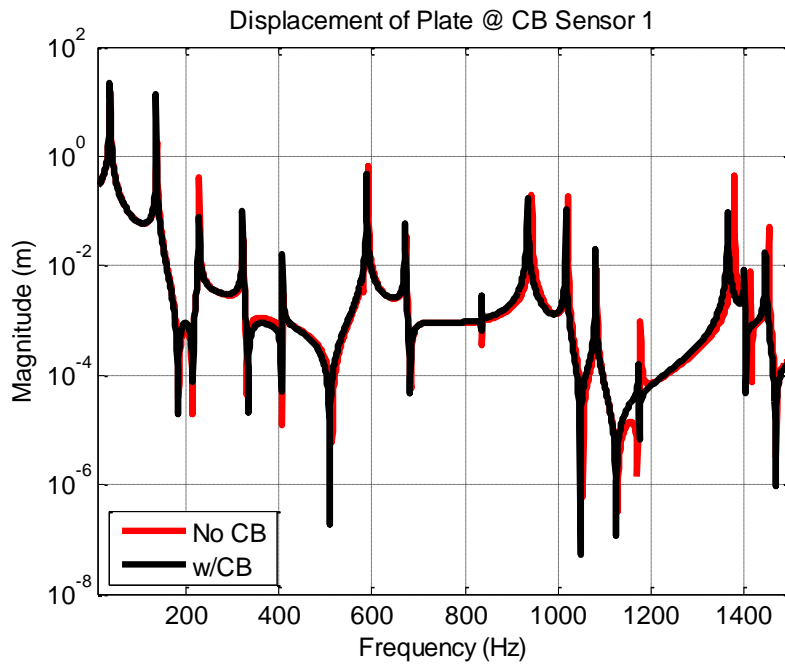


Figure 4.24: Comparison of plate displacement at *CB* sensor location 1 with and without *CB* sensor.

The results in Figure 4.24 indicate a similarity in the *Displacement* results between the two cases. The *CB* sensor array processing experimental validation, presented in Chapter 7, focuses on frequencies between 1kHz and 1.1kHz. Figure 4.25 presents the *Displacements* of the two cases over this frequency range.

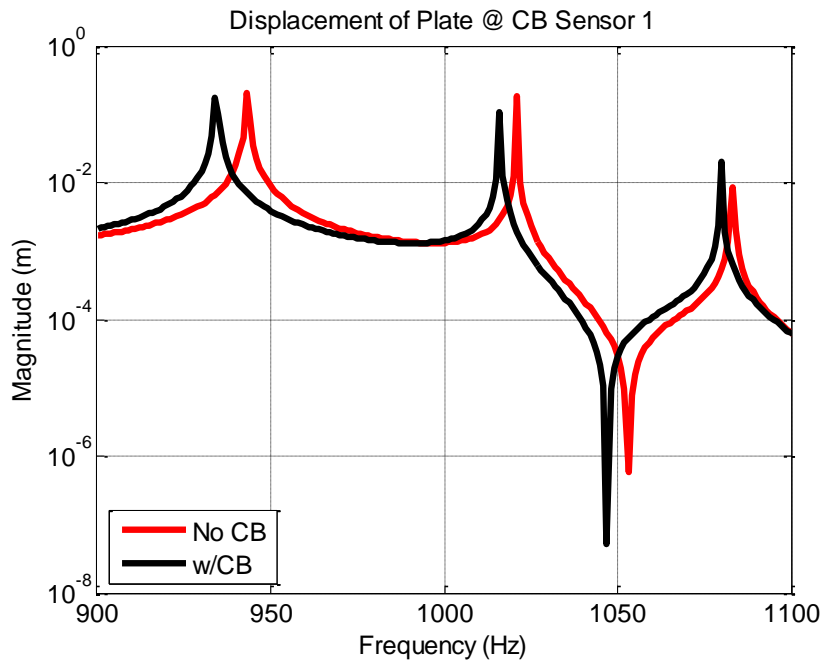


Figure 4.25: Comparison of plate displacement at *CB* sensor location 1 with and without *CB* sensor (900-1100Hz).

Figure 4.25 indicates that, upon close examination, the addition of the *CB* sensors reduces the natural frequencies of the system in the frequency range of interest (900-1100 Hz). This result is expected as the *CB* sensors add mass to the system, and adding mass to a system has the effect of reducing the system's natural frequencies. Similar results are observed for the other (9) *CB* sensors, and are presented below in Figure 4.26 through Figure 4.33

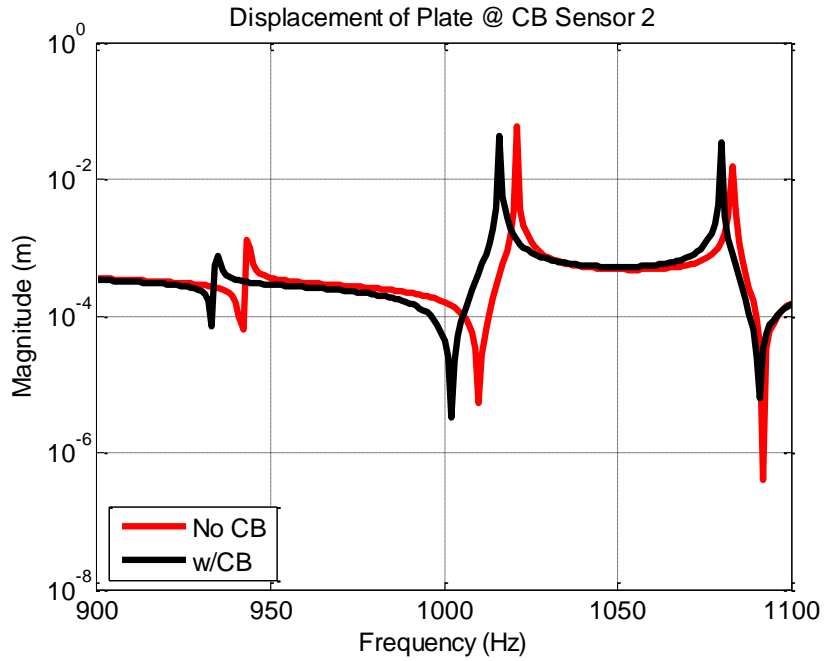


Figure 4.26: Comparison of plate displacement at *CB* sensor location 2 with and without *CB* sensor (900-1100Hz).

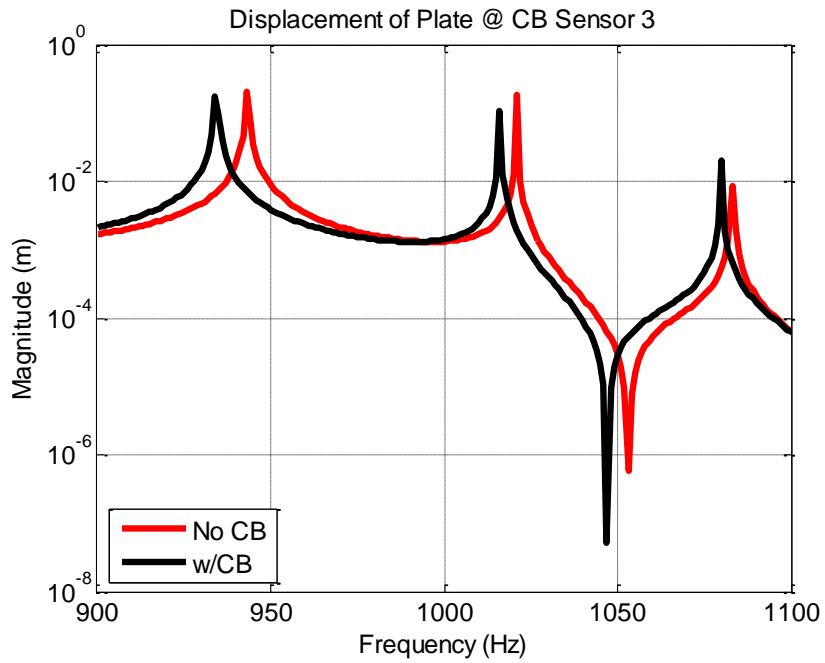


Figure 4.27: Comparison of plate displacement at *CB* sensor location 3 with and without *CB* sensor (900-1100Hz).

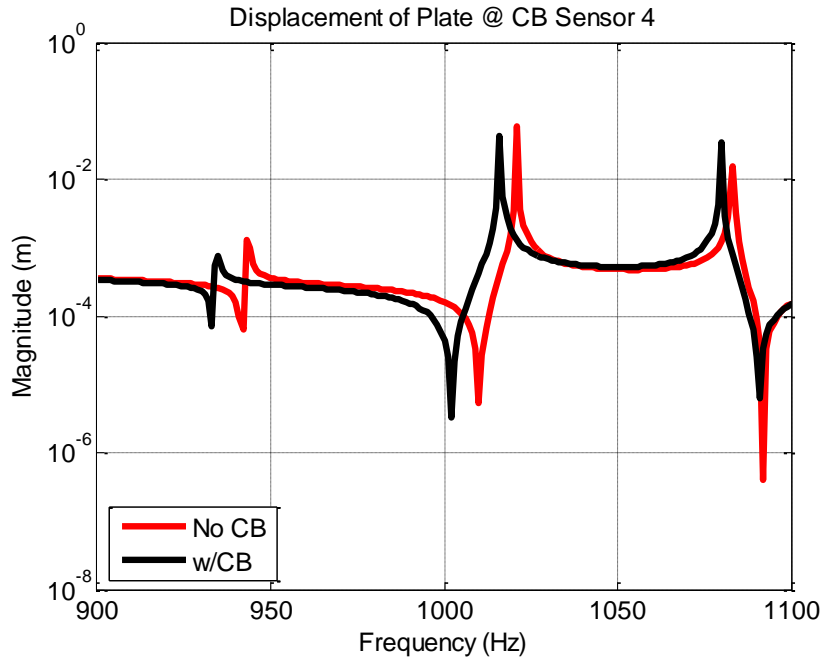


Figure 4.28: Comparison of plate displacement at *CB* sensor location 4 with and without *CB* sensor (900-1100Hz).

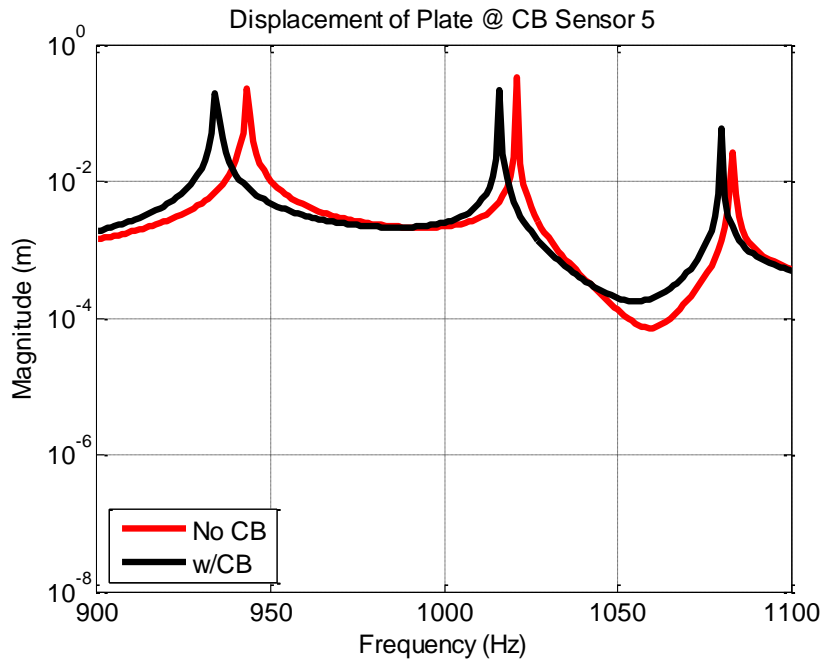


Figure 4.29: Comparison of plate displacement at *CB* sensor location 5 with and without *CB* sensor (900-1100Hz).

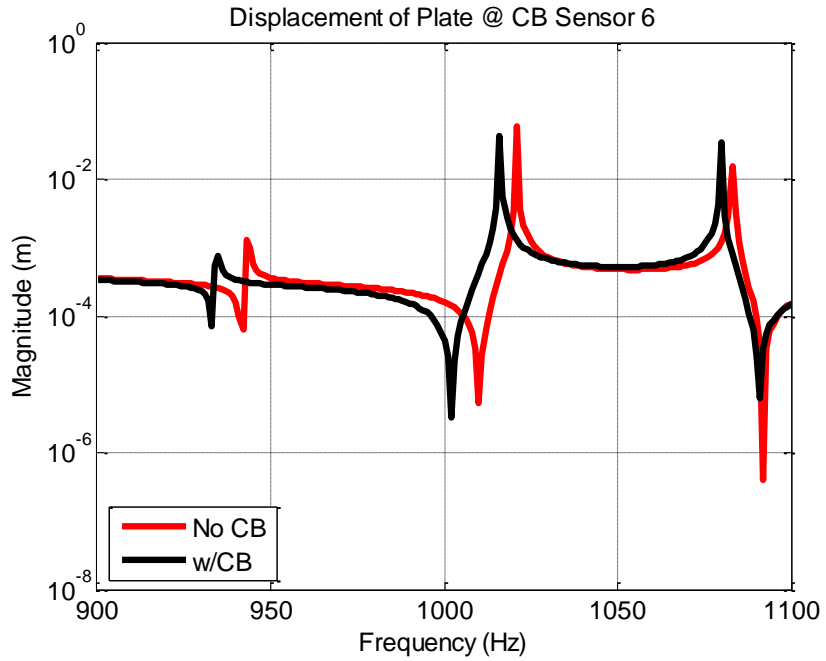


Figure 4.30: Comparison of plate displacement at *CB* sensor location 6 with and without *CB* sensor (900-1100Hz).

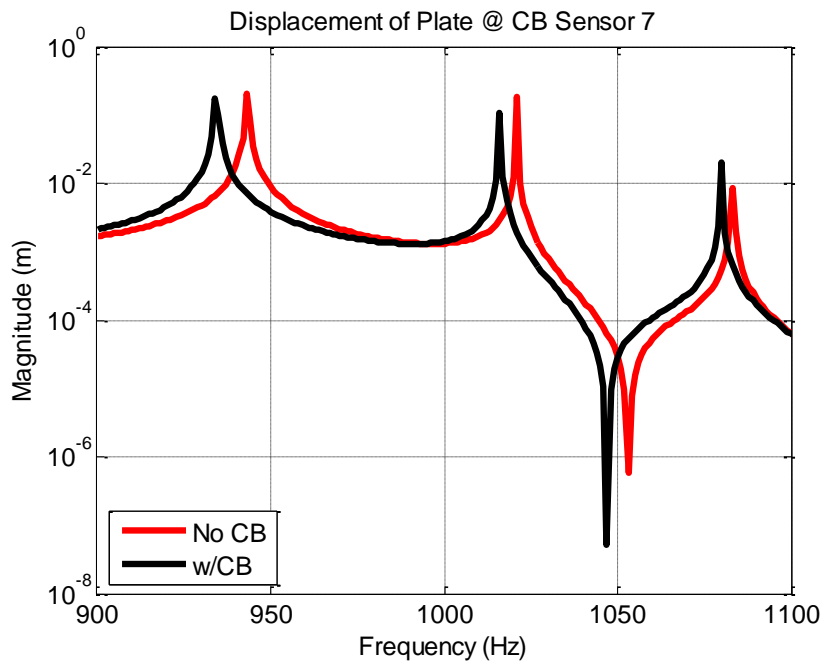


Figure 4.31: Comparison of plate displacement at *CB* sensor location 7 with and without *CB* sensor (900-1100Hz).

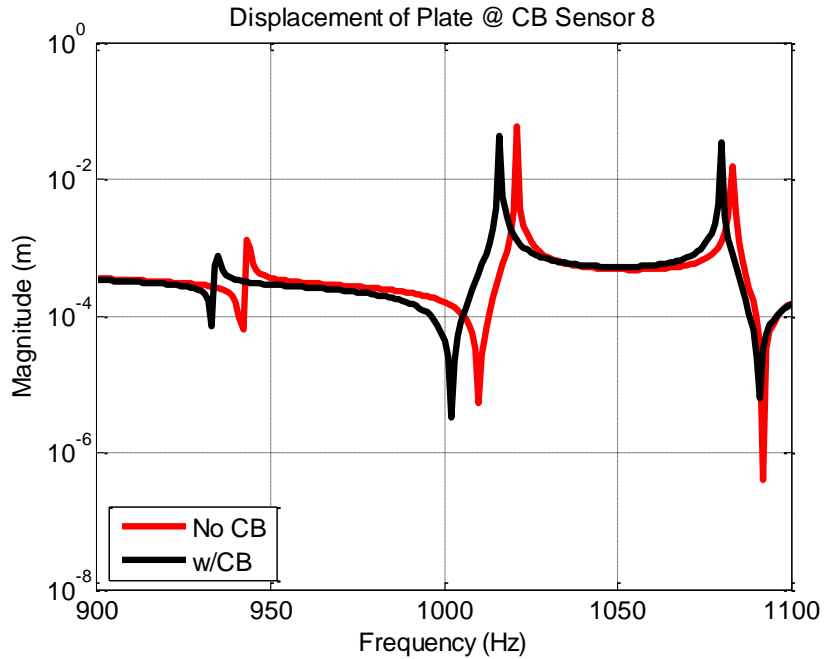


Figure 4.32: Comparison of plate displacement at *CB* sensor location 8 with and without *CB* sensor (900-1100Hz).

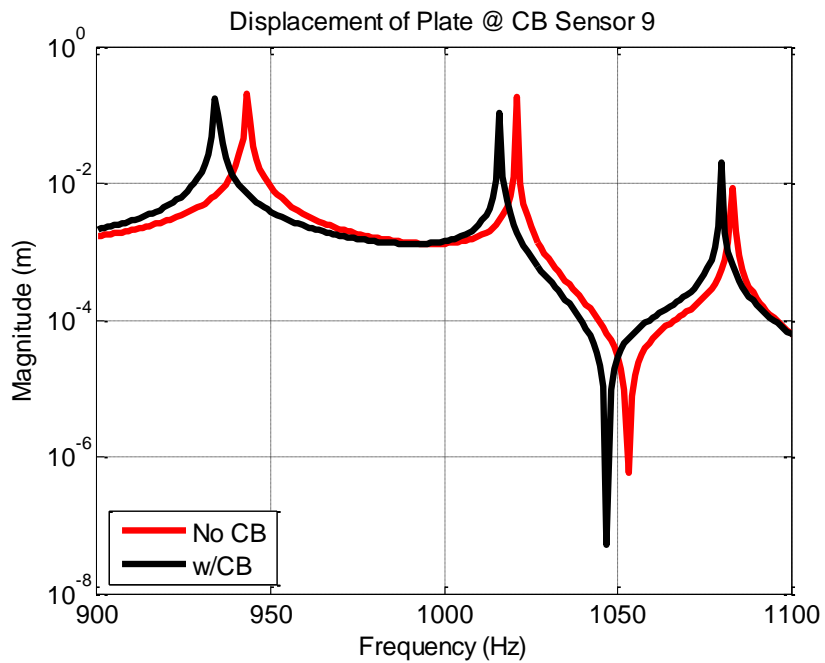


Figure 4.33: Comparison of plate displacement at *CB* sensor location 9 with and without *CB* sensor (900-1100Hz).

Equation (1.2.1) presents a relationship between the *Change in Resistivity* and the *Strain* experienced by the *CB* sensor. The *Strain* of the *CB* sensor is proportional to the relative *Displacement* between the *CB* sensor and the plate. Figure 4.34

through Figure 4.42 present a comparison of the absolute displacements of the *CB* sensor and the plate, for each *CB* sensor location, over the frequency range of interest (900-1100 Hz).

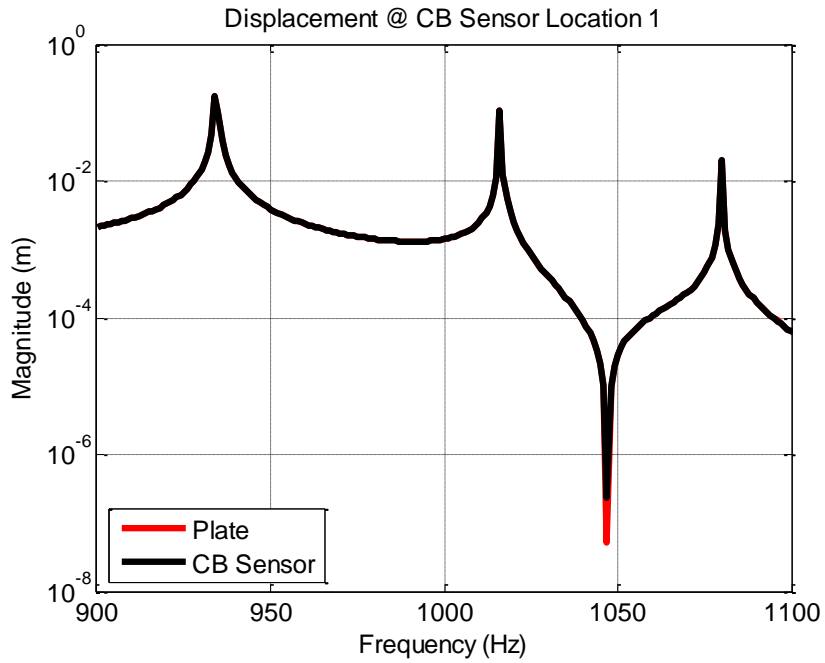


Figure 4.34: Comparison between *CB* sensor 1 displacement and corresponding plate displacement due to a 1 N distributed force (900-1100Hz).

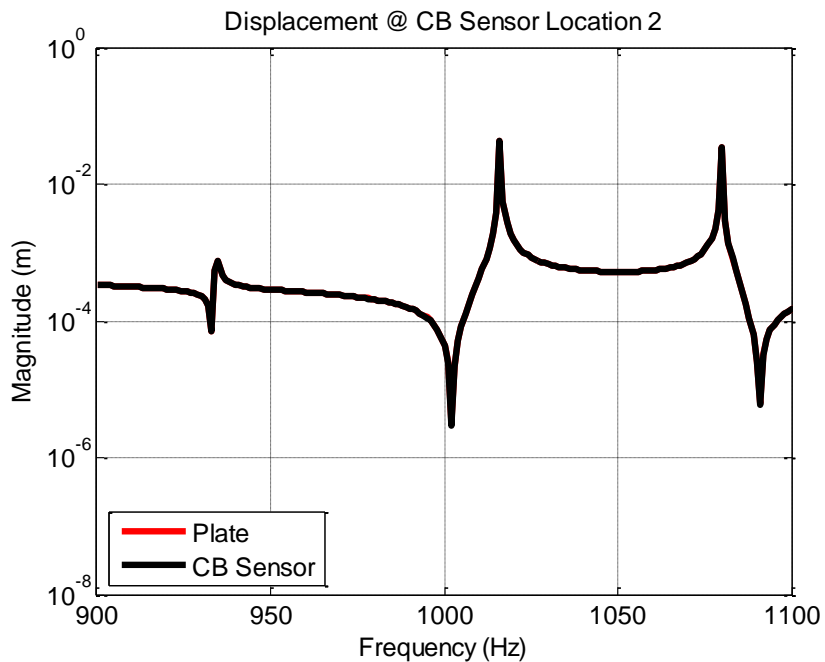


Figure 4.35: Comparison between *CB* sensor 2 displacement and corresponding plate displacement due to a 1 N distributed force (900-1100Hz).

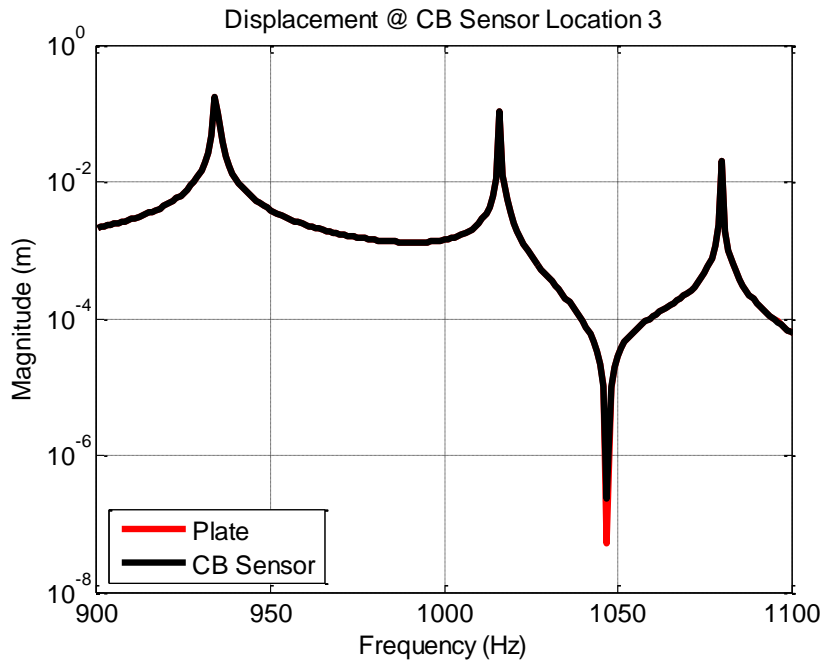


Figure 4.36: Comparison between *CB* sensor 3 displacement and corresponding plate displacement due to a 1 N distributed force (900-1100Hz).

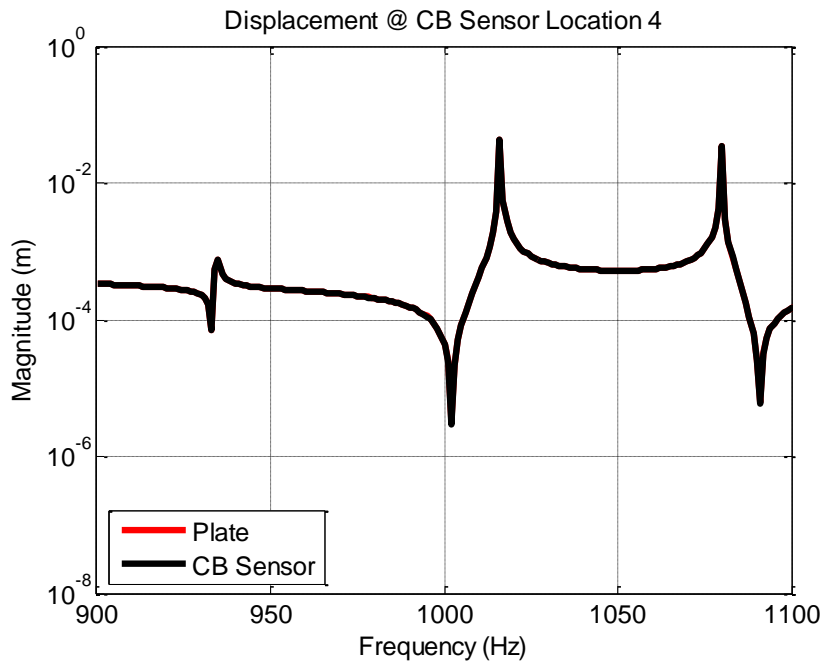


Figure 4.37: Comparison between *CB* sensor 4 displacement and corresponding plate displacement due to a 1 N distributed force (900-1100Hz).

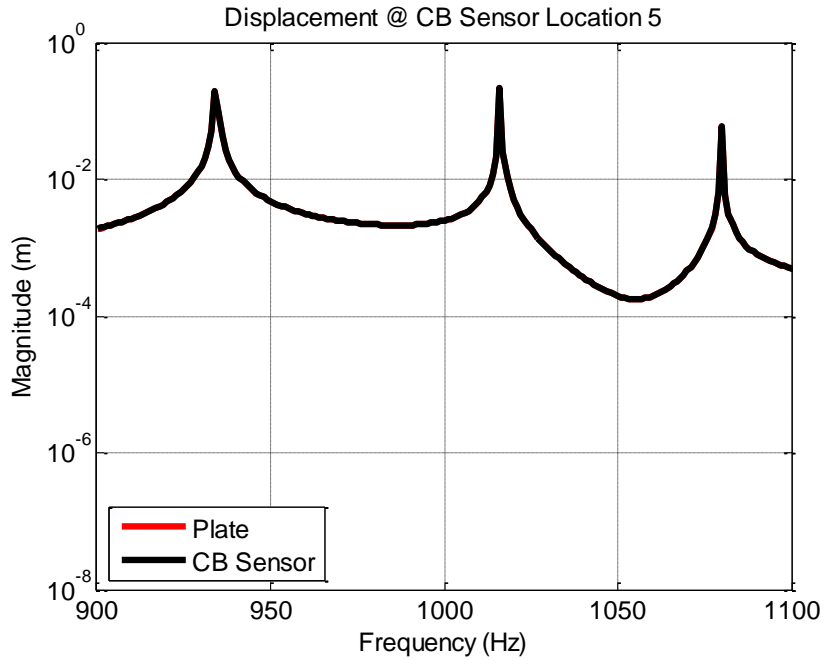


Figure 4.38: Comparison between *CB* sensor 5 displacement and corresponding plate displacement due to a 1 N distributed force (900-1100Hz).

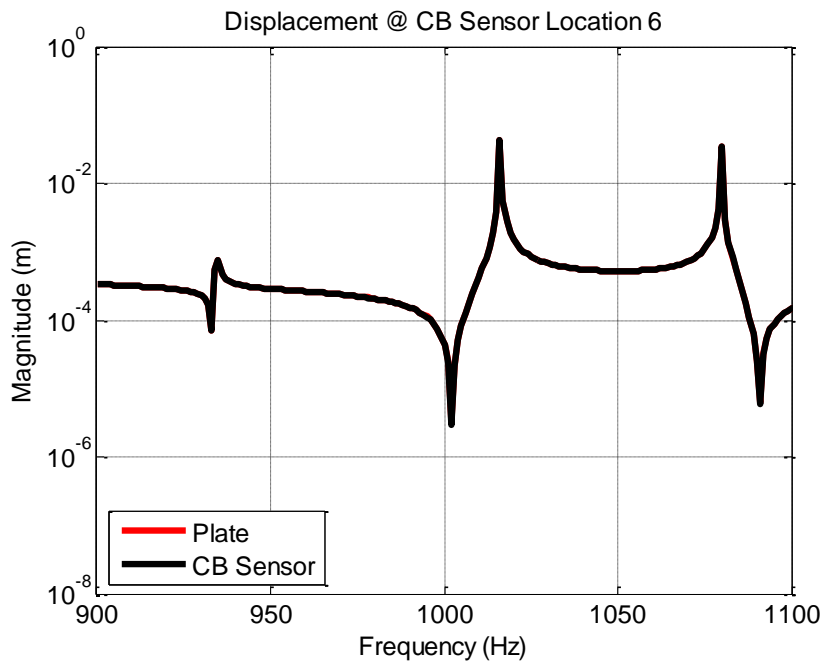


Figure 4.39: Comparison between *CB* sensor 6 displacement and corresponding plate displacement due to a 1 N distributed force (900-1100Hz).

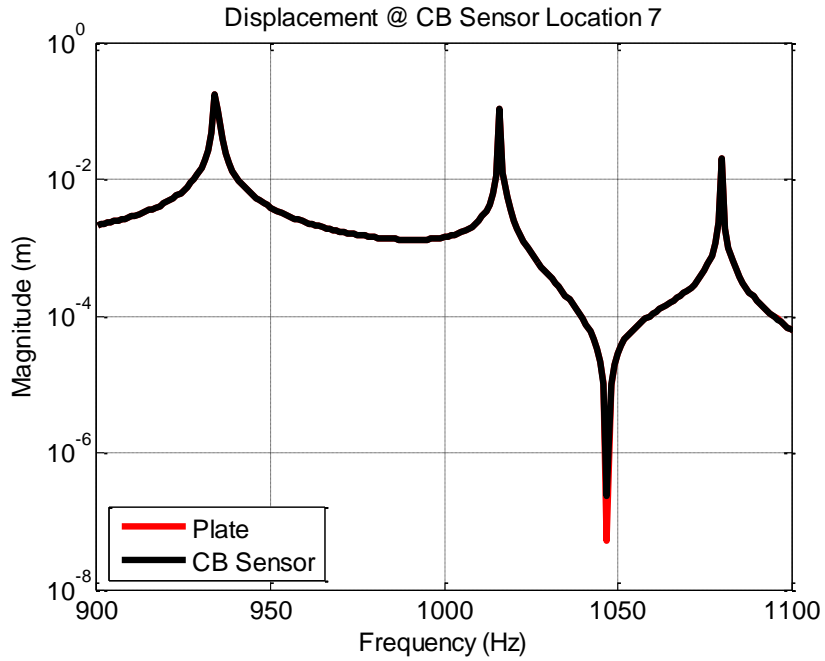


Figure 4.40: Comparison between *CB* sensor 7 displacement and corresponding plate displacement due to a 1 N distributed force (900-1100Hz).

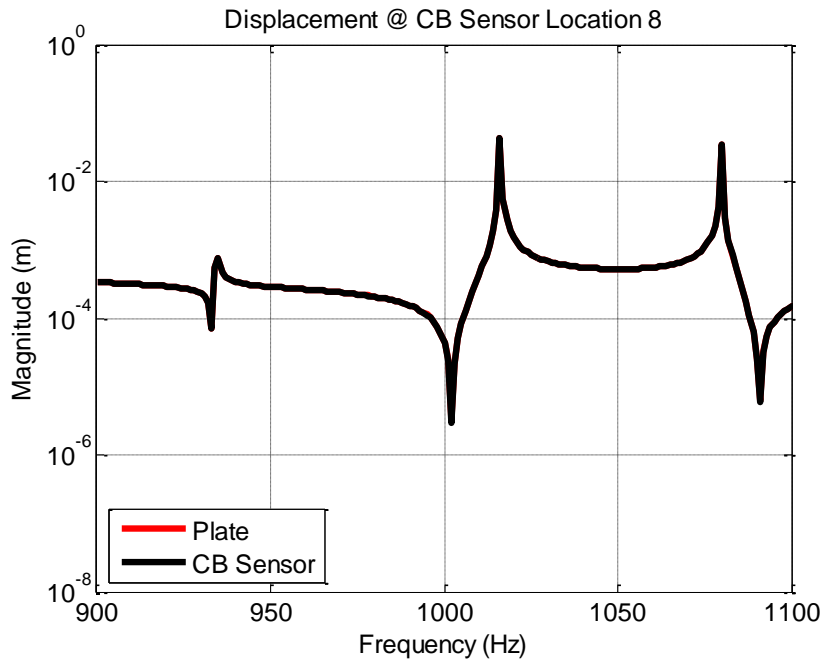


Figure 4.41: Comparison between *CB* sensor 8 displacement and corresponding plate displacement due to a 1 N distributed force (900-1100Hz).

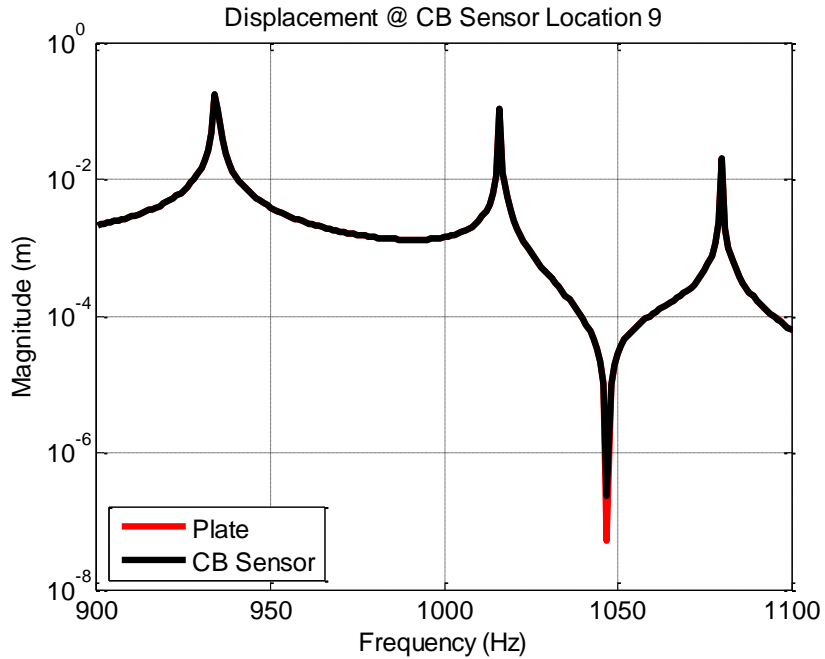


Figure 4.42: Comparison between *CB* sensor 9 displacement and corresponding plate displacement due to a 1 N distributed force (900-1100Hz).

The results in Figure 4.34 through Figure 4.42 indicate that over the frequency range of interest, the absolute displacements of the plate and the corresponding *CB* sensor are dominated by the motion of the plate.. In other words, the *CB* sensors are mostly moving with the plate. Figure 4.43 illustrates the relative motion between the *CB* sensors and the plate, which is most directly related to the output of the *CB* sensors.

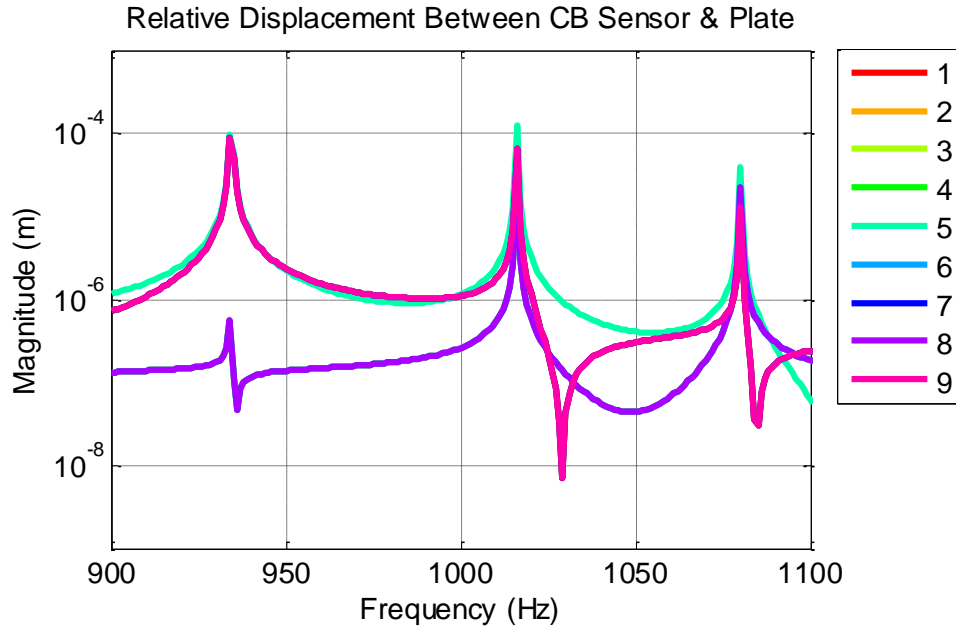


Figure 4.43: Relative displacement between *CB* sensors and plate due to a 1 N distributed force (900-1100Hz).

While not directly evident in Figure 4.34 through Figure 4.42, Figure 4.43 illustrates that there is relative motion between the *CB* sensors and the plate. Acoustic source localization using an array of *CB* sensors relies on being able to determine the input pressure force acting on each sensor. The following section demonstrates how knowledge of the relative motion between the *CB* sensors and the plate, and absolute motion of the plate, can be used to calculate the input force to the system.

4.5 Calculation of Input Force

The acoustic source localization process relies on being able to determine the input pressure force on the *CB* sensory array. The following section details how the input force can be determined by leveraging knowledge of the relative displacement between the *CB* sensor and the plate, as well as the motion of the plate.

Recall Figure 4.18, which illustrates the lumped parameter model of the n^{th} *CB* sensor. If the *Input Force* (F_n) is applied in the z -direction to the top of the n^{th} *CB* sensor mass, and assuming harmonic motion, the *Equation of Motion* describing the lumped parameter system in Figure 4.18 is as follows:

$$F_n = k_{CB,n} (w_{CB,n} - w_{plate,n}) - \omega^2 m_{CB,n} w_{CB,n} \quad (4.5.1)$$

For simplicity, the relative displacement between the *CB* sensor and the plate at the n^{th} location is defined as follows:

$$\Delta w_{CB,n} = (w_{CB,n} - w_{plate,n}) \quad (4.5.2)$$

Applying equation (4.5.2) to equation (4.5.1), and simplifying, yields the following:

$$F_n = k_{CB,n} \Delta w_{CB,n} - \omega^2 m_{CB,n} (\Delta w_{CB,n} + w_{plate,n}) \quad (4.5.3)$$

Equation (4.5.3) indicates that if the following (4) quantities of the system are known, the *Input Force* applied to each *CB* sensor can be determined:

1. *Stiffness* ($k_{CB,n}$) of the *CB* sensor
2. *Mass* ($m_{CB,n}$) of the *CB* sensor
3. *Relative motion* ($\Delta w_{CB,n}$) between the *CB* sensor and the plate
4. *Absolute motion* ($w_{plate,n}$) of the plate

Recall that the *Stiffness* ($k_{CB,n}$) and *Mass* ($m_{CB,n}$) are function of the material properties of the *CB* sensor, and are presented in equation (4.3.1) and equation

(4.3.2). In the experimental results presented in Chapter 7, the *Relative Displacement* ($\Delta w_{CB,n}$) between the *CB* sensor and the plate is measured by the *CB* sensor, and the *Absolute plate motion* ($w_{plate,n}$) is measured by a Laser Doppler Vibrometer (LDV).

Applying equation (4.5.3) to the results from Chapter 4.4 yields the following calculation of the *Input Force* applied at each of the (9) *CB* sensor locations:

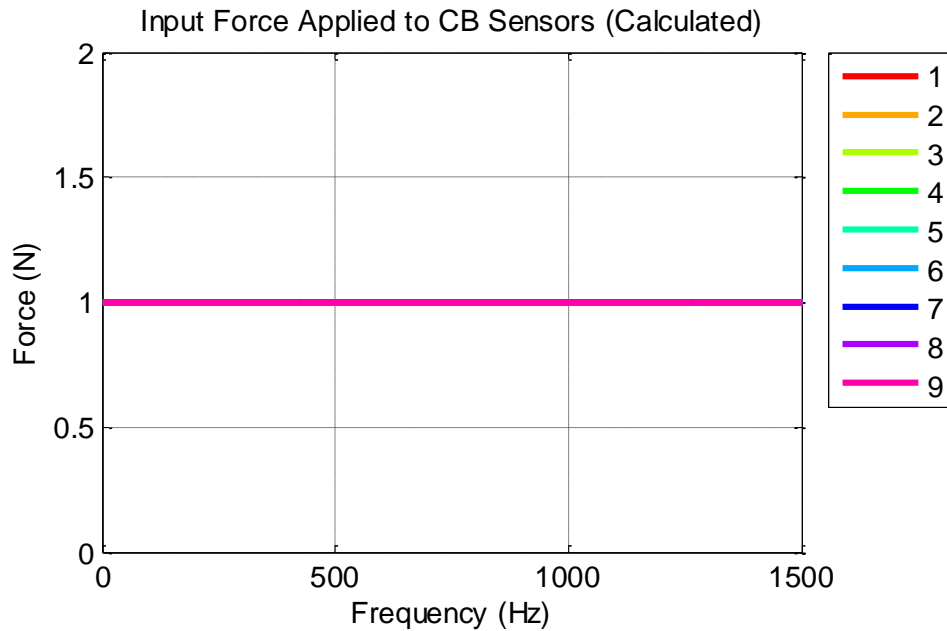


Figure 4.44: Calculation of the input force applied to the *CB* Sensors (1 N Distributed Force)

The results are in excellent agreement with the 1 N distributed force applied over the entire plate area. Chapter 5.4 presents a demonstration of this method for force identification when a more complicated source is applied.

4.6 Summary

Chapter 4 presents the results of an analytical finite-element model of the plate/*CB* sensor system. The results indicate that the addition of the *CB* sensors to the

plate system adds a small amount of mass to the system, and shifts the natural frequencies slightly lower. Additionally, the results indicate that there are no local modes of the CB sensors, and the absolute motion of the plate is dominated by local modes of the plate up to 1500 Hz.

Furthermore, Chapter 4 successfully demonstrates analytically that if the following (4) quantities of the system are known, the input force applied to each CB sensor, can be determined using Equation (4.5.3):

1. *Stiffness* ($k_{CB,n}$) of the CB sensor
2. *Mass* ($m_{CB,n}$) of the CB sensor
3. *Relative motion* ($\Delta w_{CB,n}$) between the CB sensor and the plate
4. *Absolute motion* ($w_{plate,n}$) of the plate

Chapter 5 expands upon these results, and calculates the input force on the CB sensors due to an acoustic source. Additionally, Chapter 5 uses this information to identify the location of the acoustic source.

Chapter 5: Acoustic Model

Using *CB* filled polyurethane sensors to measure the sound pressure from an acoustic source is a novel concept. Typically, an array of microphones is used for array processing and acoustic source localization. The results of a demonstration of acoustic source localization using an array of off-the-shelf condenser microphones as the receivers, and a speaker as the sound source, was conducted for comparison purposes and is presented in Chapter 6. This chapter presents an analytical interrogation of the localization procedure implemented in this study. Section 5.1 presents an acoustic source model. Section 5.2 presents the results of exciting the conductive polymer sensor model, presented in Chapter 4, by the acoustic source model. Section 5.3 presents a method of array processing the responses of an array of pressure measurements to identify the location of an acoustic source. Finally, Section 5.4 presents a method of using the responses of an array of conductive polymer sensors to identify the acoustic source location using array processing.

5.1 Acoustic Source Model

There were two different sound sources used in the experimental acoustic source localization demonstration. Chapter 6 presents the results of using an array of traditional condenser microphones to identify the location of an electromechanical speaker. Chapter 7 presents the results of using an array of *CB* sensors to identify the location of an air horn. Reference [16] was used to develop the model of the acoustic source. For both experiments, the acoustic source was modeled as an omnidirectional

point source. This assumption was validated experimentally for both cases, and the results are presented in Section 5.3.

The following equation describes the pressure seen by a receiver at location (x_n, y_n, z_n) , due to a point source at location (x_m, y_m, z_m) [16]:

$$P\left(\left|\vec{R}_{nm}\right|, f\right) = -\frac{Q_m}{4\pi\left|\vec{R}_{nm}\right|} e^{-j2\pi f\left|\vec{R}_{nm}\right|/c} \quad (5.1.1)$$

The quantity Q_m in equation (5.1.1) defines the strength of the point source. The quantity $\left|\vec{R}_{nm}\right|$ represents the magnitude of the vector between the source at location (x_m, y_m, z_m) and the receiver at location (x_n, y_n, z_n) , and is given by the following equation:

$$\left|\vec{R}_{nm}\right| = \sqrt{(x_n - x_m)^2 + (y_n - y_m)^2 + (z_n - z_m)^2} \quad (5.1.2)$$

In this thesis, the convention will be to define the location of the source based on its azimuthal angle θ , elevation angle Φ , and radius $\left|\vec{R}\right|$. The radius $\left|\vec{R}\right|$ is defined by the following equation:

$$\left|\vec{R}\right| = \sqrt{(x_m)^2 + (y_m)^2 + (z_m)^2} \quad (5.1.3)$$

The Cartesian coordinates of the source, (x_m, y_m, z_m) , can be determined from the azimuthal angle θ , elevation angle Φ , and radius $\left|\vec{R}\right|$ by the following relationships:

$$x_m = \left|\vec{R}\right| \cos \theta \sin \Phi \quad (5.1.4)$$

$$y_m = |\vec{R}| \sin \theta \sin \Phi \quad (5.1.5)$$

$$z_m = |\vec{R}| \cos \Phi \quad (5.1.6)$$

The convention for the azimuthal angle θ and elevation angle Φ is illustrated in Figure 5.1 and Figure 5.2, respectively.

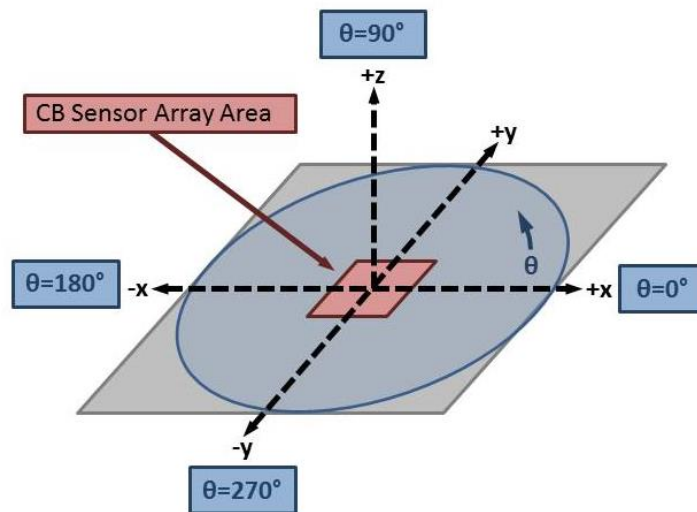


Figure 5.1: Acoustic source coordinate system convention for the azimuthal angle θ .

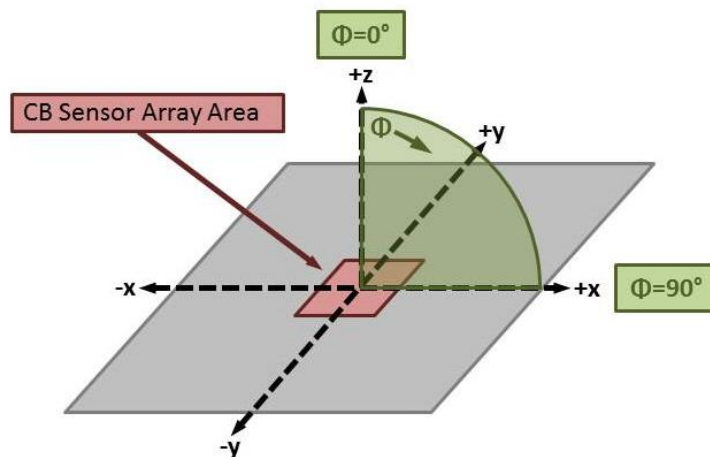


Figure 5.2: Acoustic source coordinate system convention for the elevation angle Φ .

Table 5.1 presents the source locations used in the acoustic source localization validation experiments presented in Chapter 6 and Chapter 7.

Table 5.1: Experimental source locations.

	$ \vec{R} $	θ	ϕ
Chapter 6 <i>(Condenser Mics)</i>	0.2032m	0°	0°
	0.2032m	120°	60°
Chapter 7 <i>(CB Sensors)</i>	0.2032m	0°	0°
	0.2032m	90°	45°

Models of the pressure distributions on the plate/CB sensor system were generated for each of the configurations listed in Table 5.1. All of the experimental and model results were calculated for a source frequency of 1050 Hz. Additionally, the results presented in this section assume a source strength (Q) of unity. Figure 5.3 presents the pressure distribution for the $|\vec{R}|=0.2032\text{m}$, $\theta=0^\circ$, and $\phi=0^\circ$ case.

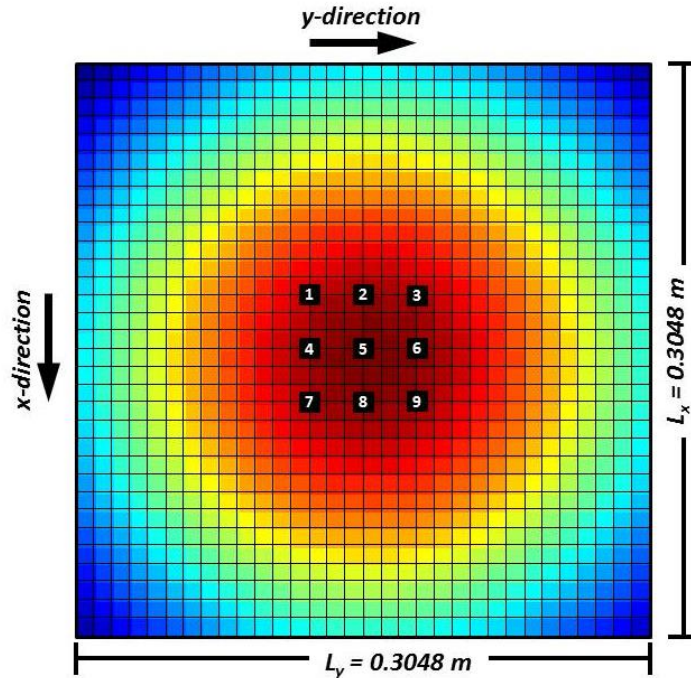


Figure 5.3: Modeled pressure distribution for a source at $|\vec{R}| = 0.2032\text{m}$, $\theta = 0^\circ$, and $\phi = 0^\circ$.

Figure 5.3 indicates that the incident pressure on the *CB* sensors is highest at *CB* sensor location 5, and decreases outward from this location. This result is expected based on the $1/|\vec{R}_{nm}|$ term in equation (5.1.1). Figure 5.4 illustrates the temporal pressure response at each of the *CB* sensor locations.

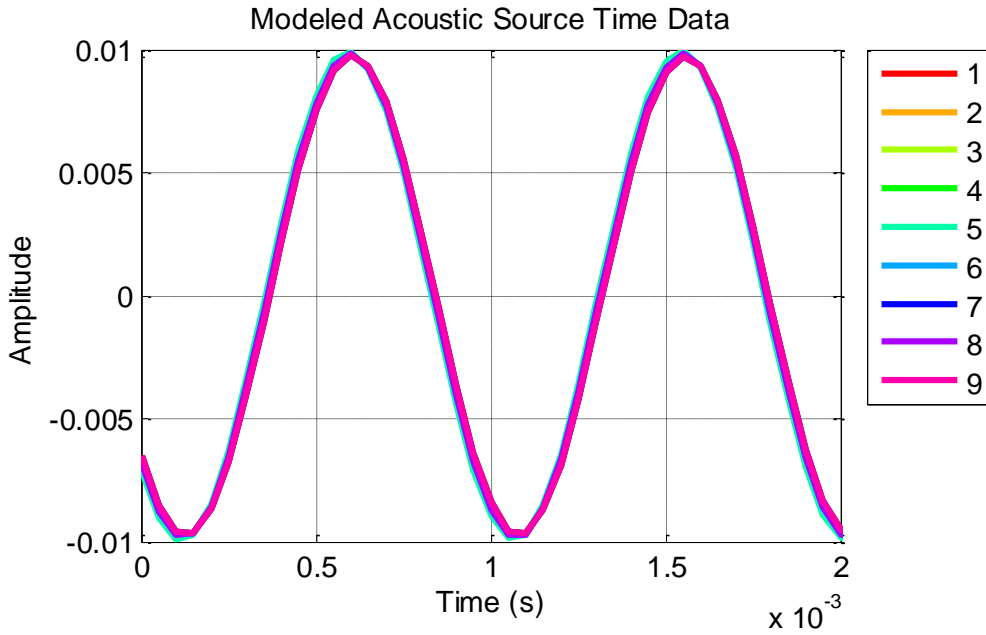


Figure 5.4: Modeled pressure time data for a source at $|\vec{R}| = 0.2032\text{m}$, $\theta = 0^\circ$, and $\phi = 0^\circ$.

Figure 5.4 illustrates the decrease in amplitude outward from the center *CB* sensor at location 5. The figure also illustrates that there is a time delay between when the pressure wavefront from the source reaches the *CB* sensors. This observation is important because acoustic source localization leverages the time delays experienced by an array of sensors to determine the location of the source.

Figure 5.5 presents the pressure distribution for the $|\vec{R}|=0.2032\text{m}$, $\theta=90^\circ$, and $\Phi=45^\circ$ case. The results are similar to the results for the previous case. The pressure

distribution on the plate/*CB* sensor system decreases by a factor of $1/|\vec{R}_{nm}|$ away from the source.

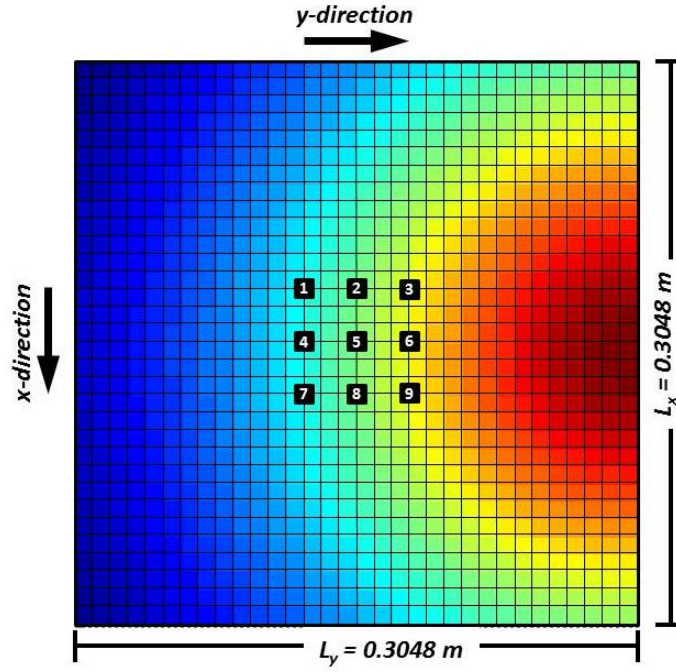


Figure 5.5: Modeled pressure distribution for a source at $|\vec{R}| = 0.2032\text{m}$, $\theta = 90^\circ$, and $\varphi = 45^\circ$.

Figure 5.6 illustrates the temporal pressure response at each of the *CB* sensor locations. The results indicate that the pressure wavefront reaches the *CB* sensors at locations 3, 6, and 9 first. Then there is a time delay and pressure amplitude decrease as the pressure wavefront reaches sensor locations 2, 5, and 8, followed by sensor locations 1, 4, and 7. Again, this result is expected due to the $1/|\vec{R}_{nm}|$ factor in equation (5.1.1).

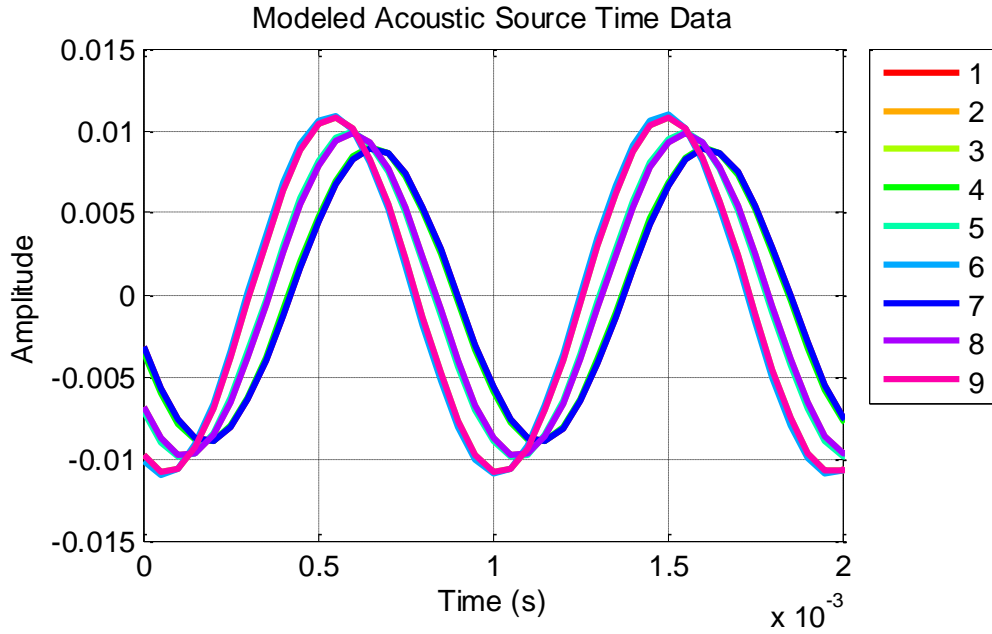


Figure 5.6: Modeled pressure time data for a source at $|\vec{R}| = 0.2032\text{m}$, $\theta = 90^\circ$, and $\phi = 45^\circ$.

Figure 5.7 and Figure 5.8 illustrate the pressure distribution and temporal pressure response, respectively, for a source located at $|\vec{R}|=0.2032\text{m}$, $\theta=90^\circ$, and $\Phi=45^\circ$.

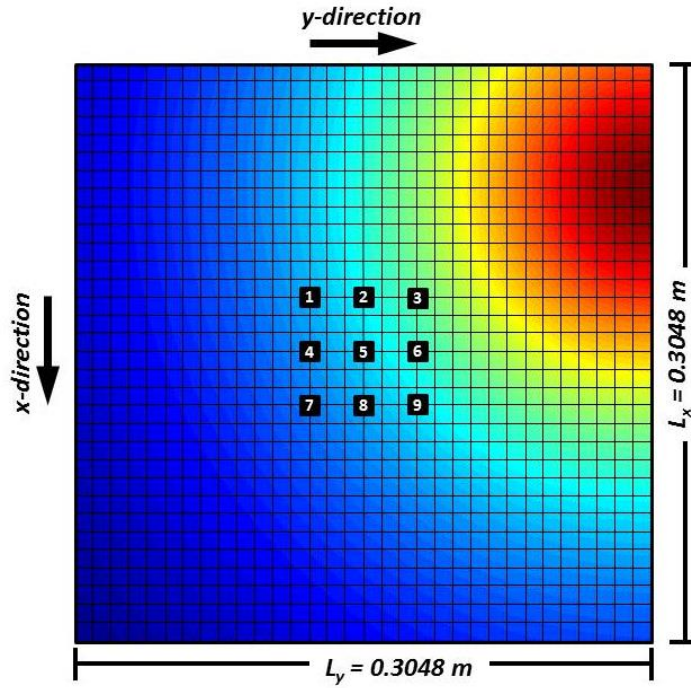


Figure 5.7: Modeled pressure distribution for a source at $|\vec{R}| = 0.2032\text{m}$, $\theta = 120^\circ$, and $\phi = 60^\circ$.

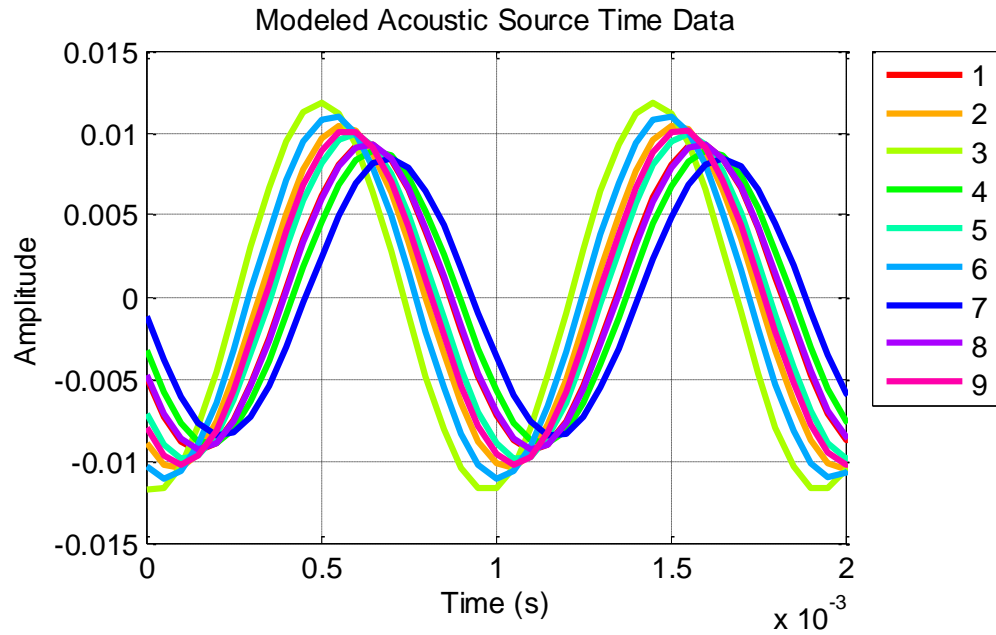


Figure 5.8: Modeled pressure time data for a source at $|\vec{R}| = 0.2032\text{m}$, $\theta = 120^\circ$, and $\phi = 60^\circ$.

The characteristics of the pressure data at the *CB* sensor locations in these figures is similar to the characteristics observed in the previous two source location cases. The model results presented in this section were used as the input to the

structural model developed in Chapter 4. The acoustically excited structural model results are presented below in Section 5.3.

5.2 Acoustic Source Localization Method (Pressure Sensor Array)

Traditional pressure sensors directly measure the surface pressure distribution due to an acoustic source, as modeled in Section 5.1. The pressure signals measured by an array of pressure sensors corresponding to the *CB* sensor locations in Figure 4.16, due to a single source at location *n*, can be modeled using equation (5.1.1). These modeled pressure signals can then be used in equation (1.3.10) to calculate the output power of the array processor, assuming a source at location *m*. This process can then be repeated for an array of assumed sources. The idea is that the maximum output power of the array processor corresponds to when the assumed source location *m* is the same as the actual source location *n*.

As discussed in Section 1.3, an important consideration in array processing is making sure that the spacing of the receivers in the array is large enough to avoid spatial aliasing. Recall that equation (1.3.10) relates the minimum separation distance between receivers (*d*) to the speed of sound in the acoustic medium (*c*), and the frequency of the source (*f*), as follows:

$$d = \frac{c}{2f} = \frac{\lambda}{2} \tag{1.3.10}$$

Plugging in the parameters of modeled and experimental setups to equation (1.3.10) yields the following minimum separation distance:

$$d = \frac{346 \text{ m/s}}{2(1050 \text{ Hz})} = 165 \text{ mm}$$

The distance between each of the sensors in Figure 4.16 is 28.575mm, which is less than the minimum required distance to avoid spatial aliasing. Having satisfied the spatial sampling requirements, equation (1.3.10) can be calculated using the modeled data from the (3) distinct source locations detailed in Table 5.1. Figure 5.9 through Figure 5.14 below present the results of calculating equation (1.3.10) for assumed source locations at $|\vec{R}|=0.2032\text{m}$, $\theta=0^\circ$ to 360° with 1° spacing, and $\Phi=0^\circ$ to 90° with 1° spacing.

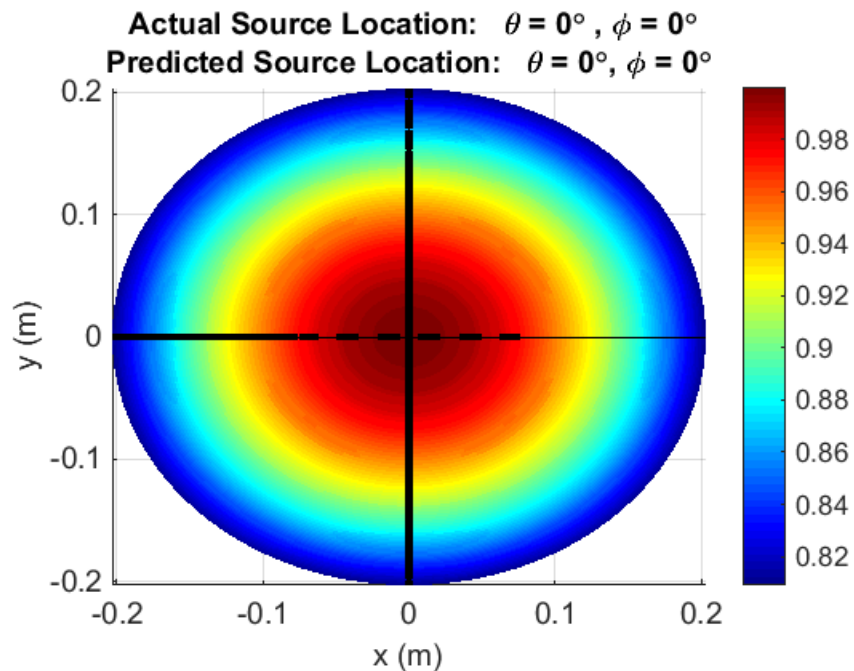


Figure 5.9: Acoustic source localization of a source at $|\vec{R}| = 0.2032\text{m}$, $\theta = 0^\circ$, and $\phi = 0^\circ$ using an array of modeled pressure sensor data.

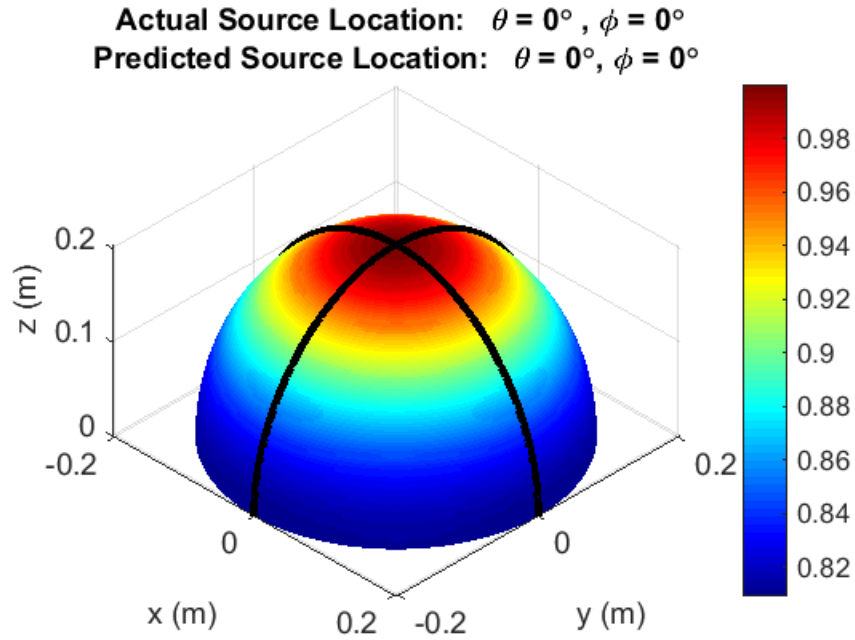


Figure 5.10: Acoustic source localization of a source at $|\vec{R}| = 0.2032\text{m}$, $\theta = 0^\circ$, and $\phi = 0^\circ$ using an array of modeled pressure sensor data.

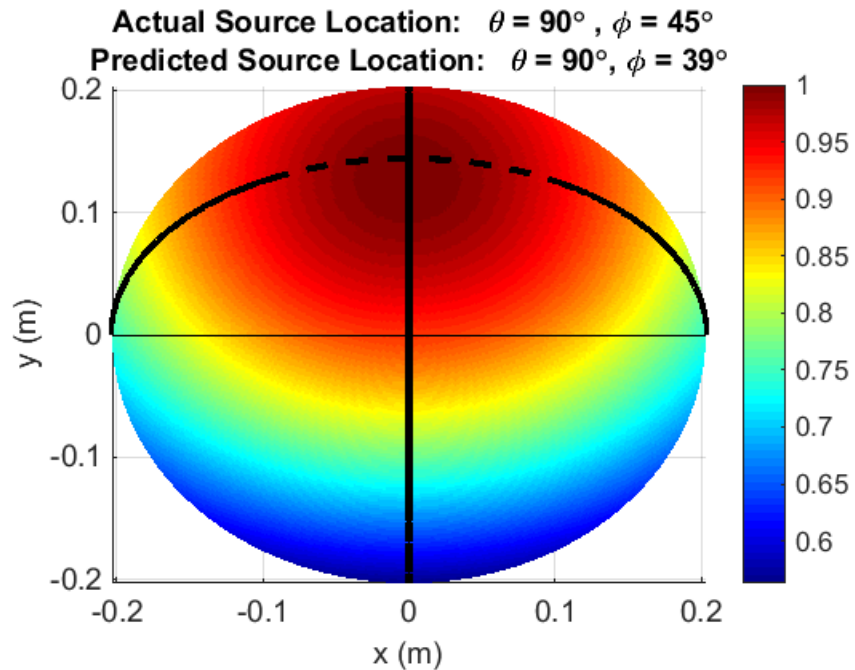


Figure 5.11: Acoustic source localization of a source at $|\vec{R}| = 0.2032\text{m}$, $\theta = 90^\circ$, and $\phi = 45^\circ$ using an array of modeled pressure sensor data.

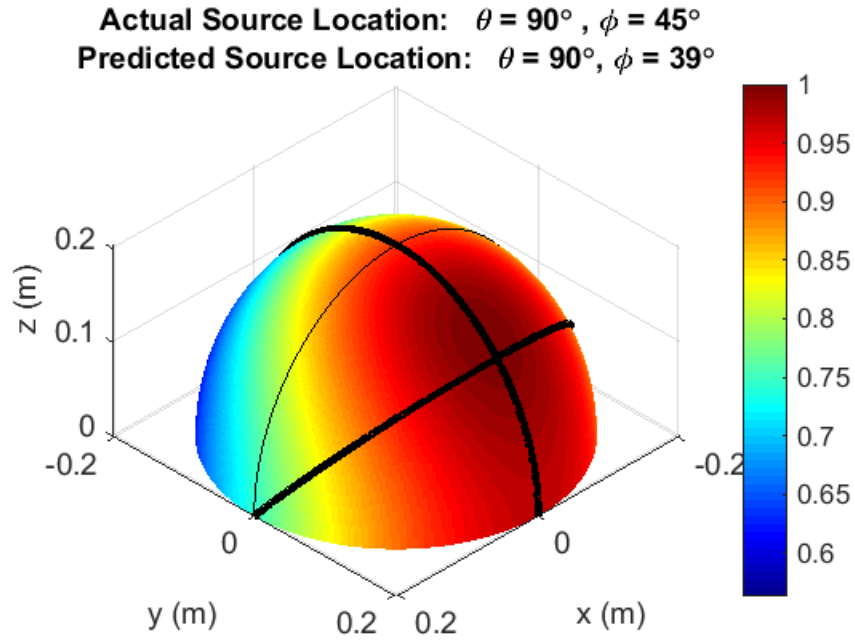


Figure 5.12: Acoustic source localization of a source at $|\vec{R}| = 0.2032\text{m}$, $\theta = 90^\circ$, and $\phi = 45^\circ$ using an array of modeled pressure sensor data.

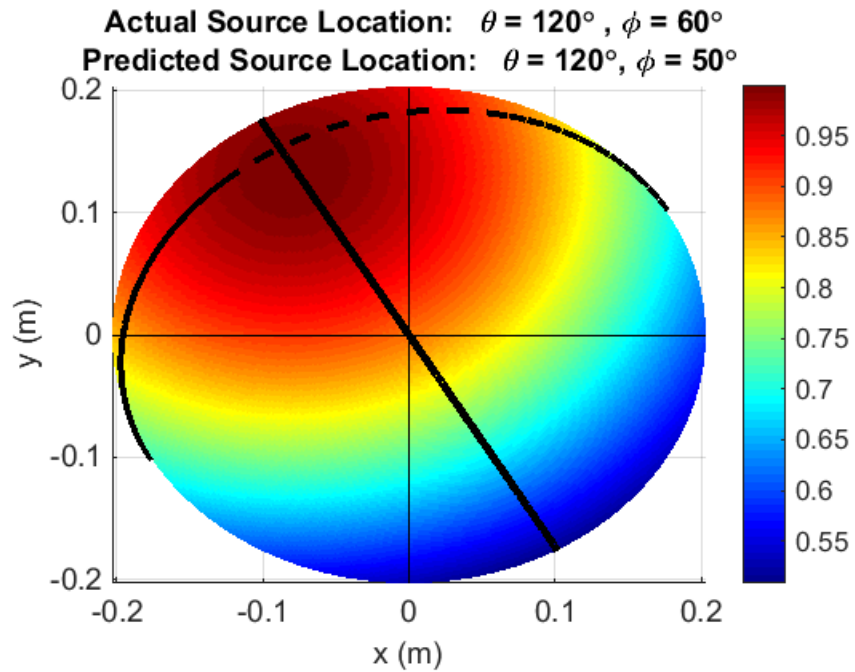


Figure 5.13: Acoustic source localization of a source at $|\vec{R}| = 0.2032\text{m}$, $\theta = 120^\circ$, and $\phi = 60^\circ$ using an array of modeled pressure sensor data.

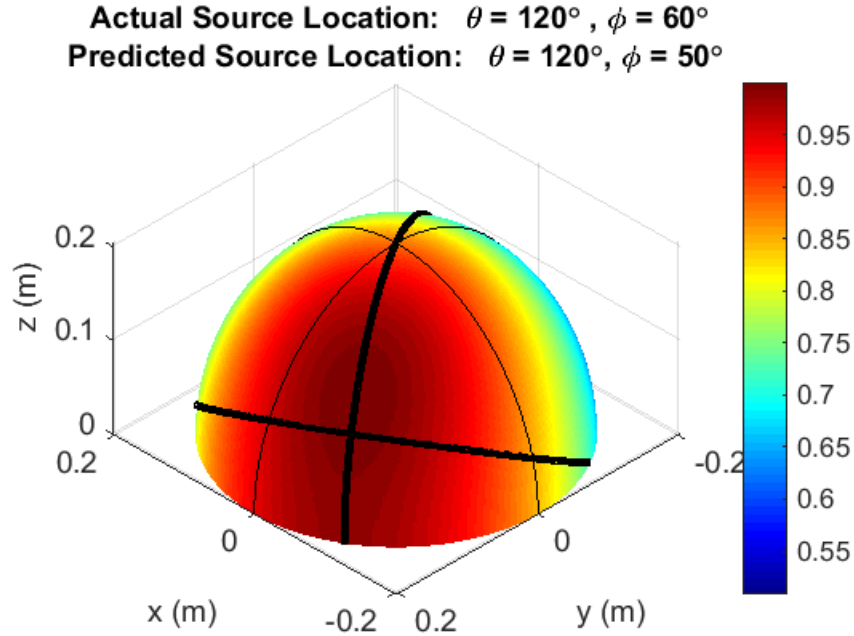


Figure 5.14: Acoustic source localization of a source at $|\vec{R}| = 0.2032\text{m}$, $\theta = 120^\circ$, and $\phi = 60^\circ$ using an array of modeled pressure sensor data.

Figure 5.9 through Figure 5.14 illustrate that the conventional array processing technique can successfully identify the location of the modeled sound source. The results indicate that the spatial filter of the array processor has a very large main lobe, with insignificant side lobes. The main lobe resolution appears to decrease as it is steered to locations approaching the plane of the receivers, as evidenced by the decreasing accuracy of the array processor as the elevation angle Φ approaches 90° . Consequently, the array processor is able to accurately identify the correct azimuthal angle of the source, and identify the elevation angle to within 15% of the actual angle. This resolution is sufficient to demonstrate the ability of the *CB* sensor array to identify the location of a sound source experimentally.

The results of this section and Section 5.1 can be directly compared to the experimental results in Chapter 6 to evaluate the validity of applying the conventional array processing technique for this particular experimental setup.

5.3 Forced Response of the System Due to Acoustic Source

Recall that equation (4.4.3) provides a relationship between the displacements of the plate/*CB* sensor system due to a distributed force of 1N at all locations. This equation can be modified to account for an acoustic source as follows:

$$\underbrace{\{X_T\}}_{(TDOF \times 1)} = \underbrace{[H_T]}_{(TDOF \times TDOF)} \underbrace{\{P_T\}}_{(TDOF \times 1)} \quad (5.2.1)$$

The vector $\{P_T\}$ is the pressure force applied to each node of the structural model. Each component of the pressure force vector $\{P_T\}$ is determined by multiplying the acoustic pressure at that corresponding location, given by equation (5.1.1), by the area of a single $6.35 \times 6.35 \times 1.59$ mm element of the structural model.

An important component of equation (5.1.1) is the source strength Q . The source strength of the horn was calculated using data from traditional condenser microphones located in the field. The microphones were located at the same radius as the horn, but at different azimuthal and elevation angles. For the case where the horn was located at $|\vec{R}|=0.2032\text{m}$, $\theta=0^\circ$, and $\Phi=0^\circ$, microphones located at $|\vec{R}|=0.2032\text{m}$, $\theta=0^\circ$, and $\Phi=0^\circ$ and $|\vec{R}|=0.2032\text{m}$, $\theta=0^\circ$, and $\Phi=0^\circ$ each measured a sound pressure level (SPL) of 123dB re $20\mu\text{Pa}$. Assuming that the plate/*CB* sensor system is a rigid surface, and there are minimal reflections in the room, these SPL measurements

correspond to a source with a $Q = 30$. This Q factor was used for all subsequent models of the horn source.

Figure 5.15 illustrates the force applied at each CB sensor location due to a source at $|\vec{R}|=0.2032\text{m}$, $\theta=0^\circ$, and $\Phi=0^\circ$. Figure 5.16 and Figure 5.17 present the displacements of the plate and CB sensors, respectively, at the CB sensor locations due to the modeled horn source. Figure 5.18 illustrates the relative displacement between the plate and CB sensors for this case.

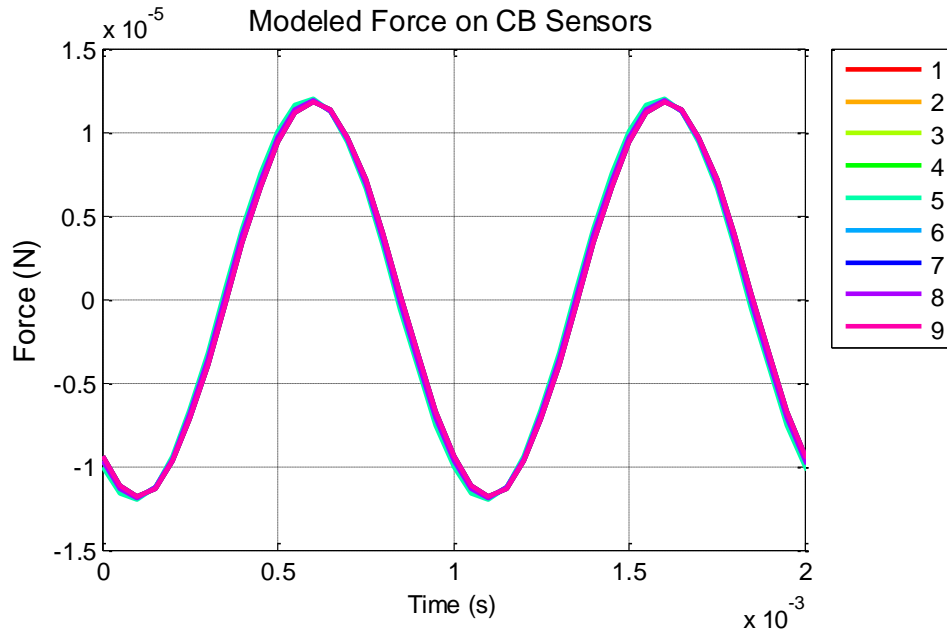


Figure 5.15: Modeled input force on the CB sensors due to an acoustic source at $|\vec{R}| = 0.2032\text{m}$, $\theta = 0^\circ$, and $\phi = 0^\circ$.

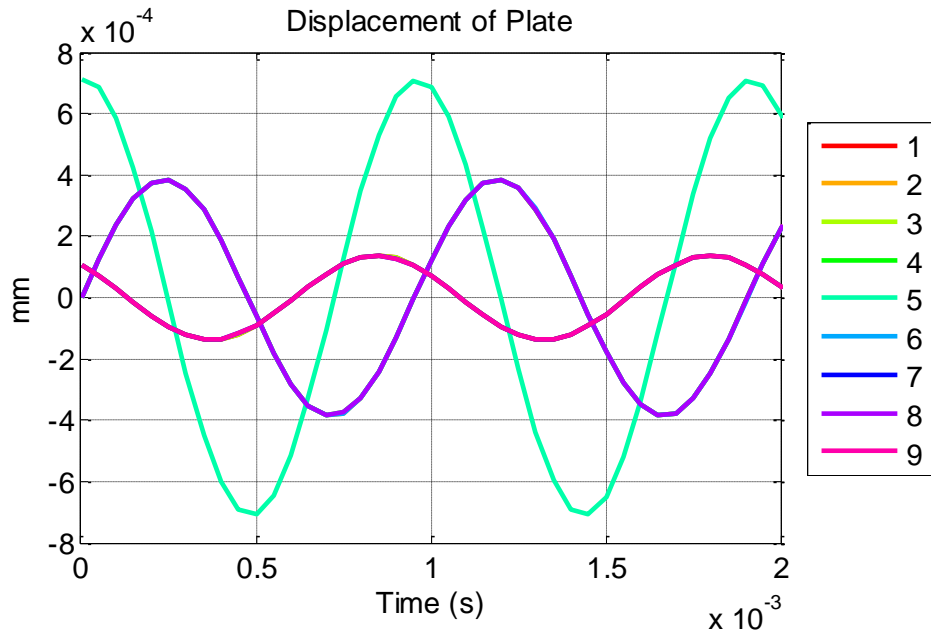


Figure 5.16: Modeled absolute plate displacement at the *CB* sensor locations due to an acoustic source at $|\vec{R}| = 0.2032\text{m}$, $\theta = 0^\circ$, and $\varphi = 0^\circ$.

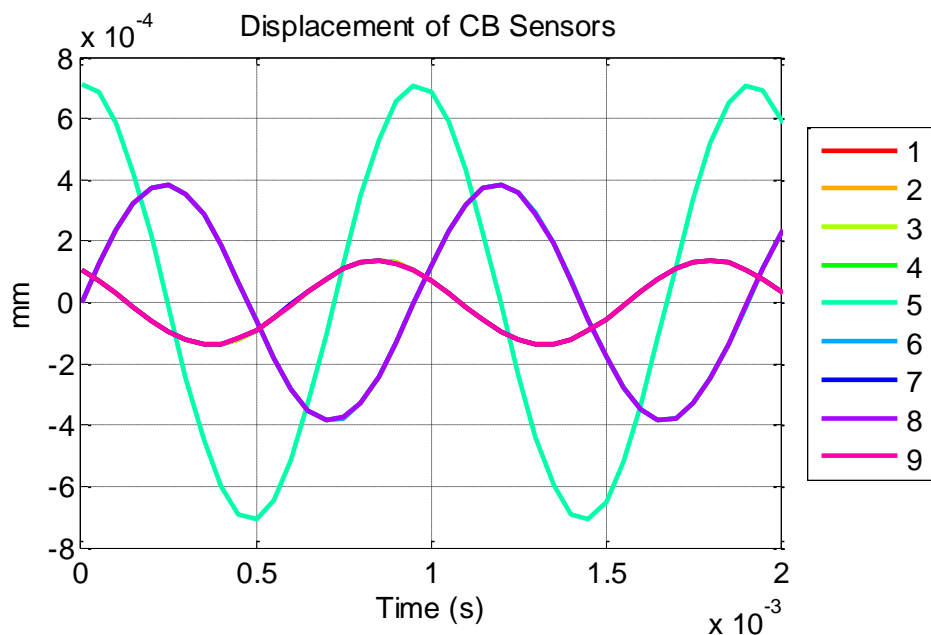


Figure 5.17: Modeled absolute *CB* sensor displacement due to an acoustic source at $|\vec{R}| = 0.2032\text{m}$, $\theta = 0^\circ$, and $\varphi = 0^\circ$.

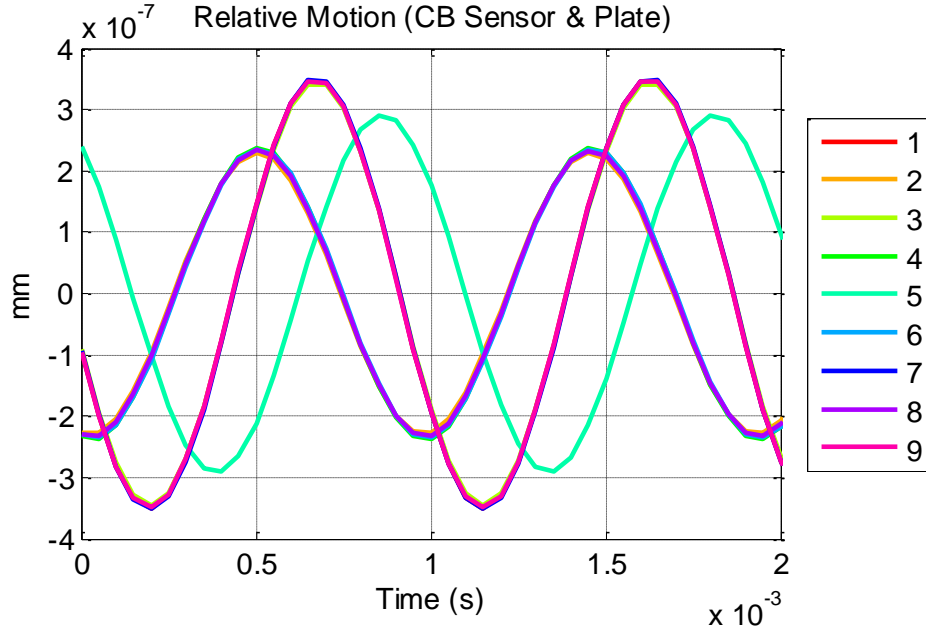


Figure 5.18: Modeled relative displacement between the *CB* sensors and the plate due to an acoustic source at $|\vec{R}| = 0.2032\text{m}$, $\theta = 0^\circ$, and $\phi = 0^\circ$.

Figure 5.16 and Figure 5.17 indicate that the absolute motion of the *CB* sensors dominated by the motion of the plate. This observation is in agreement with the results presented in Chapter 4 for the 1-N distributed force case. Figure 5.18 presents the relative displacement between the *CB* sensors in the plate, which is directly related to the output of the *CB* sensors. The results indicate that the signals measured by the *CB* sensors are not correlated with the applied pressure forces. This result is due to the motion of the plate influencing the motion of the *CB* sensors along with the incident pressure forces.

Similar results can be observed for the case where the source is located at $|\vec{R}| = 0.2032\text{m}$, $\theta = 90^\circ$, and $\Phi = 45^\circ$. Figure 5.19 illustrates the force applied at each *CB* sensor location due to the horn source. Figure 5.20 and Figure 5.21 present the

displacements of the plate and *CB* sensors, respectively, at the *CB* sensor locations due to the modeled horn source. Figure 5.22 illustrates the relative displacement between the plate and *CB* sensors for this case.

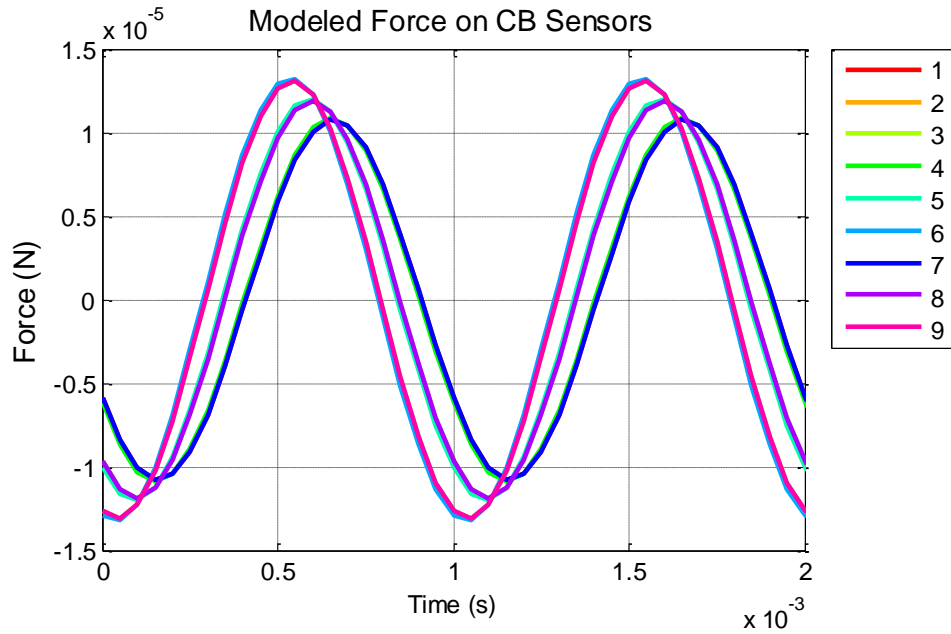


Figure 5.19: Modeled input force on the *CB* sensors due to an acoustic source at $|\vec{R}| = 0.2032\text{m}$, $\theta = 90^\circ$, and $\varphi = 45^\circ$.

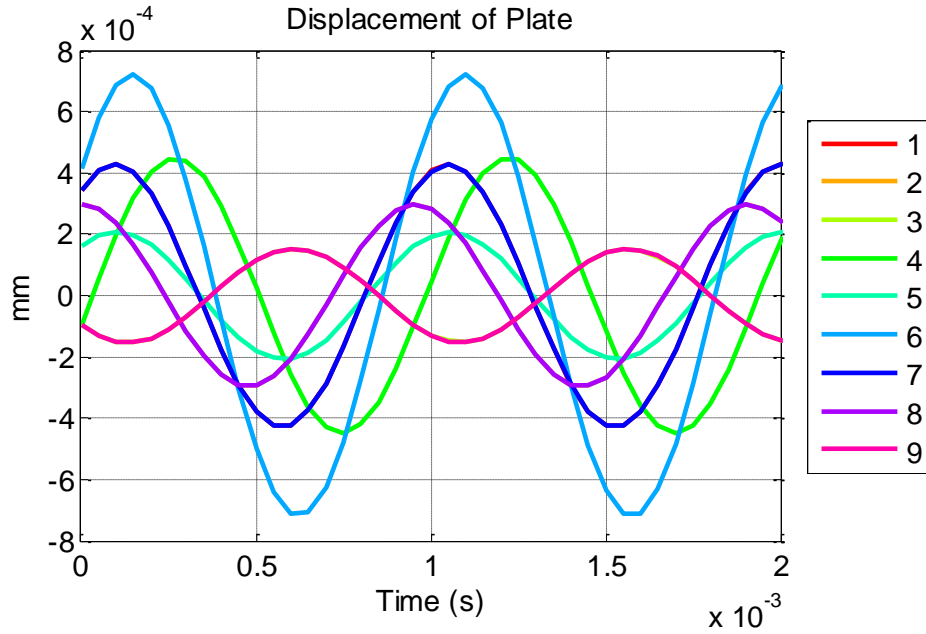


Figure 5.20: Modeled absolute plate displacement at the *CB* sensor locations due to an acoustic source at $|\vec{R}| = 0.2032\text{m}$, $\theta = 90^\circ$, and $\varphi = 45^\circ$.

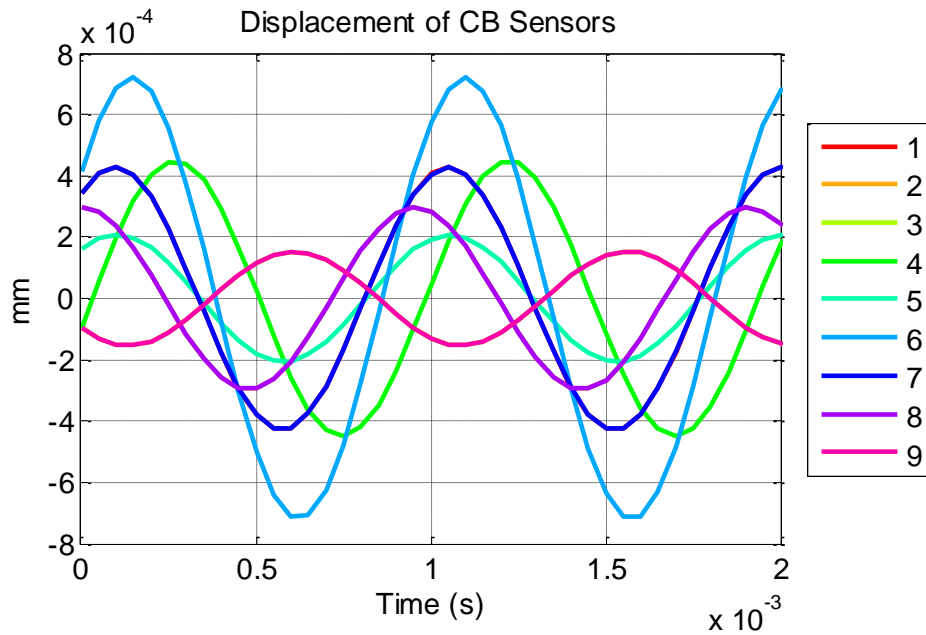


Figure 5.21: Modeled absolute *CB* sensor displacement due to an acoustic source at $|\vec{R}| = 0.2032\text{m}$, $\theta = 90^\circ$, and $\varphi = 45^\circ$.

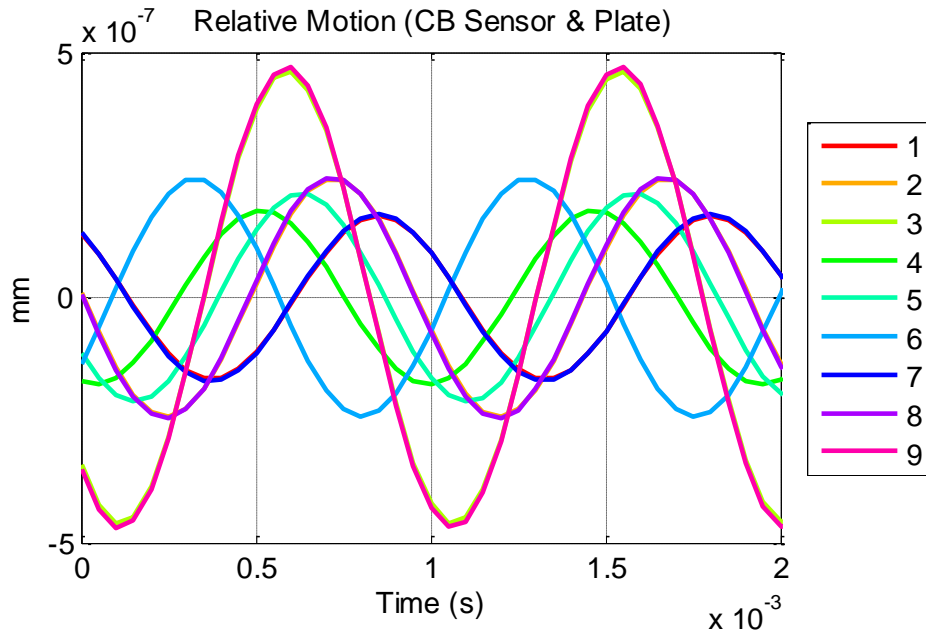


Figure 5.22: Modeled relative displacement between the *CB* sensors and the plate due to an acoustic source at $|\vec{R}| = 0.2032\text{m}$, $\theta = 90^\circ$, and $\varphi = 45^\circ$.

The consequence of these results is that the output from the *CB* sensors alone cannot be used to identify the location of an acoustic source. The following section details how the *CB* sensors can be used, in conjunction with other information, to successfully execute this task.

5.4 Acoustic Source Localization Method (CB Sensor Array)

Recall from Section 4.5 that acoustic source localization process relies on being able to determine the input pressure force on the *CB* sensory array. The input pressure force on the modeled *CB* sensors can be calculated by plugging the results from Section 5.3 into equation (4.5.3). Figure 5.23 and Figure 5.24 present the input pressure forces calculated for the (2) *CB* source location cases presented in Table 5.1.

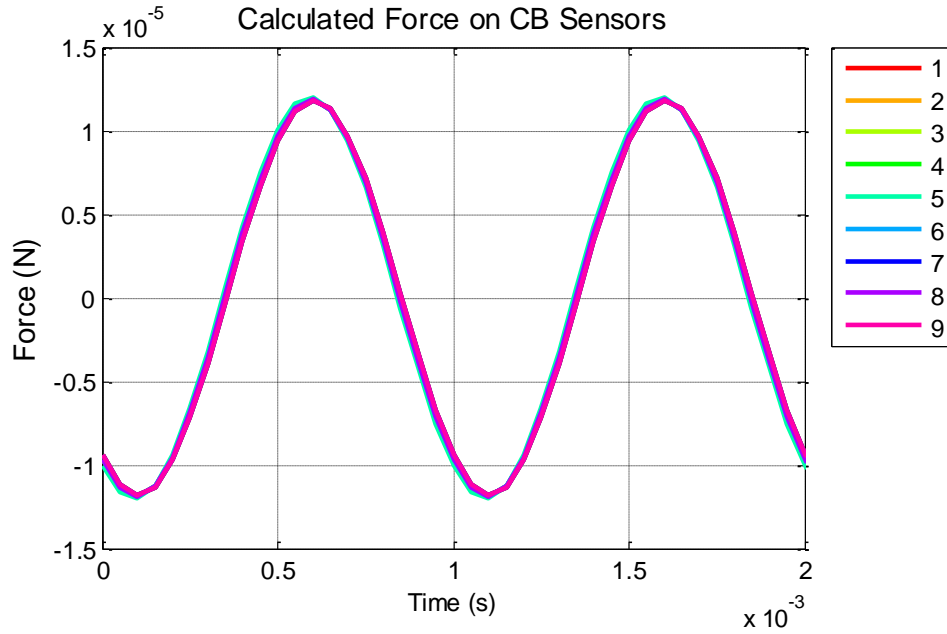


Figure 5.23: Calculated input force on the *CB* sensors due to an acoustic source at $\left| \vec{R} \right| = 0.2032\text{m}$, $\theta = 0^\circ$, and $\varphi = 0^\circ$.

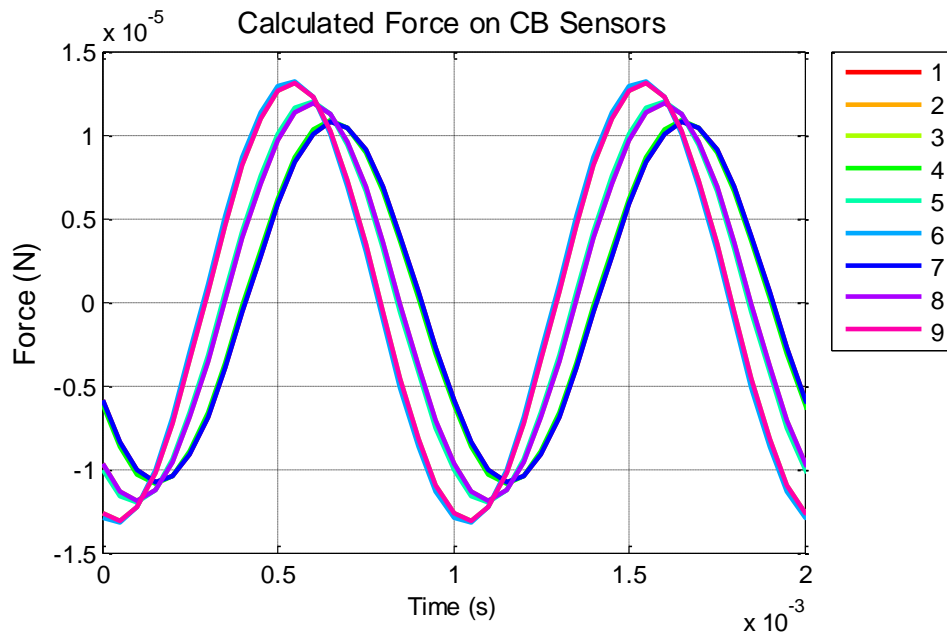


Figure 5.24: Calculated input force on the *CB* sensors due to an acoustic source at $\left| \vec{R} \right| = 0.2032\text{m}$, $\theta = 90^\circ$, and $\varphi = 45^\circ$.

The results show good agreement with the modeled results of the pressure distributions presented in Figure 5.4 and Figure 5.6. The outputs from this equation can then be used in equation (1.3.9), for an array of assumed source locations, to

calculate the maximum output power of the array processor. The source locations are assumed to be at $|\vec{R}|=0.2032\text{m}$, $\theta=0^\circ$ to 360° with 1° spacing, and $\Phi=0^\circ$ to 90° with 1° spacing. Figure 5.25 through Figure 5.28 illustrate the results of array processing the calculated pressure forces acting on the *CB* sensors for each of the (2) *CB* source locations cases presented in Table 5.1.

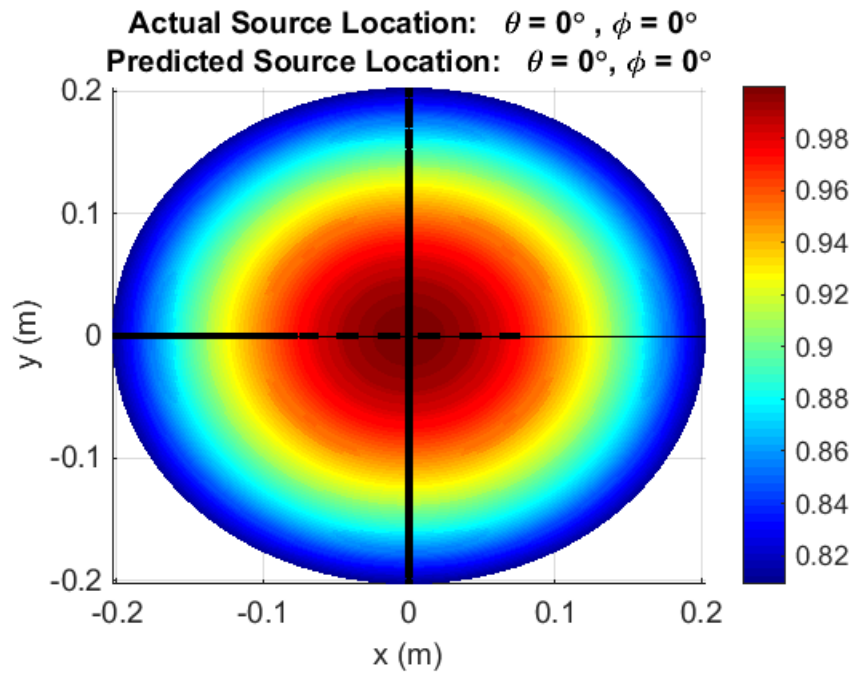


Figure 5.25: Acoustic source localization of a source at $|\vec{R}| = 0.2032\text{m}$, $\theta = 0^\circ$, and $\phi = 0^\circ$ using an array of pressure force data.

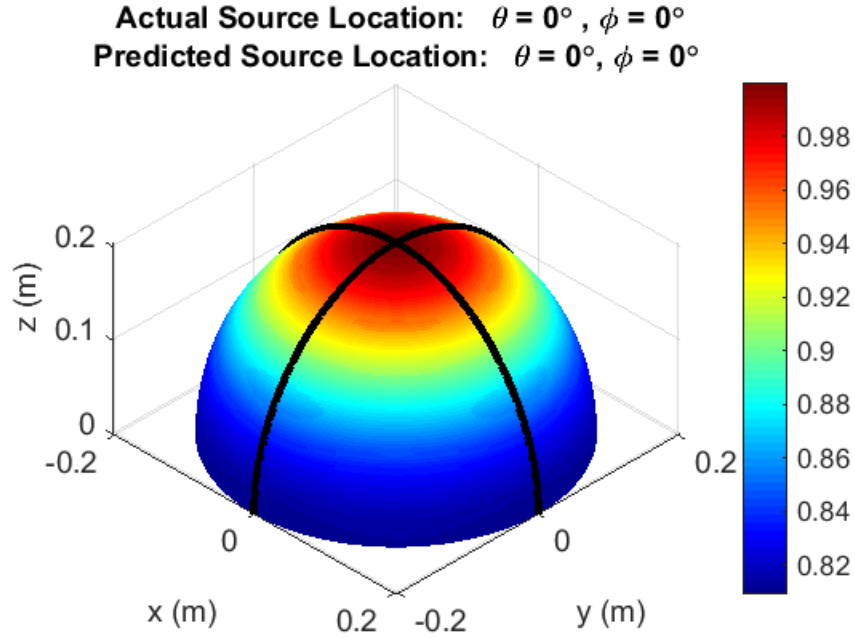


Figure 5.26: Acoustic source localization of a source at $|\vec{R}| = 0.2032\text{m}$, $\theta = 0^\circ$, and $\phi = 0^\circ$ using an array of pressure force data

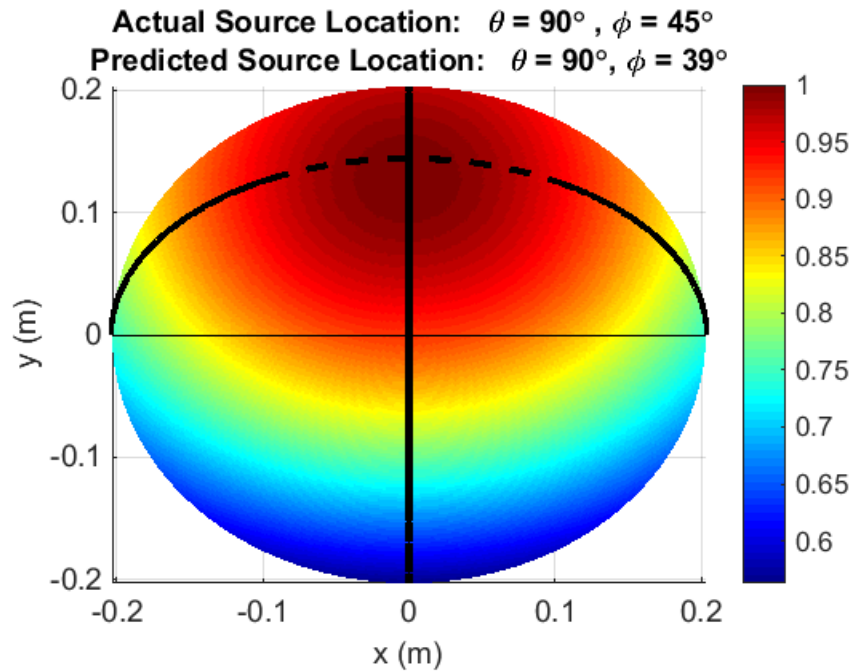


Figure 5.27: Acoustic source localization of a source at $|\vec{R}| = 0.2032\text{m}$, $\theta = 90^\circ$, and $\phi = 45^\circ$ using an array of pressure force data.

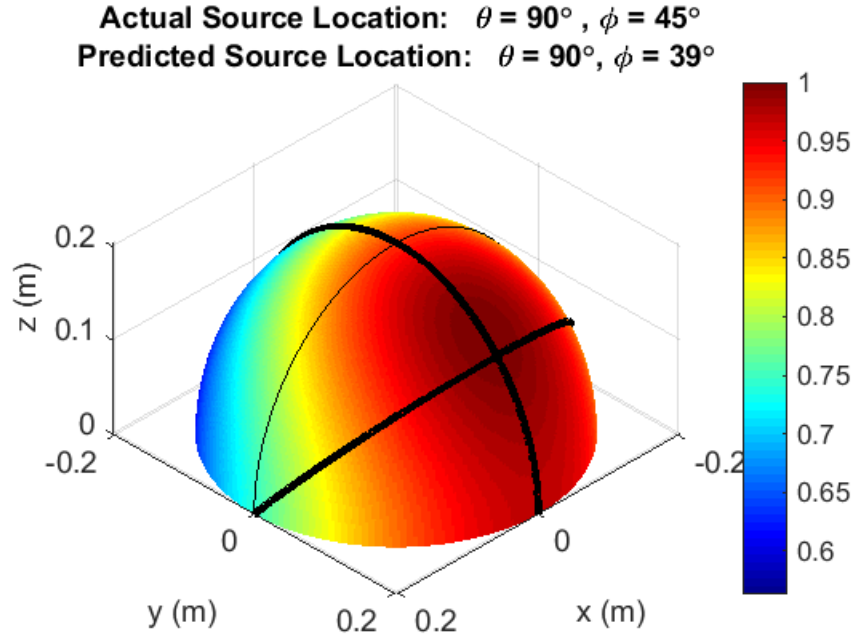


Figure 5.28: Acoustic source localization of a source at $|\vec{R}| = 0.2032\text{m}$, $\theta = 90^\circ$, and $\phi = 45^\circ$ using an array of pressure force data.

The results are similar to the results calculated in Section 5.2 for the array of conventional pressure sensors. Consequently, with knowledge of the relative motion ($\Delta w_{CB,n}$) between the *CB* sensor and the plate, the absolute motion ($w_{plate,n}$) of the plate, and the material properties of the *CB* sensor, there should be enough information to identify the location of an acoustic source.

Chapter 7 presents the experimental results of using an array of *CB* sensors to identify the location of an acoustic source. Experimentally, the voltage measured by the *CB* sensor can be used to estimate the strain of the *CB* sensor, which is directly related to the relative motion ($\Delta w_{CB,n}$) between the *CB* sensor and the plate. The absolute motion of the plate ($w_{plate,n}$) was determined using a Laser Doppler Vibrometer.

5.5 Summary

Chapter 5 successfully expands on the results from Chapter 4, and demonstrates analytically that if the following (4) quantities of the system are known, the input force applied to each *CB* sensor, due to an acoustic source, can be determined using Equation (4.5.3):

5. *Stiffness* ($k_{CB,n}$) of the *CB* sensor
6. *Mass* ($m_{CB,n}$) of the *CB* sensor
7. *Relative motion* ($\Delta w_{CB,n}$) between the *CB* sensor and the plate
8. *Absolute motion* ($w_{plate,n}$) of the plate

Furthermore, this chapter demonstrates that if the input force on the *CB* sensors is known, this information can be manipulated using array processing techniques to identify the location of the acoustic source. This process is applied to experimental data in Chapter 7.

Chapter 6: Acoustic Source Localization Experiment (Condenser Microphone Array)

The purpose of this Chapter is to demonstrate that acoustic source localization can be successfully performed using the array processing technique described in Chapter 1. In this demonstration, an electromagnetic speaker was used as the acoustic source, and a condenser microphone was used as the receiver. The speaker and receivers were placed at the same locations used in the *CB* sensor acoustic source localization experiment. In the *CB* sensor experiment presented in Chapter 8, (9) *CB* sensors comprised the receiver array. In the condenser microphone demonstration, a single condenser microphone was utilized. To generate an array of results, (9) separate experiments were conducted with the same speaker output. In each experiment, the condenser microphone was moved to one of the (9) different *CB* sensor locations. The following sections detail the setup and results of the condenser microphone acoustic source localization experiment.

6.1 Experimental Setup

The condenser microphone acoustic source localization experiment involved using a condenser microphone to measure the incident pressure waves created by an electromagnetic speaker. This experiment was repeated a total of (9) times as the condenser microphone was moved to each of the (9) locations of the *CB* sensors. In each experiment, the following (4) signals were measured and recorded:

- Condenser microphone output signal
- Pilot signal of the electromagnetic speaker
- Reference microphone signal (x2)

The pilot signal was measured to provide a reference for the output signal from the acoustic source, and was critical to generating an array of pressure sensor measurements from the (9) individual condenser microphone experiments. Further details of the importance of the pilot signal are discussed in Section 6.2. The purpose of the (2) reference microphones in the condenser microphone test was to provide the data used in Chapter 5 to validate the assumption of the type of source in the acoustic model.

Figure 6.1 below presents a photo of the condenser microphone experimental setup. Figure 6.2 presents a detailed system diagram of the experimental setup.

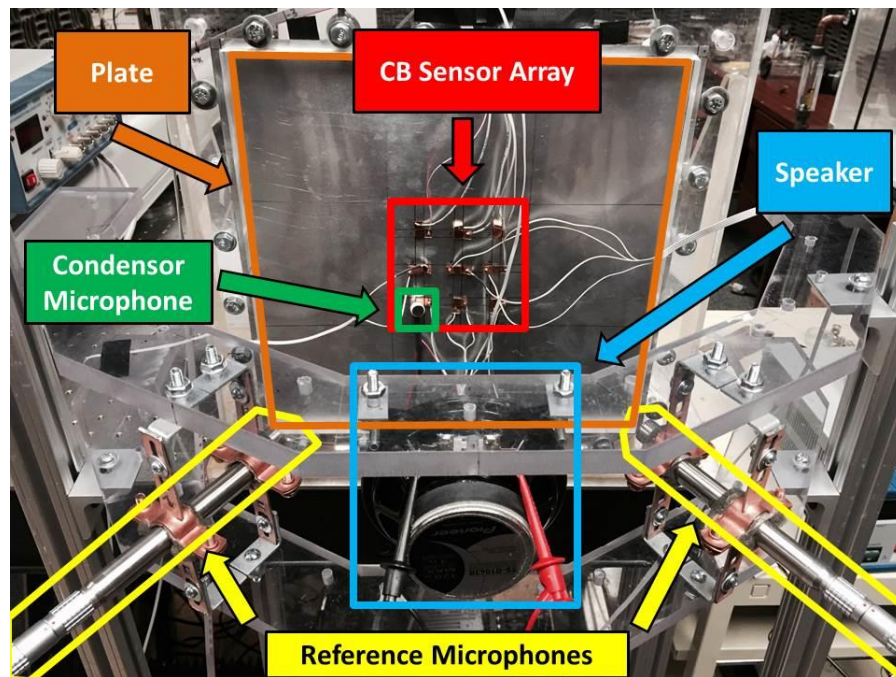


Figure 6.1: Photo of condenser microphone experiment setup.

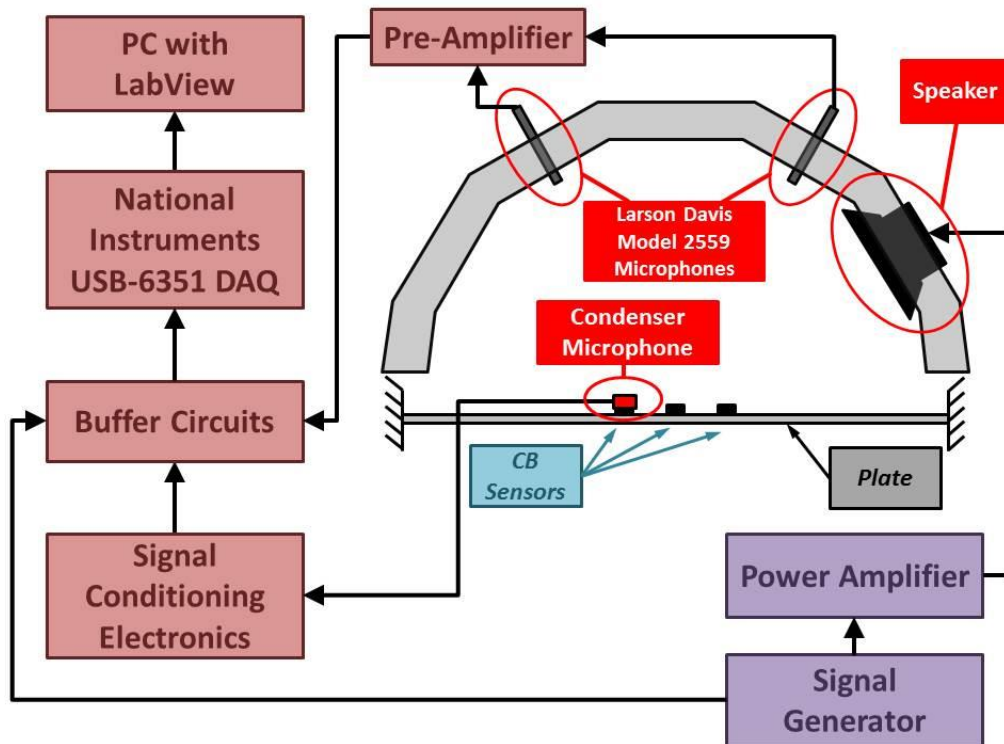


Figure 6.2: Condenser microphone experiment system diagram.

The speaker was driven by a 1050 Hz sine wave, which was generated by a signal generator and amplified by a power amplifier. The Larson Davis Model 2559 reference microphones were powered and conditioned by a Larson Davis pre-amplifier. The circuit used to power and condition the output signal from the condenser microphone is illustrated below in Figure 6.2.

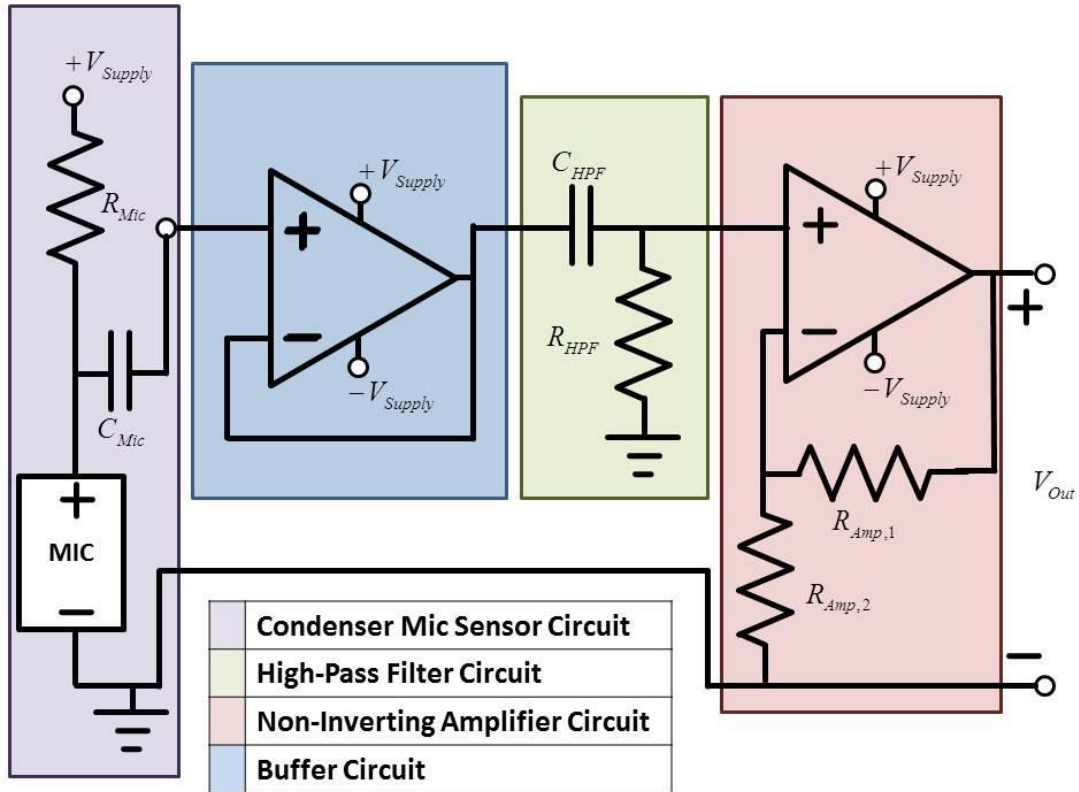


Figure 6.3: Condenser microphone signal conditioning electronics circuit diagram.

The signal conditioning of the condenser microphone signal consisted of an op-amp buffer circuit to isolate the microphone from the rest of the electronic components, a high-pass filter to eliminate any DC offset signal, and a non-inverting amplifier op-amp circuit to increase the signal-to-noise ratio (SNR). The values of the components illustrated in Figure 6.2 are presented below in Table 6.1.

Table 6.1: Condenser microphone signal conditioning circuit component values.

ELECTRICAL COMPONENT	VALUE
$+V_{Supply}$	9 V
$-V_{Supply}$	9 V
R_{Mic}	1 k Ω
C_{Mic}	975 nF
R_{HPF}	10 k Ω
C_{HPF}	468 nF
$R_{Amp,1}$	100 k Ω
$R_{Amp,2}$	10 k Ω

The pilot signal from the signal generator, the reference microphone signals, and the condenser microphone signal were recorded using a National Instruments USB-6351 data acquisition system (DAQ). Additional op-amp buffer circuits were implemented at the input of the DAQ to prevent the (4) input signals from overloading the DAQ. The (4) input signals were sampled at a rate of 20 kHz. Additionally, all of the recorded data was digitally band-pass filtered between 900 Hz and 1200 Hz. The following section presents the results of the condenser microphone acoustic source localization experiment.

6.2 Results

Only one condenser microphone was used during this experiment. To create an array of condenser microphone data, (9) separate experiments were conducted, referred to herein as (9) separate “runs”. During each run, the output signal to the speaker was the same, and the condenser microphone was moved to each of the (9) *CB* sensor locations. First consider the case where the speaker was located at $|\vec{R}| = 0.2032\text{m}$, $\theta = 0^\circ$, and $\varphi = 0^\circ$. Figure 6.4 presents the raw pilot signal data to the speaker for the (9) different runs for this case.

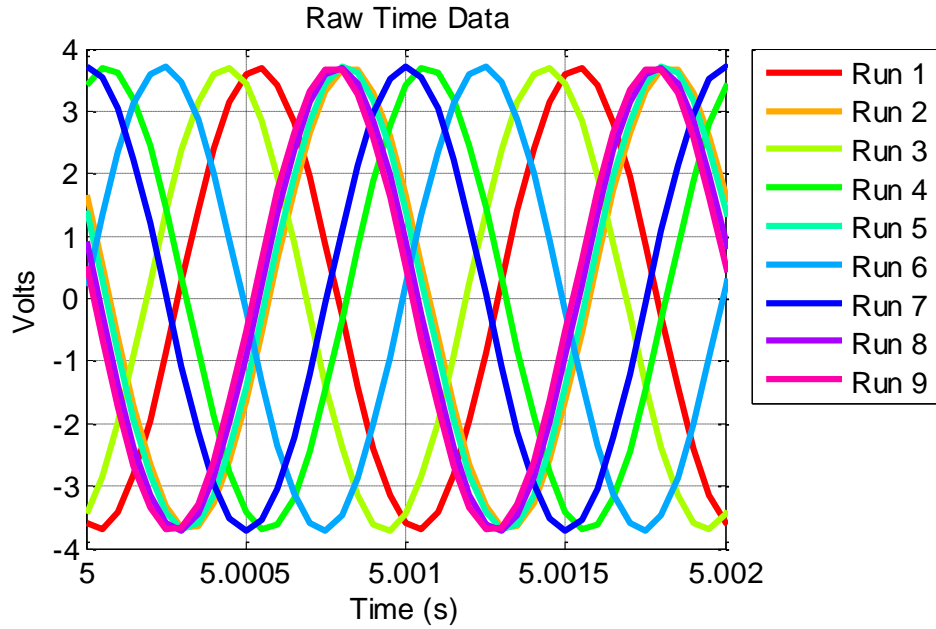


Figure 6.4: Condenser Microphone experiment raw pilot signal for source at $|\vec{R}| = 0.2032\text{m}$, $\theta = 0^\circ$, and $\varphi = 0^\circ$.

The phase delay evident in Figure 6.6 is an artifact of the recording window of each run. Figure 6.5 illustrates an example of this artifact.

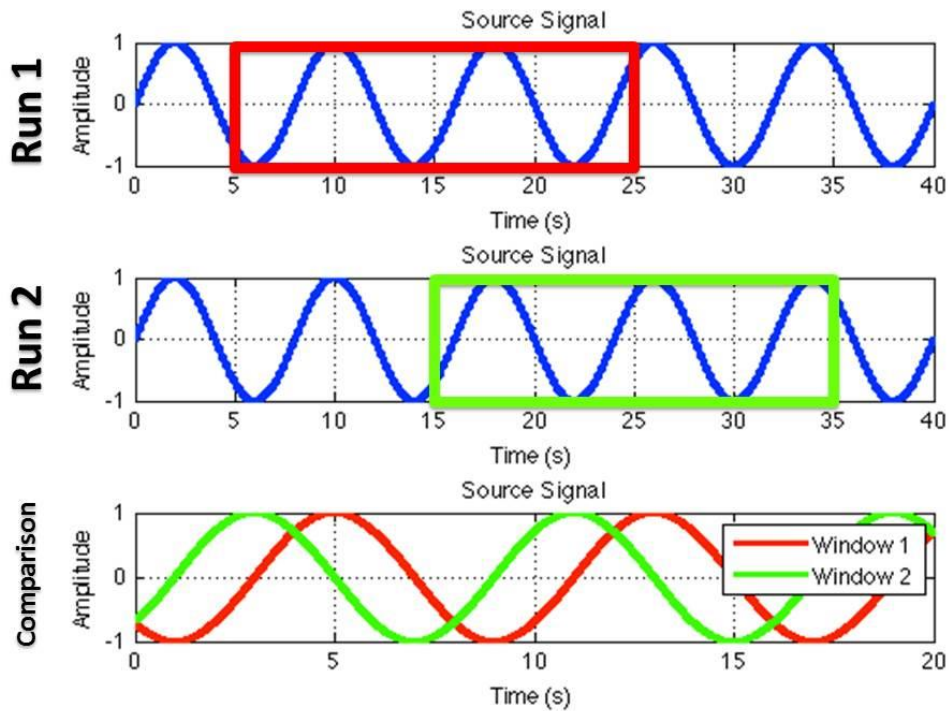


Figure 6.5: Pilot signal phase delay artifact based on data recording window.

Figure 6.5 illustrates that even though the signals in Run 1 and Run 2 start at the same time, there is an artificial phase delay between the 20 second recorded signals from the two runs due to when each recording window occurred. For the experimental data, the artificial phase delay between Runs 2-9 and Run 1 can be calculated and removed from the pilot signal data.

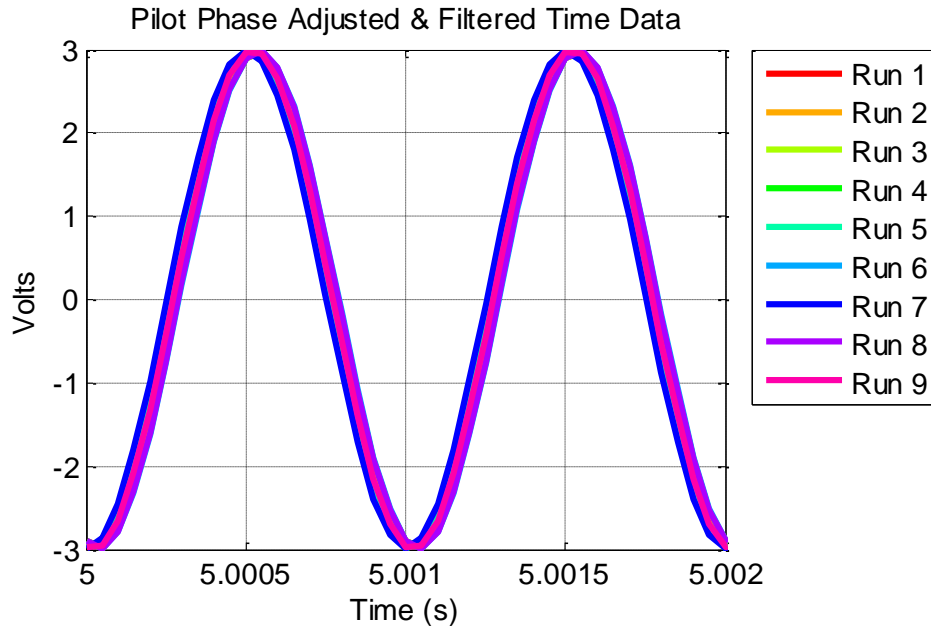


Figure 6.6: Condenser microphone experiment pilot phase adjusted & filtered pilot signal for source at $|\vec{R}| = 0.2032\text{m}$, $\theta = 0^\circ$, and $\phi = 0^\circ$.

Figure 6.7 presents the raw condenser microphone data for the (9) runs. This data can be directly compared to modeled results presented in Figure 5.4. A comparison of the two figures indicates that the raw experimental data does not agree with the modeled data. However, if the phase delay's calculated from the pilot signal data are removed from the condenser microphone data, the experimental data agrees with the modeled data. Figure 6.8 presents the experimental condenser microphone results with the pilot phase delay's removed.

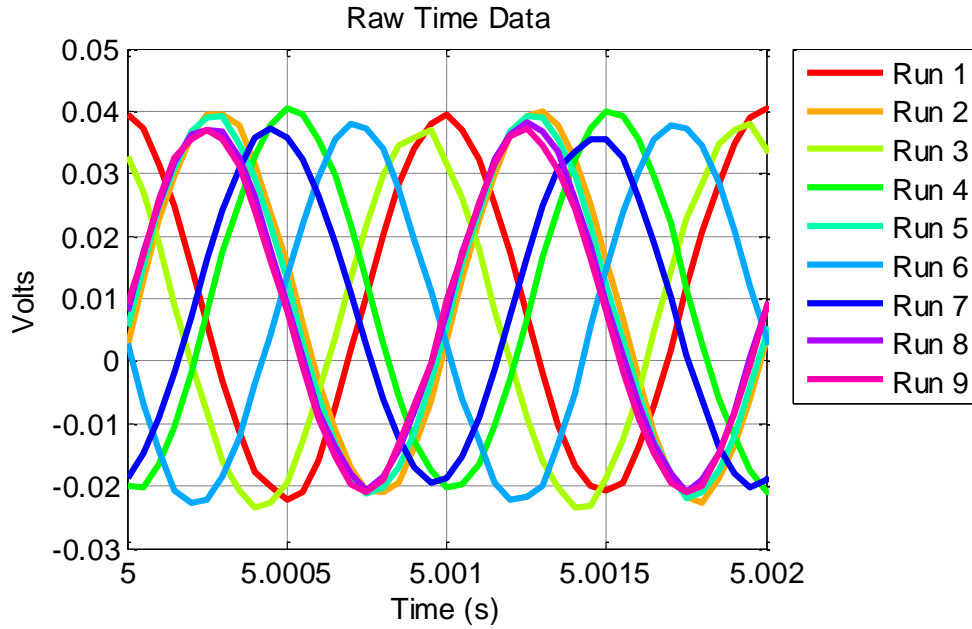


Figure 6.7: Condenser microphone experiment raw CM data for source at $|\vec{R}| = 0.2032\text{m}$, $\theta = 0^\circ$, and $\varphi = 0^\circ$.

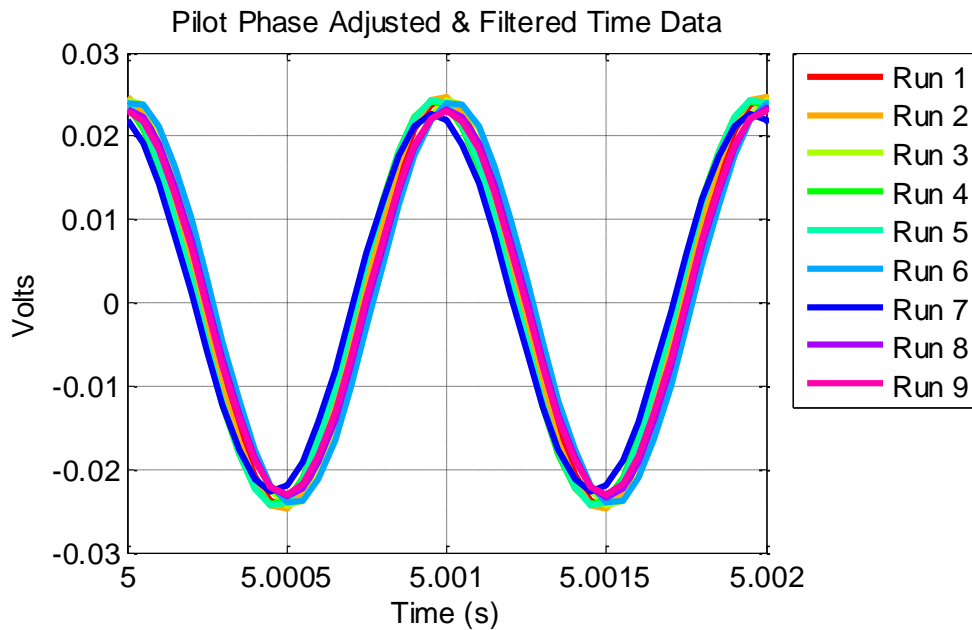


Figure 6.8: Condenser microphone experiment pilot phase adjusted & filtered CM data for source at $|\vec{R}| = 0.2032\text{m}$, $\theta = 0^\circ$, and $\varphi = 0^\circ$.

Figure 6.9 and Figure 6.10 present the results of array processing the pilot signal phase-adjusted condenser microphone signals.

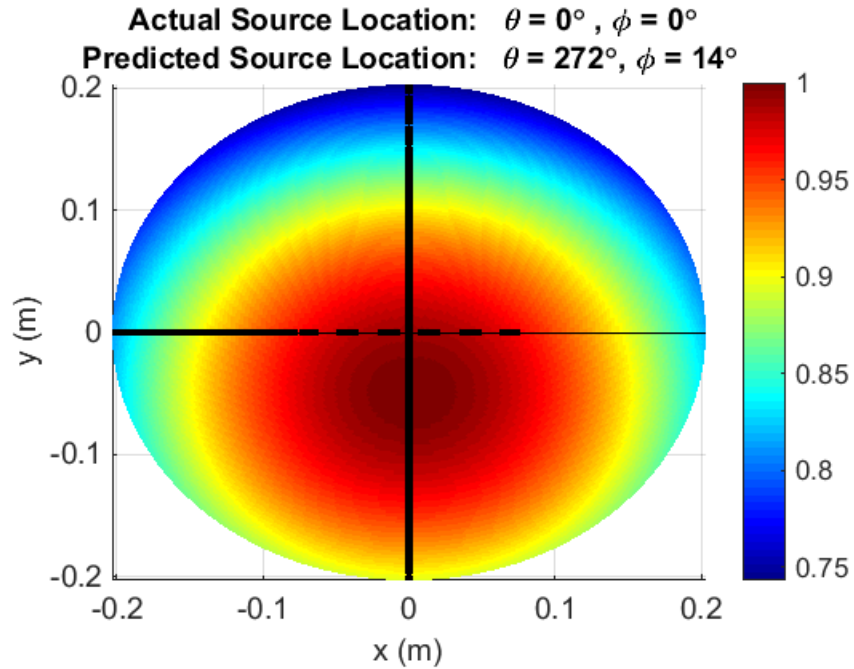


Figure 6.9: Acoustic source localization of a source at $|\vec{R}| = 0.2032\text{m}$, $\theta = 0^\circ$, and $\phi = 0^\circ$ using an array of measured CM sensor data.

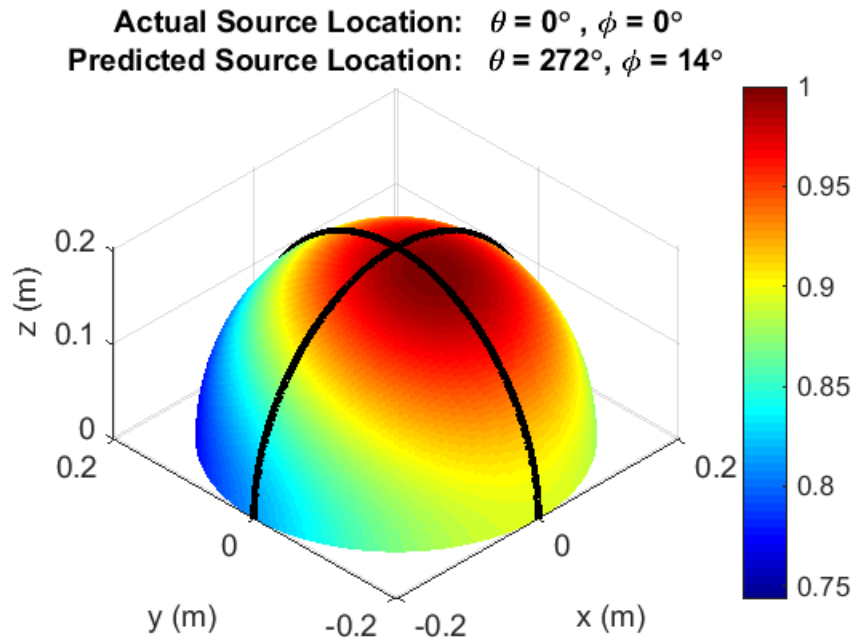


Figure 6.10: Acoustic source localization of a source at $|\vec{R}| = 0.2032\text{m}$, $\theta = 0^\circ$, and $\phi = 0^\circ$ using an array of measured CM sensor data.

Comparison of these results to the modeled results in Figure 5.13 and Figure 5.14 indicates good agreement between the modeled and experimental data for the case where the speaker was located at $|\vec{R}| = 0.2032\text{m}$, $\theta = 0^\circ$, and $\varphi = 0^\circ$.

A similar procedure can be followed for the case where the speaker was located at $|\vec{R}| = 0.2032\text{m}$, $\theta = 120^\circ$, and $\varphi = 60^\circ$. Figure 6.11 Figure 6.16

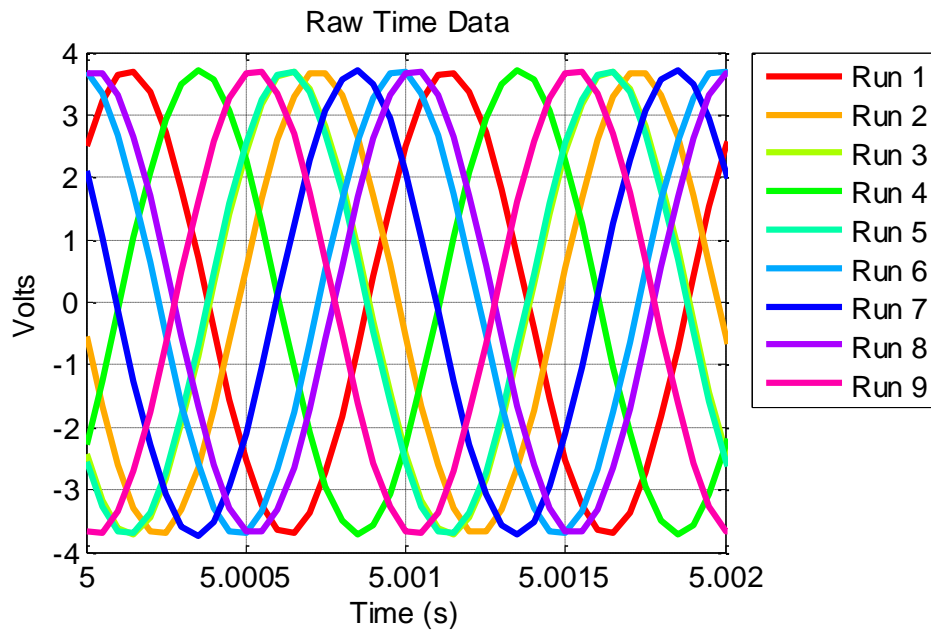


Figure 6.11: Condenser microphone experiment raw pilot signal for source at $|\vec{R}| = 0.2032\text{m}$, $\theta = 120^\circ$, and $\varphi = 60^\circ$.

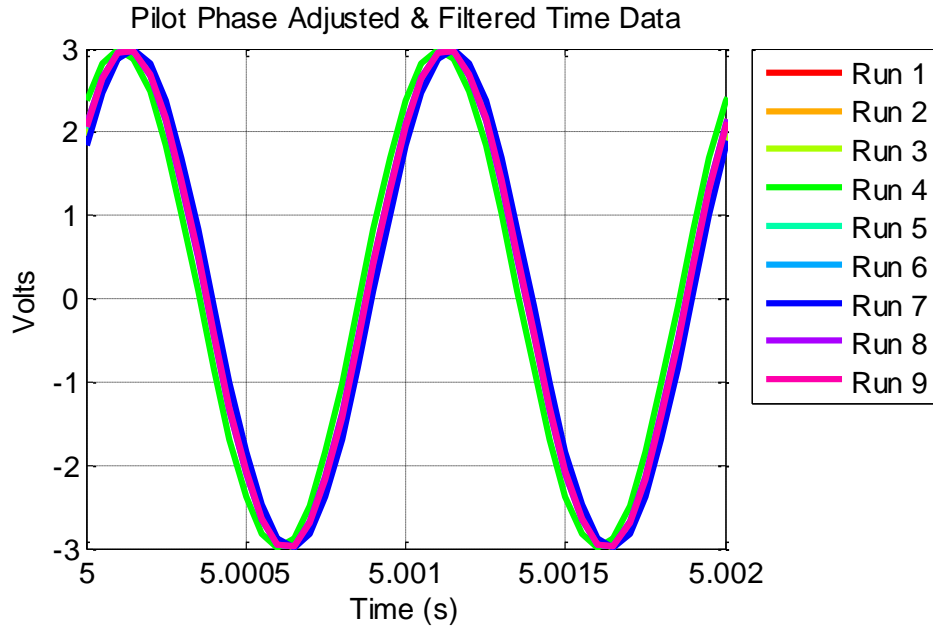


Figure 6.12: Condenser microphone experiment pilot phase adjusted & filtered pilot signal for source at $|\vec{R}| = 0.2032\text{m}$, $\theta = 120^\circ$, and $\varphi = 60^\circ$.

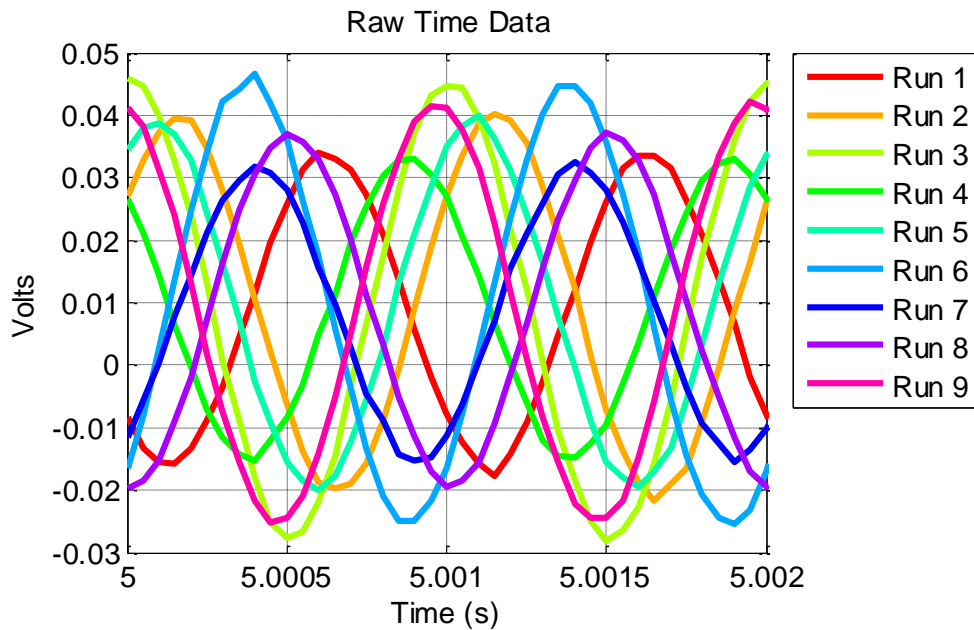


Figure 6.13: Condenser microphone experiment raw CM data for source at $|\vec{R}| = 0.2032\text{m}$, $\theta = 120^\circ$, and $\varphi = 60^\circ$.

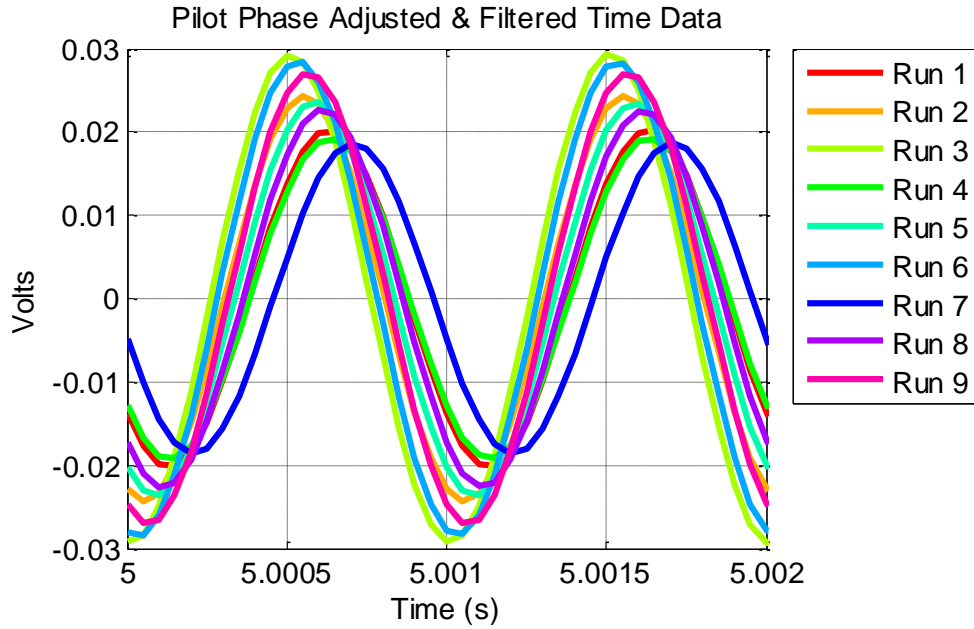


Figure 6.14: Condenser microphone experiment pilot phase adjusted & filtered CM data for source at $|\vec{R}| = 0.2032\text{m}$, $\theta = 120^\circ$, and $\phi = 60^\circ$.

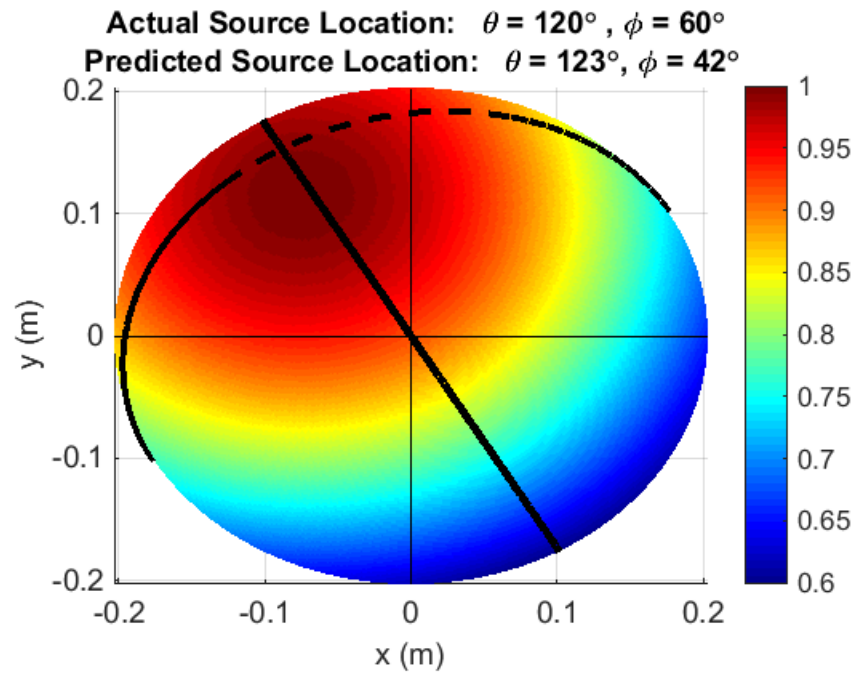


Figure 6.15: Acoustic source localization of a source at $|\vec{R}| = 0.2032\text{m}$, $\theta = 120^\circ$, and $\phi = 60^\circ$ using an array of measured CM sensor data.

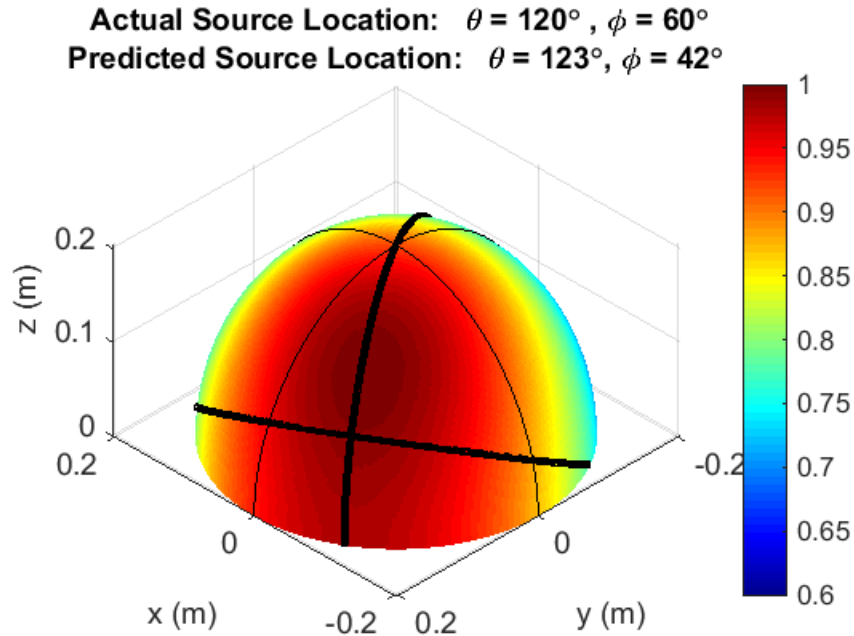


Figure 6.16: Acoustic source localization of a source at $|\vec{R}| = 0.2032\text{m}$, $\theta = 120^\circ$, and $\phi = 60^\circ$ using an array of measured CM sensor data.

The figures indicate that for this case, there is also an artificial phase delay in the pilot signal data associated with the recording window from each run. However, once this phase delay is removed from the condenser microphone data, the temporal results agree with the modeled results presented in Figure 5.8. Similarly, the array processing results presented in Figure 6.15 and Figure 6.16 agree reasonably well with the modeled results presented in Figure 5.13 and Figure 5.14.

6.3 Summary

Chapter 6 demonstrates that acoustic source localization can be successfully performed with an array of condenser microphones using the same array geometry as the *CB* sensor experiment. Chapter 7 presents the experimental results of attempting to use the array of *CB* sensors to perform the same acoustic source localization.

Chapter 7: Acoustic Source Localization (Carbon Black Sensors)

The purpose of this Chapter is to present the results from using an array of *CB* filled polyurethane sensors to identify the location of an air horn. Section 4.5 demonstrated that the acoustic source localization process relies on being able to determine the input pressure force on the *CB* sensory array. Equation (4.5.3) indicates that if the following (4) quantities of the system are known, the *Input Force* applied to each *CB* sensor can be determined:

1. *Stiffness* ($k_{CB,n}$) of the *CB* sensor
2. *Mass* ($m_{CB,n}$) of the *CB* sensor
3. *Relative motion* ($\Delta w_{CB,n}$) between the *CB* sensor and the plate
4. *Absolute motion* ($w_{plate,n}$) of the plate

In this experiment, the *Stiffness* ($k_{CB,n}$) and *Mass* ($m_{CB,n}$) of the *CB* sensor was calculated using equation (4.3.1) and (4.3.2). The *Absolute Motion* ($w_{plate,n}$) of the plate was measured using a Laser Doppler Vibrometer (LDV). The *Relative motion* ($\Delta w_{CB,n}$) between the *CB* sensor and the plate was determined using the output of the *CB* sensors.

Recall that (1.2.1) represents a linear approximation of the relationship between the *Strain* (ϵ), and *Change in Resistivity* ($\Delta R/R$), of the *CB* sensor material. The *Relative motion* ($\Delta w_{CB,n}$) between the *CB* sensor and the plate can be written in terms of the *Strain* (ϵ), and un-deformed thickness of the *CB* sensor (l_o) as follows:

$$\Delta w_{CB,n} = \mathcal{E}l_0 + l_0 \quad (7.1)$$

The change in resistance of the *CB* sensor can be measured by using a voltage divider circuit, illustrated in Figure 7.1.

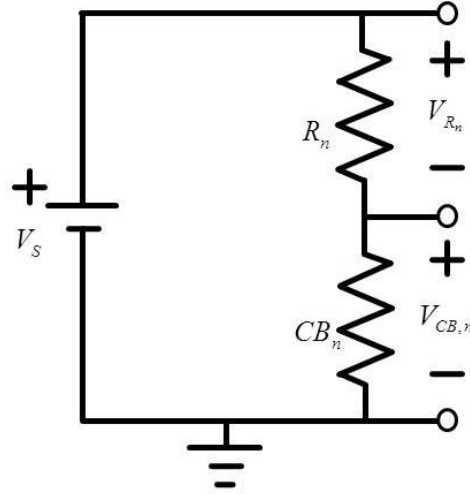


Figure 7.1: *CB* sensor voltage divider circuit.

In Figure 7.1, CB_n is the resistance of the *CB* sensor, R_n is the resistance of the voltage divider resistor, $V_{CB,n,0}$ is the baseline voltage measured across the *CB* sensor, $V_{R,n}$ is the baseline voltage measured across the voltage divider resistor, and V_s is the supply voltage. As the *CB* sensor is compressed, the voltage across the *CB* sensor becomes $V_{CB,n}$. Analyzing the circuit in Figure 7.1, and calculating the change in voltage ΔV between the baseline voltage across the *CB* sensor ($V_{CB,n,0}$), and the voltage when the *CB* sensor is compressed ($V_{CB,n}$), yields the following equation:

$$\frac{CB_{CB,n} - CB_{CB,n,0}}{CB_{CB,n,0}} = \frac{\Delta CB_{CB,n}}{CB_{CB,n,0}} = \frac{(V_{CB,n} - V_{CB,n,0}) (R_n / CB_{CB,n,0})}{V_s} \quad (7.2)$$

Notice that the left-hand-side of equation (7.2) is similar to the right-hand-side of equation (1.2.1). Plugging equation (7.2) into equation (1.2.1) yields the following:

$$\varepsilon \cong \frac{(V_{CB,n} - V_{CB,n,0})(R_n / CB_{CB,n,0})}{\bar{\gamma}V_s} \quad (7.3)$$

Plugging equation (7.3), into equation (7.1), yields the following relationship between the voltage measured across the *CB* sensor, and the relative motion between the *CB* sensor and the plate.

$$\Delta w_{CB,n} \cong \frac{(V_{CB,n} - V_{CB,n,0})(R_n / CB_{CB,n,0})}{\bar{\gamma}V_s} + l_0 \quad (7.4)$$

The following sections detail the experimental setup, the acoustic source selection process, comparison of the experimental setup to the model presented in Chapter 4, and an analysis of the measured data.

7.1 Experimental Setup

7.1.1 Setup Details

A Laser Doppler Vibrometer measured the motion of the plate where the *CB* sensor array was installed. The LDV could only measure the response of the plate at one location at a time. Consequently, the experiment was repeated (9) times as the LDV was directed to each of the (9) locations of the *CB* sensors. In each experiment, referred to herein as a “run”, the following signals were measured and recorded:

- *CB* sensor output signal (x9)
- LDV output signal
- Reference microphone signal (x2)

The LDV output signal was measured in order to have enough information to solve equation (4.5.1) and determine the input pressure force acting on each *CB* sensor. Similar to the condenser microphone experiment, the purpose of the (2) reference microphones in the condenser microphone test was to provide the data used in Chapter 5 to validate the assumption of the type of source in the acoustic model. However, the primary purpose of the reference microphones in the *CB* sensor experiment was to act as a pseudo pilot signal for the air horn source since the air horn does not have an electrical signal driving it.

Figure 7.2 through Figure 7.5 present photos of the *CB* sensor experimental setup. Figure 7.6 presents a detailed system diagram of the experimental setup.

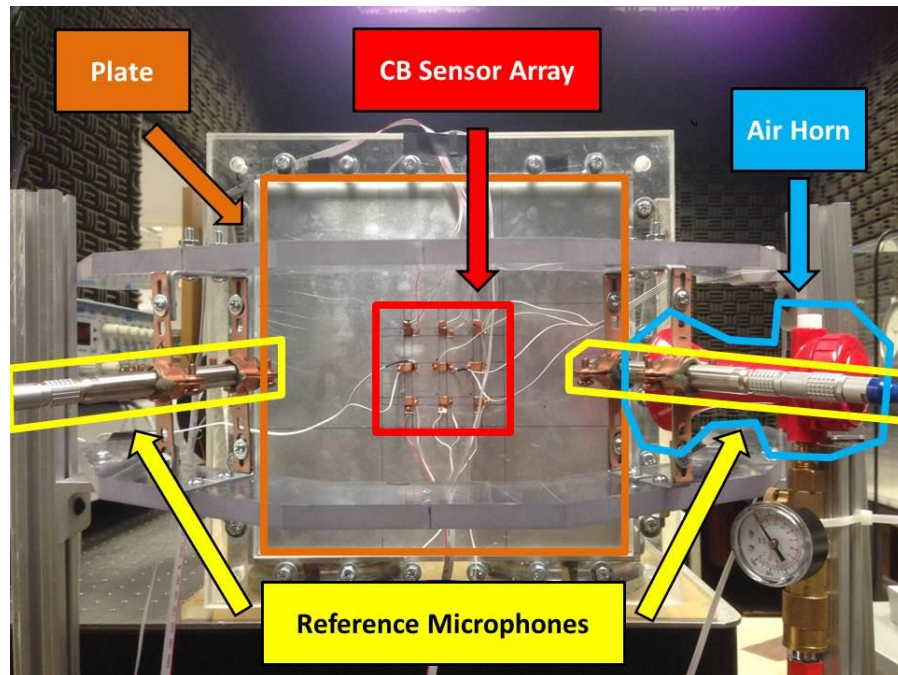


Figure 7.2: Photo of *CB* sensor experiment setup (View 1).

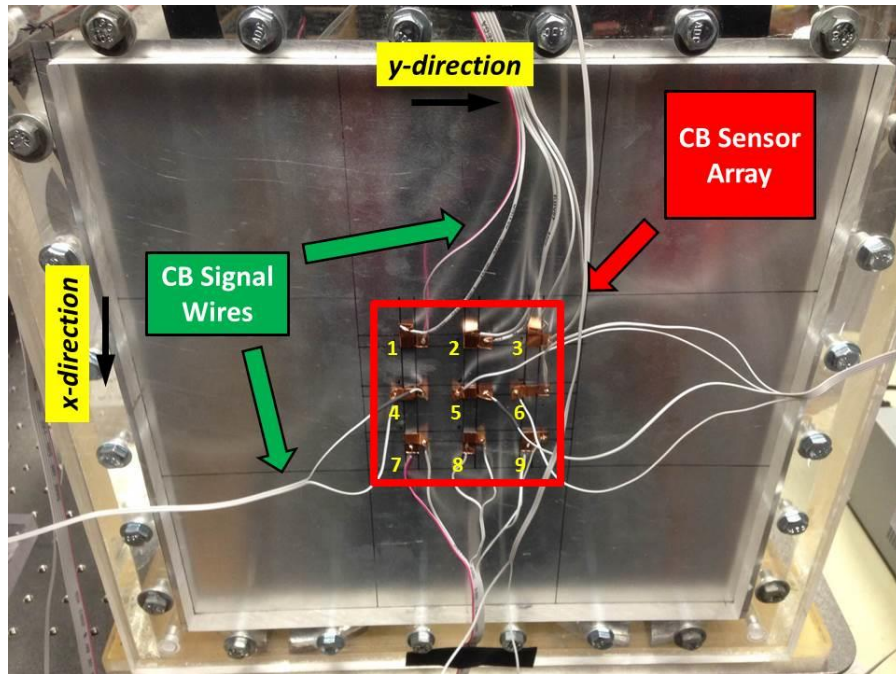


Figure 7.3: Photo of CB sensor experiment setup (View 2).

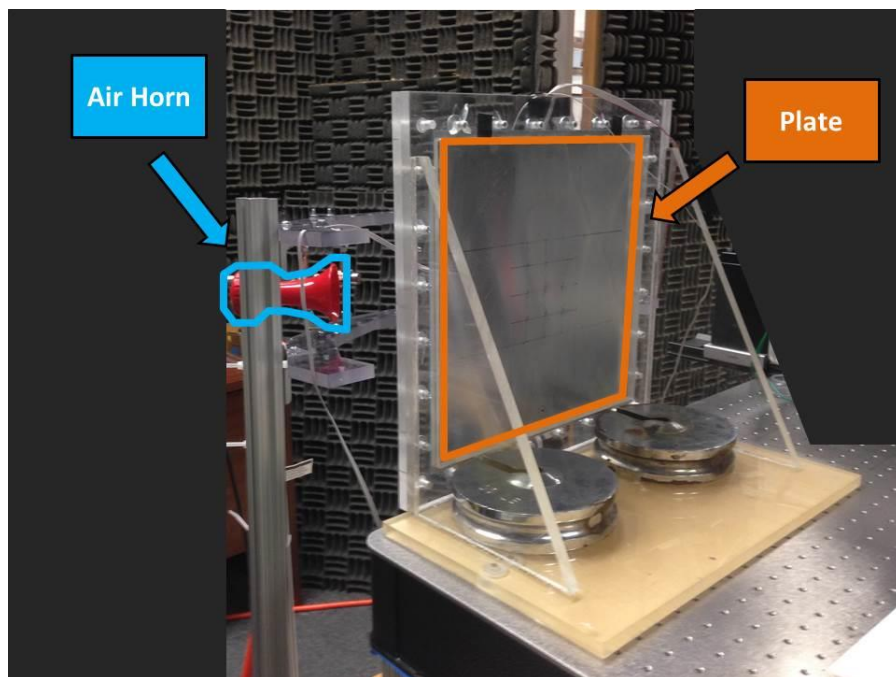


Figure 7.4: Photo of CB sensor experiment setup (View 3).

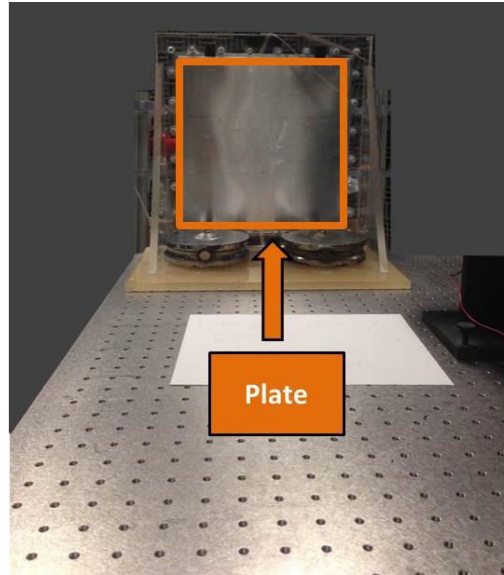


Figure 7.5: Photo of *CB* sensor experiment setup (View 4).

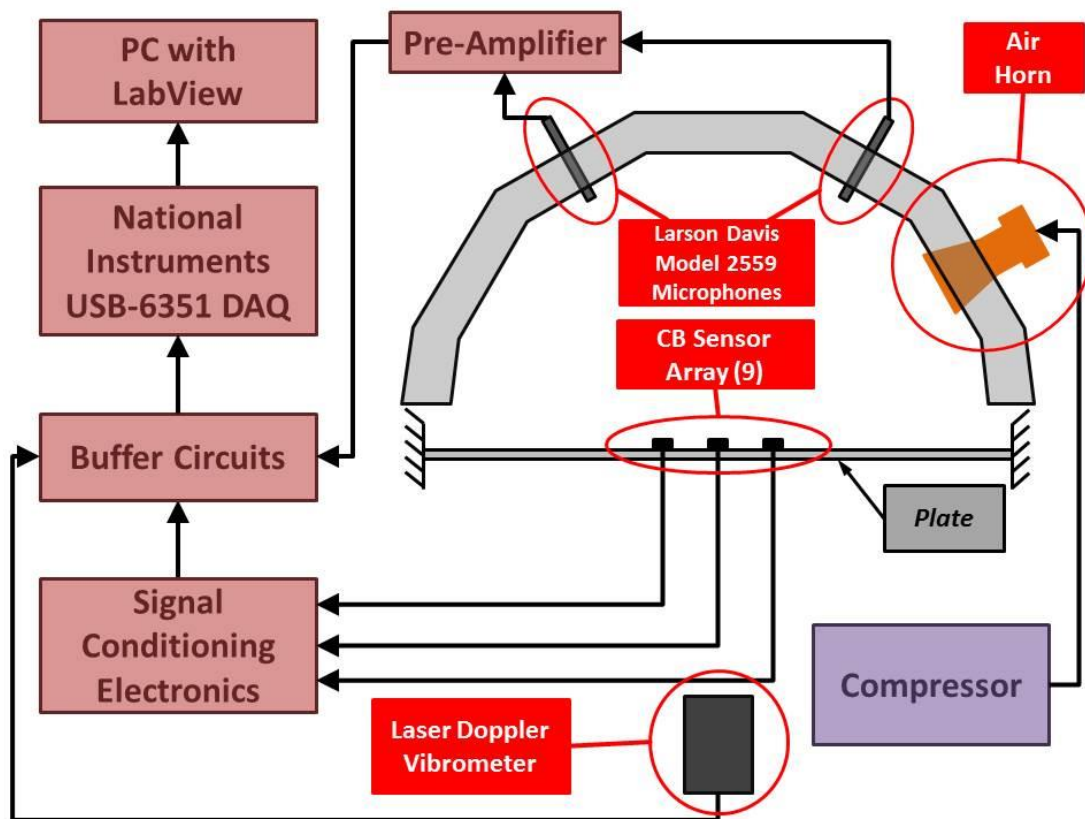


Figure 7.6: *CB* sensor experiment system diagram.

The acoustic source in the *CB* experiment was provided by an air-horn driven by a 1HP, 8 Gallon compressor. A photo of the compressor is presented below in

Figure 7.7. Section 7.1.2 provides a background on the selection of an air-horn as the acoustic source.



Figure 7.7: Compressor used to drive the air-horn.

The Larson Davis Model 2559 reference microphones in Figure 7.6 were powered and conditioned by a Larson Davis pre-amplifier. The LDV was powered and controlled by a Polytec Model OFV 3001 S Vibrometer Controller. Figure 7.8 and Figure 7.9 present the electrical circuits used to power and condition the (9) *CB* sensors. Table 7.1 presents the values of the electrical components that comprise these various circuits.

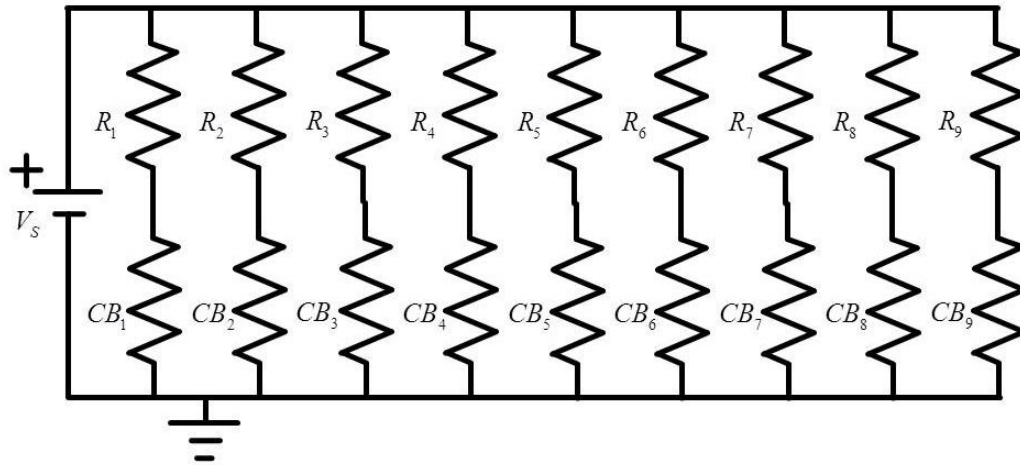


Figure 7.8: *CB* sensor voltage divider circuit.

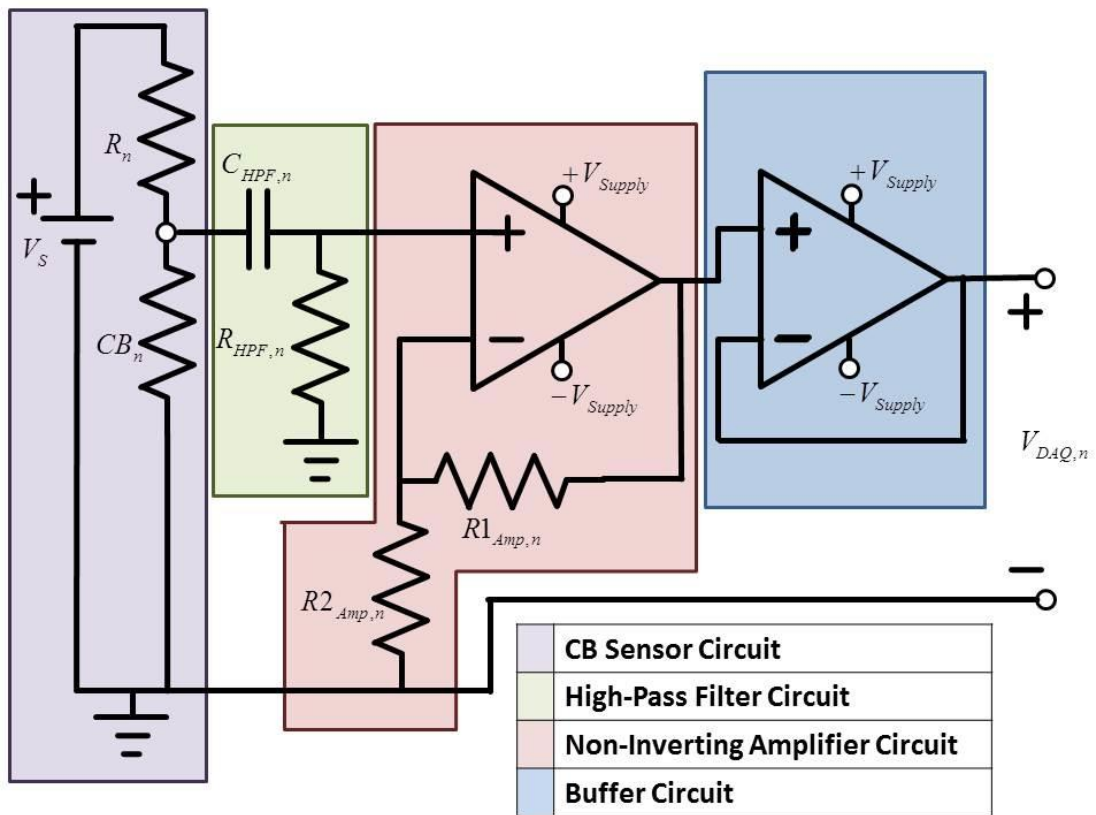


Figure 7.9: Individual *CB* sensor signal conditioning circuit diagram.

Table 7.1: *CB* sensor signal condition element values.

<i>CB</i> Sensor	R_n (kΩ)	CB_n (kΩ)	$C_{HPF,n}$ (μF)	$R_{HPF,n}$ (kΩ)	$R1_{Amp,n}$ (kΩ)	$R2_{Amp,n}$ (kΩ)
1	99.80	6.34	0.48	9.95	0.01	9.96
2	99.40	6.00	0.48	9.95	0.01	9.96
3	100.00	0.86	0.48	9.95	0.01	9.96
4	99.40	3.20	0.48	9.95	0.01	9.96
5	99.70	1.40	0.48	9.95	0.01	9.96
6	100.10	1.37	0.48	9.95	0.01	9.96
7	99.80	0.78	0.48	9.95	0.01	9.96
8	99.70	2.45	0.48	9.95	0.01	9.96
9	99.30	2.73	0.48	9.95	0.01	9.96

Figure 7.8 illustrates that each of the *CB* sensors is part of a voltage divider circuit. Each of these voltage divider circuits is then connected in parallel with a voltage source to power the circuit. In this experiment, the power to the *CB* sensors was provided by a +5V DC power supply.

Figure 7.9 illustrates the signal conditioning circuit applied to each of the voltage divider circuits in Figure 7.8. There are (9) of these signal conditioning circuits, corresponding to each of the (9) *CB* sensors. The signal conditioning circuit consists of a high-pass filter, non-inverting amplifier, and a buffer. Reference [1] showed that the change in voltage potential across the *CB* sensor can be used to estimate the strain in the sensor. Therefore, the purpose of the signal conditioning circuit is to measure this signal. The strain in the *CB* sensors due to the air-horn source was shown in Chapter 5 to be very small. Therefore, the change in voltage potential between the *CB* sensor and ground will also be very small. Consequently, it was necessary to amplify the voltage signal measured between the *CB* sensor and ground by approximately 60dB to sufficiently increase its' level above the system

electrical noise. Signal amplification was provided by a non-inverting op-amp circuit.

Prior to amplification of the signal, a high-pass filter was applied to the voltage signal to remove the DC bias signal caused by the voltage divider circuit. This step was necessary because amplifying the signal with the DC bias signal would have exceeded the input voltage limits of the NI data acquisition (DAQ) system. A buffer circuit was applied between the non-inverting amplifier and the DAQ to isolate the sensor signals and also prevent over-loading the DAQ inputs.

Equation (7.4) voltage measured across the *CB* sensor, and the relative motion between the *CB* sensor and the plate. However, the signal measured by the DAQ system contains the influence of the signal conditioning circuitry. This influence was accounted for by disconnecting the *CB* sensors from the signal conditioning electronics, inputting a broadband voltage signal into the signal conditioning electronics, and then measuring the output voltage using the DAQ. This measurement provided a transfer function between the input and output of the signal conditioning electronics, which was subsequently applied to all of the measured data to determine the voltage at the *CB* sensors.

7.1.2 Selection of Acoustic Source

Initially, a 12 inch speaker was used as the acoustic source in the *CB* sensor experiment. The speaker was driven by a power amplifier and a 1 kHz sine wave signal generator. The auto-spectra of the *CB* sensor outputs were monitored live as

the amplifier signal was increased to determine a speaker output level sufficient to induce a measurable output from the *CB* sensors. Once a sufficient amplifier level was determined, the experiment was repeated over a 20-second period and the data was recorded. Figure 7.10 presents a time-frequency plot of the conditioned output voltage of a single *CB* sensor due to the speaker source. The speaker source was started 6 seconds into the 20 second experiment, and this is reflected in the data.

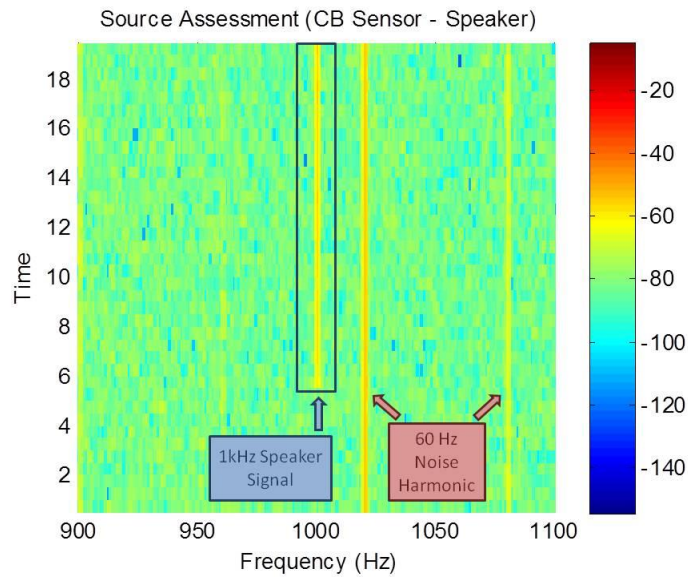


Figure 7.10: Time-frequency plot of a single *CB* sensor output voltage signal for a 1kHz speaker source.

Due to the large amount of amplification of the *CB* sensor signals, the high output of the speaker, and the unshielded nature of the *CB* sensor, an additional test was conducted to confirm that the signal measured by the *CB* sensor was due to the pressure wave produced by the speaker and not any electromagnetic interference. This experiment involved disconnecting the electrical leads from the *CB* sensor, exciting the system with a 1 kHz sine wave from the speaker, and measuring the voltage signal from the disconnected leads. Figure 7.11 presents a time-frequency

plot of the measured voltage signal. The signal was started 6 seconds into the 20 second experiment.

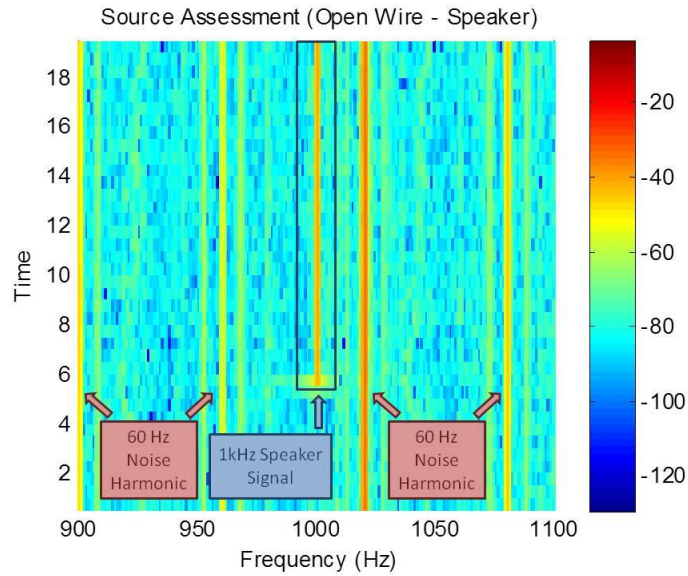


Figure 7.11: Time-frequency plot of a single *CB* sensor output voltage signal for a 1kHz speaker source, with the leads disconnected from the *CB* sensor.

Figure 7.11 indicates that the voltage signal across the *CB* sensor was not due to the incident pressure wave from the speaker, but due to electromagnetic interference (EMI) from the speaker. In order to study the ability of the *CB* sensor to successfully measure the incident pressure wave from an acoustic source, an air horn was selected as the acoustic source. The air horn source was purely mechanical and driven by an air compressor. Therefore, the voltage measured across the *CB* sensor could only be due to the incident pressure wave produced by the horn. Figure 7.12 presents a time-frequency plot of the *CB* sensor voltage signal measured when excited by an air horn source. The signal was started approximately 10 seconds into the 20 second experiment.

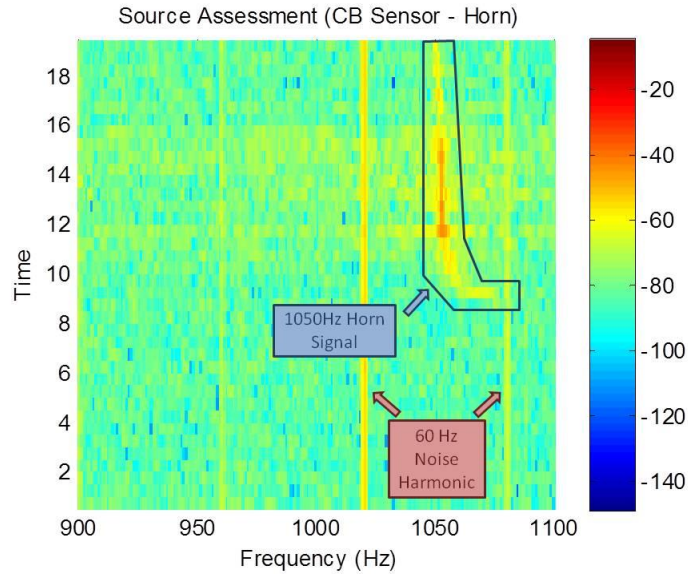


Figure 7.12: Time-frequency plot of a single *CB* sensor output voltage signal for a horn source.

Figure 7.12 indicates that the *CB* sensor seems to respond to the incident pressure wave from the horn source. To verify that the measured voltage signal was due to the incident pressure wave, the previous experiment was repeated and the leads from the *CB* sensor were disconnected. Figure 7.13 presents a time-frequency plot of the measured voltage signal when the leads were disconnected from the *CB* sensor, and the system was excited by an air horn source.

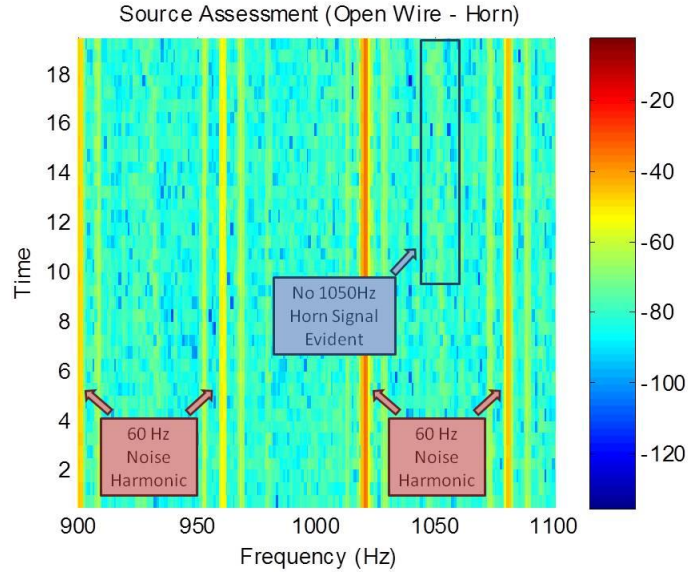


Figure 7.13: Time-frequency plot of a single *CB* sensor output voltage signal for a horn source with the leads disconnected from the *CB* sensor.

Figure 7.13 indicates that the disconnected leads do not measure a voltage when the air horn source is excited. Therefore, the *CB* sensor cannot distinguish between the actual speaker signal and electromagnetic interference noise from the speaker. However, the horn can produce a pressure wave that is measurable by the *CB* sensor, without introducing electromagnetic noise.

7.2 Results

7.2.1 Introduction

Chapter 5 demonstrated that array processing can only be performed with knowledge of the input force acting on the *CB* sensors. Equation (4.5.3) demonstrates that the input force can be calculated using the following information:

1. *Stiffness* ($k_{CB,n}$) of the *CB* sensor
2. *Mass* ($m_{CB,n}$) of the *CB* sensor
3. *Relative motion* ($\Delta w_{CB,n}$) between the *CB* sensor and the plate

4. *Absolute motion* ($w_{plate,n}$) of the plate

The *Stiffness* ($k_{CB,n}$) and *Mass* ($m_{CB,n}$) of the *CB* sensor was calculated using equation (4.3.1) and (4.3.2). Several post-processing steps were applied to the measured data in order to obtain the *Absolute Motion* ($w_{plate,n}$) of the plate from the LDV data, and the *Relative motion* ($\Delta w_{CB,n}$) between the *CB* sensor and the plate from the *CB* sensor data.

The LDV could only measure one location at a time. Therefore, (9) separate “runs” were conducted in order to get time-synchronous data between the *CB* sensors and the plate at each of the (9) *CB* sensor locations. Recall that a similar procedure was followed in the condenser microphone experiment, presented in Chapter 6. A similar procedure to the one presented in Section 6.2 was followed here to create a composite data set and remove the artificial phase caused by the (9) separate data runs. In the horn experiment, however, there was no pilot signal available to use as a reference to calculate the relative phase delay between the source for the (9) runs. Therefore, the signal from Microphone 1 was used as a “pseudo” reference signal. The phase delay between the Microphone 1 data from Run 1 and the remaining nine runs was calculated, and applied to the Microphone 2, *CB* sensor, and LDV data.

After the run-to-run phase delay was accounted for in the data, the effects of the signal conditioning electronics, described in Section 7.1.1, were removed from the *CB* sensor data. This step was required to obtain $V_{CB,n}$ in equation (7.4). Next, a

digital band-pass filter, with cut-off frequencies of 900Hz and 1200Hz, was applied to all of the data to remove the influence any out-of-band noise. The band pass filter introduces a phase-delay to the data. Consequently, it was important to apply the same filter to all of the data so that the applied phase delay was consistent across all of the data.

The next step involved time-integrating the LDV data to obtain the displacement of the plate. Finally, the *CB* sensor data was plugged into equation (7.4), and the *Absolute Motion* ($w_{plate,n}$) of the plate and *Relative motion* ($\Delta w_{CB,n}$) between the *CB* sensor and the plate were plugged into equation (4.5.3) to calculate the input pressure force acting on the *CB* sensors.

7.2.2 Comparison of Experimental Setup to Vibration Model

The following section presents a comparison of the measured data and the model results from Chapter 5. To validate the accuracy of the model, the LDV was used to measure the mode shapes of the plate in the experimental setup. Figure 7.14 and Figure 7.15 present a comparison of the modeled and measured mode shapes.

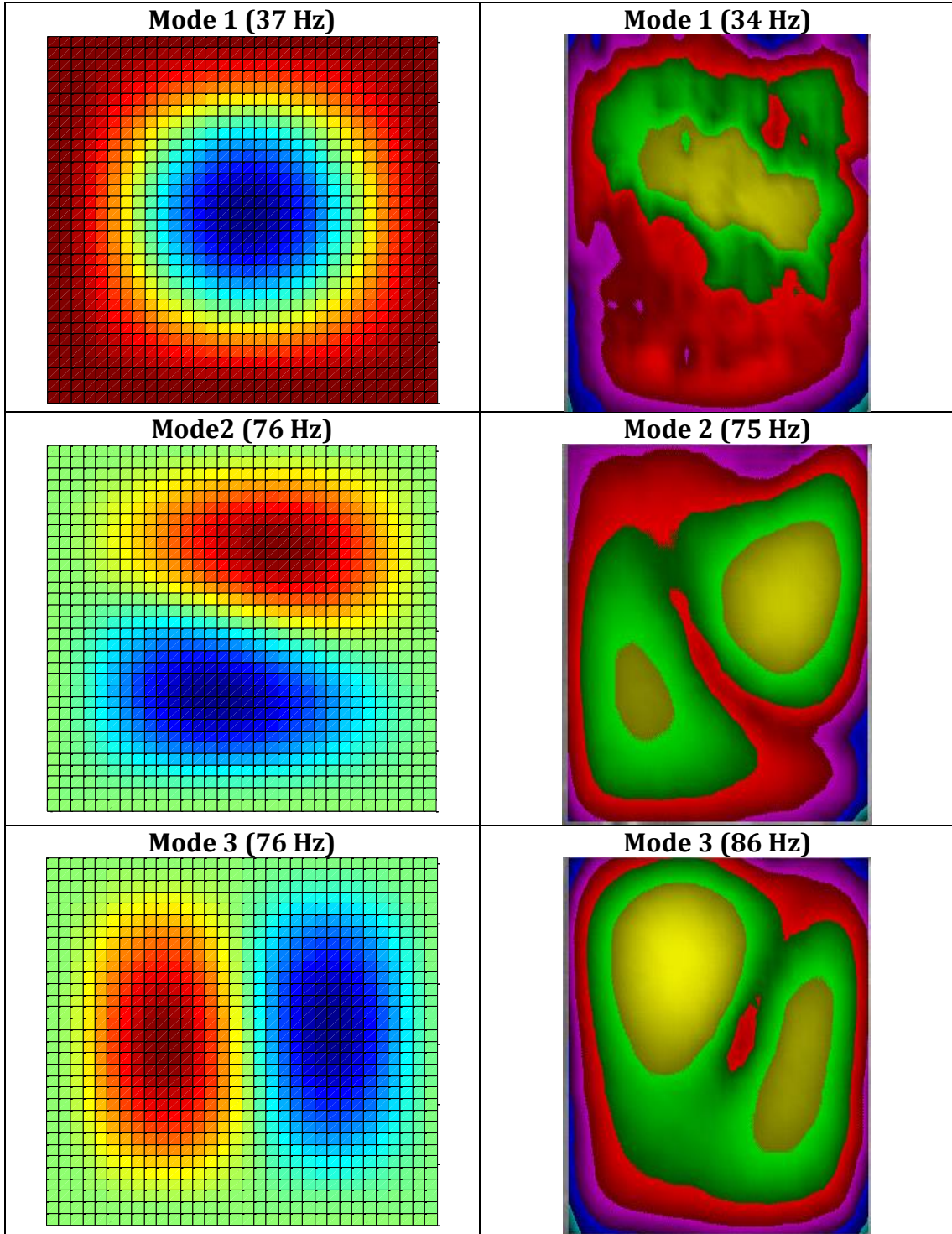


Figure 7.14: Comparison of mode shapes 1-3.

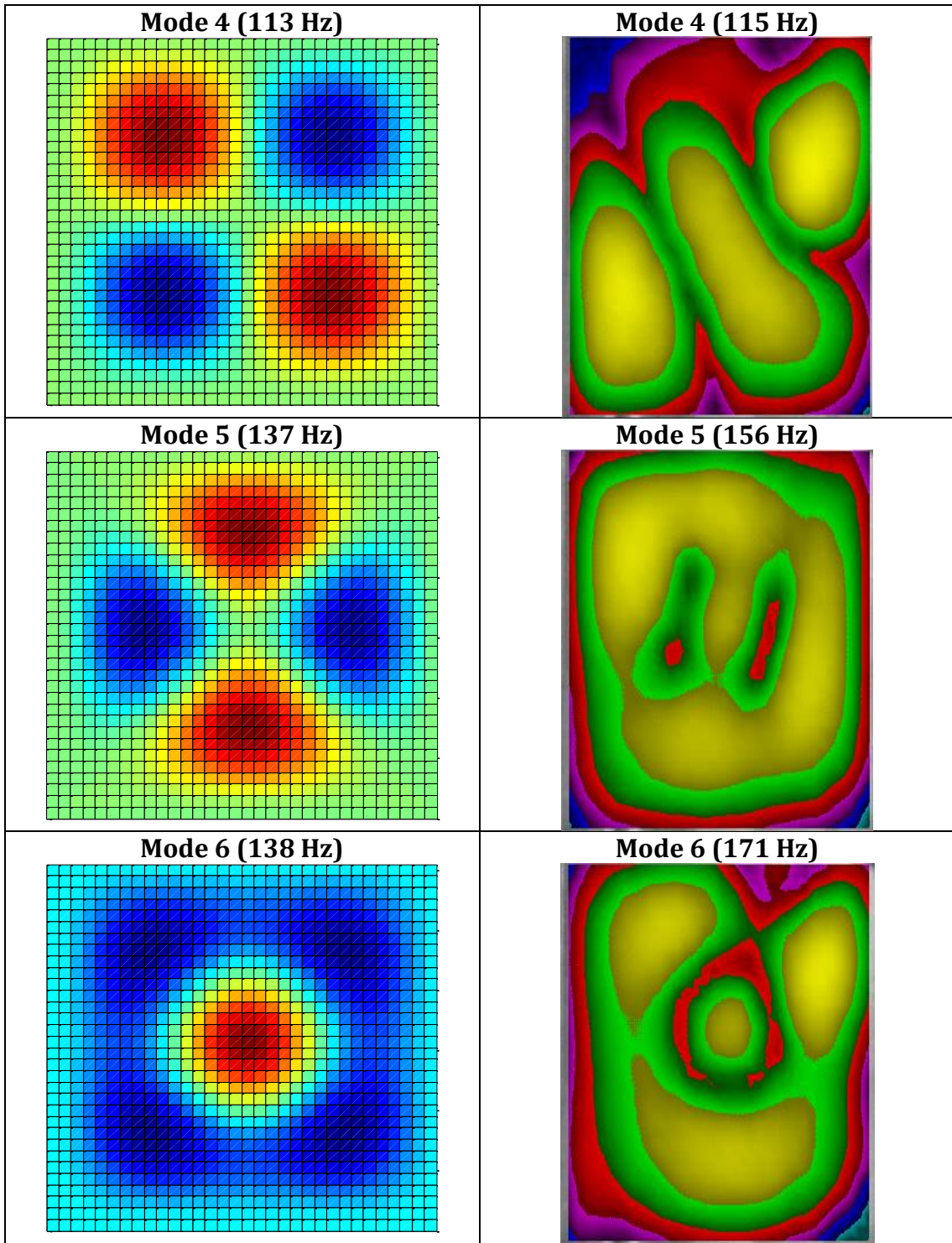


Figure 7.15: Comparison of mode shapes 4-6.

Figure 7.14 indicates relatively good agreement between the modeled and measured natural frequencies and mode shapes for the first 3 modes. However, Figure 7.15 indicates that the measured mode shapes and natural frequencies begin to deviate from the modeled results for higher modes. Examination of the plate used in the experiment indicated some local plastic deformation. It is probable that this plastic deformation is affecting the natural response of the plate. Furthermore, it is possible that the 32x32 element resolution of the model is not enough to resolve higher order modes. Therefore, the plate model may be artificially stiff at higher frequencies. However, it does not mean that the amplitudes predicted by the model are not representative of the actual system. While not ideal, this result is acceptable because the primary purpose of the model was to demonstrate the method used to calculate the input force acting on the *CB* sensors.

Consider the case when the horn was located at $|\vec{R}|=0.2032\text{m}$, $\theta=0^\circ$, and $\Phi=0^\circ$. Figure 7.16 presents the measured displacements of the plate ($w_{plate,n}$) at the (9) *CB* sensor locations. Figure 7.17 presents the measured relative motion between the *CB* sensors and the plate ($\Delta w_{CB,n}$) for all (9) *CB* sensor locations.

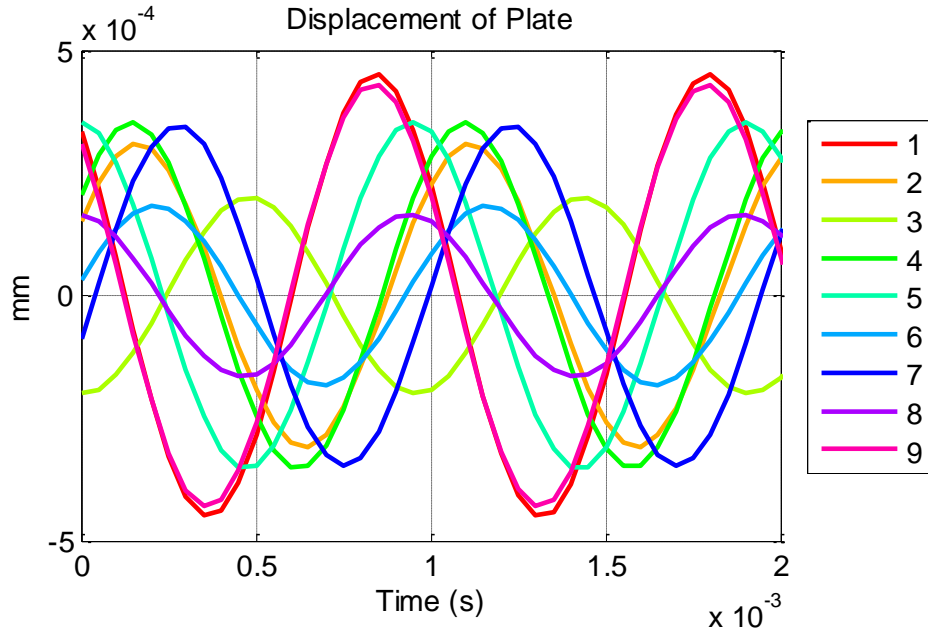


Figure 7.16: Measured absolute plate displacement at the *CB* sensor locations due to a horn source at $|\vec{R}| = 0.2032\text{m}$, $\theta = 0^\circ$, and $\varphi = 0^\circ$.

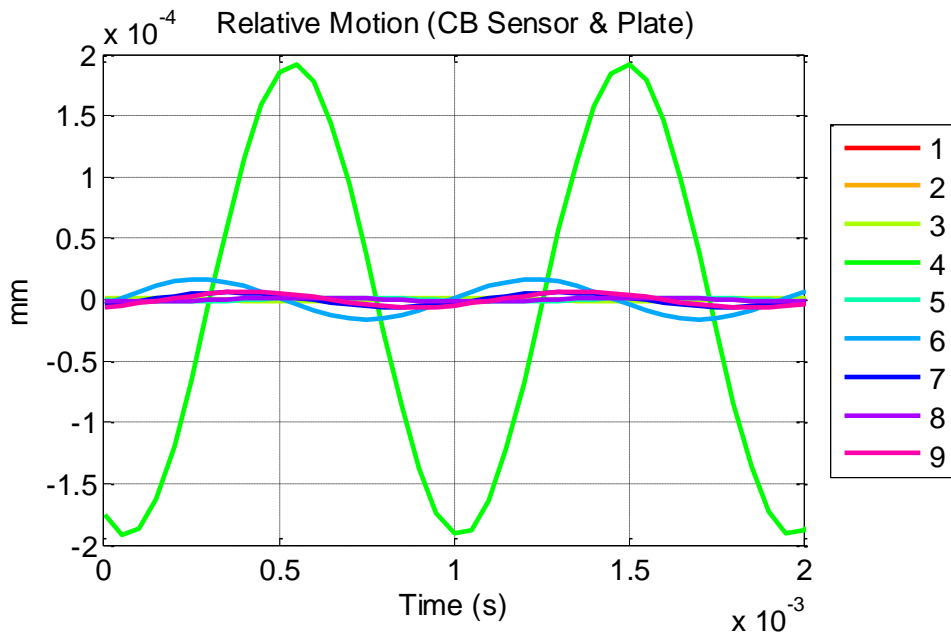


Figure 7.17: Measured relative displacement between the *CB* sensors and the plate due to a horn source at $|\vec{R}| = 0.2032\text{m}$, $\theta = 0^\circ$, and $\varphi = 0^\circ$.

The amplitudes of the results in Figure 7.16 are the same order of magnitude as the modeled plate response presented in Figure 5.16. The difference in phase

between Figure 7.16 and Figure 5.16 is expected due to the model not accurately representing the modal response of the plate in the frequency range of the horn source. Figure 7.17 indicates a large amplitude discrepancy between the measured results and the modeled results presented in Figure 5.18. This discrepancy is significant due to the dependence of equation (4.5.3), the calculation of the input force acting on the *CB* sensors, on this motion.

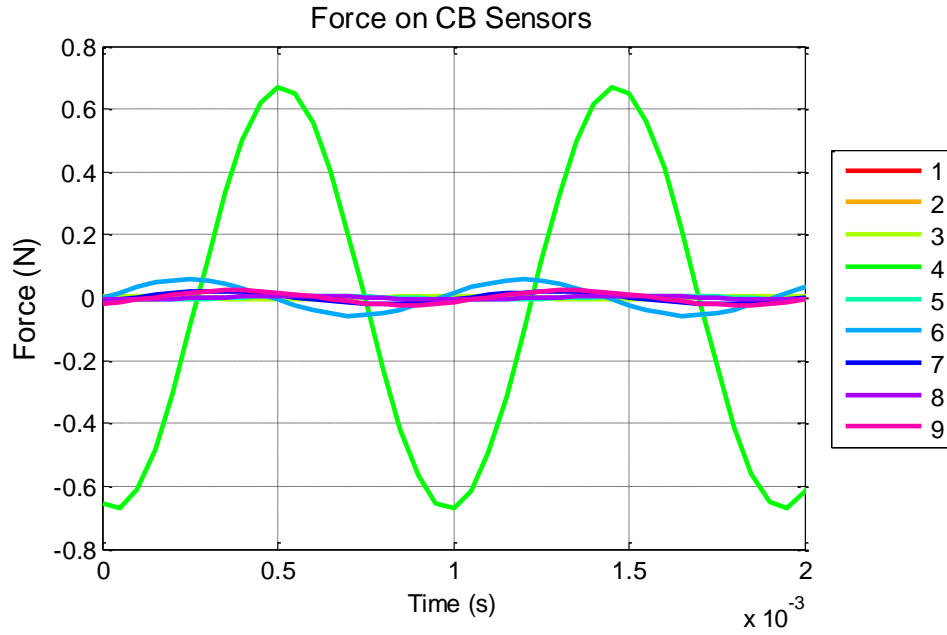


Figure 7.18: Calculated input force on the *CB* sensors due to an acoustic source at $|\vec{R}| = 0.2032\text{m}$, $\theta = 0^\circ$, and $\varphi = 0^\circ$.

The results in Figure 7.18 do not agree with the results predicted in Section 5.4, and presented in Figure 5.23. The calculated input force using the experimental data resembles a scaled version of the relative motion between the *CB* sensors and the plate ($\Delta w_{CB,n}$). The impact of this result on the array processing calculation is presented in Section 7.2.3. Figure 7.19 and Figure 7.20 present a breakdown of the forces contributing to the calculated input force in equation (4.5.3), for the experimental and modeled cases, respectively.

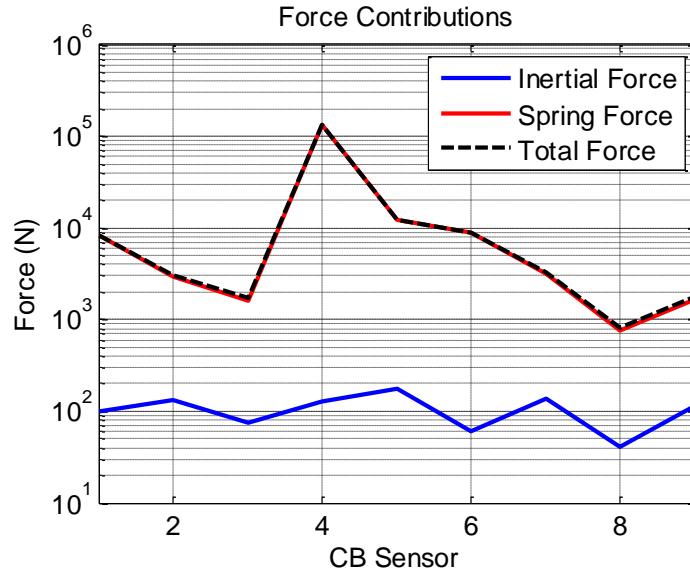


Figure 7.19: Breakdown of measured reaction forces in the *CB* sensor due to applied pressure force ($|\vec{R}| = 0.2032\text{m}$, $\theta = 0^\circ$, and $\varphi = 0^\circ$).

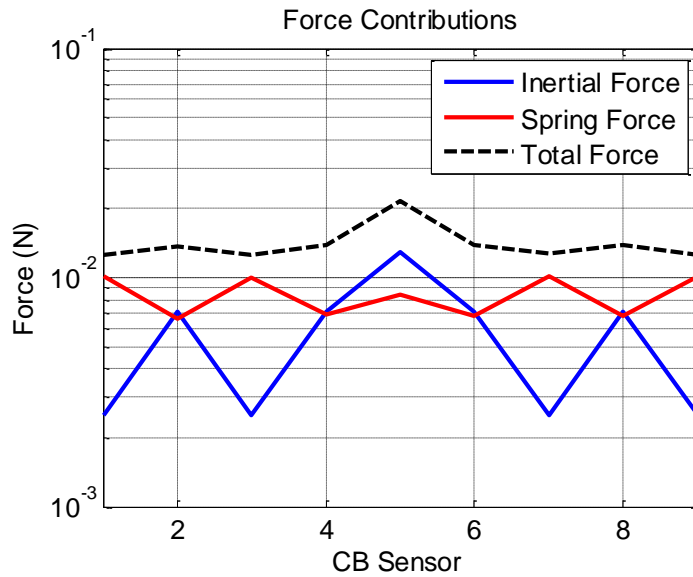


Figure 7.20: Breakdown of modeled reaction forces in the *CB* sensor due to applied pressure force ($|\vec{R}| = 0.2032\text{m}$, $\theta = 0^\circ$, and $\varphi = 0^\circ$).

The figures indicate that in the experimental case, the calculated input force on the *CB* sensors is dominated by the spring force of the *CB* sensor ($k_{CB,n} \cdot \Delta w_{CB,n}$). However, in the modeled case, the calculated input force is influenced almost equally by the inertial force and spring force of the *CB* sensor. Several takeaways can be

made from this observation. First, it is possible that *Stiffness* ($k_{CB,n}$) used in equation (4.5.3) is too large, and does not accurately represent the compressional stiffness of the *CB* sensor material. Furthermore, it is possible that equation (7.4) is not accurately calculating the relative motion between the *CB* sensors and the plate ($\Delta w_{CB,n}$).

Similar results were obtained for the case when the horn was located at $|\vec{R}| = 0.2032\text{m}$, $\theta = 90^\circ$, and $\Phi = 45^\circ$. Figure 7.21 presents the measured displacements of the plate ($w_{plate,n}$) at the (9) *CB* sensor locations. Figure 7.22 presents the measured relative motion between the *CB* sensors and the plate ($\Delta w_{CB,n}$) for all (9) *CB* sensor locations.

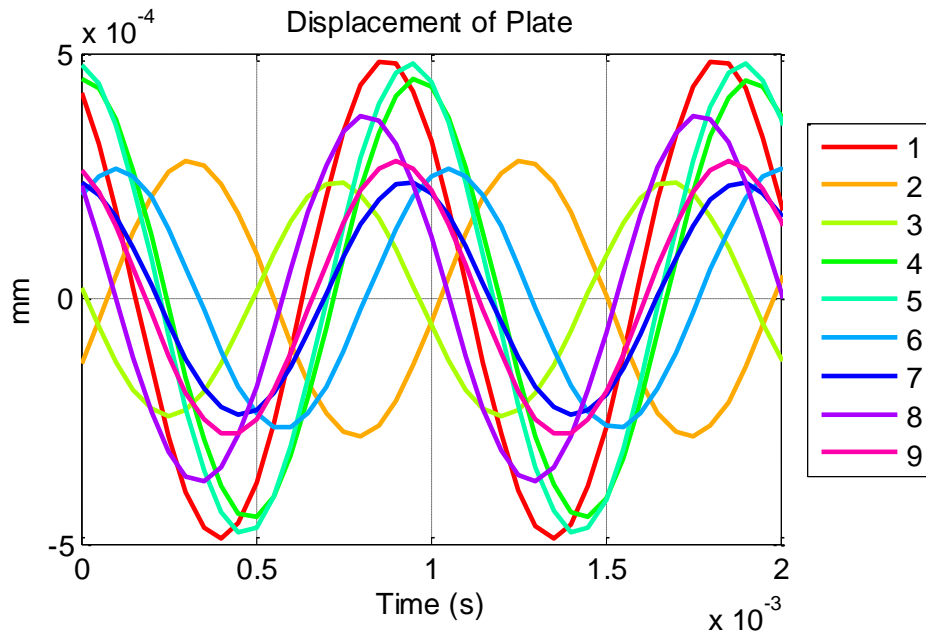


Figure 7.21: Measured absolute plate displacement at the *CB* sensor locations due to a horn source at $|\vec{R}| = 0.2032\text{m}$, $\theta = 90^\circ$, and $\varphi = 45^\circ$.

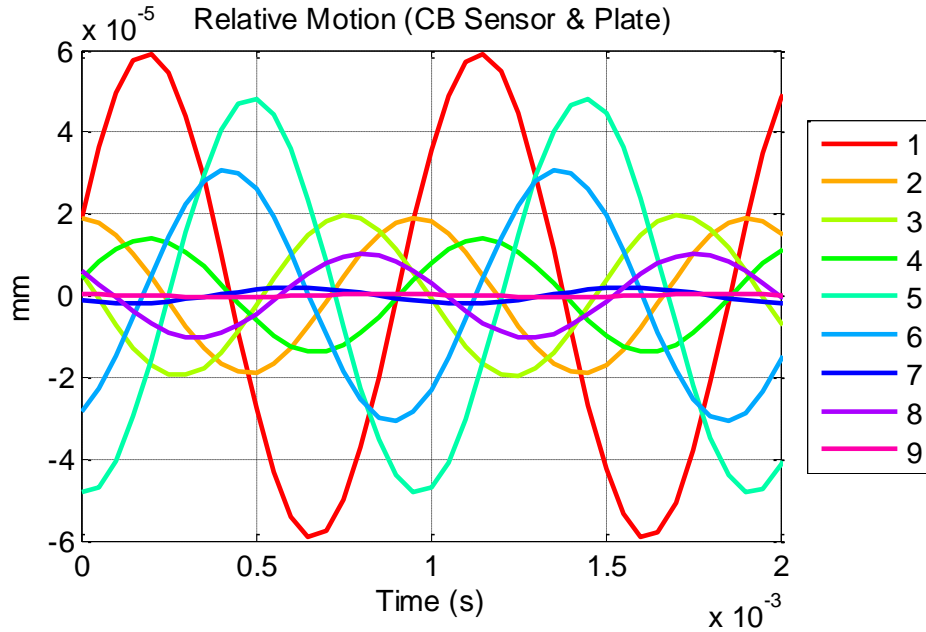


Figure 7.22: Measured relative displacement between the *CB* sensors and the plate due to a horn source at $|\vec{R}| = 0.2032\text{m}$, $\theta = 90^\circ$, and $\varphi = 45^\circ$.

The amplitudes of the results in Figure 7.21 are an order of magnitude smaller than the modeled plate response presented in Figure 5.20. The difference in phase between Figure 7.21 and Figure 5.20 is expected due to the model not accurately representing the modal response of the plate in the frequency range of the horn source. Figure 7.22 indicates a large amplitude discrepancy between the measured results and the modeled results presented in Figure 5.22. Once again, this discrepancy is significant due to the dependence of equation (4.5.3), the calculation of the input force acting on the *CB* sensors, on this motion. Figure 7.23 presents the results of plugging the measured data into equation (4.5.3).

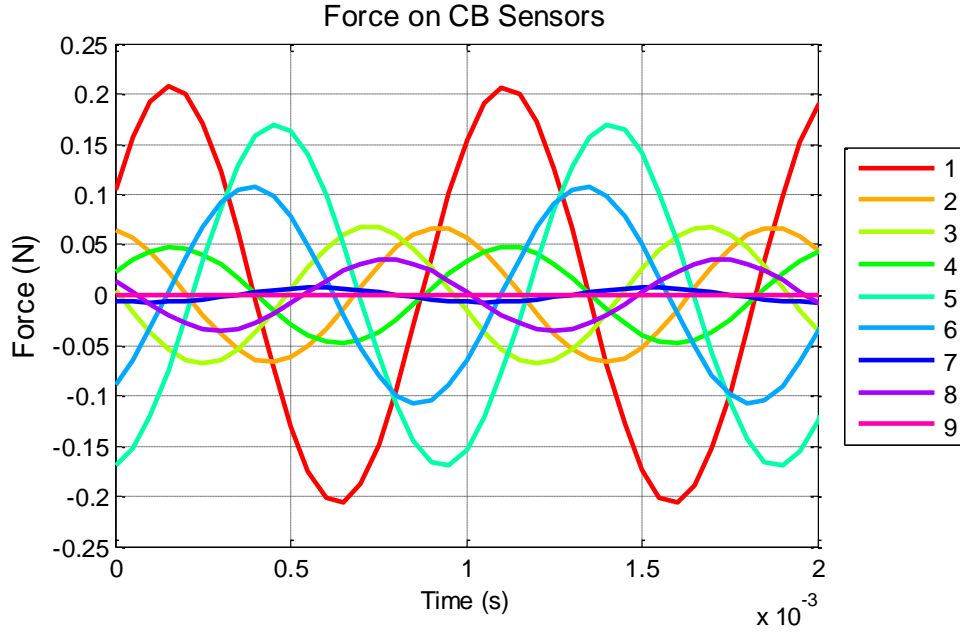


Figure 7.23: Calculated input force on the *CB* sensors due to an acoustic source at $|\vec{R}| = 0.2032\text{m}$, $\theta = 90^\circ$, and $\varphi = 45^\circ$.

The results in Figure 7.23 do not agree with the results predicted in Section 5.4, and presented in Figure 5.24. As in the previously described case, the calculated input force using the experimental data resembles a scaled version of the relative motion between the *CB* sensors and the pate ($\Delta w_{CB,n}$). The impact of this result on the array processing calculation is presented in Section 7.2.3. Figure 7.24 and Figure 7.25 present a breakdown of the forces contributing to the calculated input force in equation (4.5.3), for the experimental and modeled cases, respectively.

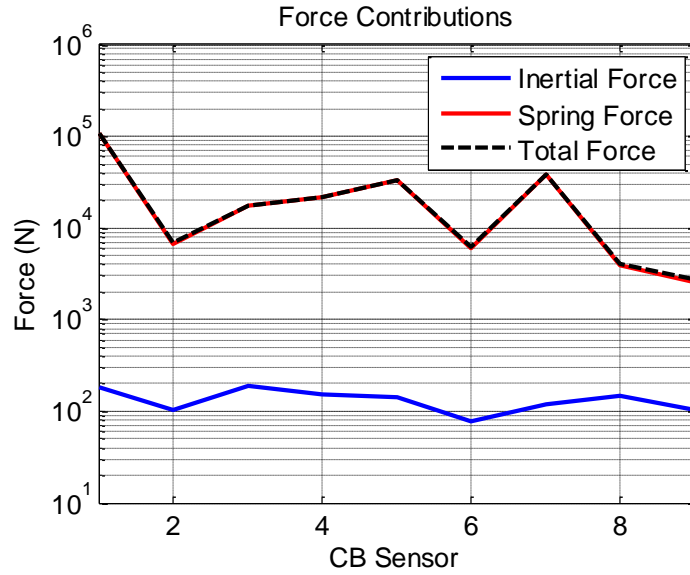


Figure 7.24: Breakdown of measured reaction forces in the *CB* sensor due to applied pressure force ($|\vec{R}| = 0.2032\text{m}$, $\theta = 90^\circ$, and $\varphi = 45^\circ$).

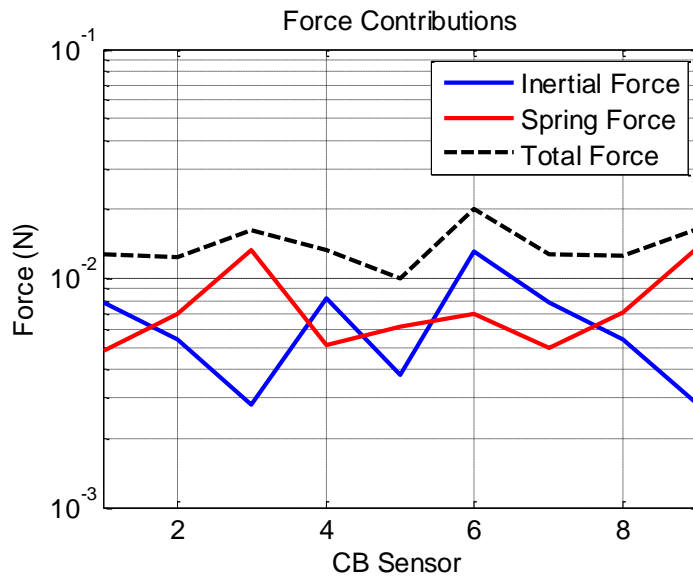


Figure 7.25: Breakdown of modeled reaction forces in the *CB* sensor due to applied pressure force ($|\vec{R}| = 0.2032\text{m}$, $\theta = 90^\circ$, and $\varphi = 45^\circ$).

The figures indicate that in the experimental case, the calculated input force on the *CB* sensors is dominated by the spring force of the *CB* sensor ($k_{CB,n} \cdot \Delta w_{CB,n}$). However, in the modeled case, the calculated input force is influenced almost equally

by the inertial force and spring force of the *CB* sensor. This result is similar to the result obtained in the case where the horn was located at $|\vec{R}|=0.2032\text{m}$, $\theta=0^\circ$, and $\Phi=0^\circ$. Section 7.2.3 presents the results of performing acoustic source localization using the forces calculated and presented in Figure 7.18 and Figure 7.23.

7.2.3 Array Processing Results

Recall from Section 4.5 that acoustic source localization process relies on being able to determine the input pressure force on the *CB* sensory array. The input pressure force on the modeled *CB* sensors can be calculated by plugging the results from Section 5.3 into equation (4.5.3). Figure 7.18 and Figure 7.23 present the input pressure forces calculated, from the experimental data, for the (2) *CB* source location cases presented in Table 5.1. As discussed in Section 7.2.2, these results are not in good agreement with the pressure distributions presented in Figure 5.4 and Figure 5.6. The outputs from this equation can be used in equation (1.3.9), for an array of assumed source locations, to calculate the maximum output power of the array processor. The source locations are assumed to be at $|\vec{R}|=0.2032\text{m}$, $\theta=0^\circ$ to 360° with 1° spacing, and $\Phi=0^\circ$ to 90° with 1° spacing. Figure 7.26 and Figure 7.27 illustrate the results of array processing the calculated pressure forces acting on the *CB* sensors for each of the (2) *CB* source locations cases presented in Table 5.1.

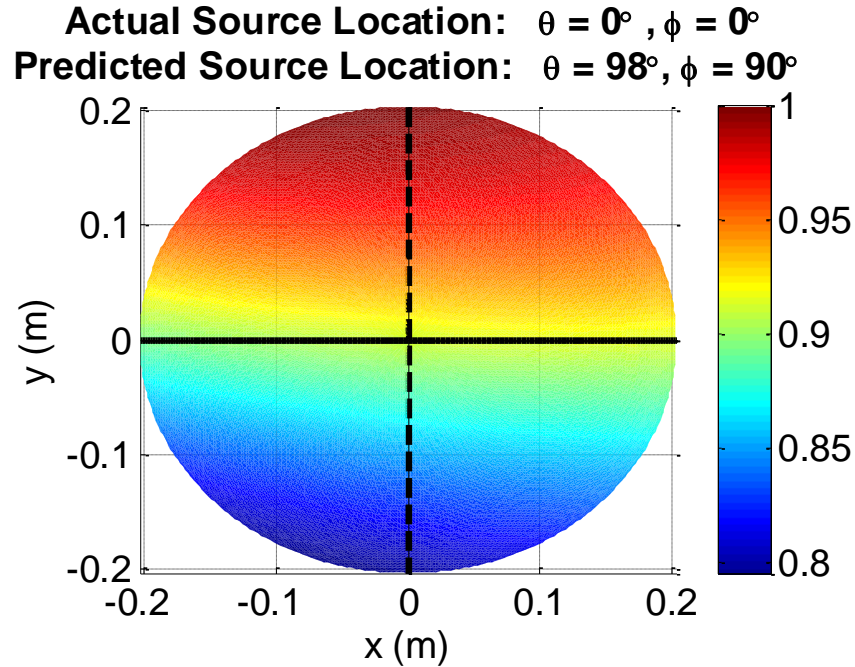


Figure 7.26: Array processing results for a horn source located at $|\vec{R}| = 0.2032\text{m}$, $\theta = 0^\circ$, and $\phi = 0^\circ$.

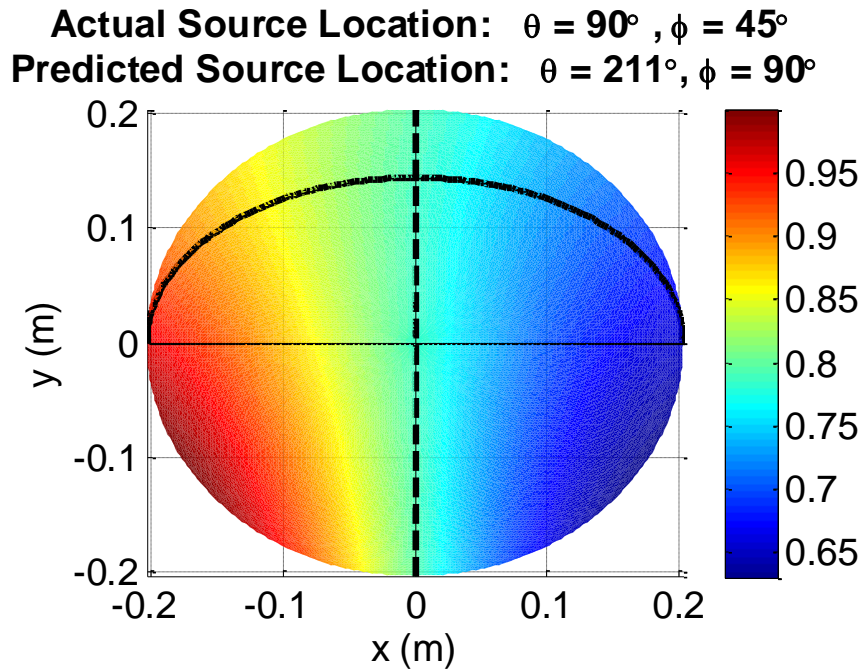


Figure 7.27: Array processing results for a horn source located at $|\vec{R}| = 0.2032\text{m}$, $\theta = 90^\circ$, and $\phi = 45^\circ$.

As expected, array processing of the input forces acting on the *CB* sensors, calculated from the experimental data, does not successfully identify the location of the horn.

A critical component of array processing is the phase between the sensors in the array. Figure 7.18 and Figure 7.23 indicate that the phase of the input force applied to the *CB* sensors does not match the expected phase due to an acoustic source, presented in Figure 5.4 and Figure 5.6. Figure 7.28 presents an examination of the how the phase delay between input forces calculated at the (9) *CB* sensor locations changes with time for the case when the source was located at $|\vec{R}| = 0.2032\text{m}$, $\theta = 0^\circ$, and $\Phi = 0^\circ$. To generate this figure, the cross-spectra was calculated between the data from the (9) *CB* sensor locations to the data from *CB* Sensor 1, over 1 second time windows. Each of these 1-second windows is referred to as an “ensemble”. Consequently, there are 20 ensembles for the 20 second run. The figure plots the angle from these cross-spectra calculations.

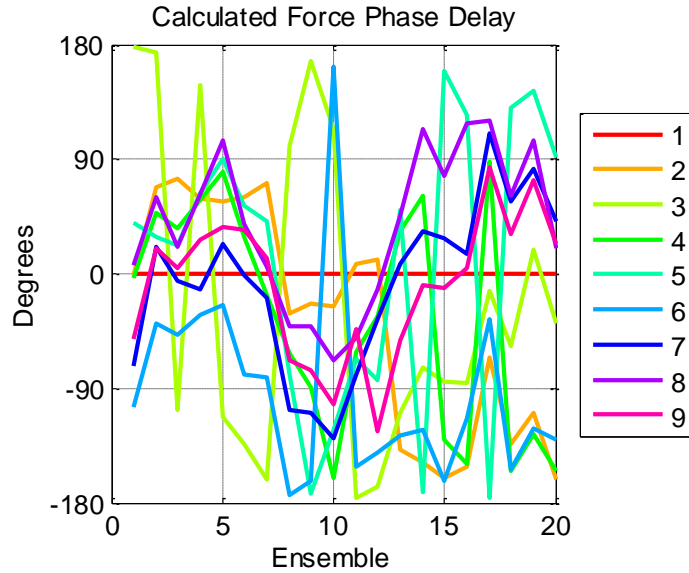


Figure 7.28: Ensemble-to-ensemble phase delay between the (9) separate *CB* sensor locations (Calculated pressure force, $|\vec{R}| = 0.2032\text{m}$, $\theta = 0^\circ$, and $\varphi = 0^\circ$).

The figure indicates that the phase of the calculated force on the *CB* sensors, referenced to the force on the *CB* sensor at location 1, varies with time. This result is not expected for a source that has reached a steady state. Additionally, the time-varying nature of the phase relationships between the forces acting at the (9) sensor locations does not lend itself to successful array processing and acoustic source localization. Note that there is no phase delay between the force calculated at location 1 and itself, which is why the straight line appears in Figure 7.28 for Location 1. The reference microphone signals were examined to determine if the source was a steady state source in terms of phase. Figure 7.29 and Figure 7.30 present the calculated phase results for Microphone 1 and Microphone 2 between the (9) separate runs.

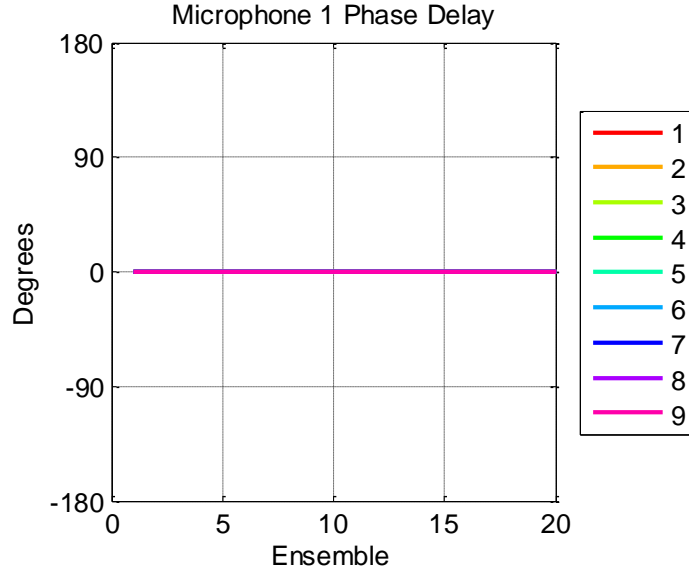


Figure 7.29: Ensemble-to-ensemble phase delay between the (9) separate runs (Microphone 1 $|\vec{R}| = 0.2032\text{m}$, $\theta = 0^\circ$, and $\varphi = 0^\circ$).

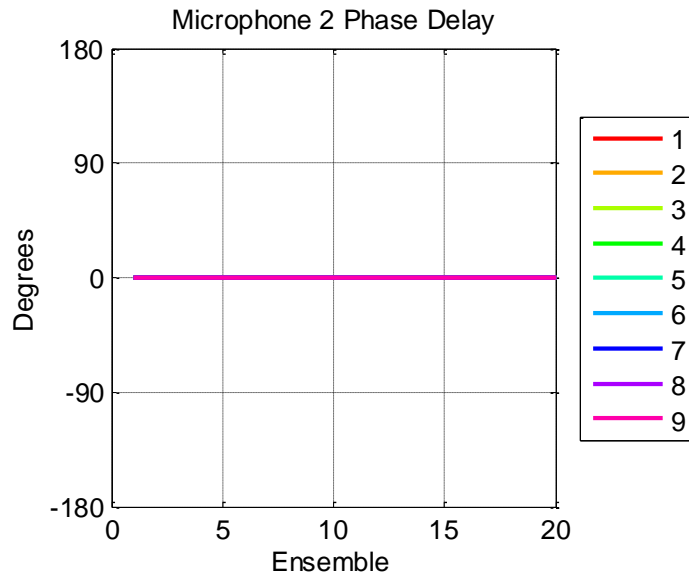


Figure 7.30: Ensemble-to-ensemble phase delay between the (9) separate runs (Microphone 2 $|\vec{R}| = 0.2032\text{m}$, $\theta = 0^\circ$, and $\varphi = 0^\circ$).

The results presented in these figures verify that the source is at a steady state. In order to understand why the phase between the forces acting on the *CB* sensors is time-varying, it is important to examine the components from equation (4.5.3). The mass and stiffness terms in equation (4.5.3) are not time-dependent. Therefore, the

two time-dependent variables that contribute to the calculation of the force applied to the *CB* sensors are the displacements of the plate ($w_{plate,n}$) relative motion between the *CB* sensors and the plate ($\Delta w_{CB,n}$). Figure 7.31 presents an examination of how the phase delay between the LDV measurements at the (9) *CB* sensor locations, and the LDV measurement at *CB* location 1, vary with time.

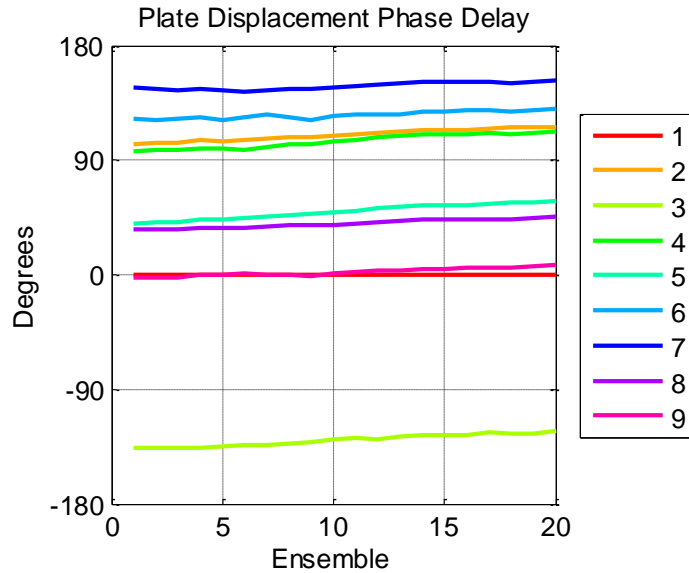


Figure 7.31: Ensemble-to-ensemble phase delay between the (9) separate LDV locations (Plate displacement, $|\vec{R}| = 0.2032\text{m}$, $\theta = 0^\circ$, and $\phi = 0^\circ$).

The above figure indicates that the phase delay between the LDV measurements at the (9) *CB* sensor locations, and the LDV measurement at *CB* location 1, remains constant in time. The relative phase between the LDV measurement at the (9) *CB* sensor locations is expected because of the higher-order motion of the plate in the frequency range of the horn excitation. Recall that Figure 7.19 demonstrated that the experimental force was dominated by the spring force in the *CB* sensors, which is linearly proportional to the relative motion between the *CB*

sensor and the plate. Figure 7.32 presents the relative motion of the plate and *CB* sensors, which is directly related to the electrical output from the *CB* sensor.

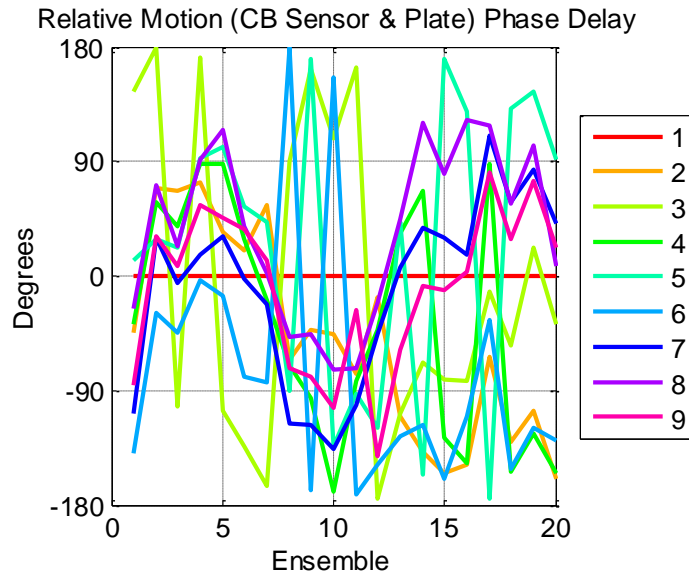


Figure 7.32: Ensemble-to-ensemble phase delay between the (9) separate *CB* sensor locations (Relative motion between the *CB* sensors and the plate, $|\vec{R}| = 0.2032\text{m}$, $\theta = 0^\circ$, and $\varphi = 0^\circ$).

Figure 7.32 indicates that the phase between the *CB* sensors is not constant in time, and is contributing to the time-varying nature of the phase between the input forces acting on the *CB* sensors. Figure 7.33 through Figure 7.37 present a similar analysis for the case when the horn was located at $|\vec{R}|=0.2032\text{m}$, $\theta=90^\circ$, and $\Phi=45^\circ$.

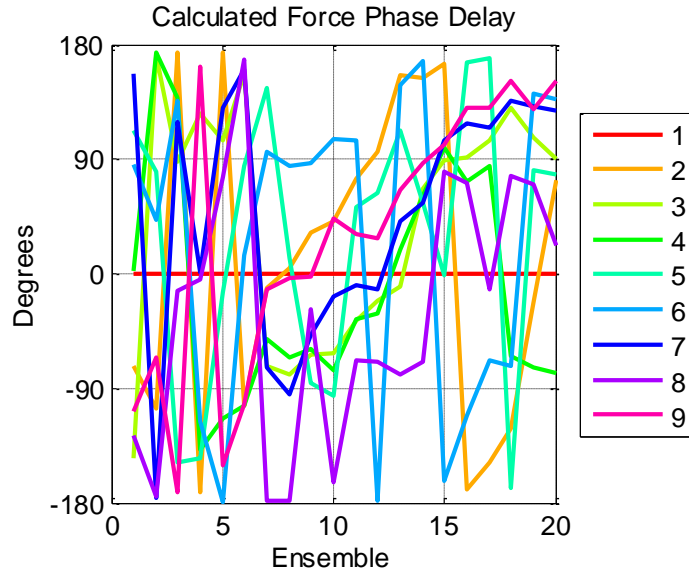


Figure 7.33: Ensemble-to-ensemble phase delay between the (9) separate *CB* sensor locations
 (Calculated pressure force, $|\vec{R}| = 0.2032\text{m}$, $\theta = 90^\circ$, and $\varphi = 45^\circ$).

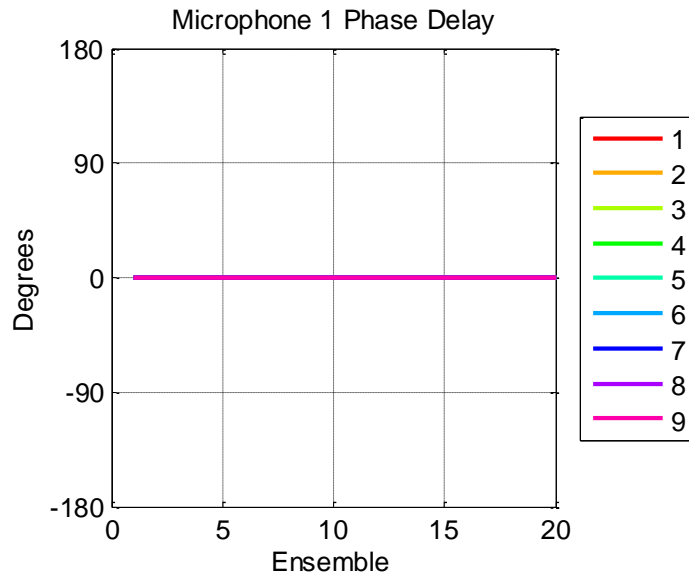


Figure 7.34: Ensemble-to-ensemble phase delay between the (9) separate runs (Microphone 1)
 $|\vec{R}| = 0.2032\text{m}$, $\theta = 90^\circ$, and $\varphi = 45^\circ$).

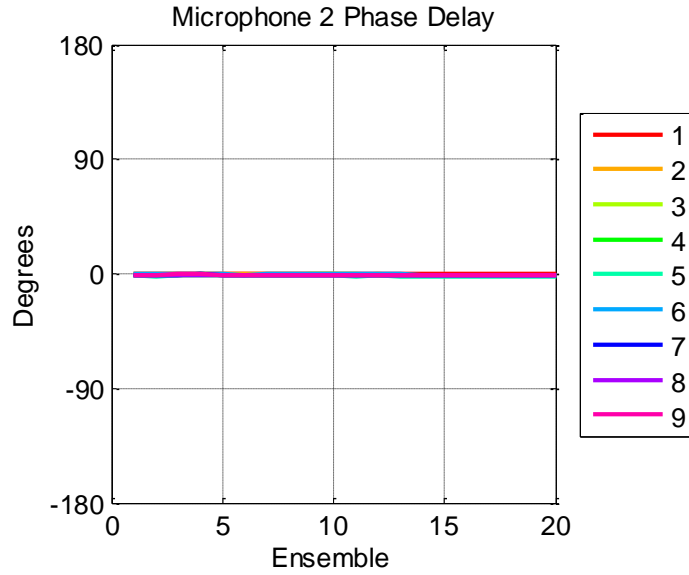


Figure 7.35: Ensemble-to-ensemble phase delay between the (9) separate runs (Microphone 2 $|\vec{R}| = 0.2032\text{m}$, $\theta = 90^\circ$, and $\varphi = 45^\circ$).

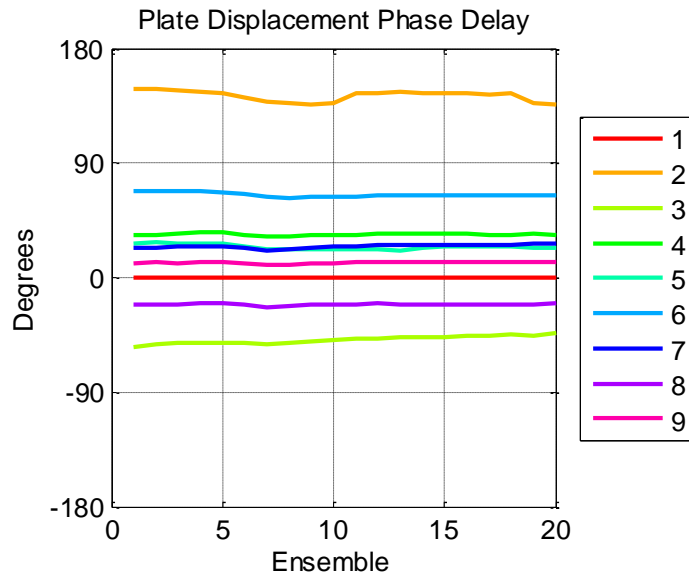


Figure 7.36: Ensemble-to-ensemble phase delay between the (9) separate LDV locations (Plate displacement, $|\vec{R}| = 0.2032\text{m}$, $\theta = 90^\circ$, and $\varphi = 45^\circ$).

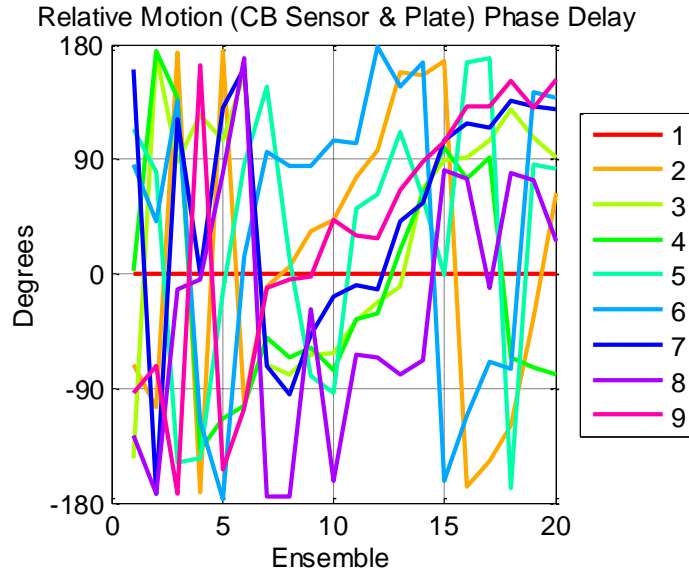


Figure 7.37: Ensemble-to-ensemble phase delay between the (9) separate *CB* sensor locations (Relative motion between the *CB* sensors and the plate, $|\vec{R}| = 0.2032\text{m}$, $\theta = 90^\circ$, and $\varphi = 45^\circ$).

Both data sets indicate that the phase between the *CB* sensors is not constant in time, and is contributing to the time-varying nature of the phase between the input forces acting on the *CB* sensors. It is possible that the compression of the *CB* sensor is producing a very small change in resistance, and consequently a very small change in output voltage in the *CB* sensors. If this is the case, it is possible that the signal conditioning circuit, which includes a non-inverting feedback amplifier, is amplifying both signal and electrical noise. This explanation would account for the random nature of the phase delays between the outputs of the *CB* sensors.

7.3 Summary

Chapter 7 presents the results from an experiment using an array of *CB* sensors to identify the location of an acoustic source. The experiment was conducted using an air horn as the acoustic source due to the susceptibility of the *CB* sensors to EMI from an electromagnetic speaker. Two separate measurements were conducted;

one measurement with the horn located at $|\vec{R}|=0.2032\text{m}$, $\theta=0^\circ$, and $\Phi=0^\circ$, and the other measurement with the horn located at $|\vec{R}|=0.2032\text{m}$, $\theta=90^\circ$, and $\Phi=45^\circ$.

In each experiment, the following data was collected:

- *CB* sensor output signal (x9)
- LDV output signal
- Reference microphone signal (x2)

The LDV could only be directed at one location at a time. Therefore, Each measurement consisted of (9) separate, 20 second duration, recording periods in order to get time-synchronous data between the *CB* sensors and the LDV at each of the (9) *CB* sensor locations. Post processing was performed on the recorded data to accomplish the following:

- Account for the relative phase delay between the (9) separate data runs
- Account for the phase delays introduced by the signal conditioning electronics connected to the *CB* sensors
- Band-pass filter the data in the frequency range of interest (900Hz – 1200Hz) to minimize the impact of out-of-band noise

The microphones were used as reference sensors to identify the source strength of the horn for modeling purposes, and to act as “pseudo” pilot signals. The data measured from the LDV and the *CB* sensors was used to calculate the input

forces acting on the *CB* sensors. These input forces were then used in an array processing algorithm in an attempt to identify the location of the horn source. The results indicate that the data measured from a horn source located at the following locations relative to the *CB* sensor array could not be used to identify the horn's location. The most likely explanation for the inability of the sensors to localize the horn source is that the horn was not producing enough pressure to produce a change in voltage in the *CB* sensors that was sufficiently above the electrical noise floor of the system.

Chapter 8: Conclusions & Future Work

8.1 Conclusions

This thesis has presented a theoretical and experimental investigation of an array of Carbon Black (*CB*) filled polyurethane sensors which is intended to identify the location and intensity of a single acoustic source.

The details of the manufacturing procedure of the proposed array are outlined in Chapter 2, and several prototypes are manufactured. In Chapter 3, the characterization of the viscoelastic and piezo-resistive material properties of different samples of the *CB* filled polyurethane are presented using Dynamic, Mechanical, Thermal Analyzer (*DMTA*) and uni-axial compression testing. These characterization tests aim also at investigating the impact of including the carbon black particles on the viscoelastic properties of the polymer. It is observed that the pristine polyurethane has a much lower *Storage Modulus* than polyurethane/carbon black composite (with 20% *CB* fill). Consequently, inclusion of the *CB* particles in the polyurethane significantly stiffens the resulting composite. This outcome is expected, and consistent with the results of the *Shore A Hardness* tests. The *Loss Factor* data indicate that the inclusion of the *CB* particles increases the *Loss Factor* at lower frequencies when compared to the polyurethane only.

In Chapters 4 and 5, the structural, dynamical, and sensing performance characteristics of the array sensor are modeled mathematically using the theory of

finite elements and utilizing the well-known localization theories of phased arrays. The predictions of the mathematical models indicate that the addition of the *CB* sensors to the base plate system adds a small amount of mass to the system, and shifts the natural frequencies slightly lower. Additionally, the results indicate that there are no local modes of the *CB* sensors, and the absolute motion of the plate is dominated by local modes of the plate up to 1500 Hz. Furthermore, Chapter 4 successfully demonstrated analytically that the input force applied to each *CB* sensor, can be determined. These forces physically represent the input force on the *CB* sensors due to the acoustic source which are used to identify the location of the acoustic source.

The experimental performance characteristics of the proposed array sensor are evaluated in comparison to an array of conventional condenser microphones in Chapter 6. The purpose of such an experimental effort is to demonstrate the capabilities and limitations of the proposed array sensor as compared with conventional condenser microphones as outlined in Chapter 7. Furthermore, the obtained experimental results are utilized to validate the theoretical predictions of the localization of acoustic sources.

It is important to note here the *CB* array has demonstrated several characteristics that limit its effectiveness. Distinct among these limitations is the susceptibility to electromagnetic interference (EMI). The sensor as it is in effect a conductive polymer acts as an antenna that is very sensitive to a wide range of electric signals such as excitation electromagnetic speakers, amplifiers, and power supplies. Therefore, excitation of the array using a pneumatic siren was considered as

a viable means for minimizing the effect of the EMI which have made the use of conventional electromagnetic speaker impossible.

Another important limitation of the *CB* array stems from its high compressional stiffness that limits the measurement sensitivity of the sensor. Such a low sensitivity leads to a low signal to noise ratio (or low signal to EMI interference ratio). This reduces the ability of the *CB* array in identifying the location and intensity of acoustic sources.

8.2 Future Work

With the wealth of information and experiences gained throughout this study, several improvements are deemed essential to enhance the potential of the *CB* sensor array.

Among the proposed future improvements is the minimization of the EMI effects in order to improve the signal to noise ratio of the sensor. Such an improvement can be achieved through the application of appropriate EMI shielding to the entire sensor array.

Furthermore, it is essential to minimize the compressional stiffness of the array by increasing its thickness and reducing its surface area. With reduced sensor surface area it would be expected to improve the signal to noise ratio of the sensor and hence enhance its source localization potential.

Better predictions of the *CB* array sensor can be achieved by improving the viscoelastic model of the *CB*/polymer through the use of more sophisticated time domain model such as the Generalized Maxwell model (GMM). Improving the predictions of the time domain characteristics of the sensor will definitely improve its source localization characteristics.

It is envisioned that the proposed *CB* filled polyurethane array sensor with such improvements would present a cost effective and viable means for identifying the location and intensity of acoustic sources which can vary from stationary to moving sources in air or underwater. Accordingly, the applications of such an array sensor are only limited by our imagination.

Appendix A

The following appendix provides a detailed derivation of the *Kinetic Energy* formula applied in this thesis. The *Work-Energy Theorem* states

$$W = \int_0^q F_q \cdot dq = T \quad (\text{A.1})$$

Recall *Newton's 2nd Law of Motion* that the *Force* (F_q) acting on an object in the q -direction is equal to the *Mass* (m) of the object multiplied by its *Acceleration* (a_q) in the q -direction, expressed below in equation (A.2):

$$F_q = ma_q \quad (\text{A.2})$$

The *Acceleration* (a_a) of the object in the q -direction can be described by the time-derivative of the *Velocity* (v_q) of the object in the q -direction, as described below in equation (A.3):

$$a_q = \frac{dv_q}{dt} \quad (\text{A.3})$$

Plugging equation (A.3) into equation (A.2), and assuming the object has an *infinitesimal Mass* (dm), yields the following:

$$F_q = dm \frac{dv_q}{dt} \quad (\text{A.4})$$

Plugging equation (A.4) into equation (A.1) yields the following:

$$T_i = \int_0^q dm \frac{dv_q}{dt} \cdot dq \quad (\text{A.5})$$

Assuming the *infinitesimal Mass* (dm) in equation (A.5) is independent of *Position* (q) yields the following:

$$T_i = dm \int_0^q \frac{dv_q}{dt} \cdot dq \quad (\text{A.6})$$

Applying the *chain-rule* to equation (A.6), and simplifying, yields the following:

$$T_i = dm \int_0^q \frac{dv_q}{dq} \frac{dq}{dt} \cdot dq$$

$$T_i = dm \int_0^q \frac{dq}{dt} dv_q \quad (\text{A.7})$$

The *Velocity* (v_q) of the object in the q -*direction* can be described by the time-derivative of the *Position* (q) of the object, as described below in equation (A.8):

$$v_q = \frac{dq}{dt} \quad (\text{A.8})$$

Plugging equation (A.8) into equation (A.7), substituting the integration limits into equation (A.8), and simplifying, yields the following:

$$T_i = dm \int_0^{dq/dt} v_q dv_q = dm \int_0^{v_a} v_q dv_q \quad (\text{A.9})$$

Evaluating the integral in equation (A.9) yields the following:

$$T_i = \frac{1}{2} dm v_q^2 \quad (\text{A.10})$$

The *infinitesimal Mass* (dm) can also be described in terms its *Density* (ρ) and *Volume* (dV) as follows:

$$dm = \rho dV \quad (\text{A.11})$$

Applying equation (A.11) to equation (A.10), and simplifying, yields the following:

$$T_i = \frac{1}{2}(\rho dV)v_q^2$$

$$T_i = \frac{1}{2}\rho v_q^2 dV \tag{A.12}$$

Integrating equation (A.12) the over the *Total Volume* (V) of the object yields the following expression for the *Total Kinetic Energy* (T) of the object:

$$T = \int_V T_i$$

$$T = \frac{1}{2} \int_V \rho v_q^2 dV \tag{A.13}$$

For the more general case where the *Velocity* (v) is a vector $\{v\}$ with components in multiple directions, equation (A.13) can be rewritten as follows:

$$T = \frac{1}{2} \int_V \rho \{v\} \cdot \{v\} dV = \frac{1}{2} \int_V \rho \{v\}^T \{v\} dV \tag{A.14}$$

Appendix B

The following appendix provides a detailed derivation of the *Potential Energy* formula applied in this thesis. In absence of non-conservative forces, the work energy theorem states that the potential energy is given by the following equation:

$$W = \int_0^q F_q \cdot dq = U \quad (\text{B.1})$$

Recall that the *Stress* (σ_q) experienced by an object in the *q-direction* is equivalent to the applied *Force* (F_q) in the *q-direction* per unit *Area* (A), as expressed below in equation (B.2):

$$\sigma_q = \frac{F_q}{A} \quad (\text{B.2})$$

Solving for the *Force* (F_q) in equation (B.2), and plugging the result into equation (B.1), yields the following:

$$\begin{aligned} U &= \int_0^q (\sigma_q A) \cdot dq \\ U &= \int_0^q \sigma A \cdot dq \end{aligned} \quad (\text{B.3})$$

Dividing equation (B.3) by the *Volume* (V) of the object yields the *Potential Energy per Unit Volume* (U_i), as follows:

$$U_i = \frac{U}{V} = \int_0^q \frac{\sigma_q A}{V} \cdot dq \quad (\text{B.4})$$

Recognizing that the *Volume* (V) of the object is equivalent to the cross-sectional *Area* (A) multiplied by the q -*direction* dimension (q), and simplifying equation (B.4) accordingly, yields the following:

$$U_i = \int_0^q \frac{\sigma_q A}{Aq} \cdot dq$$

$$U_i = \int_0^q \sigma_q \cdot \frac{dq}{q} \quad (\text{B.5})$$

The *Strain* ($d\varepsilon$) experienced by the object in the q -*direction* is defined as the change in length (dq) divided by the original size (q), as follows:

$$d\varepsilon_q = \frac{dq}{q} \quad (\text{B.6})$$

Plugging equation (B.6) into equation (B.5), substituting the integration limits into equation (B.6), and simplifying, yields the following:

$$U_i = \int_0^{dq/q} \sigma_q \cdot d\varepsilon_q = \int_0^{\varepsilon_q} \sigma_q \cdot d\varepsilon_q \quad (\text{B.7})$$

Young's Modulus (E) relates the *Stress* (σ_q) and *Strain* (ε_q) experienced by the object as follows:

$$\sigma_q = E\varepsilon_q \quad (\text{B.8})$$

Plugging equation (B.8) into equation (B.7), and evaluating the integral, yields the following:

$$U_i = \int_0^{\varepsilon_q} E\varepsilon_q \cdot d\varepsilon_q$$

$$U_i = \frac{1}{2} E\varepsilon_q^2 \quad (\text{B.9})$$

Plugging equation (B.8) into equation (B.9) yields the following:

$$U_i = \frac{1}{2} \varepsilon_q \sigma_q \quad (\text{B.10})$$

Integrating equation (B.10) over the *Total Volume* (V) of the object yields the following expression for the *Total Potential Energy* (U) of the object:

$$U = \int_V U_i dV$$

$$U = \frac{1}{2} \int_V \varepsilon_q \sigma_q dV \quad (\text{B.11})$$

For the more general case where the *Stress* (σ) and *Strain* (ε) are vectors with components in multiple directions, equation (B.11) can be rewritten as follows:

$$U = \frac{1}{2} \int_V \{\varepsilon\} \cdot \{\sigma\} dV = \frac{1}{2} \int_V \{\varepsilon\}^T \{\sigma\} dV \quad (\text{B.12})$$

Bibliography

- [1] Aldraihem O., W. Akl, and A. Baz, "Nanocomposite Functional Paint for Vibration and Noise Monitoring", *Journal of Sensors and Actuators A: Physical*, Vol. 149, pp. 233–240, 2009.
- [2] Al-Saffar, Y., Aldraihem, O., and Baz, A. "Smart paint sensor for monitoring structural vibrations." *Journal of Smart Materials and Structures*, Vol. 21, No. 4, 045004, April 2012.
- [3] Baz, A., and J. Ro. "Vibration control of plates with active constrained layer damping." *Smart Materials and Structures* 5.3 (1996): 272.
- [4] Baz, A., "Acoustic Source Localization Using Polymer-Carbon Black Composite Phased Arrays", ONR Proposal, Code 333, 2009.
- [5] Chodak, I., Krupa, I. "Percolation effect and mechanical behavior of carbon black filled polyethylene. *Journal of Material Science Letters* 18 (1999) 1457–1459.
- [6] De Abreu, G. L. C. M., J. F. Ribeiro, and V. Steffen Jr. "Finite element modeling of a plate with localized piezoelectric sensors and actuators." *Journal of the Brazilian Society of Mechanical Sciences and Engineering* 26.2 (2004): 117-128.
- [7] Douglas, B. E., and J. C. S. Yang. "Transverse compressional damping in the vibratory response of elastic-viscoelastic-elastic beams." *AIAA journal* 16.9 (1978): 925-930.

- [8] Egusa S. and Iwasawa N., "Piezoelectric paints as one approach to smart structural materials with health-monitoring capabilities", *Journal of Smart Materials & Structures*, Vol. 7, pp. 438-445, 1998.
- [9] Gillett, Philip W. *Head Mounted Microphone Arrays*. Diss. Virginia Polytechnic Institute and State University, 2009.
- [10] Gregory J. W. and Sullivan J. P., Wanis S. S., and Komerath N. M., "Pressure-sensitive paint as a distributed optical microphone array", *Journal of the Acoustical Society of America*, Vol. 119, No.1, pp. 251-261, January 2006.
- [11] Hale J. M., "Response to Application of Piezoelectric Paints to Damage Detection in Structural Materials", *Journal of Reinforced Plastics and Composites*, Vol. 17, No 4, 1998a.
- [12] Hale J. M., "Thick Film Strain Transducers Based on Piezoelectric Paint", *Proc. Computational Methods for Smart Structures and Materials - SMART 98*, Rome September 1998b.
- [13] Hale J. M. and Tuck J., "A Novel Thick-Film Strain Transducer Using Piezoelectric Paint", *Proc. IMechE Part C: J of Mechanical Engineering Science* vol.213 no.C6 1999.
- [14] Humphreys Jr, William M., et al. "Application of MEMS microphone array technology to airframe noise measurements." *AIAA Paper 2005-3004*, 11th AIAA/CEAS Aeroacoustics Conference. 2005.
- [15] Johnson, Don H., and Dan E. Dudgeon. *Array Signal Processing: Concepts and Techniques*. Englewood Cliffs, NJ: P T R Prentice Hall, 1993. Print.

- [16] Kinsler, Lawrence E. *Fundamentals of Acoustics*. 4th ed. New York: Wiley, 2000. Print.
- [17] Krause, J. S., White, R. D. , Moeller, M. J., Gallman, J. M., Holup, G. and deJong, R. "MEMS Pressure Sensor Array for Aeroacoustic Analysis of the Turbulent Boundary Layer", AIAA 2010-306, in Proceedings of the 48th AIAA Aerospace Sciences Meeting, Orlando, Florida, January 4-7, 2010.
- [18] Krim, H., Vibert, M. Two Decades of Array Processing Research: The Parametric Approach. *IEEE Signal Processing Magazine*, July 1996, 67-94.
- [19] Li, Dan, and Yu Hen Hu. "Energy-Based Collaborative Source Localization Using Acoustic Microsensor Array." *EURASIP Journal on Advances in Signal Processing*: 321-37. Web.
- [20] Leissa, Arthur W. *Vibration of Plates*. Washington, D.C.: Scientific and Technical Information Division, National Aeronautics and Space Administration, 1969. Print.
- [21] Löfdahl, Lennart, and Mohamed Gad-El-Hak. "MEMS-based Pressure and Shear Stress Sensors for Turbulent Flows." *Measurement Science and Technology* (1999): 665-86. Web.
- [22] Lum, P. et al. "High-Frequency Membrane Hydrophone". *IEEE Transactions on Ultrasonics, Ferroelectrics and Frequency Control* 43.4 (1996): 536-544. Web.
- [23] Menard, Kevin P. *Dynamic Mechanical Analysis – A Practical Introduction*. CRC Press, New York, 1999.

- [24] Mumolo, Enzo, Massimiliano Nolic, and Gianni Vercelli. "Algorithms For Acoustic Localization Based On Microphone Array In Service Robotic." *Robotics and Autonomous Systems* 42.2 (2003): 69-88. Web.
- [25] Murray, John C., Harry R. Erwin, and Stefan Wermter. "Robotic Sound-Source Localisation Architecture Using Cross-Correlation And Recurrent Neural Networks." *Neural Networks* 22.2 (2009): 173-189. Web.
- [26] Orlando, S., Bale, A. and D.A. Johnson, "Design And Preliminary Testing Of A MEMS Microphone Phased Array", *Proceedings of Berlin Beamforming Conference BeBeC, Berlin, Germany, February 24-25, 2010.*
- [27] Swaminathan, Gowthaman, Kunigal N. Shivakumar, and Larry C. Russell. "Anomalies, influencing factors, and guidelines for DMTA testing of fiber reinforced composites." *Polymer Composites* 30.7 (2009): 962-969.
- [28] Trees, Harry L. Van. *Detection, Estimation, and Modulation Theory Part IV.* Hoboken: John Wiley & Sons, 2005. Print.
- [29] Yu G., Zhang M. Q., Zeng H. M., Hou Y. H., and Zhang H. B., "Effect of Filler Treatment on Temperature Dependence of Resistivity of Carbon-Black-Filled Polymer Blends", *Journal of Applied Polymer Science*, Vol. 73, pp. 489-494, 1999.
- [30] Zhang M. Q. and Zeng H. M., *Handbook of Thermoplastics*; Olabisi, O., Ed.; Marcel Dekker: New York, 1997; p. 873.
- [31] Zhang Y., "Piezoelectric paint sensor for real-time structural health monitoring" Paper # 5765-121, *Sensors and Smart Structures Technologies for Civil,*

Mechanical, and Aerospace Systems Conference, SPIE Vol. #5765, ed. by M.
Tomizuka, San Diego, CA, 7-10 March 2005.